

REPORT DOCUMENTATION PAGE			Form Approved OMB No. 0704-0188	
Public reporting burden for this collection of information is estimated to average 1 hour per response, including the time for reviewing instructions, searching existing data sources, gathering and maintaining the data needed, and completing and reviewing the collection of information. Send comments regarding this burden estimate or any other aspect of this collection of information, including suggestions for reducing this burden, to Washington Headquarters Services, Directorate for Information Operations and Reports, 1215 Jefferson Davis Highway, Suite 1204, Arlington, VA 22202-4302, and to the Office of Management and Budget, Paperwork Reduction Project (0704-0188), Washington, DC 20503.				
1. AGENCY USE ONLY (Leave blank)		2. REPORT DATE 2.Nov.00		3. REPORT TYPE AND DATES COVERED THESIS
4. TITLE AND SUBTITLE AN APPLICATION OF H2/H00 ROBUST CONTROL SYNTHESIS TO LAUCH VEHICLE ASCENT			5. FUNDING NUMBERS	
6. AUTHOR(S) 2D LT HAGUE TYLER N				
7. PERFORMING ORGANIZATION NAME(S) AND ADDRESS(ES) MASSACHUSETTS INSTITUTE OF TECHNOLOGY			8. PERFORMING ORGANIZATION REPORT NUMBER CY00439	
9. SPONSORING/MONITORING AGENCY NAME(S) AND ADDRESS(ES) THE DEPARTMENT OF THE AIR FORCE AFIT/CIA, BLDG 125 2950 P STREET WPAFB OH 45433			10. SPONSORING/MONITORING AGENCY REPORT NUMBER	
11. SUPPLEMENTARY NOTES				
12a. DISTRIBUTION AVAILABILITY STATEMENT Unlimited distribution In Accordance With AFI 35-205/AFIT Sup 1			12b. DISTRIBUTION CODE	
13. ABSTRACT (Maximum 200 words)				
20001120 040				
14. SUBJECT TERMS			15. NUMBER OF PAGES 286	
			16. PRICE CODE	
17. SECURITY CLASSIFICATION OF REPORT	18. SECURITY CLASSIFICATION OF THIS PAGE	19. SECURITY CLASSIFICATION OF ABSTRACT	20. LIMITATION OF ABSTRACT	

CSDL-T-1371

**AN APPLICATION OF ROBUST H_2/H_∞ CONTROL
SYNTHESIS TO LAUNCH VEHICLE ASCENT**

by

Tyler Nicklaus Hague

June 2000

**Master of Science Thesis
Massachusetts Institute of Technology**

**Approved for public release;
distribution unlimited.**



The Charles Stark Draper Laboratory, Inc.
555 Technology Square, Cambridge, Massachusetts 02139-3563

An Application of H_2/H_∞ Robust Control Synthesis to Launch Vehicle Ascent

by

Tyler Nicklaus Hague

Submitted to the Department of Aeronautics and Astronautics on
May 5, 2000 in Partial Fulfillment of the Requirements for the
Degree of Master of Science in Aeronautics and Astronautics

ABSTRACT

This thesis explores the application of H_2/H_∞ control synthesis methods to launch vehicle ascent, specifically the pitch-plane control of the Kistler Aerospace launch vehicle, K1. A classical single-input, single-output design is also presented in order to assess the true applicability of a modern control synthesis approach to launch vehicle ascent. In addition, the K1 dynamics are developed to include aerodynamic, fuel-sloshing, tail-wags-dog, and body-bending effects.

The objective of the modern control synthesis approach presented here is to design compensation for pitch tracking and disturbance rejection. It combines techniques in optimal H_2 , optimal H_∞ , and sub-optimal control synthesis to create pitch control laws that provide 6 dB of gain margin and 30° of phase margin. The sensitivity and high-order of traditional H_2/H_∞ synthesis are addressed through the implementation of uncertainty in the design model and the application of balanced, model order reduction on the resulting controllers. To reduce the complexity in applying these methods, a hierarchical approach and design strategy is employed. Additionally, a graphical user interface is presented that exploits the capabilities of commercial software during the design.

A comparison of the two design methods, classical and modern, reveals that each design architecture is capable of creating controllers of equivalent order with both nominal and robust performance. The advantages of the modern approach are realized in the design process itself. The hierarchical methodology and intuitive nature of the modern approach helps to manage the selection of design parameters. Whereas, classical methods provide less insight into strategies for parameter selection and control design. Additionally, the ability to address disturbances and uncertainty in the modern approach offers a more direct alternative to the ad hoc and iterative nature of classical methods, and although not fully exploited here, the modern approach does allow coupling between channels to be accommodated. These conclusions confirm the viability of a modern control synthesis approach and establish the foundation for future development of modern-based, ascent control laws.

Thesis Supervisor: Frederick W. Boelitz
Title: Senior Member of the Technical Staff, Charles Stark Draper Laboratory

Thesis Advisor: Professor John J. Deyst
Title: Professor of Aeronautics and Astronautics

ACKNOWLEDGEMENTS

I would like to express my sincere gratitude to a number of people. Without their support, this thesis would not have been possible.

First, I would like to thank Fred Boelitz. His expertise in control design and familiarity with the Kistler control problem were an invaluable source of information and guidance. But, most importantly, I always felt that as my supervisor he cared more about my personal development and made sure I grew throughout the thesis experience. It has been a pleasure to work for him.

I also thank Dr. Brent Appleby, Professor John Deyst, and Mrs. Bette James for their contributions to the development of this thesis. Each provided invaluable comments and direction. A special thanks to Mrs. James for offering her talents and making sure that the ideas put into thesis were able to make it out.

I would also like to thank all of my MIT/Harvard friends, especially Scott, George, Jim, Troy, and Chris. Thanks for making my time in Boston a memorable one. I would like to give additional thanks to Scott for putting up with me every hour of every day for the last 4 years. He has been a valued friend, and his influence on my work is undeniable.

I want to thank my family for love and support they have given throughout my life. I have always been able to count on them. Thanks.

Finally, I want to thank Catie. Her friendship and love have brought out the best in me, and made me realize what I can accomplish. Thank you for being my constant source of inspiration.

This thesis was prepared at the Charles Stark Draper Laboratory, Inc. under Individual Research and Development funding, Project 15118. Publication of this thesis does not constitute approval by Draper or the sponsoring agency of the findings or conclusions contained herein. It is published for the exchange and stimulation of ideas.



Tyler N. Hague, 2 Lt., USAF

5 May 2000

ASSIGNMENT

Draper Laboratory Report Number T-1371

In consideration for the research opportunity and permission to prepare my thesis by and at The Charles Stark Draper Laboratory, Inc., I hereby assign my copyright of the thesis to The Charles Stark Draper Laboratory, Inc., Cambridge, Massachusetts.



Tyler N. Hague, 2 Lt., USAF 5 May 2000

Contents

CHAPTER 1	21
INTRODUCTION	21
1.1 Problem Motivation	21
1.2 General Problem Statement.....	22
1.3 Approach.....	22
1.3.1 <i>Model Referencing Adaptive Control (MRAC)</i>	23
1.3.2 <i>Dynamic Inversion</i>	24
1.3.3 <i>Constrained Convex Optimization</i>	25
1.3.4 <i>μ Synthesis</i>	25
1.3.5 <i>Robust Weighted H_2/H_∞ Based Designs</i>	26
1.4 Scope.....	26
1.4.1 <i>Continuous Time Solution</i>	26
1.4.2 <i>Boost Phase Pitch Plane Control</i>	27
1.4.3 <i>Design Point Selection</i>	27
1.4.4 <i>Design Method Portability</i>	28
1.5 Thesis Preview.....	28
CHAPTER 2	31
KISTLER LAUNCH VEHICLE MODEL.....	31
2.1 Physical System Description	31
2.1.1 <i>Kistler Launch Vehicle ("K1")</i>	31
2.1.2 <i>Thrust Vector Control Loop</i>	32
2.2 Reference Coordinate Frame.....	34

2.3 Mathematical Model	35
2.3.1 Dynamic Effects	35
2.3.2 Assumptions and Simplifications	36
2.3.3 K1 Plant Model (Stack)	37
2.3.4 Additional Control Loop Elements	39
2.4 Design Point Selection	41
2.4.1 Historical Considerations	41
2.4.2 Nominal Boost Phase Profile	41
2.4.3 Design Point System Analysis	43
2.5 K1 Frequency Response Analysis	44
CHAPTER 3	49
CLASSICAL CONTROL DESIGN	49
3.1 Classical Feedback Design Architecture	49
3.1.1 Proportional Derivative Control	50
3.1.2 N^{th} Order Bending Filter	51
3.2 Design Requirements	51
3.2.1 Frequency Requirements	51
3.2.2 Physical Constraints	52
3.2.3 Robust Requirements	53
3.3 SISO Controller Design	54
3.3.1 Bending Filter Reduction	54
3.3.2 Design Framework	56
3.3.3 Design Results	58
3.4 SISO Design Conclusions	62
CHAPTER 4	65
ROBUST WEIGHTED H_2/H_∞ CONTROL SYNTHESIS DEVELOPMENT	65
4.1 MCS Design Methodology	65
4.1.1 Canonical Problem Formulation	66
4.1.2 Non-Singularity Conditions	68
4.1.3 Input/Output Selection	70

4.1.4	<i>Design System Definition</i>	82
4.2	System Robustness	84
4.3	Design Solutions	91
4.3.1	<i>Optimal Robust Weighted H_2 Solution</i>	91
4.3.2	<i>Optimal Robust Weighted H_∞ Solution</i>	93
4.3.3	<i>Sub-Optimal Robust Weighted H_∞ Solution</i>	94
4.4	Controller Order Issues	95
CHAPTER 5	99
ROBUST WEIGHTED H_2/H_∞ CONTROL SYNTHESIS	99
5.1	Design Methodology	100
5.2	MATLAB/SIMULINK Based Design Architecture	104
5.3	Robust Weighted H_2/H_∞ Controller Design	110
5.3.1	<i>Full-Order Design</i>	111
5.3.2	<i>Robust Design</i>	123
5.3.3	<i>Reduced Order Design</i>	144
	<i>Design Analysis and Modified Iteration</i>	152
5.4	MCS Conclusions	160
CHAPTER 6	163
COMPARATIVE ANALYSIS OF CLASSICAL AND MCS DESIGN METHODS	163
6.1	Control Law Comparison	164
6.1.1	<i>Nominal Performance Comparison</i>	164
6.1.2	<i>Robust Performance Comparison</i>	173
6.2	Synthesis Approach Comparison	175
6.3	MCS Assessment	178
CHAPTER 7	179
CONCLUSIONS & RECOMMENDATIONS	179
7.1	Conclusions	179
7.2	Recommendations for Future Work	181

APPENDIX A.....	183
PITCH PLANE EQUATIONS OF MOTION	183
A.1 Variable Declaration.....	183
A.2 General Equations	186
A.3 Longitudinal EOMs.....	190
A.4 Pitch Plane External Stimuli	192
A.4.1 Gravity	192
A.4.2 Thrust.....	194
A.4.3 Engine Motion (“Tail-Wags-Dog”)	196
A.4.4 Aerodynamics	198
A.4.5 Fuel Sloshing	203
A.4.6 Accelerometer/Gyroscope	207
A.4.7 Pitch Plane EOM Summary for Inelastic Launch Vehicle.....	208
A.4.8 Body Bending (Flex)	210
A.5 Elastic Body Pitch Plane EOM Summary.....	216
APPENDIX B.....	221
NOMINAL TRAJECTORY PROFILES.....	221
APPENDIX C.....	225
MODEL VERIFICATION.....	225
C.1 Rigid Body Response.....	225
C.2 Aerodynamic Response	226
C.3 Engine Dynamics	233
C.4 Slosh Modes	234
C.5 Flex Modes	239
C.6 Baseline Model for T=72 sec (Mach 1.0)	240
APPENDIX D.....	241
GAIN VECTOR SEARCH ALGORITHM	241
D.1 MATLAB Code	241
D.2 SIMULINK Models.....	244

APPENDIX E	247
DISPERSION ANALYSIS SUMMARY	247
E.1 Individual 3- σ Perturbation Cases	247
E.2 Combined 1- σ Perturbation Cases	249
E.3 Design Alpha – 3- σ Results	251
E.4 Design Alpha – 1- σ Results	253
E.5 Design Beta – 3- σ Results	255
E.6 Design Beta – 1- σ Results	257
E.7 Design Gamma – 3- σ Results	258
E.8 Design Gamma – 1- σ Results	261
E.9 Design Delta – 3- σ Results	262
E.10 Design Delta – 1- σ Results	264
APPENDIX F	267
DISPERSION ANALYSIS TIME & FREQUENCY RESPONSE HISTORIES ...	267
F.1 Full-Order Optimal H_2 Design	268
F.2 GA Optimal H_2 Design	269
F.3 GA Sub-Optimal Design	271
F.4 $G_\Delta=1$, MU Optimal H_2 Design	273
F.5 $G_\Delta=10$, MU Optimal H_2 Design	274
F.6 $G_\Delta=20$, MU Optimal H_2 Design	275
F.7 MU Sub-Optimal Design	277
F.8 Reduced-Order GA Optimal H_2 Design	278
F.9 Reduced-Order MU Optimal H_2 Design	280
BIBLIOGRAPHY	283

List of Figures

Figure 1.1 – Indirect Adaptive Control Loop Structure	23
Figure 1.2 – Dynamic Inversion Framework	25
Figure 2.1 – Boost Phase Propulsion System Components	32
Figure 2.2 – K1 TVC Physical Description	33
Figure 2.3 – Representative TVC Loop	34
Figure 2.4 – Body Axis System	35
Figure 2.5 – Pitch Plane Free-Body Diagram	36
Figure 2.6 – Nominal Trajectory Dynamic Pressure Profile	42
Figure 2.7 – Nominal Trajectory Mach Profile	43
Figure 2.8 – Design Model Nichols Chart	45
Figure 2.9 – Design Model Bode Plot	46
Figure 3.1 – Classical Canonical Form.	50
Figure 3.2 – CSDL SISO Control Loop Realization.	50
Figure 3.3 – Modified PD Open Loop Frequency Response.....	55
Figure 3.4 – Modified PD Nichols Plot	56
Figure 3.5 – SISO Design Step Responses.....	63
Figure 3.6 – SISO Design Frequency Responses	63
Figure 4.1 – H_2/H_∞ Control Design Loop.....	66
Figure 4.2 – Reference Input in MIMO Control Loop	71
Figure 4.3 – Wind Input in MIMO Control Loop.....	72
Figure 4.4 – NASA Wind Gust Model	73
Figure 4.5 – Noise Inputs in MIMO Control Loop.....	74
Figure 4.6 – “False” Inputs in MIMO Control Loop.....	75
Figure 4.7 – Control Cost Output in MIMO Control Loop	75

Figure 4.8 – $U(s)$ Penalty Shaping Filter	76
Figure 4.9 – Sensitivity Cost Output in MIMO Control Loop.....	77
Figure 4.10 – General Control Loop Structure	78
Figure 4.11 – Sensitivity Waterbed Effect.....	79
Figure 4.12 – $S(s)$ Penalty Shaping Filter	80
Figure 4.13 – Control Inputs Input in MIMO Control Loop	81
Figure 4.14 – Control Output in MIMO Control Loop	82
Figure 4.15 – Nominal Loop Configuration	85
Figure 4.16 – Gain Augmentation	86
Figure 4.17 – Multiplicative Uncertainty	87
Figure 4.18 – Multiplicative Uncertainty Implementation.....	88
Figure 4.19 – Fit Analysis of Uncertainty Weight	89
Figure 5.1 – Control Synthesis Hierarchy	100
Figure 5.2 -- H_2/H_∞ Solution Process	102
Figure 5.3 – Robust Control Synthesis GUI	105
Figure 5.4 – Multiplicative Uncertainty Design Model	108
Figure 5.5 – Gain Augmentation Design Model	109
Figure 5.6 – Initial Weights for Cost Outputs, $z_{S(s)}$ and $z_{U(s)}$	111
Figure 5.7 – Pole-Zero Map of Full-Order, Optimal H_2 Controller	112
Figure 5.8 – Final Weights for Cost Outputs, $z_{S(s)}$ and $z_{U(s)}$	114
Figure 5.9 – Maximum Singular Values for the Optimal H_2 , Optimal H_∞ , and Sub- Optimal Designs	116
Figure 5.10 – Initial Full-Order H_2 Design Step Response.....	118
Figure 5.11 – Initial Full-Order H_2 Design Frequency Response	118
Figure 5.12 – Improved Full-Order H_2 Design Step Response	119
Figure 5.13 – Improved Full-Order H_2 Design Frequency Response.....	119
Figure 5.14 – Optimal Full-Order H_2 Design Step Response.....	120
Figure 5.15 – Optimal Full-Order H_2 Design Frequency Response	120
Figure 5.16 – Optimal Full-Order H_∞ Design Step Response	121
Figure 5.17 – Optimal Full-Order H_∞ Design Frequency Response	121
Figure 5.18 – Sub-Optimal Full-Order Design Step Response	122

Figure 5.19 – Sub-Optimal Full-Order Design Frequency Response.....	122
Figure 5.20 – K1 Plant Comparison.....	124
Figure 5.21 – $G=1.0$, GA H_2 Design Step Response	129
Figure 5.22 – $G=1.0$, GA H_2 Design Frequency Response.....	129
Figure 5.23 – $G=2.0$, GA H_2 Design Step Response	130
Figure 5.24 – $G=2.0$, GA H_2 Design Frequency Response.....	130
Figure 5.25 – GA H_∞ Design Step Response.....	131
Figure 5.26 – GA H_∞ Design Frequency Response	131
Figure 5.27 – GA Sub-Optimal Design Step Response	132
Figure 5.28 – GA Sub-Optimal Design Frequency Response.....	132
Figure 5.29 – Step Response Comparison.....	133
Figure 5.30 – Frequency Response Comparison	134
Figure 5.31 – $G_\Delta=1.0$, MU H_2 Design Step Response	139
Figure 5.32 – $G_\Delta=1.0$, MU H_2 Design Frequency Response.....	139
Figure 5.33 – $G_\Delta=10$, MU H_2 Design Step Response	140
Figure 5.34 – $G_\Delta=10$, MU H_2 Design Frequency Response.....	140
Figure 5.35 – $G_\Delta=20$, MU H_2 Design Step Response	141
Figure 5.36 – $G_\Delta=20$, MU H_2 Design Frequency Response.....	141
Figure 5.37 – MU H_∞ Design Step Response	142
Figure 5.38 – MU H_∞ Design Frequency Response.....	142
Figure 5.39 – MU Sub-Optimal Design Step Response.....	143
Figure 5.40 – MU Sub-Optimal Design Frequency Response	143
Figure 5.41 – Controller Order Comparison.....	145
Figure 5.42 – Reduced-Order, GA Robust H_2 Design Step Response	150
Figure 5.43 – Reduced-Order, GA Robust H_2 Design Frequency Response....	150
Figure 5.44 – Reduced-Order, MU Robust H_2 Design Step Response.....	151
Figure 5.45 – Reduced-Order, MU Robust H_2 Design Frequency Response ...	151
Figure 5.46 – Modified Control Loop Architecture.....	154
Figure 5.47 – Step Response of 7 th and 8 th Order Controllers.....	157
Figure 5.48 – Frequency Response of 7 th and 8 th Order Controllers	158

Figure 5.49 – Step Response of 10 th and 12 th Order Controllers	159
Figure 5.50 – Frequency Response of 10 th and 12 th Order Controllers	159
Figure 6.1 – Step Response Comparison	165
Figure 6.2 – Nichols Frequency Response Comparison.....	166
Figure 6.3 – Bode Frequency Response Comparison	166
Figure 6.4 – Wind Response Maximum Singular Value.....	169
Figure 6.5 – Angular Position Noise Response Maximum Singular Value.....	169
Figure 6.6 – Angular Rate Noise Response Maximum Singular Value	170
Figure 6.7 – Simulated Reference Input	172
Figure 6.8 – Simulated Wind Gust Input	172
Figure 6.9 – Comparison of Simulated Pitch and Gimbal Responses	173
Figure A.1 – General body with rotation about CG	187
Figure A.2 – Gravity Free-Body Diagram.....	193
Figure A.3 – Thrust Free-Body Diagram	194
Figure A.4 – TWD Free-Body Diagram	196
Figure A.5 – Angle of Attack Definition	201
Figure A.6 – Slosh Free-Body Diagram	203
Figure A.7 – IMU Reference Diagram.....	207
Figure A.8 – Body Bending Effects on Engine Gimbal.....	212
Figure B.1 -- Steady-State Pitch Angle Profile	221
Figure B.2 – Steady-State Angle of Attack Profile	222
Figure B.3 – Steady-State Center of Gravity Location Profile	222
Figure B.4 – Steady-State Acceleration Profile	223
Figure C.1 – Rigid Body Response Comparison	226
Figure C.2 – Simple Aerodynamic Response Comparison	227
Figure C.3 – Simple Aerodynamic Model Comparison	228
Figure C.4 – Complex Aerodynamic Response Comparison.....	230
Figure C.5 – Complex Aerodynamic Model Comparison	231
Figure C.6 – Small Angle Approximation Region of Validity	232
Figure C.7 – Comparison of Tail-Wags-Dog Zero Histories.....	233
Figure C.8 – Magnified View of Tail-Wags-Dog Histories	234

Figure C.9 – RP Slosh Frequency	235
Figure C.10 – RP Damping Coefficient	235
Figure C.11 – RP Slosh Mode Pole/Zero History	236
Figure C.12 – LOX Slosh Frequencies	237
Figure C.13 – LOX Damping Coefficients	237
Figure C.14 – LOX Main Slosh Mode Pole/Zero History	238
Figure C.15 – LOX Retention Mode Pole/Zero History	239
Figure C.16 – Flex Mode Pole/Zero Pairs at Mach 1.0	240
Figure D.1 – SISO Loop Transfer Function SIMULINK Model	245
Figure D.2 – SISO Closed Loop Transfer Function SIMULINK Model	245
Figure E.1 – Actuator Uncertainty Representations	249
Figure F.1 – Full-Order Optimal H_2 Design 3- σ Step Response History	268
Figure F.2 – Full-Order Optimal H_2 Design 3- σ Nichols Plot History	268
Figure F.3 – GA Optimal H_2 Design 3- σ Step Response History	269
Figure F.4 – GA Optimal H_2 Design 3- σ Nichols Plot History	269
Figure F.5 – GA Optimal H_2 Design 1- σ Step Response History	270
Figure F.6 – GA Optimal H_2 Design 1- σ Nichols Plot History	270
Figure F.7 – GA Sub-Optimal Design 3- σ Step Response History	271
Figure F.8 – GA Sub-Optimal Design 3- σ Nichols Plot History	271
Figure F.9 – GA Sub-Optimal Design 1- σ Step Response History	272
Figure F.10 – GA Sub-Optimal Design 1- σ Nichols Plot History	272
Figure F.11 – $G_\Delta=1$, MU Optimal H_2 Design 3- σ Step Response History	273
Figure F.12 – $G_\Delta=1$, MU Optimal H_2 Design 3- σ Nichols Plot History	273
Figure F.13 – $G_\Delta=10$, MU Optimal H_2 Design 3- σ Step Response History	274
Figure F.14 – $G_\Delta=10$, MU Optimal H_2 Design 3- σ Nichols Plot History	274
Figure F.15 – $G_\Delta=20$, MU Optimal H_2 Design 3- σ Step Response History	275
Figure F.16 – $G_\Delta=20$, MU Optimal H_2 Design 3- σ Nichols Plot History	275
Figure F.17 – $G_\Delta=20$, MU Optimal H_2 Design 1- σ Step Response History	276
Figure F.18 – $G_\Delta=20$, MU Optimal H_2 Design 1- σ Nichols Plot History	276
Figure F.19 – MU Sub-Optimal Design 3- σ Step Response History	277

Figure F.20 – MU Sub-Optimal Design 3- σ Nichols Plot History	277
Figure F.21 – Reduced-Order GA Optimal H_2 Design 3- σ Step Response History	278
Figure F.22 – Reduced-Order GA Optimal H_2 Design 3- σ Nichols Plot History	278
Figure F.23 – Reduced-Order GA Optimal H_2 Design 1- σ Step Response History	279
Figure F.24 – Reduced-Order GA Optimal H_2 Design 1- σ Nichols Plot History	279
Figure F.25 – Reduced-Order MU Optimal H_2 Design 3- σ Step Response History	280
Figure F.26 – Reduced-Order MU Optimal H_2 Design 3- σ Nichols Plot History	281
Figure F.27 – Reduced-Order MU Optimal H_2 Design 1- σ Step Response History	281
Figure F.28 – Reduced-Order MU Optimal H_2 Design 1- σ Nichols Plot History	282

List of Tables

Table 2.1 – LAP Design Model Parameters.....	44
Table 2.2 – Mode Shape Parameters for first 10 Bending Modes	44
Table 3.1 – Dispersion Parameter Summary	53
Table 3.2 – Classical Design Parameters	58
Table 3.3 – Successful SISO Design Results	59
Table 3.4 – Relaxed Attenuation Results.....	60
Table 3.5 – Design Alpha Dispersion Results.....	61
Table 3.6 -- Design Beta Dispersion Results	61
Table 5.1 – Full-Order Design Phase Summary	117
Table 5.2 – $G=1.0$, GA H_2 Design Performance Metrics.....	125
Table 5.3 – $G=2$, GA H_2 Design Performance Metrics.....	126
Table 5.4 – GA H_∞ Design Performance Metrics	127
Table 5.5 -- GA Sub-Optimal Design Performance Metrics	127
Table 5.6 – GA Robust Design Summary	128
Table 5.7 – $G_\Delta=1.0$, MU H_2 Design Performance Metrics	135
Table 5.8 – $G_\Delta=10$, MU H_2 Design Performance Metrics	135
Table 5.9 – $G_\Delta=20$, MU H_2 Design Performance Metrics	136
Table 5.10 – MU H_∞ Design Performance Metrics	137
Table 5.11 – MU Sub-Optimal Design Performance Metrics	137
Table 5.12 – MU Robust Design Summary.....	138
Table 5.13 – GA Robust H_2 Design HSVs	144
Table 5.14 – GA Robust H_2 Design Order Reduction Summary.....	145
Table 5.15 – MU Robust H_2 Design HSVs.....	146

Table 5.16 – MU Robust H_2 Design Order Reduction Summary	146
Table 5.17 – Reduced-Order Design Summary	147
Table 5.18 – Final Control Design Summary	160
Table 5.19 – MCS Summary	161
Table 6.1 – Performance Metric Summary	164
Table 6.2 – Figure Legend	165
Table 6.3 – Actuator Perturbation Results	174
Table E.1 – Individual 3- σ Test Cases	247
Table E.2 – Combined 1- σ Test Cases	250
Table E.3 – Design Alpha 3- σ Results	251
Table E.4 – Design Alpha – 1- σ Results	253
Table E.5 – Design Beta – 3- σ Results	255
Table E.6 – Design Beta – 1- σ Results	257
Table E.7 – Design Gamma – 3- σ Results	258
Table E.8 – Design Gamma – 1- σ Results	261
Table E.9 – Design Delta – 3- σ Results	262
Table E.10 – Design Delta – 1- σ Results	264

CHAPTER 1

Introduction

The objective of this thesis is to present a viable alternative to the classical control synthesis method currently used to design the ascent control law for the Kistler Aerospace launch vehicle, K1. Based on concepts from multivariable control systems theory, this thesis explores an alternative approach for a specified design point in the boost phase trajectory. A comparative analysis is presented, using a control law derived from classical principles, which highlights the capabilities and limitations of the Modern Control Synthesis (MCS) approach considered in this thesis. In conjunction with the modern control law development, an advanced set of linearized equations of motion (EOMs) are presented for the K1. These EOMs include rigid body motion, aerodynamic lift and drag, fuel-sloshing, engine inertia, and body-bending effects.

1.1 Problem Motivation

Classical, or Single-Input Single-Output (SISO), design techniques have been used extensively throughout the history of the launch vehicle industry, and the familiarity and success of these methods have helped to sustain their use in many in current applications. However, the SISO design process can be less intuitive, than more modern methods and usually requires numerous iterations and refinements. Furthermore, classical design techniques lack the ability to handle system disturbances and modeling errors simultaneously during the design process. Accounting for these multiple, naturally occurring factors can

quickly become an overwhelming task for the designer of a classical control system.

The maturity of modern control theory and the availability of software that supports Multiple-Input Multiple-Output (MIMO) applications now make MCS synthesis a viable alternative to classical methods. Both classical and modern methods are capable of designing successful controllers, but MCS design methods address the shortcomings of SISO synthesis. Problem formulation using MCS is intuitive and incorporates system disturbances, sensor noises, and model uncertainties: allowing it to account for multiple, coupled channels. Additionally, MCS synthesis generates controllers in a more direct manner through the solution of two Riccati equations.

1.2 General Problem Statement

Due to the shortcomings of classical design methods, there is a need to develop a more direct and intuitive approach for designing a first-stage, K1 control law. Not only are the requirements of nominal and robust performance significant, but the design process itself is also of importance. The primary goal of this thesis is to present a practical application of a systematic design methodology that can address many of the typical design challenges encountered with launch vehicles.

1.3 Approach

In order to select a proper basis for an alternative design method, initial research assessed several new areas of control synthesis for their applicability to launch vehicle boost phase control. This research explored two main control areas with an extensive background and a history of application at The Charles Stark Draper Laboratory: adaptive control and gain-scheduled linear control. Within adaptive control, Model Referencing Adaptive Control (MRAC) and Dynamic Inversion (DI) were studied. Within gain-scheduled linear control, which is the traditional ascent control law implementation, several control synthesis

techniques were also explored for ascent control application. Convex optimization, robust weighted H_2/H_∞ control, and μ -synthesis are all maturing techniques that have previously been applied to other “real-world” problems.

By successfully applying one of these possible modern control methodologies, or combining techniques from several approaches, an alternative first-stage control law can be developed. And, by comparison with a benchmark classical controller, the modern design methodology can be assessed for its applicability to K1 ascent.

1.3.1 Model Referencing Adaptive Control (MRAC)

MRAC is a form of direct adaptive control in which the controller monitors its own performance and adjusts one or more control parameters to achieve a desired response. The application of MRAC to launch vehicle control was studied by both Whitaker [30] and Best [4] since the 1960s. The drawback to this approach is the difficulty of maintaining stability in the presence of unmodeled dynamics, system disturbances, and sensor noise [2].

Variants of the direct adaptive approach have also been investigated. So-called, indirect adaptive control methods have recently been applied to, among other things, autonomous underwater vehicles by Claudberg [9]. Figure 1.1 shows a control loop representation of the indirect adaptive control approach.

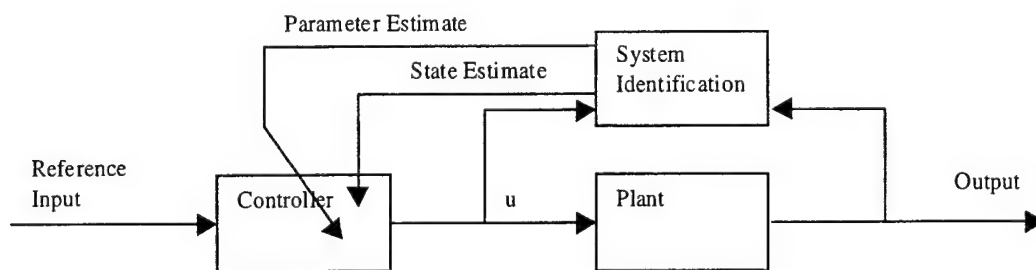


Figure 1.1 – Indirect Adaptive Control Loop Structure

This method, aided by computer technology, uses system identification techniques to overcome the problems associated with the unmodeled error

encountered by Whitaker and Best. By accessing the plant inputs and outputs, a model of the physical plant is generated using system identification techniques, which the controller uses for system state and control parameter estimates. However, this techniques requires extensive on-line computational power and is too complex an alternative for application to the K1.

1.3.2 Dynamic Inversion

The Dynamic Inversion (DI) design methodology, or feedback linearization, has been studied by Bedrossian [2], and extensively explored for its application to the micro air vehicle (MAV) by Brown [8], and the F-18 High Angle-of-Attack Research Vehicle (HARV) by Reigelsperger, et. al. [27]. With DI the controller comprises two elements (Figure 1.2). The first is a model of the desired plant dynamics, and the second is a dynamic inverter. The dynamic inverter effectively cancels the system dynamics using state and output measurements. Once the plant dynamics are inverted, the desired response shapes the closed-loop transfer function. An obvious limitation to this approach is the requirement of full state information [2]. Within the current K1 control framework, the fuel-sloshing and bending states are not measured, and the zero dynamics of the system become critical to stability [28]. To overcome a similar problem in large flexible aircraft, extra sensors were added to airframe extremities to sense the wing flex states [14]. Additionally, exact inversion of the plant dynamics make this control technique extremely susceptible to errors in the plant model. Considering the inability to sense slosh and bending states on the K1 and the need for an extremely accurate plant model, DI will not be considered as an alternative approach.

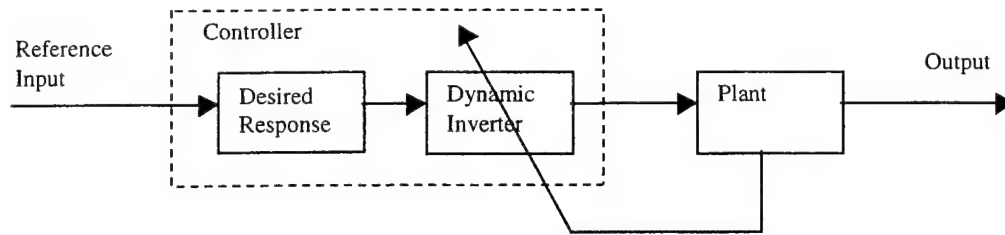


Figure 1.2 – Dynamic Inversion Framework

1.3.3 Constrained Convex Optimization

Constrained convex optimization is another synthesis method that has received much attention. Advanced by the increased capability of linear program solvers, constrained convex optimization has been applied to the Draper Small Autonomous Aerial Vehicle (DSAAV), the Earth Observing System (EOS) spacecraft, and the Active Vibration Isolation System (AVIS) in [20, 17]. Offering an alternative to both classical and model-based approaches, this method utilizes Youla (or Q) parameterization to obtain a solution from a predetermined set of basis functions. The central difficulty arises from the proper selection of basis functions, which increases the complexity of the synthesis process. In order to mature this ad hoc selection process, further research into a general set of orthonormal basis functions will be required [17].

1.3.4 μ Synthesis

μ -Synthesis is one of the more powerful synthesis tools available today, and has also been applied to the F-18 HARV [27]. An extension of the optimal H_∞ approach discussed in Chapter 4, μ -Synthesis uses structured uncertainties to achieve guaranteed robustness and specified performance levels. Composed of multiple complex techniques, μ -analysis, D-scaling, and H_∞ minimization, the design process has proven to be computationally intensive [15]. Furthermore, downfalls of this approach are the size of controllers it generates and its over-conservative guarantees for robustness, which lead to reduced performance capability [15].

1.3.5 Robust Weighted H_2/H_∞ Based Designs

Optimal H_2/H_∞ design methods are fundamental concepts in MCS theory. H_2/H_∞ refer to the norms of the cost function minimized during the design process. For an H_2 design, the norm is the average singular value; for an H_∞ design, it is the peak singular value. Alone, these model-based approaches are not particularly interesting, offering no advance to traditional loop shaping techniques [27]. Because they contain state estimates of the models for which they are designed, H_2/H_∞ designs are very sensitive to modeling errors and are high in order. However, augmenting these fundamental design methods with frequency cost-weights and system uncertainties, and applying model order reduction techniques can achieve successful results [15]. Implementing this approach can produce a synthesis process that is simple and intuitive with direct physical meaning. Not without its own drawbacks, a robust weighted H_2/H_∞ approach can still produce higher order controllers, and problem formulation can sometimes be difficult. However, this approach appears to be the most viable alternative to the current classical methods used in the K1 design and will serve as the foundation for the development of an MCS framework.

1.4 Scope

A central goal of this thesis is the successful demonstration of the alternative design process's applicability. To this end, great effort was taken to limit the simplifications and assumptions used in the multivariable framework. However, several notable simplifications and assumptions were deemed necessary and appropriate to aid in the completion of this work. These simplifications and assumptions will be discussed at length in the following sections.

1.4.1 Continuous Time Solution

Although the physical system is best described with continuous non-linear, time varying differential equations, the math models utilized in the design

framework are simplified to continuous linear time invariant (LTI) systems that characterize only the dynamics associated with small perturbations from equilibrium. This linearization process is fundamental to the gain-scheduled linear control synthesis technique, in which many point designs are made along the trajectory and blended together. However, the physical implementation of the final ascent control law is digital. For this thesis, the design process has been restricted to continuous analysis. Studies surrounding the continuous-to-digital conversion of the controllers and its impact on system performance are left for future research.

1.4.2 Boost Phase Pitch Plane Control

The development of a control synthesis methodology for K1 ascent is limited to the pitch plane only, which is defined in Chapter 2. This limitation assumes that the symmetry of the K1 permits the extension of any pitch plane analysis into the lateral plane. Therefore, the lateral and longitudinal motions will be uncoupled using reasonable assumptions consistent with past experience. Roll and yaw control are viewed as a separate, decoupled problem and are not considered in this work.

1.4.3 Design Point Selection

By choosing times during the boost phase for which control design has traditionally been difficult, the extension of the modern synthesis framework to other design points is assumed to be a relatively easy task. Traditionally, the most difficult design points during a boost phase trajectory are the transonic region (Mach 1.0) and the time at which maximum dynamic pressure, Q , occurs. For the K1, these two points occur within seconds of each other, approximately 72 seconds after launch. Therefore, only one point (Mach 1.0, $Q = 480$ psf) during the mission trajectory will be used as a basis for the comparison of the classical and multivariable synthesis methods. In developing the modern control synthesis method for this dynamically severe point in the trajectory, it is assumed that the design method can be extended with less challenge to further design

points in order to develop a control law for the entire boost phase. Obviously there will be issues surrounding the blending of controllers for the various point designs, but those issues are common to all gain-scheduled linear control approaches, both modern and classical, and are not investigated here.

1.4.4 Design Method Portability

Although the Kistler flight control problem has several unique aspects, many of the issues that must be addressed in its design are common to a larger, more general class of launch vehicles. Dynamic effects associated with forces caused by flexure, slosh, aerodynamics, engine motion, and actuators are topics central to a majority of launch vehicle control law designs; these effects are considered for the Kistler launch vehicle. The research presented here is intended to provide a viable engineering example from which concepts can be extracted and applied to a large class of launch vehicle control problems.

1.5 Thesis Preview

Following the introductory chapter, this thesis is organized as follows.

Chapter 2 presents the K1 physical system description and its associated reference frames. The development of the K1 pitch plane linearized EOMs is also presented along with discussion of the frequency response contributions of each dynamic effect. Inertial measurement unit (IMU) and actuator dynamics are briefly discussed, as well as associated computational delays.

Chapter 3 summarizes the classical design approach used to develop a pitch plane controller for the Mach 1.0 point. A brief summary of the existing Proportional-Derivative boost phase controller is presented to establish the need for a forward path bending filter. A gain vector search algorithm is used to automate the design process, and successful resulting controllers are analyzed.

Chapter 4 contains the background necessary to understand the modern control framework created to design robust H_2/H_∞ controllers. The canonical

problem formulation is discussed along with controllability and observability issues. Insight into weighting function selection is also provided. Finally, concepts surrounding the implementation of uncertainty in control law design, as well as controller order reduction, are addressed.

Chapter 5 presents the implementation of the framework addressed in Chapter 4. The MATLAB graphical user interface (GUI) and its supporting SIMULINK models are used to develop a series of MIMO control laws, which are analyzed against system performance specifications.

Chapter 6 provides a comparison of the control laws synthesized with modern techniques to the classical controllers developed in Chapter 3. Nominal and robust performance are analyzed, and simulated pitch and engine gimbal responses subject to wind disturbance and sensor noises are generated for each control design. Additionally, the capabilities and limitations of the two design processes are examined.

Chapter 7 summarizes the finding of this thesis and concludes with recommendations on areas for further investigation.

CHAPTER 2

Kistler Launch Vehicle Model

Mathematical models of the system to be controlled are of vital importance in any model-based design method. Large errors in modeled dynamics and parameter values will render any solutions useless in actual application. Therefore, a high level of attention must be paid to the development and verification of the models used in the synthesis architecture.

This chapter presents the K1 pitch plane control loop architecture and the mathematical models developed for each element in the loop. The dynamics of the K1 plant model at the Mach 1.0 design point are described. Appendices A (model development), B (nominal trajectory profiles), and C (model verification) support the work summarized here.

2.1 Physical System Description

2.1.1 Kistler Launch Vehicle (“K1”)

The K1 is a medium-sized launch vehicle designed to inject payloads into low Earth orbit. Totally reusable, the rocket consists of a first-stage Launch Assist Platform (LAP) and a second-stage Orbital Vehicle (OV). The LAP is propelled by three Russian built NK-43 liquid kerosene (RP) and oxygen (LOX) engines. The engines, mounted along a common thrust structure beam, each possesses 6° pitch and yaw axis gimbal authority. Vehicle attitude control

is achieved by modulating the thrust vectors of all three main engines within the physical constraints imposed by the gimbals.

During ascent, all three NK-43 engines are employed to boost the LAP and OV stages along a predefined attitude profile to an altitude of approximately 140,000 ft. The end of the ascent phase occurs when all three main engines are shut down and the LAP separates from the OV. Following separation, the LAP center engine is re-ignited, and the LAP is ballistically flown back to the launch site.

The physical configuration of the stack's boost phase propulsion system is presented in Figure 2.1. As shown, the RP is stored in a donut shaped tank and surrounds the cylindrical LOX retention tank. The main LOX tank is located forward of the other two propellant tanks. The main LOX and RP tank provide the necessary propellant during boost. (Only the main LOX tank is completely depleted by the end of the ascent phase.) Sufficient RP fuel remains along with the LOX in the retention tank for the LAP return burn.

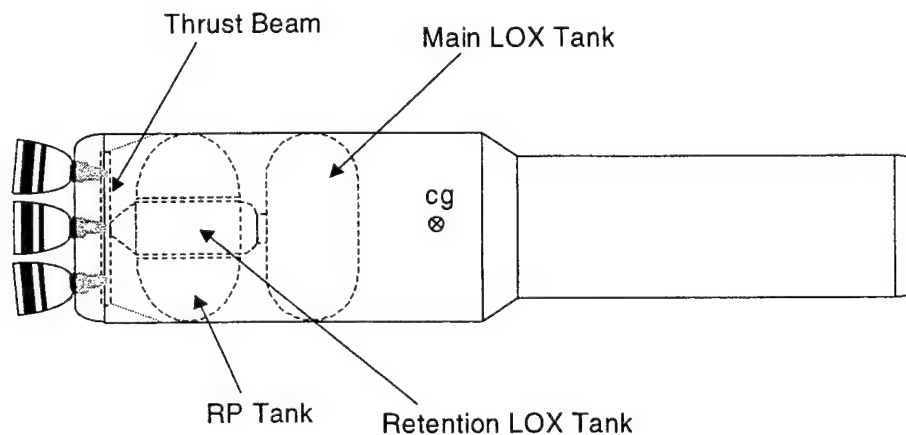


Figure 2.1 – Boost Phase Propulsion System Components

2.1.2 Thrust Vector Control Loop

In order to construct a Thrust Vector Control (TVC) loop to design a boost phase control law, the physical system must be translated into a representative model. Figure 2.2 shows the three main components of the K1 TVC.

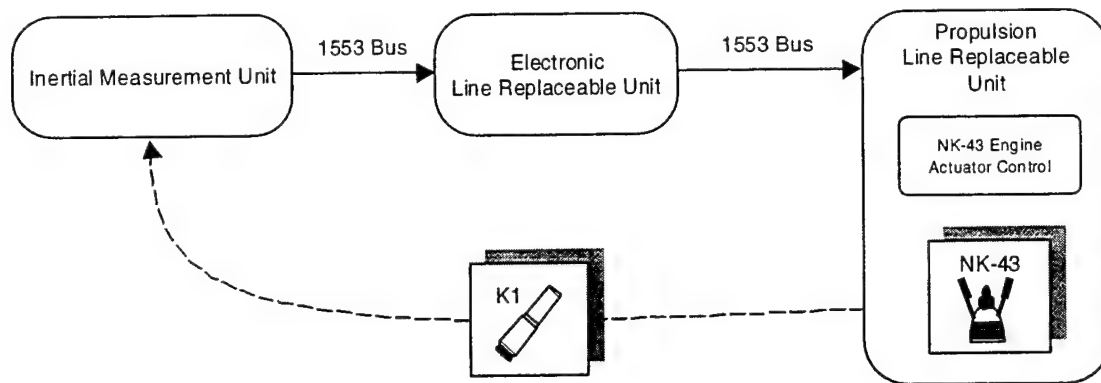


Figure 2.2 – K1 TVC Physical Description

The Inertial Measurement Unit (IMU) is composed of accelerometers and gyroscopes that sense the vehicle's rotational and translational accelerations. The IMU also integrates these measurements to produce pitch angle and pitch rate signals, which it sends to the Electronic Line Replaceable Unit (ELRU) on a standard 1553 bus. The ELRU, among other things, is the attitude control computer. Using references on the desired pitch angle and the information supplied by the IMU, the ELRU calculates necessary thrust vector angles to eliminate any attitude errors. These engine angles are transmitted over the 1553 bus to the Propulsion Line Replaceable Unit (PLRU). The PLRU is composed of all of the propulsion-related elements, such as fuel tankage, feed lines, and actuators. However, the most significant parts from a control design perspective are the Vehicle Motor Control (VMC), and the NK-43 engines. The VMC translates the control commands from the ELRU into commands for the hydraulic actuators that move the engines. The final and less tangible component of the K1 TVC, is the vehicle itself. The dynamics of the stack (combined first and second stages) translate engine motion into new sensor data for the IMU, which completes the TVC loop.

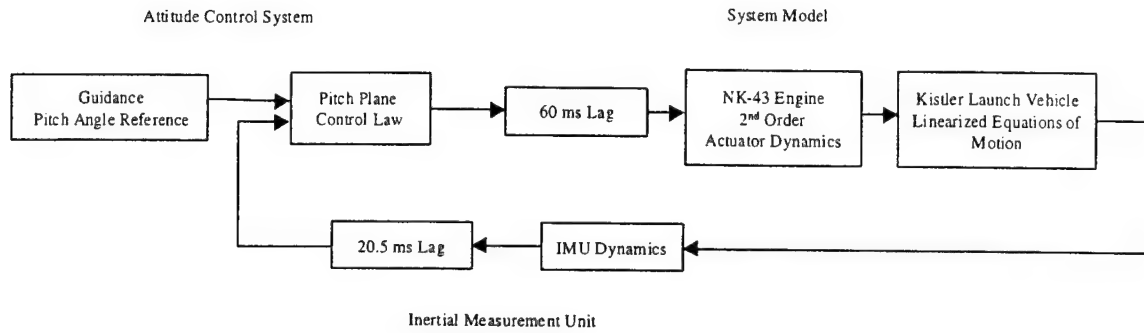


Figure 2.3 – Representative TVC Loop

The objective of the representative control loop is to characterize adequately the response of the physical system with a series of mathematical approximations. Figure 2.3 shows the control loop realization of the physical system. First, the IMU receives sensor information and provides calculated angular rate and attitude to the ELRU on a 1553 data bus. In order to characterize the dynamics and computation lags associated with the IMU, a 0.0205 second delay and a 17 Hz low-pass filter have been added to the feedback [6]. Second, the ELRU is represented by a pitch angle reference and the pitch plane control law. The focus of this thesis is the technique involved with designing the pitch plane control law portion of the ELRU. Third, the PLRU is represented by a mathematical model of the dynamics involved with the hydraulic actuators and a 0.06 second delay, which characterizes the computation and transportation times associated with the forward path from the VMC to the actuators [6]. Finally, the dynamics of the K1 are represented by a system of linearized Equations of Motion (EOMs).

2.2 Reference Coordinate Frame

Two main coordinate systems served as the reference frames for the development of the K1 mathematical model. The inertial reference frame is fixed, right handed, orthonormal, and centered near the K1 center of gravity (CG). The body axis system (Figure 2.4) is similar but free to move. Initially, the

two reference frames are aligned with the z-direction axis pointing down. Positive roll, pitch, and yaw rotations are also defined in Figure 2.4.

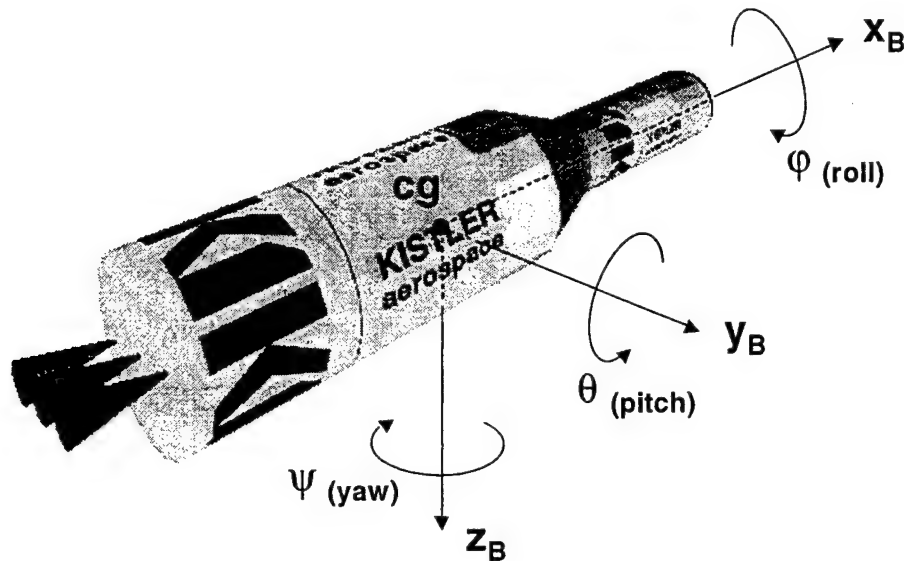


Figure 2.4 – Body Axis System

2.3 Mathematical Model

2.3.1 Dynamic Effects

The K1 Equations of Motion (EOMs) were derived to include the disturbance effects of gravity, thrust, Tail-Wags-Dog (TWD), fuel sloshing, and body bending, in addition to simple rigid body motion. Appendix A contains a full derivation of the elastic body, pitch plane EOMs. This set of continuous linear time invariant (LTI) EOMs was developed using a simple approach modeled after that used in the Space Shuttle EOM development [3]. First, the force and moment equations were derived from free-body diagram analysis. Figure 2.5 presents the pitch plane free-body diagram used in the math model development of thrust, gravity and aerodynamic forces. The specific diagrams for slosh, TWD, and flex are contained in Appendix A. Then, the equations were expanded into steady-state and perturbation elements. Next, appropriate trigonometric

identities were applied in conjunction with the small angle assumption. Finally, after removing the steady-state terms, a set of LTI EOMs remained.

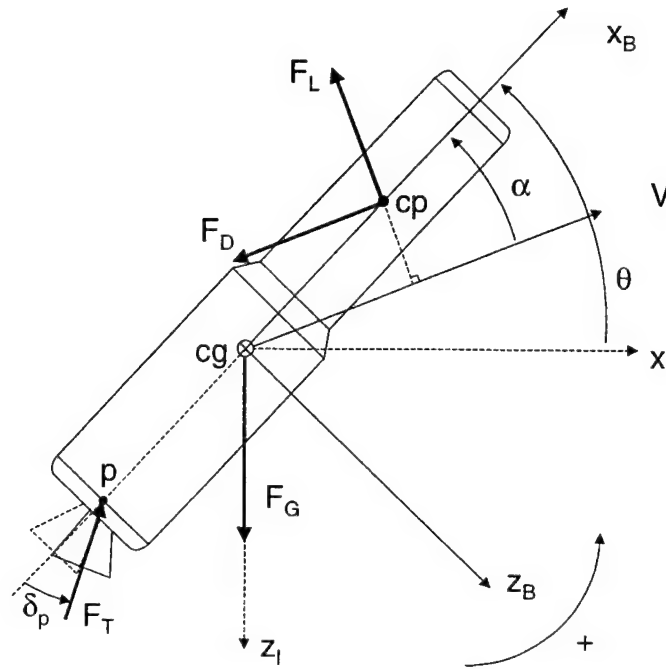


Figure 2.5 – Pitch Plane Free-Body Diagram

2.3.2 Assumptions and Simplifications

To support the gain-scheduled linear control approach, equations derived for the system model have been linearized about the nominal trajectory. Specifically, these equations are continuous LTI EOMs, which define perturbations from trim conditions. However, this approach requires that the dynamics of the system are slowly varying and that perturbations to the system are small in magnitude. It was also assumed that the three engines are not independently controllable. Therefore, a single engine with properties characteristic of the three NK-43 engines was used. Body-bending effects on the fuel-sloshing mass were assumed to be negligible as there was no data available on rotational and translational flex coefficients at the slosh nodes. Finally, due to the large difference in magnitude between the steady-state axial acceleration and

the perturbations to the axial acceleration, the axial disturbance force was also neglected, and the axial force EOM was removed.

2.3.3 K1 Plant Model (Stack)

The set of equations, 2.1 through 2.7, characterize the pitch plane disturbance response of the K1 vehicle. The simplifications presented in Section 2.3.2 were applied to the final set of pitch plane EOMs in Appendix A, and the resulting plant model state equations are summarized here.

Vertical Velocity State Equation:

$$\begin{aligned}
 m[\Delta \dot{w} + U_o \Delta q] = & -mg_o \sin \theta_o \Delta \theta - T \cos \delta_p (\Delta \delta_p + \sum_{j=1}^{\# \text{ flex modes}} \sigma_{ye} q_j) \\
 & - m_e l_e \cos \delta_p (\Delta \ddot{\delta}_p + \sum_{j=1}^{\# \text{ flex modes}} \sigma_{ye} \ddot{q}_j) \\
 & + S q C_{z\alpha} \Delta \alpha + \frac{S q L_{cp} C_{zq}}{2U_o} \Delta q \\
 & + \sum_{k=1}^{\# \text{ slosh mass}} m_{s_k} (\omega_{s_k}^2 Z_{s_k} + 2\zeta_{s_k} \omega_{s_k} \dot{Z}_{s_k})
 \end{aligned} \tag{2.1}$$

Pitch Angular Velocity State Equation:

$$\begin{aligned}
 \Delta \dot{q} l_{yy} = & \sum_{j=1}^{\# \text{ flex modes}} T \left[(l_{px} \cos \delta_{po} - l_{pz} \sin \delta_{po}) (\Delta \delta_p + \sigma_{ye} q_j) \right. \\
 & \left. + \phi_{xe} q_j \sin \delta_{po} + \phi_{ze} q_j \cos \delta_{po} \right] \\
 & + (m_e l_e (l_{px} \cos \delta_{po} - l_{pz} \sin \delta_{po}) - l_{yye}) (\Delta \ddot{\delta}_p + \sum_{j=1}^{\# \text{ flex modes}} \sigma_{ye} \ddot{q}_j) \\
 & + S q L_{cp} C_{m\alpha} \Delta \alpha + \frac{S q L_{cp}^2 C_{mq}}{2U_o} \Delta q \\
 & - \sum_{k=1}^{\# \text{ slosh mass}} m_{s_k} \left[\begin{aligned} & Q_o l_{sz_k} \Delta w + l_{sz_k}^2 \Delta \dot{q} + (W_o - 2Q_o l_{sx_k}) l_{sz_k} \Delta q \\ & + g_o l_{sz_k} \cos \theta_o \Delta \theta + 2(l_{sx_k} \omega_{s_k} \zeta_{s_k} + Q_o l_{sz_k}) \dot{Z}_{s_k} \\ & + (\dot{U}_o + Q_o W_o + g_o \sin \theta_o + (\omega_{s_k}^2 - Q_o^2) l_{sx_k}) Z_{s_k} \end{aligned} \right]
 \end{aligned} \tag{2.2}$$

Slosh Mass State Equation:

$$\begin{aligned} \ddot{Z}_{s_k} = & -\Delta\dot{w} + l_{sx_k} \Delta\dot{q} + (U_o + 2Q_o l_{sz_k}) \Delta q - g_o \sin \theta_o \Delta\theta \\ & - 2\omega_{s_k} \zeta_{s_k} \left(\dot{Z}_{s_k} - \sum_{j=1}^{\# \text{ flex modes}} \phi_{zs_k} \dot{q}_j \right) + Q_o^2 Z_{s_k} - \omega_{s_k}^2 \left(Z_{s_k} - \sum_{j=1}^{\# \text{ flex modes}} \phi_{zs_k} q_j \right) \end{aligned} \quad (2.3)$$

Angle of Attack State Equation:

$$\Delta\dot{w} - V\Delta\dot{\alpha} \cos \alpha_o = (U_o - V \cos \alpha_o) \Delta q \quad (2.4)$$

Flex Mode State Equation:

$$\begin{aligned} \ddot{q}_{lm} = & -2\zeta_m \omega_m \dot{q}_{lm} - \omega_m^2 q_{lm} \\ & - \sum_{j=1}^{\# \text{ flex modes}} \phi_{xe_m} \frac{T}{m_m} \sin \delta_{po} (\Delta\delta_p + \sigma_{ye_j} q_j) \\ & - \sum_{j=1}^{\# \text{ flex modes}} \phi_{ze_m} \frac{T}{m_m} \cos \delta_{po} (\Delta\delta_p + \sigma_{ye_j} q_j) \\ & + \sum_{j=1}^{\# \text{ flex modes}} \sigma_{ye_m} \frac{T}{m_m} \left[(l_{px} \cos \delta_{po} - l_{pz} \sin \delta_{po}) (\Delta\delta_p + \sigma_{ye_j} q_j) \right. \\ & \quad \left. + \phi_{xe_j} q_j \sin \delta_{po} + \phi_{ze_j} q_j \cos \delta_{po} \right] \\ & - \sum_{j=1}^{\# \text{ flex modes}} \phi_{xe_m} \frac{m_e}{m_m} l_e \sin \delta_{po} (\Delta\ddot{\delta}_p + \sigma_{ye_j} \ddot{q}_j) \\ & - \sum_{j=1}^{\# \text{ flex modes}} \phi_{ze_m} \frac{m_e}{m_m} l_e \cos \delta_{po} (\Delta\ddot{\delta}_p + \sigma_{ye_j} \ddot{q}_j) \\ & - \sum_{j=1}^{\# \text{ flex modes}} \frac{\sigma_{ye_m}}{m_m} (l_{yye} - m_e l_e (l_{px} \cos \delta_{po} - l_{pz} \sin \delta_{po})) (\Delta\ddot{\delta}_p + \sigma_{ye_j} \ddot{q}_j) \end{aligned} \quad (2.5)$$

Gyroscopic Output Equations:

$$\Delta q_{\text{actual}} = \Delta q_{\text{sensed}} - \sum_{j=1}^{\# \text{ flex modes}} \sigma_{y \text{ gyros}} \dot{q}_j \quad (2.6)$$

$$\Delta \dot{q}_{\text{actual}} = \Delta \dot{q}_{\text{sensed}} - \sum_{j=1}^{\# \text{ flex modes}} \sigma_{y \text{ gyros}} \ddot{q}_j \quad (2.7)$$

All the parameters used in equations 2.1 through 2.7 are defined in Appendix A. The state-space representation of these equations used in design is defined by,

$$\begin{aligned}\dot{x}_p &= A_p x_p + B_p u_p \\ \theta &= C_{p1} x_p \\ \dot{\theta} &= C_{p2} x_p\end{aligned}\tag{2.8}$$

The system inputs, u_p , are gimbal angle and gimbal angular acceleration, and the outputs are obviously pitch angle and pitch rate. The order of the stack model ranges from 2nd order when all dynamics have been neglect except for rigid body motion to 29th order when all dynamic effects are included.

2.3.4 Additional Control Loop Elements

It is important to present the math models of all the pitch plane control loop elements. A more thorough discussion of these elements and of the control loop structure is provided in Chapters 3 and 5. Unlike the K1 plant model that has time varying parameters, these elements remain essentially constant over the entire flight profile.

Actuator Model

The engine actuators have been modeled as a simple 2nd order spring-mass-damper system consistent with specifications [6]. The actuator differential equation is given by equation 2.9, where the frequency is nominally 25.13 rad/s and the damping coefficient is 0.707.

$$\ddot{\delta} + 2\zeta_A \omega_A \dot{\delta} + \omega_A^2 \delta = \omega_A^2 \delta_C\tag{2.9}$$

In order to provide the actuator acceleration information necessary to model TWD, the output equation has been modified to include attitude and angular acceleration information. The resulting state-space representation is,

$$\begin{aligned}\dot{x}_A &= A_A x_A + B_A u_A \\ u_p &= C_A x_A + D_A u_A\end{aligned}\tag{2.10}$$

IMU Model

IMU attitude and angular rate have been shown to act like 1st order low-pass filters with a bandwidth of 17 Hz (~100 rad/s) and unit DC gain [6]. Using this guidance, the state-space representations shown by equations 2.11 and 2.12 were implemented in the feedback path for both pitch and pitch rate signals.

$$\begin{aligned}\dot{x}_\theta &= A_\theta x_\theta + B_\theta \theta \\ \theta_S &= C_\theta x_\theta\end{aligned}\tag{2.11}$$

$$\begin{aligned}\dot{x}_{\dot{\theta}} &= A_{\dot{\theta}} x_{\dot{\theta}} + B_{\dot{\theta}} \dot{\theta} \\ \dot{\theta}_S &= C_{\dot{\theta}} x_{\dot{\theta}}\end{aligned}\tag{2.12}$$

Computational Delay Models

Computation and Transportation delays of 0.06 s and .0205 s are respectively present in both the forward path and feedback path of the control loop [6]. Several different ordered Pade approximations were analyzed for modeling these delays. However, adequate system lag was introduced using only a 1st order Pade approximation. Using MATLAB function *pade.m* to create the appropriate system, the following state-space representations were introduced into the control loop:

$$\begin{aligned}\dot{x}_{60} &= A_{60} x_{60} + B_{60} u \\ u_A &= C_{60} x_{60} + D_{60} u\end{aligned}\tag{2.13}$$

$$\begin{aligned}\dot{x}_{20_1} &= A_{20_1} x_{20_1} + B_{20_1} \theta_S \\ y_2 &= C_{20_1} x_{20_1} + D_{20_1} \theta_S\end{aligned}\tag{2.14}$$

$$\begin{aligned}\dot{\mathbf{x}}_{20_2} &= \mathbf{A}_{20_2} \mathbf{x}_{20_2} + \mathbf{B}_{20_2} \dot{\theta}_S \\ y_3 &= \mathbf{C}_{20} \mathbf{x}_{20} + \mathbf{D}_{20_2} \dot{\theta}_S\end{aligned}\tag{2.15}$$

The system in equation 2.13 is the 0.06 VMC delay in the forward path, and equations 2.14 and 2.15 are the IMU delays in the feedback path. Two separate, but identical, state-space models of the IMU delays were incorporated—one to account for pitch angle and one to account for pitch rate.

2.4 Design Point Selection

2.4.1 Historical Considerations

In developing an MCS framework for point design controller synthesis, a decision was made to formulate the process around a trajectory point that has historically proven to be difficult. Typically, the two most demanding regions of a boost profile are the transonic and maximum dynamic pressure regions. The transonic region is characterized by large fluctuations in the aerodynamic derivative coefficients. These dramatic changes create elevated levels of uncertainty in the linearized equations, and emphasize the importance of a quality controller during this region. The maximum dynamic pressure on the vehicle also places increased importance on controller quality. During this section of the trajectory, the structural load created by a non-zero angle-of-attack is the most extreme. The size of the load, which is characterized by dynamic pressure and angle-of-attack ($Q\alpha$), serves as a physical limitation that must be accommodated by the control law. The historical importance of successful control within these two regions immediately identifies them as candidates on which to base the development of an MCS control synthesis framework.

2.4.2 Nominal Boost Phase Profile

In order to apply the pitch plane EOMs summarized in equations 2.1 through 2.7 and begin the process of creating a controller point design, a nominal

pitch plane profile was generated. The nominal trajectory information applied herein is based on simulation results performed on the UNIX Simulation Framework at Draper Laboratory. Using a preliminary Proportional-Derivative (PD) controller data for the pitch plane boost phase was collected to serve as steady-state response information. Figure 2.6 shows the dynamic pressure profile of the nominal trajectory. Figure 2.7 shows the Mach profile of the same trajectory. As alluded to earlier, the critical points of these profiles are highlighted. The Mach 1.0 point occurs 72 seconds into the boost phase, and the maximum dynamic pressure point occurs at 81 seconds. Because both of these points occur within only seconds of each other, the Mach 1.0 point will serve as the design point during the development of the MCS framework. Using this point, the design process should be capable of being extended to the remaining design points in the trajectory. Appendix B contains further information on the nominal pitch plane profile, detailing pitch angle, angle-of-attack, acceleration, and CG location histories.

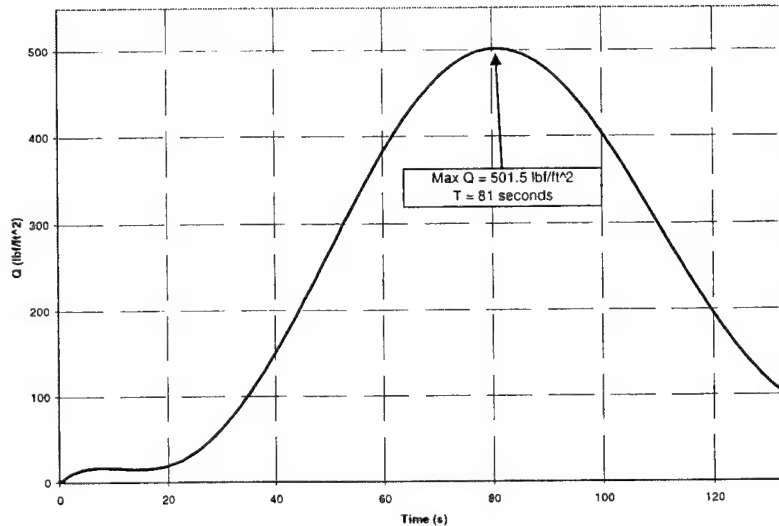


Figure 2.6 – Nominal Trajectory Dynamic Pressure Profile

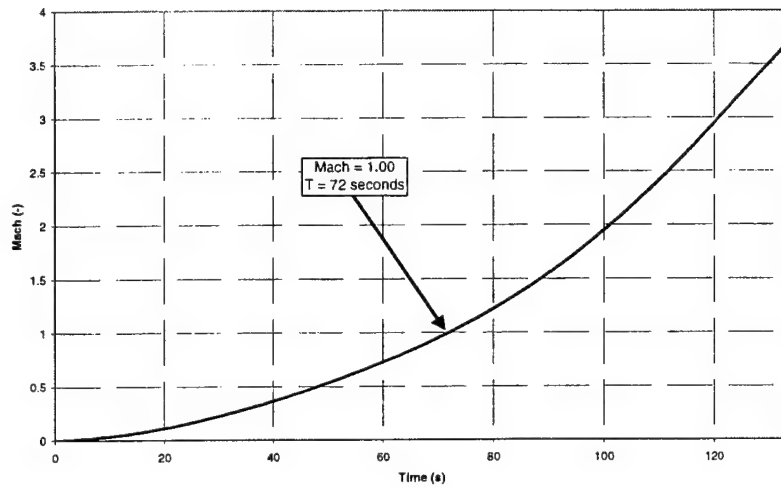


Figure 2.7 – Nominal Trajectory Mach Profile

2.4.3 Design Point System Analysis

A thorough verification of the pitch plane dynamics was performed to ensure the correctness of the K1 mathematical model. Using the nominal trajectory data, pole/zero histories of the pitch plane dynamics were compared to the reference models and assessed for discrepancies. Appendix C contains a full description of the pitch-plane, K1 EOM verification for the pitch plane.

The results of this process support using the pitch plane model (equations 2.1 through 2.7) in the development of a control design process. Using this model, the K1 frequency response was generated at the Mach 1.0 design point. Tables 2.1 and 2.2 summarize the parameter values for the K1 model at $T = 72$ s (Mach 1.0).

Table 2.1 – LAP Design Model Parameters

Parameter	Value (units)		
T	1.0991×10^6 (lbf)	I_{sxlx_ret}	-33.3214 (ft)
M	1.8565×10^4 (slugs)	I_{szlx_ret}	0 (ft)
I_{yy}	1.63×10^7 (slug-ft ²)	m_{srp}	1340.3 (slugs)
I_{px}	-44.468(ft)	ω_{srp}	2.3208 (rad/s)
I_{pz}	0 (ft)	ξ_{srp}	.000375
M_e	304.125 (slugs)	I_{srxp}	-37.4796 (ft)
I_{eyy}	8023.1 (slug-ft ²)	I_{szrp}	0 (ft)
I_e	4.05 (ft)	U_0	985.9607 (ft/s)
m_{slx}	3285.2 (slugs)	S	201 (ft ²)
ω_{slx}	2.6675 (rad/s)	\bar{q}	480 (lbf/ft ²)
ξ_{slx}	.000087	L	16 (ft)
I_{sxlx}	-23.35 (ft)	$C_{z\alpha}$	-.0721 rad ⁻¹
I_{szlx}	0 (ft)	$C_{m\alpha}$.0921 rad ⁻¹
m_{slx_ret}	104.824 (slugs)	C_{mq}	-34.58 rad ⁻¹
ω_{slx_ret}	5.9148 (rad/s)	α_0	-.71 deg
ξ_{slx_ret}	.0027		

Table 2.2 – Mode Shape Parameters for first 10 Bending Modes

Flex Mode	ϕ_{xe}	ϕ_{ze}	σ_{ye}	σ_{IMU}	ω_i (rad/s)	ξ_i
1	-.00069	.000069	.00000052	.00000002	18.47	0.01
2	-.0000016	-.000824	-.00000385	-.00000022	20.77	0.01
3	-.000035	.00371	.000017	.0000122	20.83	0.01
4	.000116	-.00576	-.0000347	-.0000289	24.60	0.01
5	-.000615	.0315	.000212	.000126	24.74	0.01
6	.000255	.00018	.00000119	.00000084	27.71	0.01
7	.000553	-.00187	-.0000273	-.00000838	30.41	0.01
8	.000445	-.0067	-.000273	-.000026	32.26	0.01
9	-.000759	-.00986	-.0000181	-.0000577	32.53	0.01
10	.00054	-.00309	-.00000499	-.0000166	33.28	0.01

2.5 K1 Frequency Response Analysis

Two types of frequency responses will be used for analysis throughout this thesis. Figure 2.8 presents a Nichols representation of the K1 system model

frequency response. Nichols plots will be used primarily because of their easily interpreted graphical representation of stability and various stability margins. In addition, dynamic effects are more distinguishable when the frequency response is plotted as magnitude versus phase. Bode plots will also be used to reference specific dynamic effects to points in the frequency spectrum. Figure 2.9 presents a Bode plot of the plant's frequency response. Together, these representations provide an adequate means of assessing the system dynamics.

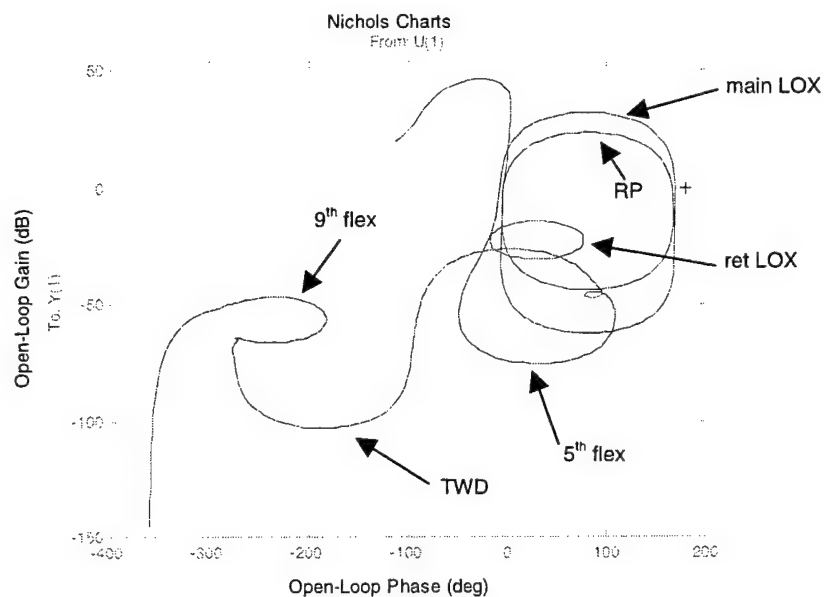


Figure 2.8 – Design Model Nichols Chart

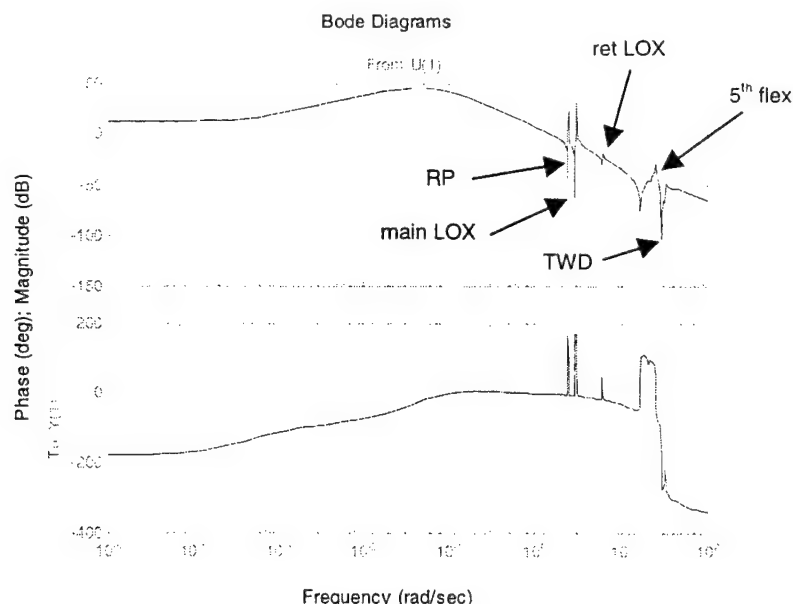


Figure 2.9 – Design Model Bode Plot

Understanding the effects or stability of different dynamics within the system can prove to be very beneficial in formulating and solving MCS problems. First, consider the gain plot in Figure 2.9, in which the gain of the system frequency response is plotted against a logarithmic frequency scale. Using Table 2.1 and data, it is easy to interpret the source of the different resonant peaks. The first resonant frequency is at 2.3 rad/s and is attributable to the RP slosh mode. The Nichols plot realization of this mode is the second largest loop centered around 100° and 0 dB in Figure 2.8. Returning to Figure 2.9, the second peak at 2.6 rad/s is created by fuel sloshing in the main LOX tank. This appears as the largest loop in the Nichols plot centered again at 100° and 0 dB. The LOX retention tank slosh mode is realized occurs at 5.9 rad/s in Figure 2.9. In Figure 2.8, this mode is represented by the small loop centered at approximately 50° and -25 dB. The remaining dynamics in the 20-40 rad/s range of the bode plot are due to the ten flex modes and TWD. Because of vehicle rigidity and IMU placement, only a few of the flex modes are observable at the Mach 1.0 design point. Not easily seen in Figure 2.9, the flex modes become much more distinguishable in the Nichols plot. The magnitudes of the IMU node flex coefficients in Table 2.2 indicate that the 5th and 9th flex modes will be

predominant in the system response. The 5th flex mode is visible in Figure 2.1 as the large lower loop centered around 50° and -50 dB. The small inclusion on the right side of this loop can be attributed to an almost unobservable flex mode. Continuing left in the Nichols plot, the large trough centered at -180° is created by TWD dynamics. It is at this frequency (~30 rad/s) that an input signal will achieve no output response. Thus, the trough represents dramatic input attenuation. Finally, the 9th flex mode appears as a loop centered at approximately -250° and - 50 dB. This knowledge of the relative importance of the K1 dynamics will prove useful in Chapter 5, as the uncontrollable and more insignificant modes are eliminated during problem formulation.

CHAPTER 3

Classical Control Design

A preliminary boost phase control law has been developed for the K1. Using a modified Proportional-Derivative (PD) approach, this controller was designed for a simplified version of the K1 dynamics that included rigid body and aerodynamic effects. The control gains for this preliminary control law are:

$$\begin{aligned} K_p &= 1.1917 \\ K_d &= 0.5137 \end{aligned} \tag{3.1}$$

Dynamics such as slosh, TWD, and flex were not considered in this design, and results will show that the existing PD controller is not capable of meeting the system requirements in the presence of these additional dynamics. Instead, additional forward loop compensation is required to achieve successful results.

The following chapter discusses the performance requirements for the K1 boost phase as well as the approach taken to design a control law capable of meeting these requirements. The classical design presented here will form the basis of comparison for a new design approach employing MCS methods.

3.1 Classical Feedback Design Architecture

The canonical, classical control loop representation shown in Figure 3.1 can be transformed into one specific to the K1 boost phase problem. Using the control loop information presented in Chapter 2, the addition of proportional and

derivative gains, as well as a bending filter in the forward path, completes the classical control architecture. Figure 3.2 shows the implementation of the CSDL control loop for Single-Input, Single-Output (SISO) design.

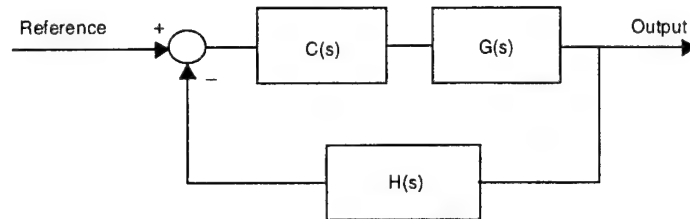


Figure 3.1 – Classical Canonical Form.

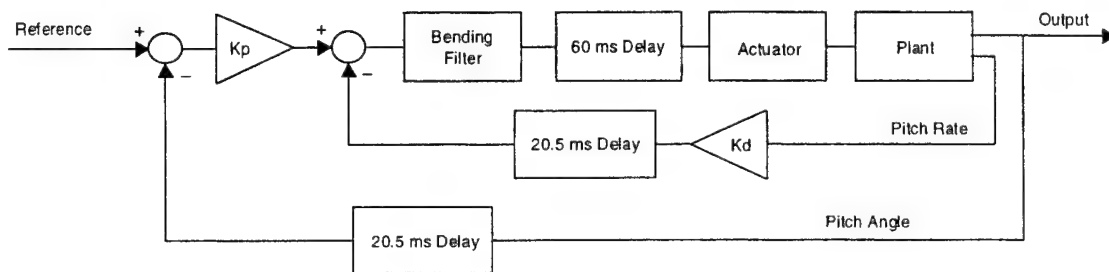


Figure 3.2 – CSDL SISO Control Loop Realization.

Additional IMU dynamics were discussed in Chapter 2. However, adding a low-pass filter with such a high bandwidth (well beyond any other system dynamics) into the feedback paths was expected to have little effect on the controller design. Therefore, the IMU dynamics were neglected during the SISO design process. Later analysis confirms this assumption, when IMU dynamics were added to the feedback with no noticeable change in system performance.

3.1.1 Proportional Derivative Control

Proportional control by itself can raise or lower the system gain, which shifts both Bode magnitude and Nichols plots up or down. A combined PD controller introduces a zero into the system at the value $s = -K_P/K_D$. Thus, PD control is a type of phase-lead compensation, which adds phase and gain to the loop transfer function [26]. The standard form of a PD pitch plane controller is

defined by equation 3.2. However, the existing architecture outlines the implementation of a modified PD controller that makes use of the pitch rate information provided by IMU sensors. Equation 3.3 defines the K1 implementation of PD control.

$$\delta_C = K_P (\theta_{Ref} - \theta_{Sensed}) + K_D \frac{d(\theta_{Ref} - \theta_{Sensed})}{dt} \quad (3.2)$$

$$\delta_C = K_P (\theta_{Ref} - \theta_{Sensed}) - K_D \dot{\theta}_{Sensed} \quad (3.3)$$

3.1.2 Nth Order Bending Filter

Beyond modified PD compensation, an nth order filter is added to the forward loop to address the effects of advanced model dynamics. Specifically, the bending filter helps reduce the effects of slosh, TWD, and flex. Designated to have a maximum of 10 states, the filter is generally a system of lead and lag filters used to shape the loop response [34]. Notch filters are another, potentially more risky, type of compensation. Notch filters are pole-zero pairs that attempt near cancellation of complex pairs in the vehicle dynamics [11]. However, relatively large uncertainties associated with the controlled dynamics reduce the effectiveness of this approach, and the application of notch filters to K1 boost control is not pursued herein.

3.2 Design Requirements

3.2.1 Frequency Requirements

Traditionally, requirements placed on controller performance laws are based on system frequency response characteristics. The basic rigid body frequency domain requirements are:

- 1) Gain margin (GM) in excess of 6 dB at the initial 180° crossover, and
- 2) Phase margin (PM) in excess of 30° at the initial 0 dB crossover.

Due to the multiple loop structure of the CSDL pitch plane architecture, GM and PM are calculated for a break in the inner loop immediately after the bending filter. In general, all loops present in the problem should be analyzed to find the one most critical to system stability [25]. However, previous analysis has shown the inner loop in the CSDL architecture to be most critical to stability [6].

In addition to these basic requirements, further requirements have been self imposed to limit the controller's susceptibility to dynamic uncertainties. They are:

- 3) -6 dB attenuation of the LOX retention slosh mode; and
- 4) -10 dB attenuation on all modes higher than the LOX retention slosh mode frequency.

These requirements were derived from those presented for application to a similar pitch plane control problem [7]. The only notable departure from those requirements was that the LOX retention mode should also be gain stabilized to accommodate uncertain phase reduction caused by system delays. Uncertain delays in the system cause the Nichols plot to shift left or right as a function of frequency. This could lead to a reduction in the GM and PM, unless adequate attenuation of the LOX retention mode and the 5th flex mode is maintained.

3.2.2 Physical Constraints

Two main physical constraints are associated with the K1 launch vehicle structure. The first constraint is that the engine gimbal angle is limited to $\pm 6^\circ$ [6]. The second constraint is that the level of lateral acceleration, G's, is limited to ± 3 G's. In order for the control system to be feasible, it must be capable of successfully stabilizing the pitch response of the K1 without violating these restrictions. Presently, analysis has revealed that the constraint on the range of engine motion dominates the constraint on lateral G's. Therefore, the constraint on the maximum engine deflection will be used in control system performance analysis.

3.2.3 Robust Requirements

Stability in the presence of K1 model error is a final control system requirement. To ensure that the controller remains stable, SISO design processes typically include extensive dispersion analysis. During this analysis, the K1 model parameters are varied by expected values and assessed for their impact on system stability. One method of testing parameter variations consists of two phases, testing all significant model parameters first for individual 3- σ perturbations and then for their combined 1- σ perturbations. However, testing all of these possible cases can become time intensive, considering there are over 50 different parameters with associated uncertainties. Instead, a reduced set of dispersion cases has been designed to provide a realistic testing of each controller's robustness [24]. In the first phase, 42 parameter variations were identified as having potentially significant impact on system stability. These parameters and their associated levels of uncertainty are summarized in Table 3.1. The uncertain transfer function representation for the actuators is presented in Appendix E. Each parameter was then individually perturbed by its 3- σ variation and analyzed for its impact on GM and PM.

Table 3.1 – Dispersion Parameter Summary

Parameter	3- σ (%)	Used in 1- σ			
T	1	-	ω_{srp}	10	-
Actuator	TF	Y	ξ_{srp}	10	-
I_{px}	.7	-	I_{srxp}	10	-
cg	.5	-	q	20	-
I_{yy}	.8	-	$C_{z\alpha}$	25	-
m_{slx}	10	-	$C_{m\alpha}$	15	-
ω_{slx}	10	Y	C_{mq}	15	-
ξ_{slx}	10	-	ω_1	10	-
I_{sxlx}	10	-	ζ_1	1	-
m_{slx_ret}	10	Y	ω_2	10	-
ω_{slx_ret}	10	Y	ζ_2	1	-
ξ_{slx_ret}	10	Y	ω_3	10	-
I_{sxlx_ret}	10	Y	ζ_3	1	-
m_{srp}	10	-	ω_4	10	-
			ζ_4	1	-

ω_5	10	Y	ζ_8	1	-
ζ_5	1	-	ω_9	10	-
ω_6	10	-	ζ_9	1	-
ζ_6	1	-	ω_{10}	10	-
ω_7	10	-	ζ_{10}	1	-
ζ_7	1	-	t	5	-
ω_8	10	-			

For the second phase, the 7 most predominant parameters in phase one were used to create a reduced variable set for combined disturbances [24]. These are summarized in Appendix E. Restricted to only 3 parameter variations per test case, each 3 parameter combination of 1- σ perturbations was analyzed for its impact on system stability. The result of this two-phase process is a “guarantee” that the controller is robust to the most likely model uncertainties.

3.3 SISO Controller Design

3.3.1 Bending Filter Reduction

Implementation of the existing modified PD compensation provides some insight into the bending filter's structure. Figure 3.3 is the controlled K1 frequency response using the PD control defined by equation 3.1 without an additional filter in the forward loop. The Nichols representation is given by Figure 3.4. The GM and PM achieved using the existing PD controller are 4.23 dB and 24.49°, respectively. This is evinced by the overlap of the horizontal and vertical lines centered at 180° and 0 dB, which signify 30° PM and 6 dB GM respectively. (In Nichols analysis, the stability criterion is that there are no right-to-left crossings over the stability points, which are located at $[180^\circ \pm n \bullet 360^\circ, 0 \text{ dB}]$ [16].) This system may not meet requirements, but it does provide clues for the form of additional compensation that is necessary to satisfy the requirements. In Figure 3.4, the LOX and RP slosh modes are clearly phase stabilized, and the flexible modes at higher frequencies are gain stabilized.

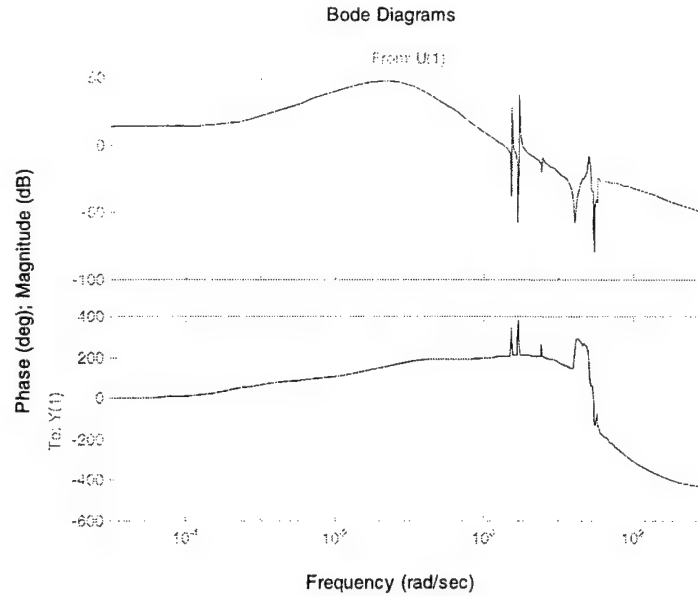


Figure 3.3 – Modified PD Open Loop Frequency Response

Figure 3.3 also indicates that in order to meet margins, phase must be added near the 0.16 Hz point, and further gain attenuation is needed near the system's flex modes at 4 Hz. This indicates that a type of lead-lag compensation will be required in the forward path. Therefore, to reduce the complexity of the SISO control design process, the bending filter was assumed to have the form of a lead-lag network.

To further simplify the development of the n^{th} order bending filter, the filter's order was limited. By reducing the filter from 10^{th} to 4^{th} order filter, defined by equations 3.4 through 3.6, the number of design parameters in the filter design was reduced from 36 to 8. In addition to order reduction, the form of the lead and lag compensation was assumed to be the complex pole-zero pair form defined in equations 3.4 and 3.6. All of these simplifications were made to decrease the complexity of the filter design, while maintaining the capability of designing a control system that met system requirements.

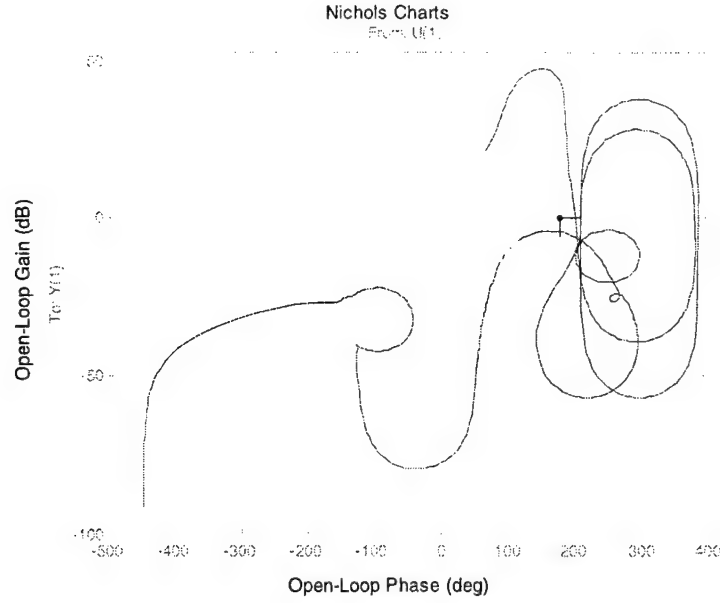


Figure 3.4 – Modified PD Nichols Plot

$$B(s) = B_{\text{Lead}}(s) * B_{\text{Lag}}(s) \quad (3.4)$$

$$B_{\text{Lead}}(s) = \left(\frac{\omega_{\text{LdP}}}{\omega_{\text{LdZ}}} \right)^2 \cdot \frac{s^2 + 2\zeta_{\text{LdZ}} \omega_{\text{LdZ}} s + \omega_{\text{LdZ}}^2}{s^2 + 2\zeta_{\text{LdP}} \omega_{\text{LdP}} s + \omega_{\text{LdP}}^2}, \quad \omega_{\text{LdZ}} < \omega_{\text{LdP}} \quad (3.5)$$

$$B_{\text{Lag}}(s) = \left(\frac{\omega_{\text{LgP}}}{\omega_{\text{LgZ}}} \right)^2 \cdot \frac{s^2 + 2\zeta_{\text{LgZ}} \omega_{\text{LgZ}} s + \omega_{\text{LgZ}}^2}{s^2 + 2\zeta_{\text{LgP}} \omega_{\text{LgP}} s + \omega_{\text{LgP}}^2}, \quad \omega_{\text{LgZ}} > \omega_{\text{LgP}} \quad (3.6)$$

3.3.2 Design Framework

By fixing the controller's form, designing a successful control law has been reduced to a smart selection of 10 design parameters (2 control gains and 8 filter parameters). Although it is possible to manually select each of the 10 design parameters, advances in computer technology present an alternative approach in which a family of controllers can be tested against the requirements in a search for the best design. To accomplish the design search, the following 6 step approach was implemented.

- 1) Each design parameter was given a discretized range of approximate values based on observations of the controlled responses in Figures 3.3 and 3.4.
- 2) All possible controller configurations were created.
- 3) Each controller was then tested for its GM and PM.
- 4) Those configurations that satisfy the GM and PM requirements were analyzed for their attenuation levels on the retention tank LOX slosh mode and the body-bending modes.

Until this point, the time domain performance of the K1 pitch response had not been directly evaluated. In order to account for the time domain performance of the system, a new metric was needed. Using the Integral Time of Absolute Error metric, ITAE, the time-weighted error response was integrated to reflect the stability and performance of the system. The equation form of ITAE is given by equation 3.7. The remaining process steps were:

- 5) Using ITAE as a final design metric, those compensation designs that met the design requirements were sorted based on their ITAE value.
- 6) A final cursory check of the control design was performed to ensure compliance with system physical constraints.

After the control design results were tabulated, the most promising designs were selected and evaluated for their robustness properties. Using the process already outlined, all of the 3- σ and combined 1- σ test cases were analyzed for each selected control design. Any design that maintained stability during the perturbation analysis was considered as successful.

$$\int_0^{t_f} |e(t)| \cdot t \, dt \quad (3.7)$$

Appendix D contains the MATLAB code used to perform steps 2, 3, 4, and 5 from above. Additionally, SIMULINK models were used in conjunction with the

MATLAB command *linmod.m* to create the various system transfer functions needed to assess each controller's design metrics. These models are also contained in Appendix D.

3.3.3 Design Results

Using the general form of the bending filter defined by equations 3.4 through 3.6, each of the 10 control parameters was assigned a vector of values, and each vector was centered at its expected value from open loop analysis using the existing modified PD control. Table 3.2 summarizes the control design gain vectors used in the classical design framework.

Table 3.2 – Classical Design Parameters

Control Parameter	Description	Search Vector
K_P	Proportional Gain	[.5 1 1.5]
K_D	Derivative Gain	[.3 .5 .7]
ω_{LdZ}	Lead Complex Zero Frequency	[2 3 4 5]
ζ_{LdZ}	Lead Complex Zero Damping	[.6 .7 .8]
ω_{LdP}	Lead Complex Pole Frequency	[3 4 5 6]
ζ_{LdP}	Lead Complex Pole Damping	[.6 .7 .8]
ω_{LgZ}	Lag Complex Zero Frequency	[10 20 30 40]
ζ_{LgZ}	Lag Complex Zero Damping	[.6 .7 .8]
ω_{LgP}	Lag Complex Pole Frequency	[6 8 10 20]
ζ_{LgP}	Lag Complex Pole Damping	[.6 .7 .8]

Even with a very coarse search of the likely parameter values, there are 186,624 possible value combinations. This number is only slightly reduced when pole-before-zero or zero-before-pole constraints are added to ensure a lead-lag architecture. Of all possible combinations, 1910 design configurations achieved satisfactory GM and PM. Of these 1910 successful results, only 7 designs provided the required -6 dB and -10 dB attenuation for the retention slosh mode

and flex modes, respectively. These seven configurations are summarized in Table 3.3 .

Table 3.3 – Successful SISO Design Results

Parameter\Design	1	2	3	4	5	6	7
K_P	0.5	0.5	0.5	0.5	0.5	0.5	0.5
K_D	0.3	0.3	0.3	0.3	0.3	0.3	0.3
ζ_{LdZ}	0.8	0.8	0.6	0.8	0.6	0.6	0.6
ω_{LdZ}	2.0	3.0	2.0	3.0	2.0	2.0	2.0
ζ_{LdP}	0.6	0.6	0.6	0.6	0.6	0.6	0.6
ω_{LdP}	3.0	4.0	3.0	4.0	3.0	3.0	3.0
ζ_{LgZ}	0.6	0.8	0.8	0.7	0.7	0.8	0.7
ω_{LgZ}	10.0	20.0	20.0	20.0	20.0	30.0	30.0
ζ_{LgP}	0.8	0.7	0.8	0.7	0.8	0.8	0.8
ω_{LgP}	6.0	6.0	6.0	6.0	6.0	6.0	6.0
GM	9.90	8.00	8.21	8.08	8.29	7.92	7.92
PM	35.3	32.1	33.1	30.5	32.5	31.1	30.0
Ret LOX	-6.03	-6.06	-6.00	-6.27	-6.21	-6.14	-6.23
Flex	-10.8	-21.9	-20.1	-22.9	-21.1	-23.7	-24.7
ITAE	9.36	11.3	11.5	11.5	11.7	12.1	12.3

Design 1 from Table 3.3 clearly meets all the expected requirements and has the best time response characteristics according to its ITAE value. Designated as design Alpha, this controller was selected for perturbation analysis.

In addition to design Alpha, a second design was selected for perturbation analysis. A close review of all the control designs that successfully met the GM and PM specifications revealed that the restriction on the level of attenuation for the retention tank slosh mode appeared to be eliminating control designs with superior time response characteristics compared to those listed in Table 3.3. Relaxing this requirement to a level of -4 dB achieved a marked improvement in

ITAE at no cost to the other system requirements. This relaxation was permissible without creating robust stability concerns considering the dipole of the retention tank slosh mode is expected to grow away from the stability point if the damping decreases or if the slosh mass increases [29]. Table 3.4 shows the compensation designs with minimum ITAE that satisfy a relaxed requirement on retention tank slosh mode attenuation.

Table 3.4 – Relaxed Attenuation Results

Parameter \ Design	1	2	3	4	5	6	7
K_P	0.5	0.5	0.5	0.5	0.5	0.5	0.5
K_D	0.7	0.7	0.5	0.5	0.5	0.5	0.5
ζ_{LdZ}	0.6	0.6	0.8	0.6	0.7	0.8	0.6
ω_{LdZ}	4	4	3	3	3	3	3
ζ_{LdP}	0.7	0.8	0.7	0.6	0.7	0.7	0.6
ω_{LdP}	5	5	4	4	4	4	4
ζ_{LgZ}	0.8	0.8	0.7	0.8	0.8	0.6	0.7
ω_{LgZ}	20	20	20	20	20	20	20
ζ_{LgP}	0.8	0.7	0.8	0.8	0.8	0.8	0.8
ω_{LgP}	6	6	6	6	6	6	6
GM	8.16	8.57	6.42	6.66	7.04	6.48	6.74
PM	30.33	30.76	32.81	39.32	35.92	30.92	38.21
Ret LOX	-4.17	-4.12	-4.14	-4.08	-4.48	-4.36	-4.29
Flex	-16.05	-16.01	-18.74	-17.76	-17.79	-20.02	-18.75
ITAE	6.18	6.19	7.27	7.31	7.41	7.41	7.42

Analysis showed that there was no significant gain made in ITAE by further reducing attenuation requirements. On the other hand, no significant gains were made by reducing the requirement by a lesser amount. The -4 dB appeared to be an important point in the design space at which the time response could be significantly improved. This is showcased by the 15% reduction in ITAE between designs 2 and 3 in Table 3.4. For this reason, design

1 from Table 3.4 was retained for dispersion analysis and designated as design Beta.

Both phases of dispersion analysis were performed for designs Alpha and Beta. Appendix E contains full tabular results of all dispersion cases run with these designs. During robustness testing, each of the designs maintained stability, and is therefore an acceptable product of the SISO design process. To further discriminate between control designs, the percent change in GM, PM, and ITAE was calculated for each perturbation case in an attempt to understand the parameter sensitivities of each compensator. Cases that had the most impact for each design metric are summarized in Table 3.5 and Table 3.6. The definitions for 1- σ cases are given in Appendix E, Table E.2.

Table 3.5 – Design Alpha Dispersion Results

	3- σ	1- σ
GM:	73, 3, 45	11, 13, 27, 31, 43
PM:	45, 8, 50	32, 28, 16, 12, 42
ITAE:	45, 16, 50	28, 32, 10, 14, 44

Table 3.6 -- Design Beta Dispersion Results

	3- σ	1- σ
GM:	3, 54, 45	33, 45, 31, 17, 15
PM:	45, 3, 8	32, 28, 16, 12, 42
ITAE:	45, 16, 50	10, 14, 32, 28, 44

Between the designs there was no significant difference in the parameters that impacted performance. When disturbed individually, actuator perturbations and the frequencies of the 5th flex mode, retention tank slosh, LOX slosh, and RP slosh have the most effect. In combined analysis, the actuator perturbations appear to dominate, as every disturbance combination above included engine actuators. One general trend was noticed: Positive actuator perturbations during

the combined analysis had the largest effect on GM, while negative perturbations drove changes in the PM and ITAE.

3.4 SISO Design Conclusions

Analysis of the two designs, Alpha and Beta, that were developed using the SISO architecture indicates that both designs satisfy the system requirements for nominal and robust stability and performance. Furthermore, using a relaxed requirement on the retention tank slosh mode attenuation allowed for increased time domain performance. Figure 3.5 and Figure 3.6 show the closed-loop step and open-loop frequency response of both designs, respectively. A framework was also established to perform rudimentary dispersion analysis. Even the application of this simple framework adds to the level of confidence in the capability of each design. Therefore, designs Alpha and Beta should provide a quality benchmark to which the stability and performance of a modern based control law can be compared. The gains and filters in equations 3.8 and 3.9 summarize designs Alpha and Beta, respectively.

$$\begin{aligned} K_P &= 0.5 \\ K_D &= 0.3 \\ B(s) &= 0.81 \cdot \frac{(s^2 + 3.2s + 4)(s^2 + 12s + 100)}{(s^2 + 3.6s + 9)(s^2 + 9.6s + 36)} \end{aligned} \tag{3.8}$$

$$\begin{aligned} K_P &= 0.5 \\ K_D &= 0.7 \\ B(s) &= 0.14063 \cdot \frac{(s^2 + 4.8s + 16)(s^2 + 32s + 400)}{(s^2 + 7.0s + 25)(s^2 + 9.6s + 36)} \end{aligned} \tag{3.9}$$

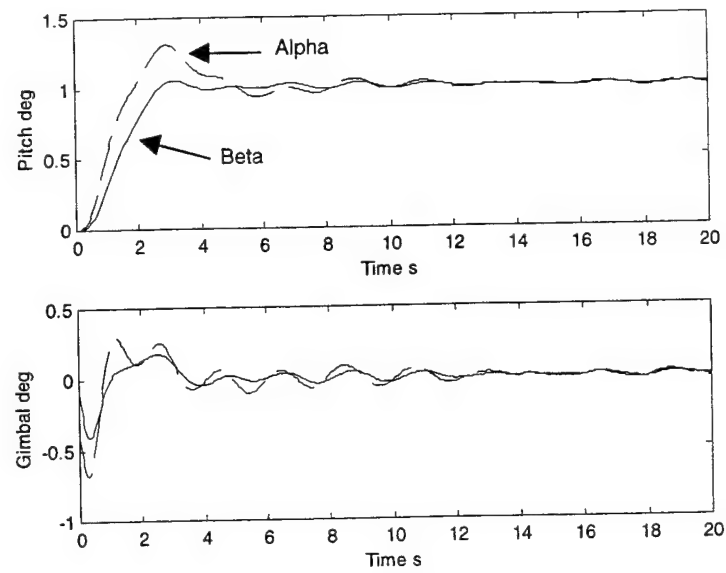


Figure 3.5 – SISO Design Step Responses

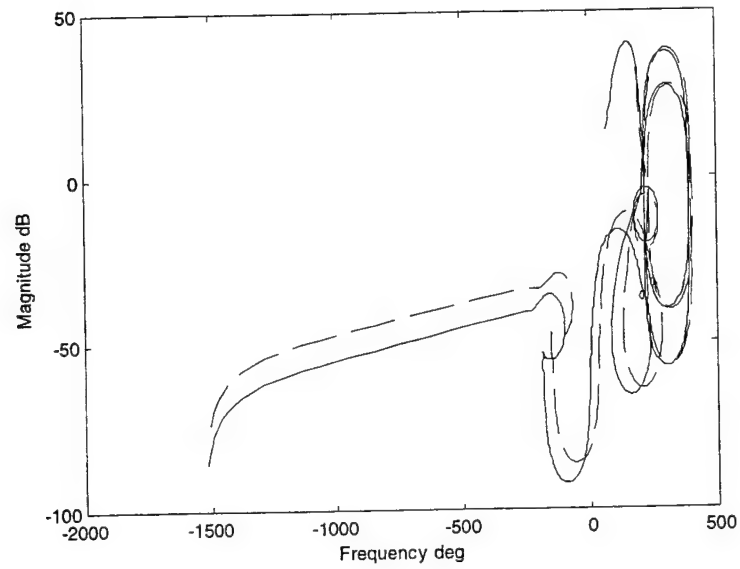


Figure 3.6 – SISO Design Frequency Responses

Notice that the original control gains in equation 3.1 have been changed in the final classical designs. First, consider the proportional gain, which is used to shift the Nichols plot up or down as a function of frequency. The difference between the original controller and the final designs was used to help achieve gain margin requirements. Now consider the derivative gain, which acts as a form of lead compensation. The derivative gain was determined because extra phase was needed around the 1-2 rad/s range to meet phase margin requirements. The effective zero created by derivative control is located at $s = -K_P/K_D$. Thus, the derivative gain in the final classical controllers ensures phase lead in the 1 rad/s frequency range. The effective pole in design Alpha, equation 3.8, is -1.67 , and the effective pole in design Beta, equation 3.9, is -0.7 .

Even though the SISO design process was able to develop controllers that met system specifications, it has one obvious limitation: the controller search algorithm. Even using very coarse gain vectors for the controller parameters and previous results to guide the search, the number of cases searched and the time required to search all the possible control laws can quickly become prohibitive. The time required to run a search using the parameter vectors in Table 3.2 was approximately 3 hours. If the search had been expanded to include high resolution gain vectors or a full 10^{th} order bending filter, it would have taken days or weeks to complete. Yet, this was the best approach considering the difficulty in manually selecting the pole and zero locations of the SISO controller.

CHAPTER 4

Robust Weighted H_2/H_∞ Control Synthesis Development

It is possible to recast the SISO control synthesis problem in Chapter 3 into the general modern control synthesis framework. Using well established techniques in frequency-weighted H_2/H_∞ control synthesis, a well-posed formulation of the ascent control design problem was developed. This chapter presents the background information for, and development of, a MIMO formulation of the K1 pitch control problem. The selected exogenous inputs and outputs are detailed along with the implications of associated singularity conditions. A general form of the frequency weights used to shape system disturbances and performance penalties is also presented. Furthermore, system uncertainty is addressed in its relationship to controller order and robust stability. Finally, a procedure is formulated to explore compensator reduction using Hankel Singular Values (HSV) and balanced model truncation.

4.1 MCS Design Methodology

Reformulating the classical design problem into a modern approach achieves two main benefits. First, the design process within the modern framework is capable of addressing the multiple, naturally occurring disturbances on the system, while simultaneously achieving desired performance objectives. Second, the actual process of creating a compensator is transformed from an ad

hoc approach into a model-based solution that directly incorporates information on vehicle dynamics. However, these advantages do come at a cost. Unlike the SISO design process where the designer has ultimate control over compensation form, the engineer yields the ability to dictate the form of the dynamic compensation that results from the H_2/H_∞ design process. Therefore, developing a well-posed design framework that encapsulates design objectives is the fundamental challenge in creating robust H_2/H_∞ based compensation.

4.1.1 Canonical Problem Formulation

To take advantage of MCS methods, the SISO control loop from Chapter 3 was translated into that of Figure 4.1, a standard representation for model-based control. A quick analysis of the elements in Figure 4.1 facilitates an understanding of the general design setup.

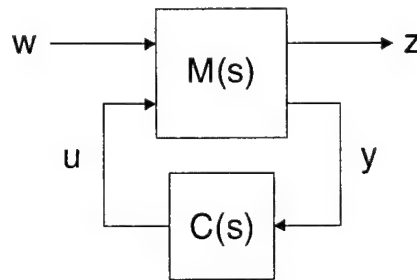


Figure 4.1 – H_2/H_∞ Control Design Loop

There are two vector input and two vector output signals in the general design framework. \mathbf{u} is defined as the control output from the controller to the system. \mathbf{y} is defined as the control input from the system to the controller. Both of these signals are present in the standard SISO feedback control loop, Figure 3.1. However, the exogenous vector input, \mathbf{w} , and the exogenous vector output, \mathbf{z} , are not generally present in the SISO problem. Instead, they are constructs introduced into the design model to aid in controller design. Typically, the inputs, \mathbf{w} , are chosen to model expected disturbances and noises, while, the outputs, \mathbf{z} , are selected to create design objectives and penalties.

The design model, $M(s)$, contains all of the dynamics and interactions defined by the traditional, pitch-plane control loop architecture, in addition to those exogenous inputs and outputs which are added during problem formulation.

$$\begin{aligned}\dot{x} &= Ax + B_1 w + B_2 u \\ z &= C_1 x + D_{11} w + D_{12} u \\ y &= C_2 x + D_{21} w + D_{22} u\end{aligned}\tag{4.1}$$

The general form of the state-space representation of the design model is given by equation 4.1. The specific state-space matrices of $M(s)$ will be defined later, after some attention has been given to the selection of exogenous inputs and outputs.

The dynamic compensator, $C(s)$, is the result of the MIMO design process. Using standard H_2 - and H_∞ -norm definitions, optimal H_2 (H_∞) design generates a controller, $C(s)$, which minimizes the H_2 -norm (H_∞ -norm) of the closed-loop transfer function from w to z . Thus, the norm of the closed-loop transfer function is referred to as the objective function; its minimization produces an optimal control law.

Two important assumptions are made in the development of the MCS framework. First, equation 4.2 is assumed to ensure a strictly proper compensator and simplifies problem formulation. Second, equation 4.3 is necessary to bound the H_2 -norm of the objective function. It also guarantees that exogenous input information is not directly fed through into the cost outputs. Both of these assumptions are standard in H_2 control theory and are not viewed as restrictive in application to H_∞ control [16, 1].

$$D_{22} = 0\tag{4.2}$$

$$D_{11} = 0\tag{4.3}$$

4.1.2 Non-Singularity Conditions

Before a proper selection of exogenous inputs and outputs was made, the restrictions from singularity conditions on the general state space model were investigated. A well-posed, or non-singular, problem not only supports software-based solution techniques, but also translates physical information correctly into the design model.

The coefficient matrices of the general system, equation 4.1, should satisfy the standard non-singularity conditions [23]. These conditions are:

- 1) D_{21} must be right invertible (full row rank), which ensures full measurement noise.
- 2) D_{12} must be left invertible (full column rank), which ensures full control penalty.
- 3) Matrices 4.4 and 4.5 must be right and left invertible, respectively, for any $s \in j\mathbb{R}$. (\mathbb{R} refers to the set of all real numbers.)

$$\begin{bmatrix} sI - A & B_1 \\ C_2 & D_{21} \end{bmatrix} \quad (4.4)$$

$$\begin{bmatrix} sI - A & B_2 \\ C_1 & D_{12} \end{bmatrix} \quad (4.5)$$

Right and left invertibility are standard matrix properties in linear algebra, but they can also be interpreted as controllability and observability characteristics of a state-space system. A matrix is right invertible if it has full row rank, or correspondingly, if there exists no input (column) vector by which it can be right multiplied to produce a zero vector, or right zero. Right invertibility can be thought of as a condition on system controllability by realizing that the right zeros of the B-matrix in a state-space system lead to control inputs which do not affect system states. Left invertibility is a concept dual to right invertibility. Thus, a matrix is termed left invertible if it has full column rank. In other words, the matrix

cannot be left multiplied by an output (row) vector to produce a zero vector, or left zero. Left invertibility of a system relates its observability, because left zeros of a state-space C-matrix result in states that cannot be sensed.

Conditions 1 and 2 are simple enough to check, considering D_{12} and D_{21} are constant matrices. It can be much more computationally intensive to ensure full row or column rank over all frequencies as per condition 3. However, it is possible to transform this condition using the basic definition of left and right zeros. The resulting, equivalent condition can be substituted for 3) above [23].

- 4) Check the eigenvalues of equation 4.6 or 4.7. If there are eigenvalues with positive real part, then the formulation is singular. If there is a purely imaginary eigenvalue, substitute this eigenvalue into its associated singularity matrix (4.4 and 4.5) and check for left and right invertibility according to condition 3. Otherwise, the formulation is non-singular.

$$A + B_1 D_{21}^{-1} C_2 \quad (4.6)$$

$$A + C_1 D_{12}^{-1} B_2 \quad (4.7)$$

These non-singularity conditions have a direct physical interpretation. Condition 1 requires that all sensor information contains noise, which guards against the assuming perfect state knowledge of the plant. Condition 2 ensures that the objective function penalizes control effort and aids in translating the physical limitations of control system actuators. Finally, condition 3 addresses the controllability and observability of the design plant states. Matrix 4.4 requires that all unstable modes are excitable by disturbances, w , and observable in the sensor measurements, y . This effectively places a criterion on stability in developing a compensator design. Matrix 4.5 requires that all unstable modes are controllable by the controls, u , and are observable in the penalty outputs, z . Without this constraint, the plant could not be stabilized by the controller [23, 1].

Another important consideration in developing a well-posed problem is the presence of unstable transmission zeros in the design plant. A transmission zero can simply be thought of as an “input absorbing frequency”, in which some frequency can drive the system and no output response is generated. In Appendix C, it has been shown that a complex pair of possibly non-minimum phase zeros exists due to the Tail-Wags-Dog effect. The importance of these zeros is two-fold. First, according to Bode’s Sensitivity Integral, equation 4.15, a stable, minimum phase open-loop system’s area of disturbance attenuation is equal to its area of disturbance amplification, and this property will be used later in selecting a proper objective function. However, non-minimum phase systems may have greater areas of amplification than attenuation [16], and the relaxation of Bode’s Sensitivity Integral would require additional complexity in the problem formulation. Second, the presence of open-loop poles near the vicinity of unstable transmission zeros can create pole-zero cancellations and result in uncontrollable, or unobservable, unstable modes in the system model. In light of these adverse conditions, caution was used when including TWD dynamics in the design plant. Careful analysis shows that the frequency of TWD zeros is much greater than the expected system bandwidth, and the TWD dynamics can be removed without a significant effect on the design process.

4.1.3 Input/Output Selection

With non-singularity conditions in mind, the selection of exogenous inputs and outputs was centered around formulating an objective function that characterized the desired specifications of a satisfactory controller design. To this end, a frequency-weighted design method was selected, which makes it possible to discriminate I/O signals over specified frequency ranges. These weighting functions together with the actual I/O selections enabled the objective function to be tailored to the problem at hand. During the following development of the MIMO design model I/O signals, block diagram structures of the design model, $M(s)$, are presented to highlight signals of interest.

4.1.3.1 w , Exogenous Inputs

Exogenous, or disturbance, inputs are intended to represent expected inputs into the design plant and should characterize these accordingly. During objective function minimization, all inputs are assumed to be stationary, Gaussian, white noise processes. Therefore, each input was shaped to reflect its expected form. For this application, the input shaping filters were held fixed over all designs once they were established during problem development. In total, six different disturbance inputs were included in the design plant.

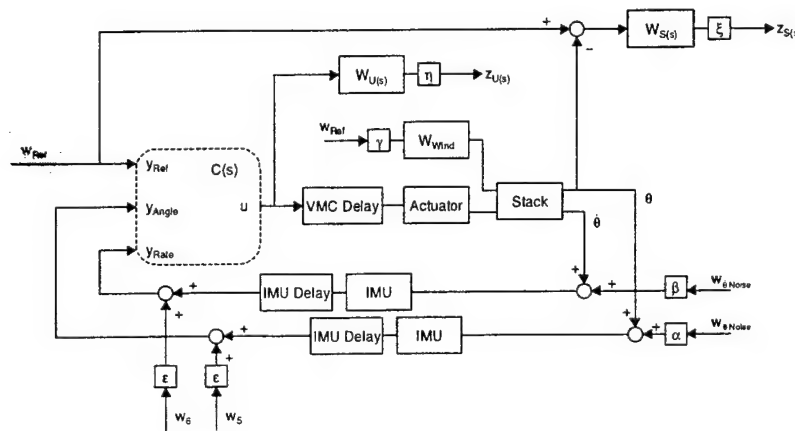


Figure 4.2 – Reference Input in MIMO Control Loop

The disturbance input, w_{Ref} , in Figure 4.2 represents the reference pitch angle. This data, which is taken directly from a nominal trajectory profile, is assumed to need no scaling or filtering. It is simply a steady-state signal which the launch vehicle control system strives to match.

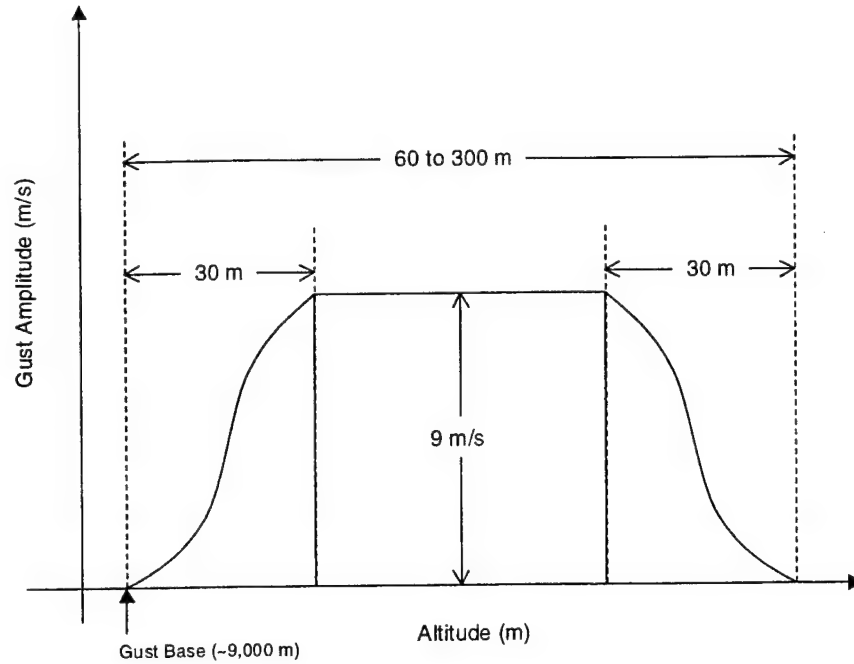


Figure 4.4 – NASA Wind Gust Model

Wind disturbances were viewed as a disturbance on the Angle-of-Attack (AOA) state within the design model, as they change the effective direction of the air-relative velocity vector. Basic geometry revealed that a horizontal gust magnitude of 9 m/s, indicated by Figure 4.4, at the Mach 1.0, trim pitch angle of 73° was bounded by AOA disturbance angles of $\pm 1.6^\circ$.

Using magnitude and spectral information on the resultant AOA disturbances, the appropriate shaping filter, $W_{\text{Wind}}(s)$, and scaling gain, γ , can be established. Equation 4.8 presents the full state-space representation of the shaped wind input. The shaping filter is low-pass with a bandwidth of 2.5 rad/s and unity, low frequency gain. The wind input is also scaled by γ which has a value of 1.6, which is consistent with the maximum expected AOA disturbances.

$$\begin{aligned}\dot{\mathbf{x}}_w &= \mathbf{A}_w \mathbf{x}_w + \gamma \mathbf{B}_w w_{\text{Wind}} \\ w_p &= \mathbf{C}_w \mathbf{x}\end{aligned}\tag{4.8}$$

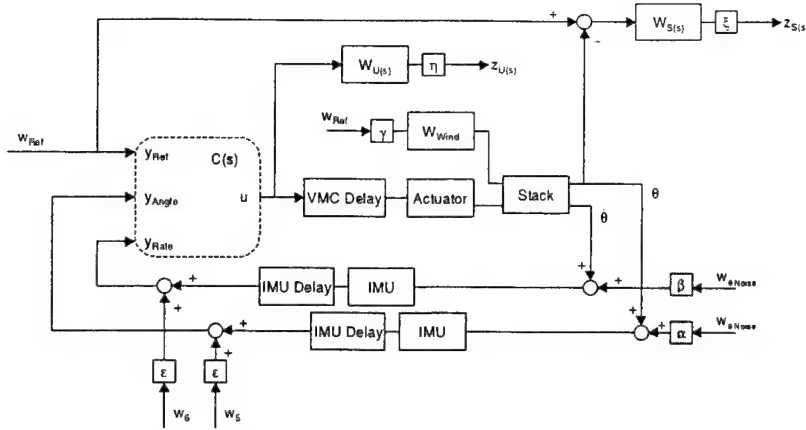
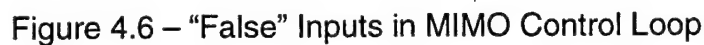


Figure 4.5 – Noise Inputs in MIMO Control Loop

In Figure 4.5, the inputs, $w_{\theta Noise}$ and $w_{\dot{\theta} Noise}$, respectively represent noise in the pitch angle and pitch rate feedback paths. The location of these noises in the control-loop were selected to reflect a physical interpretation in which error enters the feedback path through inaccurate IMU measurements. Furthermore, IMU specifications indicate that the noises present in the feedback signals are characterized by random number disturbances with zero mean and 0.001 variance. Because the design inputs are assumed to be stationary, Gaussian, white noise processes, these inputs needed only proper scaling. Using α to scale noise in the pitch angle signal and β to scale the noise in the pitch rate signal, each was set to 0.01 to correctly shape the noise inputs.

Finally, inputs w_5 and w_6 were added as shown in Figure 4.6 to fulfill non-singularity requirements. Specifically, they were added to maintain the right invertibility of D_{21} . With the inclusion of the low-pass IMU dynamics in the feedback path, the sensor noises, $w_{\theta Noise}$ and $w_{\dot{\theta} Noise}$, were now included in B_1 . As a result, D_{21} lost full row rank. By adding these two “false” disturbances to the system, the integrity of the design solution method was preserved. To ensure that these constructs had no impact on design solutions, each was scaled by a gain essentially equal to zero ($\epsilon = 0.0001$). In this manner, the mathematical solution methods hold, and the design problem is equivalent to the previous singular formulation.



The selection of the exogenous outputs, or cost outputs, lies at the heart of creating the objective function, and unlike the exogenous input shaping filters and scaling gains, the cost output filters and gains are tools that are continually changed to achieve acceptable designs. Two cost outputs were selected to form the K1 pitch control objective function. Each one has both a physical interpretation and a transfer function representation that provide insight to its role in the design process.



75

function defined by equation 4.9. Having a control penalty is required to maintain the non-singularity conditions. However, it makes sense physically, as well. If no cost were placed on control effort, then a resulting control design could require more control authority than physically possible. This case is considered cheap control. On the other hand, there can be also instances of expensive control, in which so much cost is placed on control effort that performance deteriorates and stability may be lost. By including the control cost as part of the objective function, it becomes possible to balance cheap and expensive control to shape the SISO transfer function, equation 4.9.

$$U(s) = \frac{C}{1 + PC} \quad (4.9)$$

To provide for a level of control penalty that does not permit either cheap or expensive control, a weighted control cost output was introduced into the design model. It has already been established in Chapter 2 that the engine actuators have a bandwidth of 25 rad/s. It is immediately apparent that control commands of greater frequency are not acceptable in the final control design. Therefore, control effort should be subject to high frequency cost. Furthermore, a small low frequency cost was placed on control effort to alleviate a situation of cheap control. The magnitude versus frequency plot of the resulting control penalty shaping filter is illustrated by Figure 4.8.

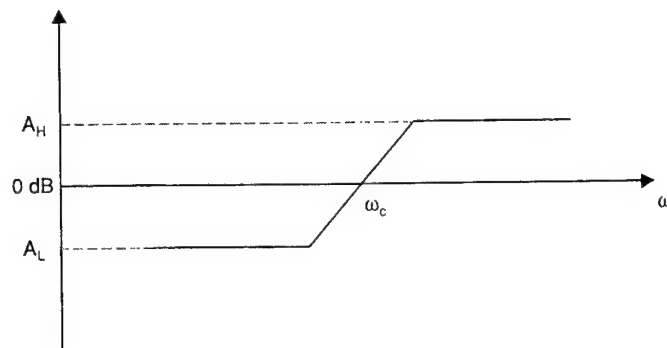


Figure 4.8 – $U(s)$ Penalty Shaping Filter

The three filter parameters defined in Figure 4.8 are used to define the control cost filter, $W_{U(s)}$. A_H defines the high frequency cost, A_L defines the low frequency cost, and ω_C defines the crossover frequency of the filter. The state-space representation of this control cost filter is given by,

$$\begin{aligned}\dot{\mathbf{x}}_{UC} &= \mathbf{A}_{UC}\mathbf{x}_{UC} + \mathbf{B}_{UC}\mathbf{u} \\ \mathbf{z}_2 &= \boldsymbol{\eta}\mathbf{C}_{UC}\mathbf{x}_{UC} + \boldsymbol{\eta}\mathbf{D}_{UC}\mathbf{u}\end{aligned}\quad (4.10)$$

An additional design parameter has been added to the output of the control cost filter. The scaling gain, η , was used to raise or low control cost across all frequencies.

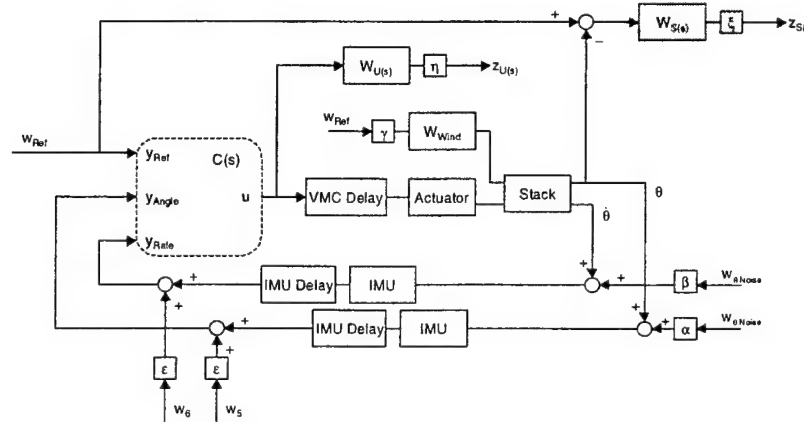


Figure 4.9 – Sensitivity Cost Output in MIMO Control Loop

The second cost output introduced into the design model was placed on the error between the reference and actual pitch angles as shown in Figure 4.9. This cost output also corresponds to a penalty on a transfer function equivalent to the closed-loop sensitivity transfer function, defined by equation 4.11 [23]. The equivalence between the standard idea of the sensitivity transfer function and the implementation in Figure 4.9 is easier to see using the general control loop structure in Figure 4.10. Typically, the notion of sensitivity refers to the closed-loop transfer function from d to θ_A . Yet with simple analysis, it can be realized that the closed-loop transfer function from θ_{Ref} to y is also equivalent to the transfer function in equation

4.11. This alternative implementation is beneficial because it allows the penalty on error to also be viewed as a penalty on system sensitivity. In fact, the effect of the pitch error cost output in the objective function is most easily understood when viewing the penalty as a cost on the sensitivity transfer function.

Within the context of the general system in Figure 4.10, the closed-loop sensitivity and complimentary sensitivity transfer functions are defined by equations 4.11 and 4.12, respectively. It is easy to show these two transfer functions must also satisfy the condition in equation 4.13.

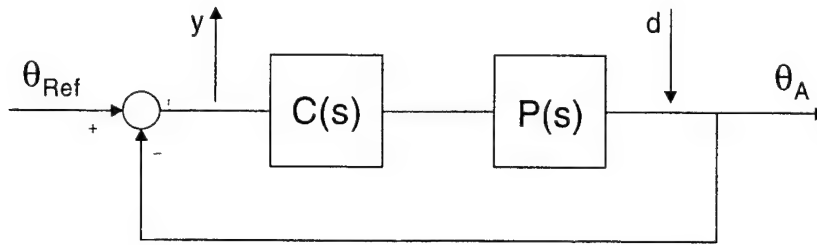


Figure 4.10 – General Control Loop Structure

$$S(s) = \frac{1}{1+PC} \quad (4.11)$$

$$T(s) = \frac{PC}{1+PC} \quad (4.12)$$

$$T(s) + S(s) = 1 \quad (4.13)$$

Regarding K1 ascent, the complimentary sensitivity transfer function, $T(s)$, represents the system's closed-loop pitch response to a reference input. The sensitivity transfer function, $S(s)$, characterizes the system's pitch response to plant output disturbances. The goal is to shape successfully both of these responses to achieve performance specifications.

However, it is sufficient to place a cost output on only one of these transfer functions. Using a low-frequency weight on the sensitivity transfer

function, shown in Figure 4.9, effectively places a high-frequency weight on the complementary sensitivity of the system at the same time.

$$\int_0^{\infty} \ln |S(j\omega)| d\omega = \pi \sum_{i=1}^m \text{Re}(p_i) \quad (4.14)$$

$$\int_0^{\infty} \ln |S(j\omega)| d\omega = 0 \quad (4.15)$$

For proof, consider the Bode Sensitivity Integral in equation 4.14. For stable, minimum-phase systems, the area of disturbance attenuation is equal to that of disturbance amplification, according to equation 4.15 [32]. This implies what is known as the “Waterbed Effect.” Figure 4.11 helps illustrate that for a stable system the area above and below 0 dB must sum to zero. Therefore, by placing a low frequency cost on sensitivity, high-frequency sensitivity must be increased. Moreover, equation 4.13 indicates that if high-frequency sensitivity is increased, then high-frequency tracking (complementary sensitivity) is decreased. This produces an indirect weight on closed-loop system bandwidth.

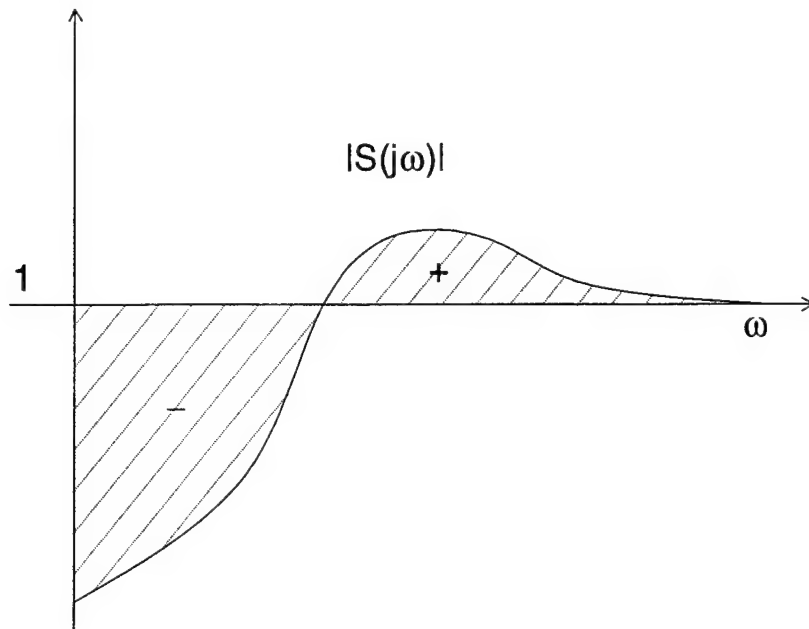


Figure 4.11 – Sensitivity Waterbed Effect

Applying these conclusions, a low-pass shaping filter was added to the pitch error output. Figure 4.12 defines the design parameters that were varied to change the level and range of low-frequency sensitivity cost.

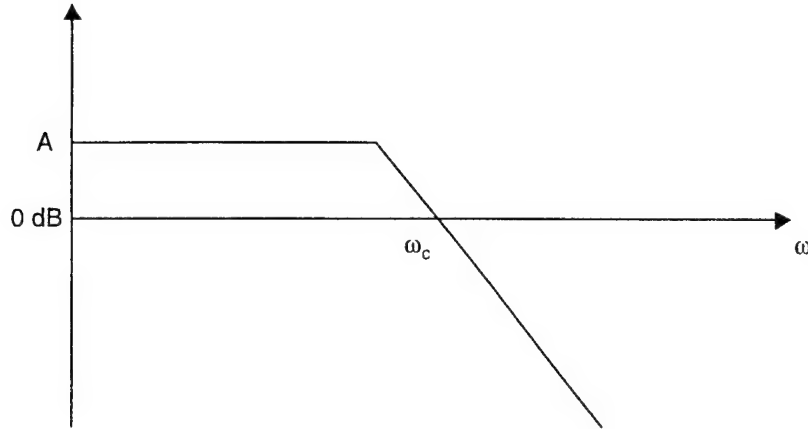


Figure 4.12 – S(s) Penalty Shaping Filter

Again, this filter was given a state-space form, which is shown in equation 4.16. A scaling gain, ξ , was also introduced here to allow for cost increases and decreases across all frequencies.

$$\begin{aligned}\dot{x}_{SC} &= A_{SC}x_{SC} + B_{SC}(w_{Ref} - \theta_A) \\ z_1 &= \xi C_{SC}x\end{aligned}\tag{4.16}$$

It is important to note that, due to the model-based nature of the H_2/H_∞ control design process, compensation order will be equal to the order of the design model. Therefore, to minimize the impact of adding shaping filters to the design model, each filter was implemented as a first-order system.

A more trivial task is that of selecting the control I/O signals, which are traditionally dictated from the control loop architecture. The representative TVC loop architecture presented in Chapter 2 served as a guide for selecting the control I/O signals.

4.1.3.3 y , Control Inputs

The three control inputs, shown in Figure 4.13, provided to the control law were the pitch reference signal, the pitch angle feedback signal, and the pitch rate feedback signal. In this way, the problem was formulated to give the control design process the most freedom in creating the form of the controller. Another possible selection could have been to provide it with a pitch angle error signal and a pitch rate feedback signal, which is essentially the same loop structure as the PD design in Chapter 3. However, this forces the design process to work with undue constraints on its form and could possibly limit the achievable performance of the resulting controller.

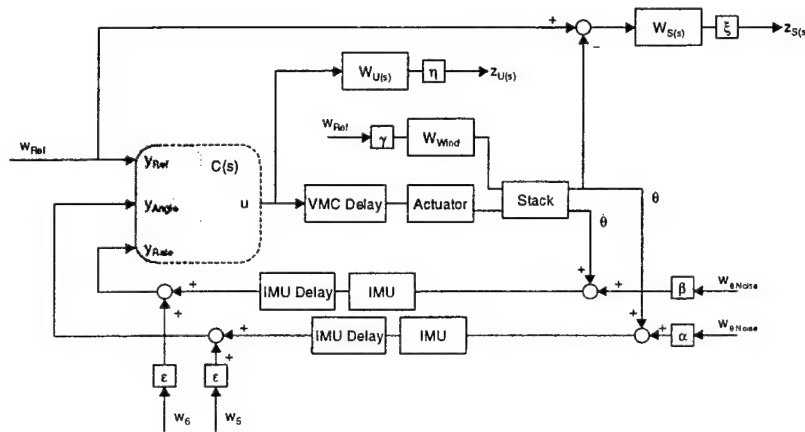


Figure 4.13 – Control Inputs Input in MIMO Control Loop

4.1.3.4 u , Control Outputs

The last of the four general design system signals in Figure 4.14 is the control output. Again, this is dictated by the control loop architecture. In the K1 pitch plane ascent control problem, there is only a single, scalar control signal which commands the engine actuators. It was assumed in Chapter 2 that the three NK-43 engines were controlled together. If that assumption were not made, then the control output could be modified to accommodate the three independent engine gimbal commands. Yet, this was viewed as unnecessary since there is no obvious benefit in pitch plane control by having independently controlled engines.

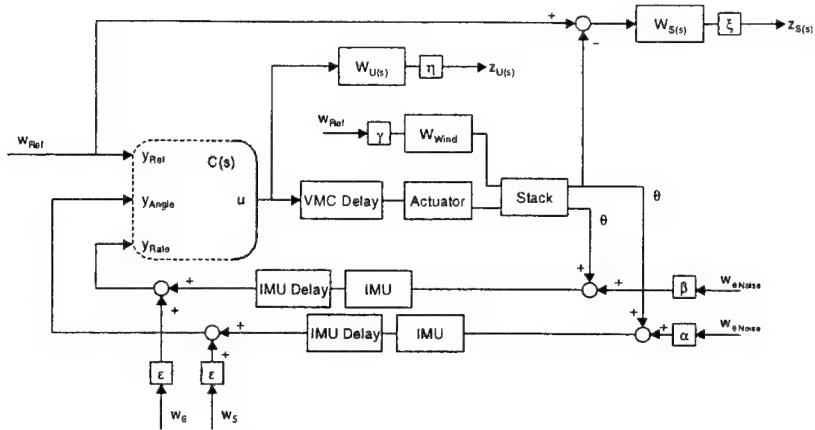


Figure 4.14 – Control Output in MIMO Control Loop

4.1.4 Design System Definition

To establish the design system matrices from equation 4.1, it was necessary to define the input, output, and state vectors. These are summarized by equations 4.17 through 4.20, and the previously defined scalar control output, u .

$$x = [x_P \quad x_A \quad x_{60} \quad x_W \quad x_\theta \quad x_{20_1} \quad x_{\dot{\theta}} \quad x_{20_2} \quad x_{SC} \quad x_{UC}]^T \quad (4.17)$$

$$w = [w_{Ref} \quad w_{Wind} \quad w_{\theta Noise} \quad w_{\dot{\theta} Noise} \quad w_5 \quad w_6]^T \quad (4.18)$$

$$y = [y_{Ref} \quad y_{Angle} \quad y_{Rate}]^T \quad (4.19)$$

$$z = [z_S \quad z_U]^T \quad (4.20)$$

In order to implement the AOA disturbance input into the stack model presented in Chapter 2, a disturbance input was added and the input matrices were redefined. The original B_P matrix was renamed B_{P2} , and a B_{P1} matrix was created to reflect the dynamics associated with AOA perturbations. The resulting system definition was:

$$\begin{aligned}
\dot{x}_P &= A_P x_P + B_{P1} w_P + B_{P2} u_P \\
\theta_A &= C_{P1} x_P \\
\dot{\theta}_A &= C_{P2} x_P
\end{aligned} \tag{4.21}$$

Using relatively simple block diagram reduction techniques and the state-space definitions previously developed here as well as in Chapter 2, it was possible to form a non-unique set of design model matrices. They are:

$$A = \begin{bmatrix}
A_P & B_{2P} C_A & B_{2P} D_A C_{60} & B_{1P} C_W & 0 & 0 & 0 & 0 & 0 & 0 \\
0 & A_A & B_A C_{60} & 0 & 0 & 0 & 0 & 0 & 0 & 0 \\
0 & 0 & A_{60} & 0 & 0 & 0 & 0 & 0 & 0 & 0 \\
0 & 0 & 0 & A_W & 0 & 0 & 0 & 0 & 0 & 0 \\
B_{\theta} C_{P1} & 0 & 0 & 0 & A_{\theta} & 0 & 0 & 0 & 0 & 0 \\
0 & 0 & 0 & 0 & B_{2P} C_A & A_{20_1} & 0 & 0 & 0 & 0 \\
B_{\dot{\theta}} C_{P2} & 0 & 0 & 0 & 0 & 0 & A_{\dot{\theta}} & 0 & 0 & 0 \\
0 & 0 & 0 & 0 & 0 & 0 & B_{2P} C_A & A_{20_2} & 0 & 0 \\
-B_{SC} C_{P1} & 0 & 0 & 0 & 0 & 0 & 0 & 0 & A_{SC} & 0 \\
0 & 0 & 0 & 0 & 0 & 0 & 0 & 0 & 0 & A_{UC}
\end{bmatrix}$$

$$B_1 = \begin{bmatrix}
0 & 0 & 0 & 0 & 0 & 0 \\
0 & 0 & 0 & 0 & 0 & 0 \\
0 & 0 & 0 & 0 & 0 & 0 \\
0 & \gamma B_W & 0 & 0 & 0 & 0 \\
0 & 0 & \alpha B_{\theta} & 0 & 0 & 0 \\
0 & 0 & 0 & 0 & 0 & 0 \\
0 & 0 & 0 & \beta B_{\dot{\theta}} & 0 & 0 \\
0 & 0 & 0 & 0 & 0 & 0 \\
B_{SC} & 0 & 0 & 0 & 0 & 0 \\
0 & 0 & 0 & 0 & 0 & 0
\end{bmatrix}$$

$$B_2 = [B_{2P} D_A D_{60} \quad B_A D_{60} \quad B_{60} \quad 0 \quad 0 \quad 0 \quad 0 \quad 0 \quad 0 \quad B_{UC}]^T$$

$$C_1 = \begin{bmatrix} 0 & 0 & 0 & 0 & 0 & 0 & 0 & 0 & 0 & \xi C_{SC} & 0 \\ 0 & 0 & 0 & 0 & 0 & 0 & 0 & 0 & 0 & 0 & \eta C_{UC} \end{bmatrix}$$

$$C_2 = \begin{bmatrix} 0 & 0 & 0 & 0 & 0 & 0 & 0 & 0 & 0 & 0 & 0 \\ 0 & 0 & 0 & 0 & D_{20_1} C_{\theta} & C_{20_1} & 0 & 0 & 0 & 0 & 0 \\ 0 & 0 & 0 & 0 & 0 & 0 & D_{20_2} C_{\theta} & C_{20_2} & 0 & 0 & 0 \end{bmatrix}$$

$$D_{12} = \begin{bmatrix} 0 \\ \eta D_{UC} \end{bmatrix}$$

$$D_{21} = \begin{bmatrix} 1 & 0 & 0 & 0 & 0 & 0 \\ 0 & 0 & 0 & 0 & \varepsilon & 0 \\ 0 & 0 & 0 & 0 & 0 & \varepsilon \end{bmatrix}$$

The state size of this model depends on the fidelity of the K1 plant model used during the design. At its maximum, the K1 plant model includes all the modeled dynamic effects, and the design model has 39 states. At its minimum, the stack is modeled as a rigid body, and the design model has 13 states.

4.2 System Robustness

An unfortunate result of the weighted H_2/H_∞ design process is that it typically creates high order compensation that is extremely sensitive to design model parameter variations. This occurs as a result of the H_2/H_∞ design process, which is covered later in more detail. During this process, optimization of the objective function uses the design model to create dynamic compensation which inverts the vehicle dynamics to produce a desired system response. The implication of the optimal inversion process is that the design model is viewed as a “perfect” model, and an exact inversion occurs that notches out the modes contained in the design model. Just as with the classical design, this system of

notch filters can be extremely sensitive to parameter changes, and even slight variation in modal parameters can render the compensator ineffective.

Therefore, steps must be taken during problem formulation to relax the optimization's dependence on the design model's modal properties, thereby achieving robust stability. Additionally, the techniques used to add robustness will result in reduced design model order, which has been shown to be the best approach in controller order reduction [1]. Two techniques were used in the K1 pitch control design with the ultimate goal of adding robust stability to and reducing the order of the resulting control laws.

The first technique, which will be referred to as Gain Augmentation (GA), is a rudimentary device applied under the philosophy that the simplest approach of achieving quality results is often the best. In order to understand its implementation in the design model, consider Figure 4.15 and Figure 4.16. Figure 4.15 establishes a simplified form of the control loop without any robust techniques applied. $P_O(s)$ represents the nominal plant model, which includes all dynamic effects. $C(s)$ is the dynamic compensation designed with H_2/H_∞ tools. In Figure 4.16, $P_R(s)$ represents the plant model used to design a robust control system. This plant model is reduced in order and provides only the minimal amount of information necessary to roughly characterize the system dynamics. Finally, G is a gain placed in the forward path.

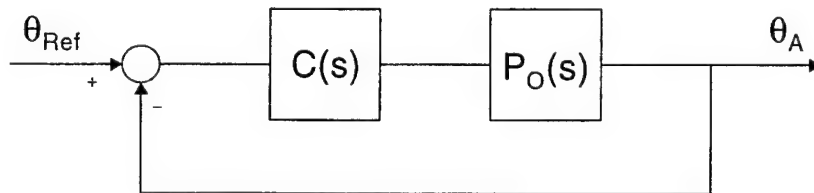


Figure 4.15 – Nominal Loop Configuration

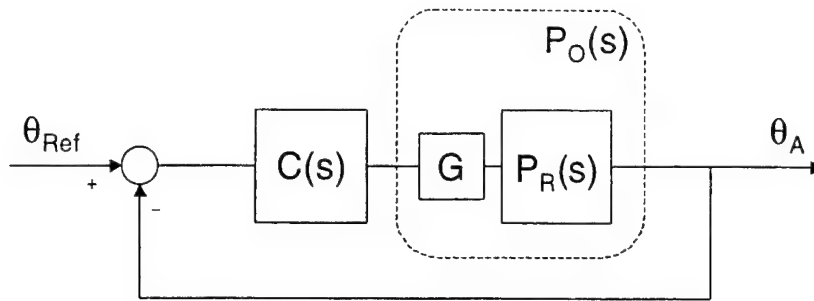


Figure 4.16 – Gain Augmentation

The logic in using GA to develop an acceptable control law is straightforward. Applying compensation developed for controlling $P_R(s)$ in the nominal loop configuration results in reductions in GM and PM. However, gain augmentation of the reduced-order plant can influence the optimization process into providing larger stability margins than normally achieved. Then, when the controller is applied to $P_O(s)$, the larger stability margins ensure performance requirements are met after expected GM and PM reductions occur. The art of this technique is finding a value for G that will cause the controller to “overcompensate” the reduced-order plant enough to achieve frequency domain specifications.

A simple strategy was used to find this gain value. Initially given a value of 1, G was slowly increased until it achieved performance requirements in the nominal loop configuration. It was then checked for robust stability. If it did not maintain stability during dispersion analysis, the gain was increased further until robust stability was achieved.

The second technique used to introduce robustness consisted of applying unstructured Multiplicative Uncertainty (MU) at the plant input. Figure 4.17 presents the implementation. This technique is more methodical in accounting for the neglected dynamics in the reduced-order model [32]. However, it does result in controllers with higher order than those produced using GA. It is important to note that several other implementations of unstructured uncertainty have been developed. Additive Uncertainty and Coprime Factor Uncertainty were also considered for the K1 pitch control problem. However, preliminary

analysis revealed each had a more complicated implementation with no apparent advantage over the MU technique.

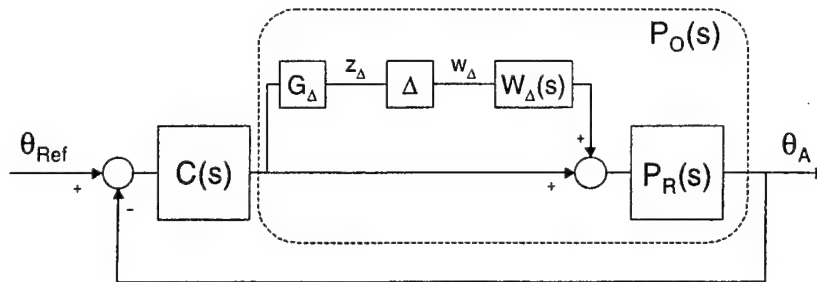


Figure 4.17 – Multiplicative Uncertainty

The implementation of MU into the design model can occur at any point in the control loop. However, input uncertainty was selected because the GM and PM of importance in the design are located at the plant input.

Typically, unstructured uncertainty is used in conjunction with the Small Gain Theorem to guarantee robust stability by achieving below unity H_{∞} -norms in the closed-loop design system [27, 16]. Unfortunately, this process is extremely conservative [15], which causes the system to exhibit poor nominal performance. For the K1 pitch control problem, the MU convention was used only as another set of design tools by not enforcing below unity H_{∞} -norms. The method provides no guarantees for robust stability, but it does allow the varying levels of system robustness to be introduced into the design.

Again, Figure 4.17 shows a general implementation of MU. $P_R(s)$ is the same as in the GA technique. Δ represents an uncertain input into the system, and is bounded with unity magnitude. $W_{\Delta}(s)$ is a weighting function used to characterize the uncertain input, and G_{Δ} is a gain used to shape the magnitude of the system uncertainty.

Using standard techniques, MU was actually implemented into the design model as an exogenous I/O pair, indicated in both Figure 4.17 and Figure 4.18. The weighting function, $W_{\Delta}(s)$, and gain, G_{Δ} , are contained within the design plant. G_{Δ} became a cost gain on the exogenous output, z_{Δ} , and was used to

adjust the level of system robustness throughout the design process. $W_{\Delta}(s)$ became a shaping filter for the new exogenous input, w_{Δ} . It, on the other hand, was established during problem formulation and remained constant throughout the design process.

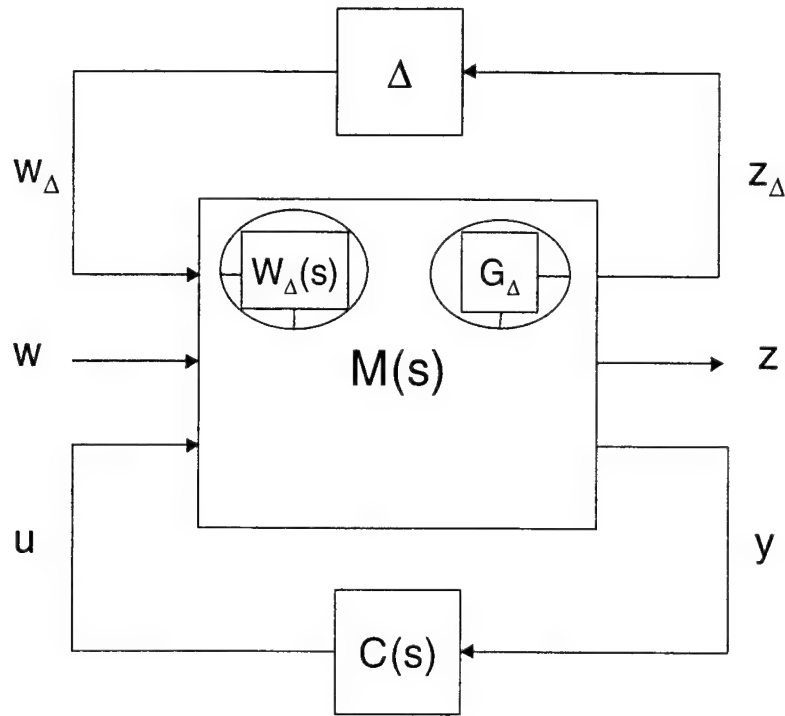


Figure 4.18 – Multiplicative Uncertainty Implementation

The creation of $W_{\Delta}(s)$ was achieved through a systematic procedure. According to equation 4.22, the nominal design plant can be equivalently expressed by the reduced order plant and MU structures. It is also possible to solve equation 4.22 for $W_{\Delta}(s)$ in terms of the nominal plant, the reduced order plant, and the cost gain. Using this expression, the cost gain and Δ structure were fixed with unit magnitude because they represent design tools and should not affect the uncertainty input into the system. The resulting expression is given by equation 4.23.

$$P_O = P_R(1 + G_{\Delta}\Delta W_{\Delta}) \quad (4.22)$$

$$W_{\Delta} = \frac{P_O - P_R}{P_R} \quad (4.23)$$

In order to evaluate equation 4.23, the frequency responses of the nominal and reduced order models were generated. Then, using only magnitude information, calculations of equation 4.23 were performed across a discrete spectrum of frequencies. The resulting magnitude data set characterized the shaping filter, $W_{\Delta}(s)$.

Continuing, it was possible to utilize the MATLAB function, `fitmag.m`, which fits a stable, minimum phase system of user-defined order to a magnitude data set. However, if the above data set were fit exactly, the same dynamics that were removed from the nominal plant model would appear in the input weighting function. Thus, they would still be in the design model, and the resulting controller would still be high order and sensitive to parameter variations in these dynamics. Therefore, $W_{\Delta}(s)$ was generated from a magnitude data set which loosely characterized the exact data calculated from 4.23. Figure 4.19 presents the uncertainty weight used during the control synthesis process presented in Chapter 5.

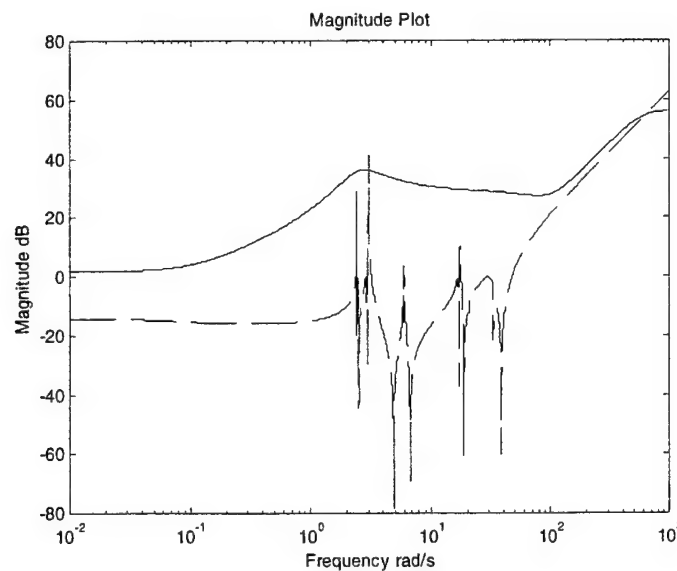


Figure 4.19 – Fit Analysis of Uncertainty Weight

As shown, the exact data (dashed) was fit with a sixth order transfer function (solid). This representation of the weighting function is not unique, as many functions can be used to loosely characterize the exact data. The exact degree to which the transfer function fits the data provided another design tool. The state-space definition of the uncertainty input shaping filter is

$$\begin{aligned}\dot{x}_{\Delta} &= A_{\Delta}x_{\Delta} + B_{\Delta}w_{\Delta} \\ u_{A\Delta} &= C_{\Delta}x_{\Delta} + D_{\Delta}w_{\Delta}\end{aligned}\tag{4.24}$$

Both of these techniques, GA and MU, will be shown to achieve adequate results in Chapter 5. In order to apply these methods to the non-singular problem formulation presented earlier, simple modifications needed to be made to the design model. Some of these have already been mentioned briefly.

To introduce the forward path gain used in GA, the scaling gain was added to the input of the engine actuators, and its input matrix, B_A , was redefined as $B'_A = B_A G$. All subsequent changes to the non-singular formulation were then performed.

Incorporating MU into the non-singular formulation required a bit more work. First, the extra exogenous I/O pair were appended to the existing w and z vectors. Next, the states of the uncertainty shaping filter, $W_{\Delta}(s)$, were appended to the existing state matrix, A , and the input into the actuators was redefined to $u'_A = u_A + u_{A\Delta}$ in order to incorporate the uncertainty input from equation 4.24. After performing subsequent modifications in the state matrix, the new output cost defined. The uncertainty penalty was defined as

$$z_{\Delta} = G_{\Delta}C_{60}x_{60} + G_{\Delta}D_{60}u_A\tag{4.25}$$

which is the scaled output of the VMC delay model.

4.3 Design Solutions

Once the control problem has been formulated into a well-posed design model, the actual calculation of the robust weighted H_2/H_∞ controller can be performed. For optimal H_2 calculation, this task is separated into two independent problems. Using the Linear Quadratic Gaussian (LQG) separation principle, a Kalman Filter Algebraic Riccati Equation (ARE) and a Full-State Feedback ARE were formulated [16, 12, 21]. For optimal H_∞ calculation, similar separation techniques resulted in analogous formulations [12]. The solution of these AREs is used to establish the dynamic compensation.

It is convenient to define the closed-loop transfer function in equation 4.26 for the design model, as the norm of the closed-loop transfer function from w to z is the objective function of the H_2/H_∞ design process.

$$z = T_{w \rightarrow z}(s) w \quad (4.26)$$

4.3.1 Optimal Robust Weighted H_2 Solution

The objective of optimal H_2 control is to design an output feedback compensator that minimizes the H_2 -norm of the closed-loop transfer function from w to z . This can also be thought of as a minimization of the average Singular Value (SV) of closed-loop design model. This problem can be posed as the determination of a compensator $C(s)$ such that,

$$C(s) = \min_C \|T_{w \rightarrow z}(s)\|_2 = \min_C \sqrt{\frac{1}{\pi} \int_0^\infty \sum_{i=1}^n \sigma_i^2 [T_{w \rightarrow z}(j\omega)] d\omega} \quad (4.27)$$

In equation 4.27, σ_i indicates the i^{th} singular value of n ordered singular values.

This is equivalent to a LQG design problem with the following cost function [25]:

$$J = \lim_{t_f \rightarrow \infty} E \left[\int_0^{t_f} z(t)^T z(t) dt \right] \quad (4.28)$$

subject to stationary, Gaussian, white noise inputs. In equation 4.28, E represents the expectation operator. To solve the LQG design problem, two AREs are formed for the associated Full-State Feedback and Kalman Filter problems [31, 21]. Respectively, they are:

Full-State Feedback

$$A^T P + P A - P \Sigma P + C_1^T C_1 = 0, \quad P \geq 0 \quad (4.29)$$

$$\Sigma = B_2 (D_{12}^T D_{12})^{-1} B_2^T \quad (4.30)$$

Kalman Filter

$$Q A^T + A Q - Q \Lambda Q + B_1^T B_1 = 0, \quad Q \geq 0 \quad (4.31)$$

$$\Lambda = C_2^T (D_{21} D_{21}^T)^{-1} C_2 \quad (4.32)$$

Once the two AREs are solved, their associated control gains can be calculated according to equations 4.33 and 4.34.

$$K = (D_{12}^T D_{12})^{-1} B_2^T P \quad (4.33)$$

$$L = Q C_2^T (D_{21} D_{21}^T)^{-1} \quad (4.34)$$

The resulting optimal H_2 model based compensator is defined by,

$$\begin{aligned} \dot{x}_C &= (A - L C_2 - B_2 K) x_C + L y \\ u &= -K x_C \end{aligned} \quad (4.35)$$

It is easy to see that the compensator has the same order as the model, $M(s)$, from which it is designed.

4.3.2 Optimal Robust Weighted H_∞ Solution

Analogous to the optimal H_2 design problem, H_∞ optimal control methodology minimizes the H_∞ -norm of the design model's closed-loop transfer function from w to z . This optimization is equivalent to the minimization of the maximum SV of the closed-loop design model. The optimal robust weighted H_∞ problem can be formulated as the determination of the compensator, $C(s)$ such that [16]

$$C(s) = \min_C \|T_{w \rightarrow z}(s)\|_\infty = \min_C \max_\omega \sigma_{\max}(T_{w \rightarrow z}(j\omega)) \quad (4.36)$$

Using a γ -iteration provided in [12], the optimal H_∞ problem can be formulated as a set of AREs very similar to those used in the H_2 solution. Using equations 4.29 and 4.30 from the H_2 solution, slight modifications are needed for equations 4.31 and 4.32 to formulate the H_∞ AREs. The new expressions are:

$$\Sigma = B_2(D_{12}^T D_{12})^{-1} B_2^T - \frac{1}{\gamma^2} B_1 B_1^T \quad (4.37)$$

$$\Lambda = C_2^T (D_{21} D_{21}^T)^{-1} C_2 - \frac{1}{\gamma^2} C_1 C_1^T \quad (4.38)$$

In equations 4.37 and 4.38, γ represents the upper-bound of the H_∞ -norm of the closed-loop transfer function from w to z . The acceptance of the assumed value of γ is conditional upon [16],

- 1) $A - \Sigma P$ is stable
- 2) $A - Q \Lambda$ is stable
- 3) $\rho(PQ) < \gamma^2$

In condition 3, ρ indicates spectral radius (maximum magnitude of the matrix eigenvalues).

The optimal H_∞ control design is achieved by finding the minimum value of γ for which conditions 1 through 3 hold. This process is commonly referred to as γ -iteration. Beginning with an initial guess that satisfies Conditions 1-3, the value of γ is lowered until the conditions are not satisfied. The smallest value of γ which satisfies the 3 conditions is the optimal γ value, and its associated controller is the optimal H_∞ control law. An accepted practice is to use the H_∞ -norm of the closed-loop design model in the optimal H_2 problem as the upper-bound, or initial guess, for the γ -iteration.

Again, the feedback control and estimation control gains can be calculated once the two AREs are solved. For optimal H_∞ design, they are

$$K = (D_{12}^T D_{12})^{-1} B_2^T P \left(I - \frac{1}{\gamma^2} QP \right)^{-1} \quad (4.39)$$

$$L = QC_2^T (D_{21} D_{21}^T)^{-1} \quad (4.40)$$

and the resulting model-based controller is

$$\begin{aligned} \dot{x}_c &= (A - LC_2 - B_2 K + \frac{1}{\gamma^2} QC_1^T C_1) x_c + Ly \\ u &= -Kx_c \end{aligned} \quad (4.41)$$

Note that in the two ARE, γ -iteration approach, the optimal H_2 compensator is produced as γ increases to infinity. Thus, optimal H_2 and H_∞ designs may be viewed as the two extremes of the γ -iteration process.

4.3.3 Sub-Optimal Robust Weighted H_∞ Solution

As mentioned before, the optimal H_2 solution can be viewed as the minimization of the average SV of the closed-loop design model, and the optimal H_∞ solution can be viewed as the minimization of the maximum SV of the same model. A control that achieves a compromise between flattening the SVs over the entire frequency range and pressing down a single peak can exhibit better

performance for many problems. These solutions are considered sub-optimal (both in an H_2 and H_∞ sense), and they were also explored during the K1 pitch control design process.

To create sub-optimal designs, the γ -iteration process was given a “false” lower-bound, which caused the process to terminate before the optimal γ value was discovered. The “false” lower-bound given to the γ -iteration process was constrained to lie between the upper-bound given by the optimal H_2 solution and the lower-bound given by the optimal H_∞ solution. The sub-optimal value of γ at the “false” lower-bound and its associated controller were assessed for performance and compared to the optimal solutions.

4.4 Controller Order Issues

Even though measures were taken to reduce controller order when developing robust weighted H_2/H_∞ designs, the resulting controllers were still relatively high order. To explore the possibility of eliminating states within the controller that were not important to performance, the Hankel Singular Values (HSVs) of the different control laws were examined. The magnitude of the HSV indicates the level of controllability and observability its associated state possesses. Those with comparatively insignificant magnitudes are prime candidates for being removed from the system. This method of controller order reduction is called Balanced Model Order Reduction (BMOR) [23].

It should be noted that several other techniques have been developed to accomplish model order reduction [17, 16]. However, these, along with BMOR, can reduce order only so far before significant performance loss occurs. The best way to minimize controller order is to minimize the order of the design model through the smart selection and judicious use of shaping filters and minimal order realizations in the design model [1].

To find the HSVs of a controller, first consider the full-order controllers, equations 4.35 and 4.41, that result from either H_2 or H_∞ optimization. Either of

these controllers can be expressed by the form in equation 4.42. Provided that this system is stable, the HSVs are calculated through the controllability and observability Grammians. If the system is not stable, BMOR, as presented here, will not work.

$$\begin{aligned}\dot{x}_c &= A_c x_c + B_c y \\ u &= C_c x_c\end{aligned}\tag{4.42}$$

The controllability Grammian, P , and the observability Grammian, Q , can be found using the following Lyapunov equations [22]:

$$P A_c^T + A_c P + B_c^T B_c = 0, P \geq 0\tag{4.43}$$

$$A_c^T Q + Q A_c + C_c^T C_c = 0, Q \geq 0\tag{4.44}$$

Now, by choosing R such that,

$$P = R^T R\tag{4.45}$$

and diagonalizing RQR^T such that,

$$RQR^T = U \Sigma^2 U\tag{4.46}$$

where U is a unitary matrix, it is possible to define a transformation matrix, T , which will balance the full-order controller in a sense that system states are as controllable as they are observable.

$$T^{-1} = R^T U \Sigma^{1/2}\tag{4.47}$$

Using the transformation matrix, the balanced realization of the full-order controller is given by equation 4.48. This controller's associated HSVs are along the entries of the diagonal matrix, Σ , which can be found with equation 4.49.

$$\begin{aligned}\dot{x}_c &= (TA_c T^{-1})x_c + (TB_c)y \\ u &= (C_c T^{-1})x_c\end{aligned}\tag{4.48}$$

$$TPT^T = (T^{-1})^T QT^{-1} = \Sigma\tag{4.49}$$

$$\Sigma = \begin{bmatrix} \sigma_1 & & & & & \\ & \ddots & & & & \\ & & \sigma_r & & & \\ & & & \sigma_{r+1} & & \\ & 0 & & & \ddots & \\ & & & & & \sigma_N \end{bmatrix}\tag{4.50}$$

Proceeding under the assumption that the HSVs in equation 4.50 are ordered in a decreasing manner such that,

$$\sigma_1 > \dots > \sigma_r > \sigma_{r+1} > \dots > \sigma_N\tag{4.51}$$

it is possible to conclude that those states corresponding to the SVs, $\sigma_1 \dots \sigma_r$, are more observable and controllable than those corresponding to the SVs, $\sigma_{r+1} \dots \sigma_N$. Consequently, truncating those states with less controllability and observability will have less effect in changing the controller [32].

Using the comparative size of the controller's HSVs to form a partition in Σ , shown by equation 4.52, a corresponding partition can be established on the balanced realization of the full-order controller, which has been redefined in equation 4.53.

$$\Sigma = \begin{bmatrix} \Sigma_1 & 0 \\ 0 & \Sigma_2 \end{bmatrix}\tag{4.52}$$

$$\begin{aligned}\dot{x}_c &= \hat{A}_c x_c + \hat{B}_c y \\ u &= \hat{C}_c x_c\end{aligned}\tag{4.53}$$

$$\mathbf{x}_C = \begin{bmatrix} \mathbf{x}_{C_R} \\ \mathbf{x}_{C_T} \end{bmatrix} \quad \hat{\mathbf{A}}_C = \begin{bmatrix} \hat{\mathbf{A}}_{C_{11}} & \hat{\mathbf{A}}_{C_{12}} \\ \hat{\mathbf{A}}_{C_{21}} & \hat{\mathbf{A}}_{C_{22}} \end{bmatrix} \quad \hat{\mathbf{B}}_C = \begin{bmatrix} \hat{\mathbf{B}}_{C_1} \\ \hat{\mathbf{B}}_{C_2} \end{bmatrix} \quad \hat{\mathbf{C}}_C = \begin{bmatrix} \hat{\mathbf{C}}_{C_1} & \hat{\mathbf{C}}_{C_2} \end{bmatrix} \quad (4.54)$$

The individual partitioned state-space matrices are defined in equation 4.54.

Truncation of the insignificant states results in the final balanced, reduced-order controller,

$$\begin{aligned} \dot{\hat{\mathbf{x}}}_{C_R} &= \hat{\mathbf{A}}_{C_{11}} \hat{\mathbf{x}}_{C_R} + \hat{\mathbf{B}}_{C_1} y \\ u &= \hat{\mathbf{C}}_{C_1} \hat{\mathbf{x}}_{C_R} \end{aligned} \quad (4.55)$$

In order to find the minimum-order controller realization during the control synthesis process in Chapter 5, the number of states truncated was successively increased until significant performance loss occurred. Once the lowest order realization with minimal nominal performance loss was identified, it was checked to ensure robust stability. If robust performance was lost, truncated states were added back until it was achieved. The result was a control law reduced in order that met nominal and robust stability requirements.

CHAPTER 5

Robust Weighted H_2/H_∞ Control Synthesis

The fundamental mathematics required to solve robust weighted H_2/H_∞ control synthesis for the K1 pitch control problem were presented in Chapter 4. Furthermore, commercially available control synthesis software tools have the capability to efficiently solve AREs, perform γ -iteration, and apply BMOR methods. In order to create a simple, efficient process for developing robust weighted H_2/H_∞ control laws, a MATLAB-based Graphical User Interface (GUI) was created, which exploited existing built-in robust control synthesis functions. Using the GUI, computer aided design of robust weighted H_2/H_∞ control systems was performed successfully achieving low-order compensator design.

This chapter presents two design methodologies which were employed during the development of robust weighted H_2/H_∞ control designs. The first details high-level tasks for developing low-order, robust weighted control laws. The second describes the low-level steps used to create optimal H_2 and H_∞ controllers, as well as sub-optimal controllers. A brief summation of the MATLAB-based GUI's structure and capabilities is also presented along with the results from the entire control synthesis process. Finally, two low-order controllers with acceptable performance are selected for comparison with the classically developed designs of Chapter 3.

5.1 Design Methodology

During the classical design, the development of the SISO control law was reduced to a selection of approximately 10 parameters, which translated into an extremely large number of possible controller designs. The MCS design framework contained an equivalent number of design parameters. Therefore, it became obvious that a systematic design methodology was needed to manage successfully all of the design variables.

With that goal in mind, two architectures were developed to limit the number of design options at any particular step during the synthesis process. The first, referred to in Figure 5.1 as the Control Synthesis Hierarchy, was developed to gradually progress from optimal solutions to robust solutions, and finally to low-order solutions. The second, called the H_2/H_∞ Solution Process in Figure 5.2, was aimed at producing optimal H_2 , optimal H_∞ , and sub-optimal design solutions in a sequential manner. Together, these two schemes were incorporated into a single design framework and used to create low-order, robust weighted H_2/H_∞ control laws.

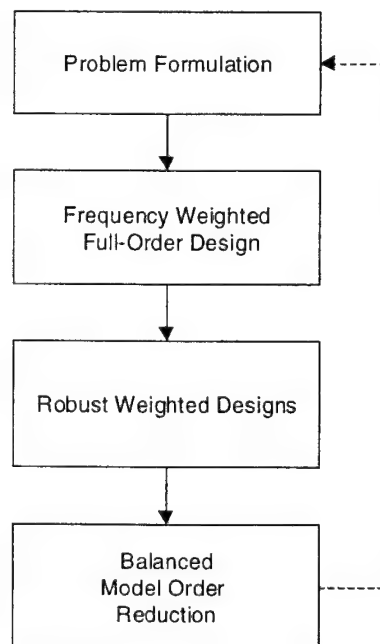


Figure 5.1 – Control Synthesis Hierarchy

The Control Synthesis Hierarchy is illustrated in Figure 5.1. This iterative, four step method began with the problem formulation presented in Chapter 4, and then proceeded through the full-order, robust, and BMOR design phases. The advantage of using this hierarchical approach was that each design phase was focused on selecting a specific set of design variables. Once an acceptable controller was achieved in a particular phase, that phase's design variables were fixed for the remainder of the synthesis process. In this manner, it was necessary to work with only a few parameters at a time, so that the size of the problem was kept manageable.

After problem formulation, the second phase in the Control Synthesis Hierarchy was the solution of the full-order design problem. In this problem, compensation was designed based on a high fidelity model of the K1 dynamics. The goal of this phase was to define the shape of the weighting functions for the cost outputs that were necessary to achieve the frequency domain specifications. Using the general shapes established during problem formulation, this phase boiled down to establishing values for the design parameters A_H , A_L , and ω_c for the filter on the control effort cost, and A and ω_c for the filter on the pitch angle error cost.

Once acceptable cost weights were found, the cost weighting functions of the full-order, weighted H_2/H_∞ design problem were fixed, and the stability margins achieved with this compensation were used as "nominal" guidelines for the robust synthesis problem. Any subsequent changes in the order and robustness of the design model during later phases were aimed at maintaining performance near the "nominal," which would ensure a similar degree of performance.

The third phase in the Control Synthesis Hierarchy was the design of robust weighted H_2/H_∞ control laws. Using the cost weights from the full-order solutions, two different methods were pursued to develop robust control designs. However, selecting a reduced-order plant was first necessary and common to both procedures. Specific to GA, the only remaining design parameter to be

determined was the forward path gain. MU, on the other hand, had several design parameters. The uncertainty penalty gain and the uncertainty input shaping filter were design variables inherent to MU methods. However, the low frequency gain of the sensitivity cost weight was also a necessary design variable in the MU approach. This gain was used to increase the level of steady-state performance, which deteriorated as a result of increasing the uncertainty cost gain. With the establishment of these parameters, successful control laws were developed for each method and carried forward into model reduction analysis.

The final phase in the Control Synthesis Hierarchy was the application of BMOR techniques to the acceptable robust control laws. The single design variable in this phase was the final order of the reduced compensator. By choosing a level of reduction that minimized both controller order and adverse effects on system performance, low-order, robust weighted H_2/H_∞ control laws were achieved. Analysis of these control laws was then used to make changes in the problem formulation, and the entire Control Synthesis Hierarchy was repeated.

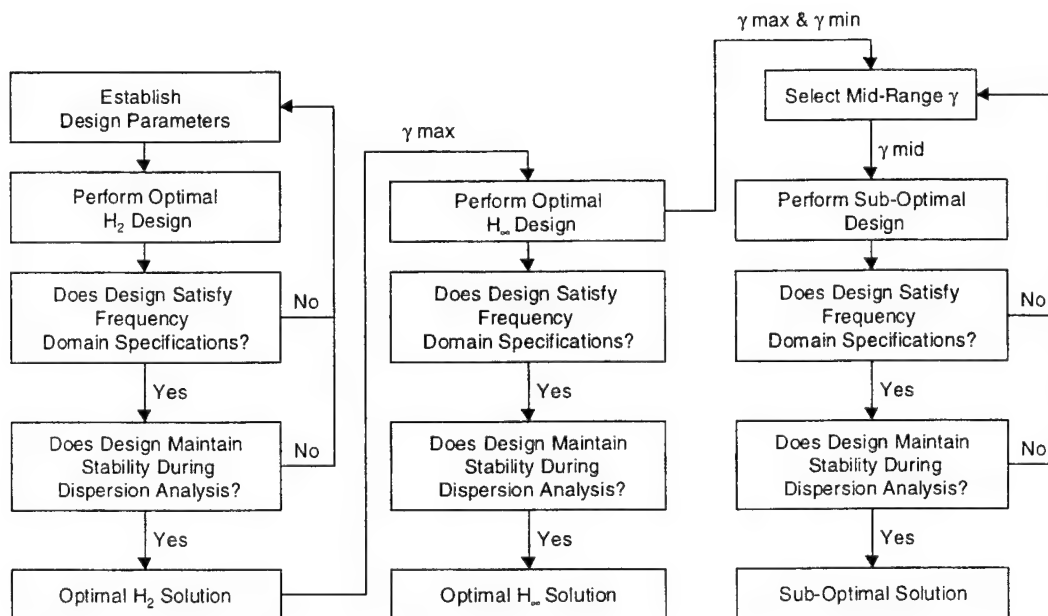


Figure 5.2 -- H_2/H_∞ Solution Process

The structure of the Control Synthesis Hierarchy provided useful constraints on the problem size. Selecting and analyzing the effects of a few design variables at a time kept the problem manageable. However, another scheme was needed to specifically address the multiplicity of objective functions.

The H_2/H_∞ Solution Process was the second decision architecture established for the development low-order, robust weighted H_2/H_∞ control laws. Performed as a sub-task within the full-order and robust problem phases in the Control Synthesis Hierarchy, it provided a sequential method for generating and evaluating optimal H_2 , optimal H_∞ , and sub-optimal solutions. Figure 5.2 shows the H_2/H_∞ Solution Process.

The H_2/H_∞ Solution Process began with a selection of the design parameters specific to the current phase of the Control Synthesis Hierarchy. Then, an optimal H_2 design was generated using MATLAB software and assessed for both nominal stability using frequency domain specifications and robust stability using the dispersion analysis framework. If the design did not meet specifications, its associated design parameter selection was rejected and another one was attempted. However, if the design did succeed, it was designated as a optimal H_2 solution, and the H_∞ -norm of the closed-loop design model was used as an initial guess for γ in the optimal H_∞ design.

Using that guess, the optimal H_∞ solution was obtained for the exact same design model, and the same analysis tools were applied. If the resulting compensator did not meet specifications, then it was concluded that the optimal H_∞ control law for that design model was inadequate and incapable of meeting performance specifications. Otherwise, it was designated as an optimal H_∞ solution.

Using the H_∞ -norm from the optimal H_2 problem and the H_∞ -norm from the optimal H_∞ problem as the upper- and lower- bounds of a γ search "space," sub-optimal designs were performed with mid-range γ values. By selectively choosing mid-range γ values, an attempt was made to fine tune the nominal and

robust performance of the sub-optimal controller. If this was accomplished, then the resulting controller was designated as a sub-optimal solution. Otherwise, the conclusion was made that the sub-optimal solution provided no advantage in performance over the optimal H_2 or H_∞ solutions.

Through the H_2/H_∞ Solution Process, it was possible to compare the performance of controllers created by the three different optimizations based on the same design model. It proved to be an effective and systematic way of exploring the solution possibilities.

5.2 MATLAB/SIMULINK Based Design Architecture

A MATLAB based GUI was developed to facilitate the robust weighted H_2/H_∞ control synthesis process. This not only increased the speed with which control laws were developed, but it also provided a concise presentation of all the significant design parameters. Figure 5.3 shows the control synthesis GUI, which is divided into seven main areas.

The upper left third of the GUI is devoted to defining the dynamic effects included in the K1 plant model. This plant model was used in the problem formulation to define the design model. Toggles specific to individual modes in the K1 dynamics provided the ability to include/exclude different dynamic effects in the design model. However, the AOA state could not be removed from the design model because it was needed to incorporate the wind disturbance input. Edit boxes are also provided to define the size and order of system delays associated with the IMU and VMC. The size (in seconds) and order of the delays were used by MATLAB to create Pade approximations of the transportation lags.

The upper middle third is devoted to defining the same parameters as the upper left third. However, these parameters were used for the response model and not the design model. The response model was used to generate system responses and calculate stability margins for an “actual” system, which was different if dynamics had been excluded from the design model. For the K1 pitch

control problem, all dynamics were included in the response model. In this way, robust control laws were designed on reduced-order systems and assessed for its performance in the full-order system.

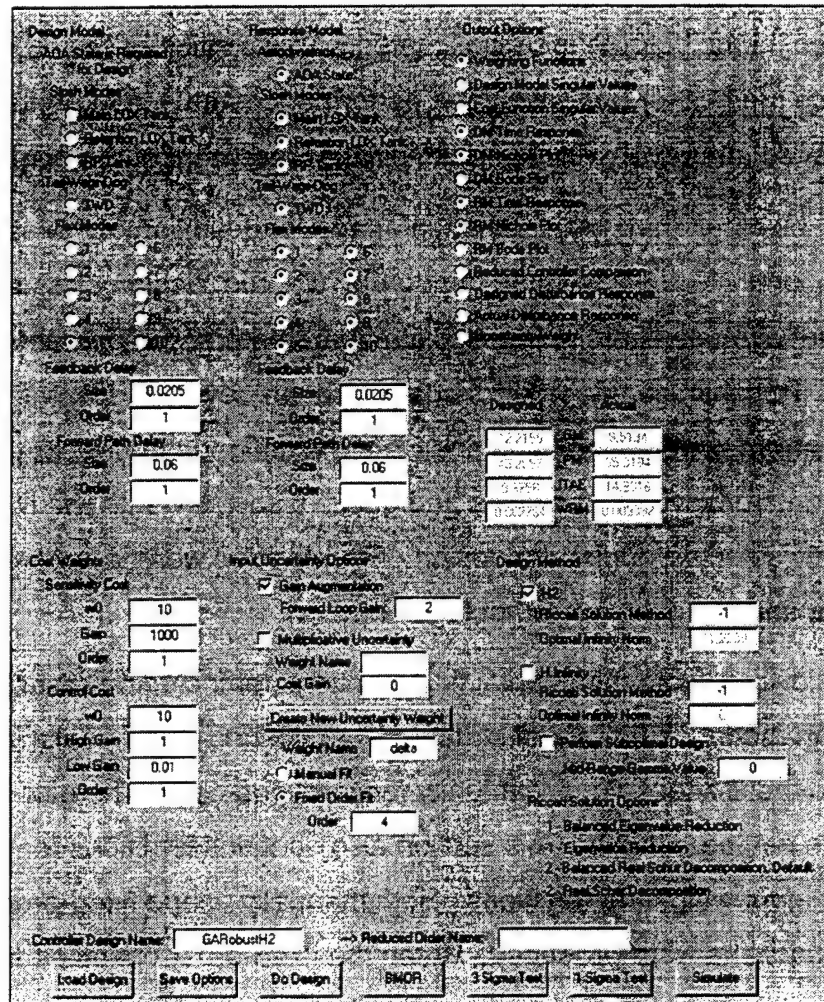


Figure 5.3 – Robust Control Synthesis GUI

The upper right third of the GUI presents several different output options that were used to assess control designs. Independent options for design model (DM) and response model (RM) responses were established to aid in comparative analysis. Open-loop frequency responses were used for visual assessment of stability margins. While, the closed-loop, reference step response aided transient performance analysis. Additionally, outputs of the cost weighting functions and the singular values of both the open- and closed-loop design

models provided objective function insight. Step responses to disturbance inputs were also checked to ensure adequate disturbance rejection during the design process. Other analysis tools included options for comparing reduced- and full-order controllers, and viewing the uncertainty input shaping filter. The performance metric outputs are also located in this section of the GUI. Four performance metrics for both designed performance and actual performance were displayed after every run for rapid initial assessment of the control design.

The lower left third provided an interface for definition of the cost output filters, $W_{U(s)}$ and $W_{S(s)}$, established during the full-order design phase. The development of these filters and associated parameters was presented in Chapter 4. To minimize the order of compensation developed by the design process, first-order weighting functions were maintained throughout the design. However, the crossover frequencies and gains associated with the two cost filters were actively selected during the design. Frequencies were in units of radians per second, and the gains were not logarithmic.

The lower middle third contains the options for including robust structures in the design model. If no robust structure was desired in the design, the GUI defaulted to the GA technique with unity forward loop gain. The gains for GA and MU are also not logarithmic. This section also contains functions for generating uncertainty input weighting functions. Both manually fit and fixed-order fit weighting functions were produced. When the fixed-order option was used, the MATLAB function `magfit.m` internally generated a weighting function of desired order for the MU architecture. When the manual option was used, a frequency plot of the exact weighting function was created to help guide an interactive magnitude-fit function. This is the method in which the course-fit system presented in Chapter 4 was generated.

The lower right third presents options for the three different solution types. According to the H_2/H_∞ Solution Process, an H_2 design was first performed, after which the design's optimal H_∞ -norm was automatically calculated. Then, an H_∞ design was performed using the H_2 design's H_∞ -norm for its initial guess. Once

the H_∞ process was complete its optimal H_∞ -norm was also calculated to serve as the lower-bound in the γ -iteration. Only then, was a sub-optimal design performed using a user-defined mid-range γ between the two optimal H_∞ -norm bounds.

Finally, the bottom portion of the GUI houses the executable functions necessary to complete the MCS process. The design of H_2 controllers was supported with the `h2syn.m` MATLAB function, and the design of H_∞ controllers used the `hinfyn.m` function. BMOR was performed using `sysbal.m` to balance the control system and find its HSVs. This function also truncates states associated with HSVs that are extremely small ($<10^{-15}$). The final truncation of the controller was attained using the `hankmr.m` function, which truncated the controller to a desired size.

Fundamental to the GUI framework are the SIMULINK models that were used to create state-space realizations of the control loop architecture. Using the `linmod.m` function in MATLAB, it was possible to eliminate the need for manual block diagram reduction similar to that performed in Chapter 4. Although it was not possible to dictate the arrangement of states in the systems `linmod.m` produces, the inputs and outputs were defined, and the graphical nature of the models allowed rapid changes to the architecture without time-intensive coding.

Two of the models used within the MCS framework are presented in Figure 5.4 and Figure 5.5. In particular, these models were used to generate the GA and MU state-space realizations of the design model. Several other models were also developed to support functions in the control synthesis GUI, because different SIMULINK models were required to generate open- and closed-loop transfer functions. However, the differences among the models were negligible and their presentation is not necessary to convey the structure of the techniques used to execute the GUI.

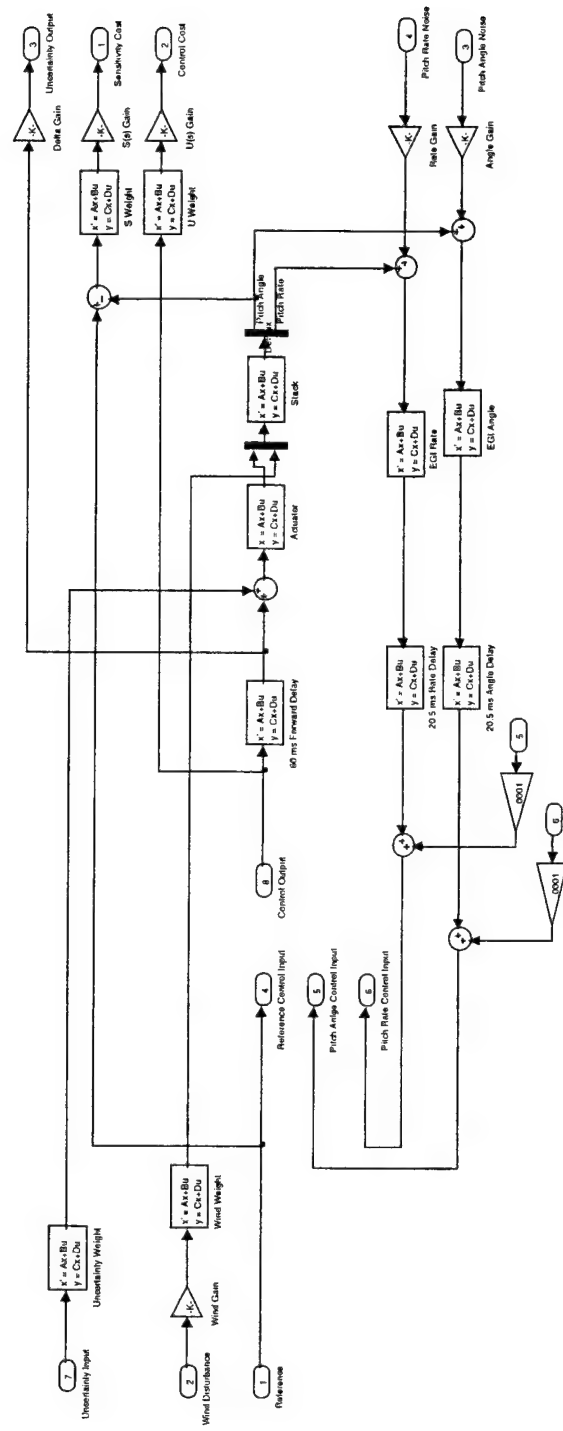


Figure 5.4 – Multiplicative Uncertainty Design Model

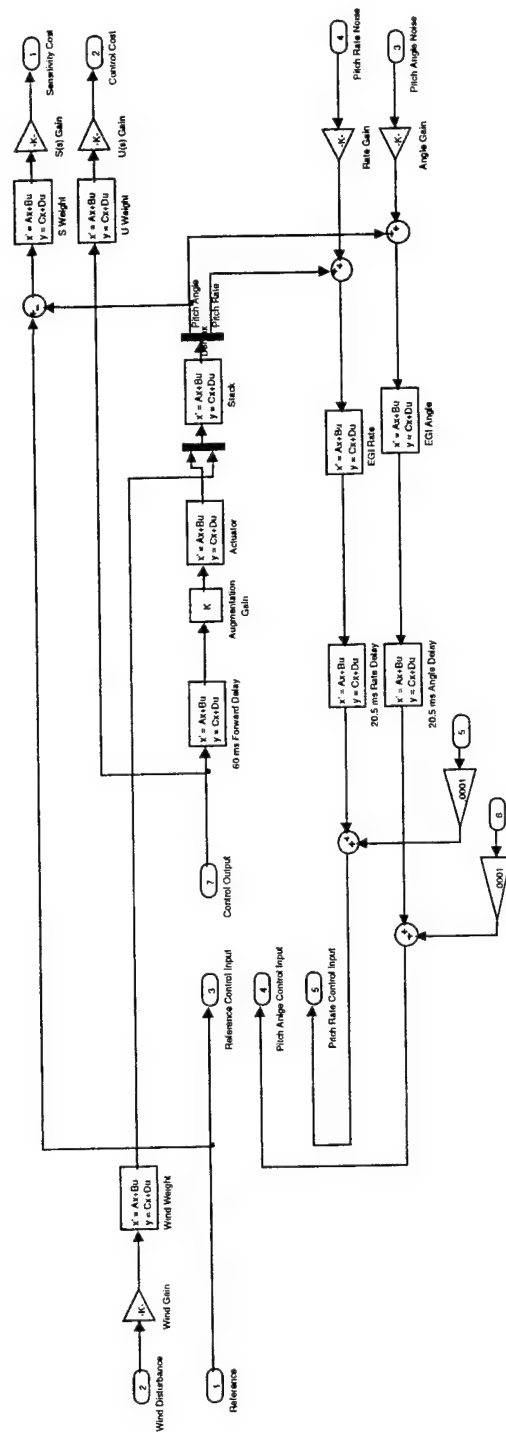


Figure 5.5 – Gain Augmentation Design Model

5.3 Robust Weighted H_2/H_∞ Controller Design

The Control Synthesis Hierarchy and the H_2/H_∞ Solution Process were applied to the Kistler pitch control problem with the goal of achieving the same frequency specifications required of the SISO designs. An additional performance metric, the Wind Response Metric, was established to aid in the analysis of controller disturbance rejection. The Wind Response Metric (WRM) reflects the wind disturbance to reference response ratio of a stable system. WRM is defined by equation 5.1, which shows that it is the integral of a system's step response to a wind gust input divided by the integral of the system's step response to a pitch reference input. Minimization of the WRM was a secondary objective of the MCS process, as its value depends on the quality of the system's pitch response.

$$WRM = \frac{\int_0^{t_f} |\theta_{Wind}(t)| dt}{\int_0^{t_f} |\theta_{Pitch}(t)| dt} \quad (5.1)$$

During the analysis presented for each of the following control laws, the open-loop frequency response and closed-loop time response of the system are provided. In the Nichols plots, the reduced-order design model response is shown in dark, and the full-order response model response shown in light. The primary stability point, $[180^\circ, 0 \text{ dB}]$, in the magnitude-phase plane is indicated by a small dot. For the reference step response plots, the design model response is indicated with dashed lines, and the response model is indicated with solid lines. Additionally, summaries of the $3\text{-}\sigma$ and combined $1\text{-}\sigma$ dispersion cases for selected controllers are contained in Appendix F. Moreover, detailed summaries of the dispersion runs are presented in Appendix E for the final reduced-order, robust designs.

5.3.1 Full-Order Design

In light of issues concerning the sensitivity of full-order designs, the primary goal of this phase was the establishment of the cost output weighting functions and not a controller with robust stability. Using first-order filters to maintain low order, the selection of five design variables was necessary to define the cost shaping filters in Chapter 4. With respect to the control effort penalty, the A_H , A_L , and ω_c were needed. For the pitch error penalty, only A and ω_c were needed. The H_2/H_∞ Solution Process, Figure 5.2, was used to complete the full-order control designs

To establish the initial guess for the weighting function for the control effort output, actuator specifications were used as a guideline. According to the specifications, nominal actuator bandwidth is 25 rad/s. Understanding that any control output issued higher than this frequency will exceed physical capabilities, the crossover frequency of the control weight was initially placed at the 25 rad/s point, and the high frequency gain, A_H was set to 0 dB. The low gain was set at -40 dB. This level established a cost which eliminated cheap control while not over-penalizing low frequency control effort. The initial control weight, $W_{U(s)}$ is shown in Figure 5.6.

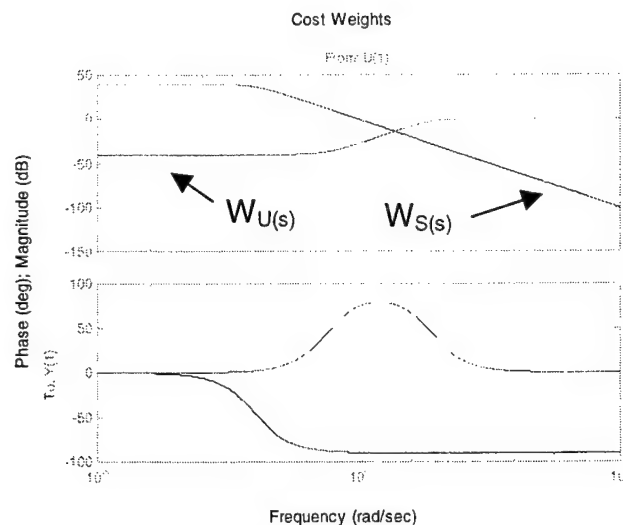


Figure 5.6 – Initial Weights for Cost Outputs, $z_{S(s)}$ and $z_{U(s)}$

The initial pitch error weighting function, $W_{S(s)}$, was also guided by previous knowledge. From the SISO designs in Chapter 3, the achievable bandwidth of the classical control laws was approximately 1 rad/s. Therefore, the crossover frequency for the error weight was initially set to 1 rad/s, because the crossover frequency of the sensitivity cost has been shown to influence system bandwidth. As an initial guess, the low-frequency gain of this filter was established at 40 dB. The initial guess for $W_{U(s)}$ is also shown in Figure 5.6.

Applying these initial configurations in the GUI framework, an optimal H_2 design was obtained, and the resulting system step response and Nichols plots are presented in Figure 5.10 and Figure 5.11. The resulting optimal H_2 control law provided the open-loop system with approximately 4 dB of GM, 31° of PM, and its Nichols plot, Figure 5.11, indicates adequate high frequency attenuation. Unfortunately, the size and dimension of this optimal control law, as well as the others presented in this development, make it cumbersome to present the results for each design. Therefore, a decision was made to present only a final few of the products of the design process, though, it is beneficial to closely investigate one design to gain a feel for how optimal H_2/H_∞ control designs attempt to achieve stability.

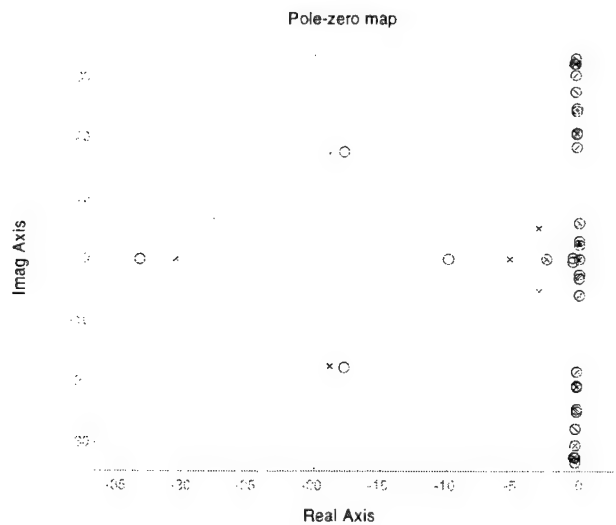


Figure 5.7 – Pole-Zero Map of Full-Order, Optimal H_2 Controller

Figure 5.7 illustrates the pole (x) and zero (o) locations of the optimal H_2 control design developed using the initial cost weight configurations. (Note: This is a magnified view in which some poles and zeros with large magnitudes were omitted in order to focus in on the region where vehicle dynamics exist. Furthermore, the zeros shown are only for the reference-to-control signal channel. This omission helps reduce the clutter of the zeros in other channels, which have nearly the same location, but still conveys the way in which the control design works.) Here, it was clear that the controller contains pole-zero pairs, or notch filters, that attempt to cancel out the dynamics of the design model. Thus, performance was achieved by “notching out” the existing dynamics and replacing them with a desired response. The presence of notches in the control design is also noticeable in Figure 5.11, which shows that the resonant peaks of the main LOX and RP slosh modes were significantly reduced from the nominal plant dynamics in Figure 5.20. With regards to all of the full-order step and frequency responses presented here, the designed and actual responses are the same, because the control was designed from a full-order model. In this way, the control designs had “perfect” information about the system dynamics and were able to control the system exactly.

Returning to the design process, the bandwidth of the sensitivity weight was increased from 1 rad/s to 5 rad/s and all other filter parameters were kept the same in an attempt to increase the GM and achieve the primary frequency domain specifications. Inspection of the corresponding Nichols plot in Figure 5.13 shows this change increased the open-loop GM to approximately 5 dB and the PM to 34° , while maintaining high frequency attenuation. Increasing the bandwidth of the sensitivity cost weight also had an adverse effect in time domain performance as shown in Figure 5.12. The amount of control effort generated in response to a step in pitch reference was significantly increased. As expected, the bandwidth of the system had been increased because of the 5 rad/s bandwidth change in the sensitivity cost weight. This increase can be seen in the reduction in the size of the slosh mode dipoles between Figure 5.11 and Figure 5.13 that resulted from increased control effort in the 2-5 rad/s range.

Considering these effects, three changes were applied to the cost weights in order to achieve an acceptable design. First, the sensitivity weight crossover frequency was increased further from 5 rad/s to 10 rad/s to achieve needed increases in open-loop GM. The second change was in the crossover frequency of the control weight. In an attempt to mitigate the apparent increase control effort that arises from an increase in sensitivity weight bandwidth, the bandwidth of the control weight was reduced from 25 rad/s to 10 rad/s. The final change in the cost weights was aimed at increasing the steady-state performance of the closed-loop system, which was realized as a necessary consequence of control weight bandwidth reduction. A 60 dB level was set for the low frequency gain of the sensitivity weight to enforce an increased level of steady-state performance. The final cost weights are presented in Figure 5.8.

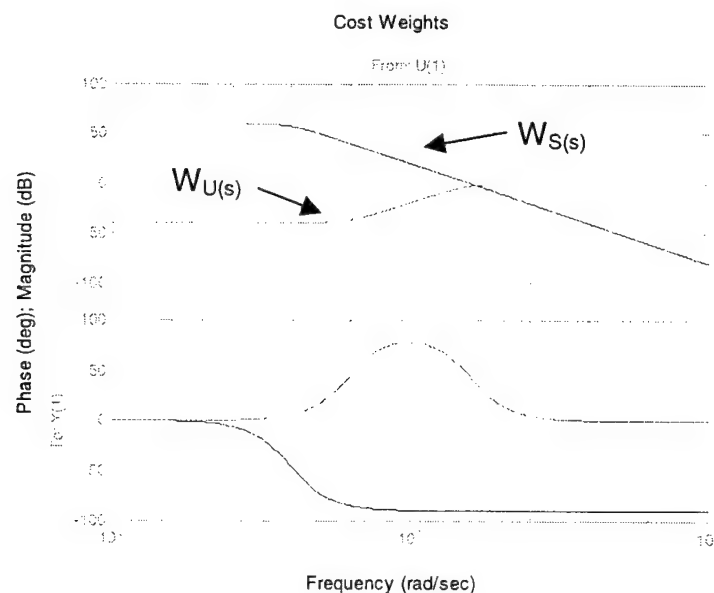


Figure 5.8 – Final Weights for Cost Outputs, $z_{S(s)}$ and $z_{U(s)}$

Implementing these modifications in the GUI framework produced a system with acceptable performance characteristics, as shown in Figure 5.14 and Figure 5.15. The open-loop GM and PM were 6 dB and 38° , respectively. The step responses, Figure 5.14, also shows quality time domain performance having an ITAE of 10.5. The system's WRM was 0.0014. Additionally, the

control effort by the system was lowered as a result of the reduction in the control cost weight bandwidth, which can be seen as the slight increase in the size of the slosh dipoles between Figure 5.13 and Figure 5.15.

However, it was very apparent from the gimbal response, Figure 5.14, that the control system was actively controlling the slosh states. Moreover, this level of control was expected because the final H_2 optimal design had essentially the same form as shown in Figure 5.7. This high level of control highlights the model inversion properties within the H_2 control law. Unfortunately, the performance of the inversion is extremely dependent on the actual location of the system dynamics. This dependence makes the controller sensitive to deviations from the pole-zero locations for which the "notches" were designed, and this sensitivity was realized when the optimal H_2 controller failed several of the $3\text{-}\sigma$ perturbation cases as shown in Appendix F.

Although the goal of establishing satisfactory cost weights was completed, solutions to the optimal and sub-optimal H_∞ control problems were also explored to analyze the differences among the solution types. The optimal H_∞ solution was produced effortlessly using the initial guess of $\gamma_{\max}=11.7$ from the H_2 solution process. Its step response and Nichols plots are presented as Figure 5.16 and Figure 5.17, respectively. However, the optimal H_∞ solution did not meet design requirements, having only 4.5 dB of GM and 43° of PM. Additionally, a Nichols plot of the resulting open-loop system reveals inadequate attenuation of the retention tank LOX mode.

The optimal H_∞ solution did provide a lower bound for the γ -search space, $\gamma_{\min}=9.3$. Using the bounds provided by the optimal H_2 and H_∞ solutions, a sub-optimal H_∞ control law was developed by slowly raising the mid-range value from the lower bound until adequate GM and PM were achieved. Its frequency response, as shown in Figure 5.19, shows that at a mid-range value of $\gamma_{\text{mid}}=11$ achieves a GM of 6 dB and PM of 39° . The step response, shown in Figure 5.18, has satisfactory time domain performance. The associated ITAE and WRM were 8.5 and 0.0028, respectively.

In comparing the three solutions, each was able to provide a stabilizing controller and exhibit essentially the same time response characteristics. However, only two of the solutions, the optimal H_2 and sub-optimal solution, were able to satisfy frequency domain performance requirements. The Nichols plots of the three different open-loop systems revealed that, unlike the optimal H_2 and sub-optimal solutions, the optimal H_∞ solution had inadequate attenuation of the nominal retention tank LOX mode. This lack of open-loop system roll-off is undesirable and makes the system even more susceptible to disturbances and uncertainties.

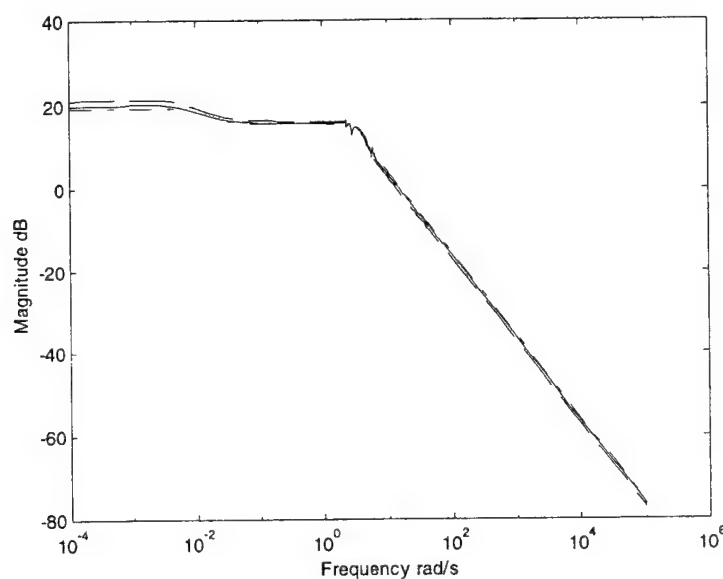


Figure 5.9 – Maximum Singular Values for the Optimal H_2 , Optimal H_∞ , and Sub-Optimal Designs

Finally, the similarities in the time and frequency domain performance of the optimal H_2 and sub-optimal solutions were seen as attributable to two factors. First, the maximum singular values of the closed-loop design models are flat over a large frequency range, as shown in Figure 5.9. It is intuitive that having a maximum SV common to a large portion of the frequency spectrum creates a condition in which the H_2 -norm and the H_∞ -norm are essentially equivalent. This helps explain the high degree of similarity in the maximum SV of each closed-

loop design model in Figure 5.9. Second, the mid-range γ value used in the sub-optimal solution, 11.0, was very close to the optimal H_2 value, 11.7, which indicates an even closer match of closed-loop design model SVs.

The design results of the full-order design phase are summarized in Table 5.1. With insight into the comparative advantages of the different approaches gained from this phase, subsequent robust design solutions were expected to have similar characteristics.

Table 5.1 – Full-Order Design Phase Summary

Metric \ Design	Initial H_2	Improved H_2	Optimal H_2	Optimal H_∞	Sub-Optimal
GM (dB)	4	5	6	4.5	6
PM (deg)	31	34	38	43	39
ITAE	14.8	41.1	10.5	8.38	8.5
WRM	0.0015	0.0008	0.0014	0.013	0.0028
High Freq Attenuation	Yes	Yes	Yes	No	Yes
Robust Stability	No	No	No	No	No

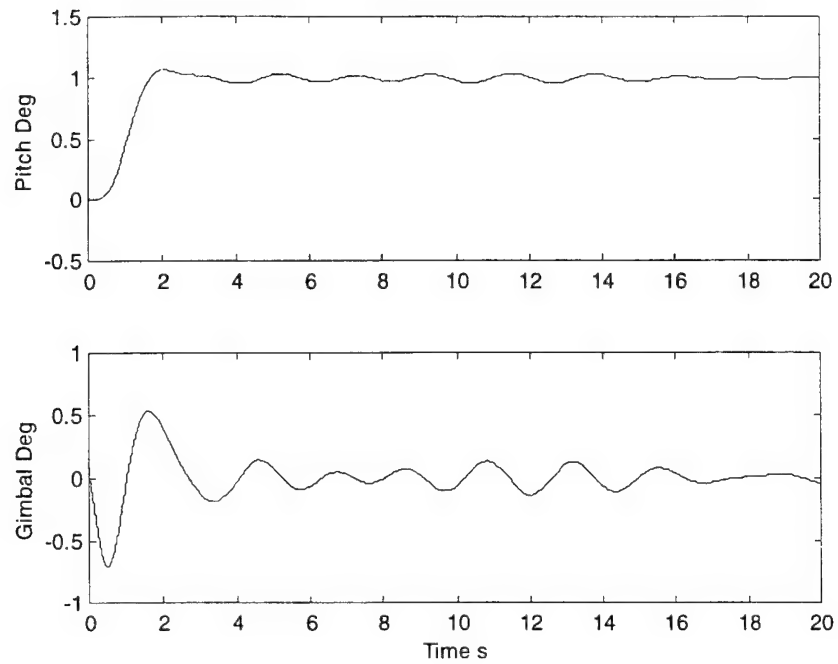


Figure 5.10 – Initial Full-Order H_2 Design Step Response

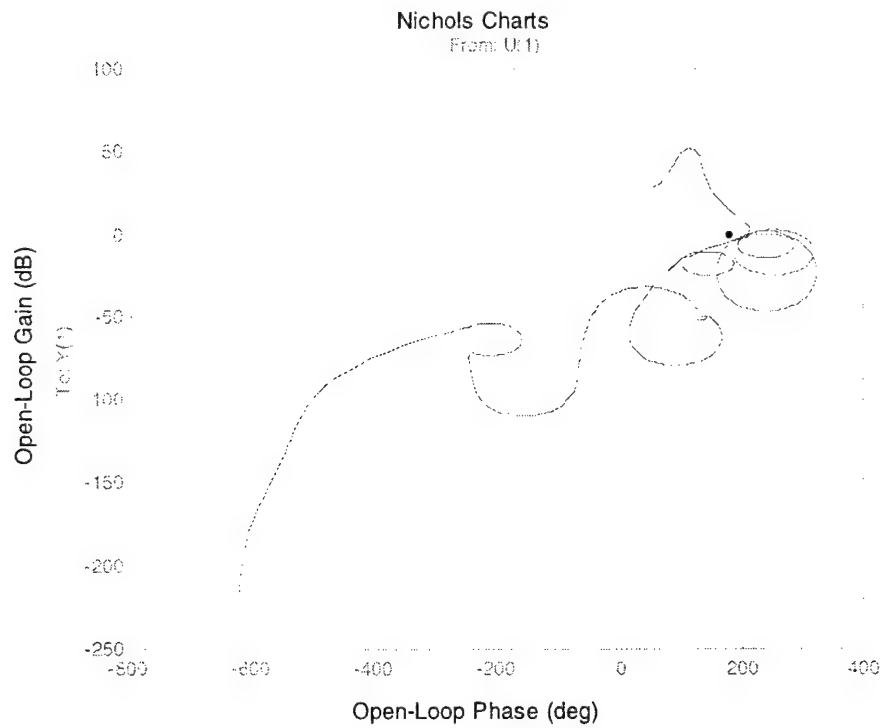


Figure 5.11 – Initial Full-Order H_2 Design Frequency Response

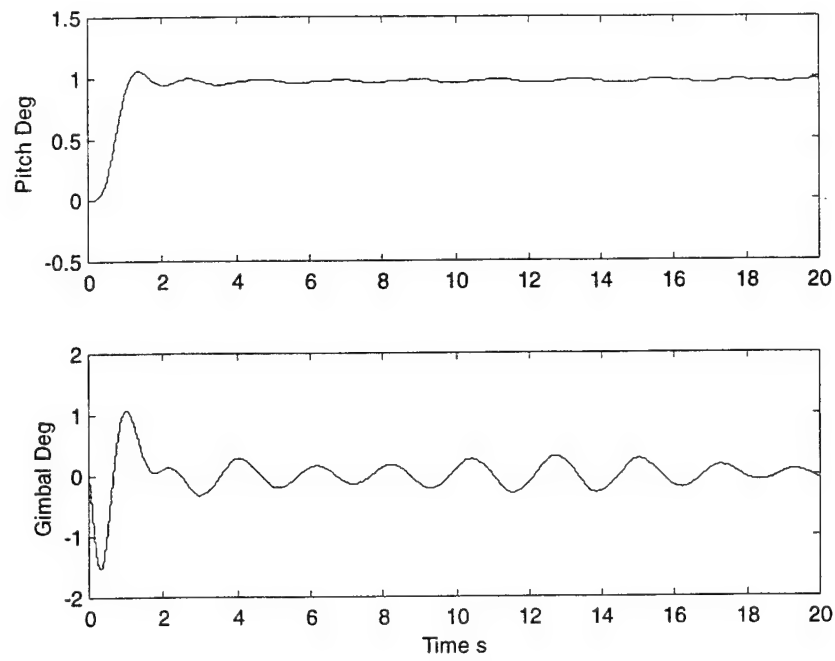


Figure 5.12 – Improved Full-Order H_2 Design Step Response

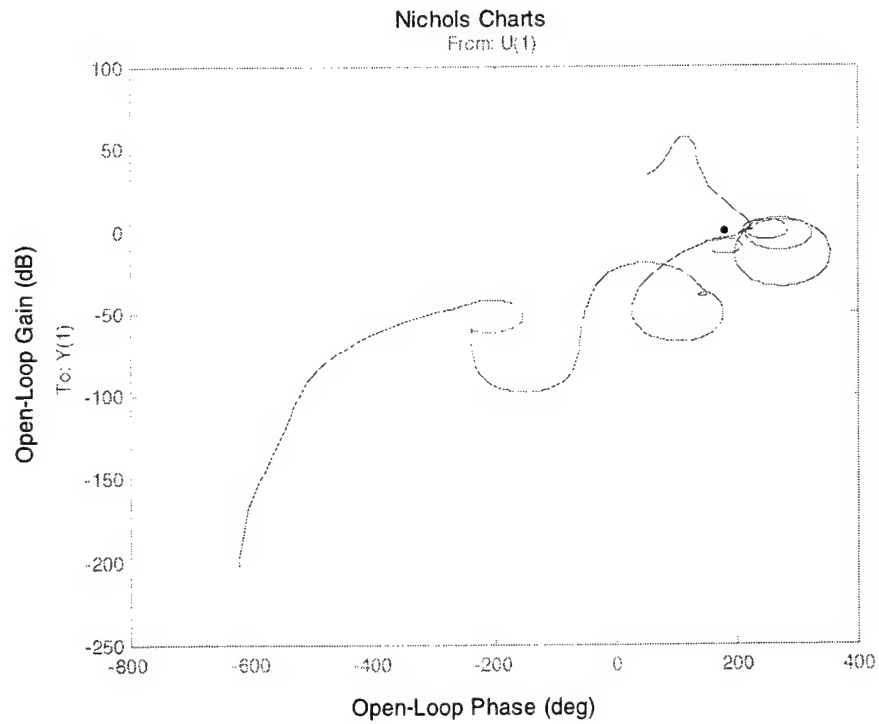


Figure 5.13 – Improved Full-Order H_2 Design Frequency Response

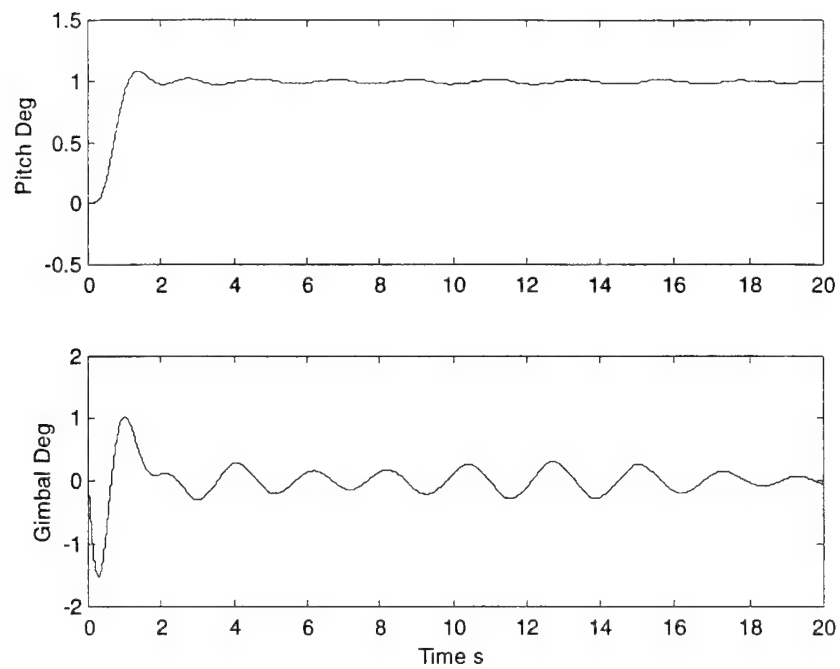


Figure 5.14 – Optimal Full-Order H_2 Design Step Response

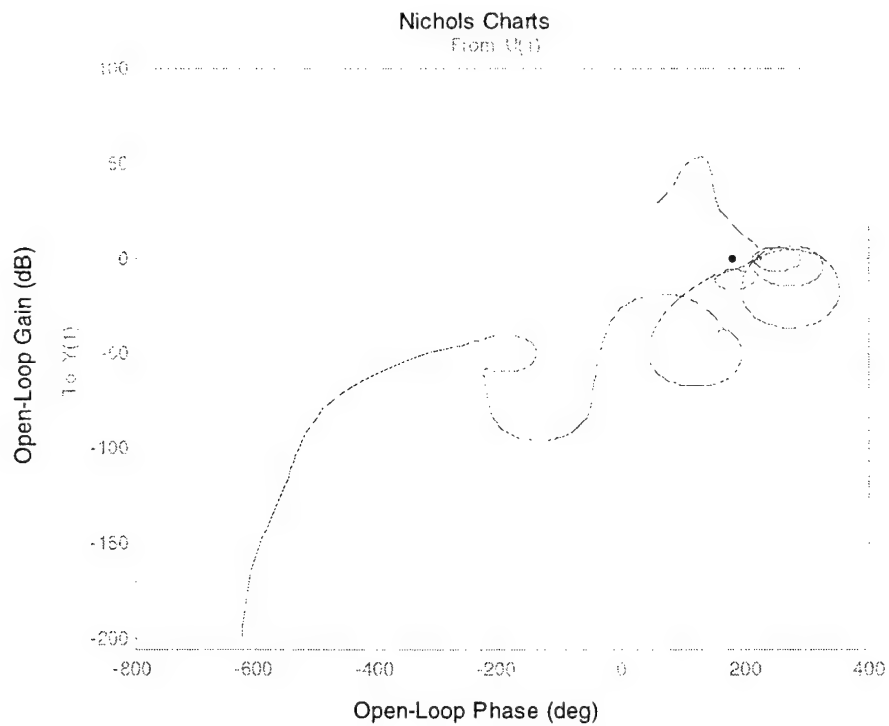


Figure 5.15 – Optimal Full-Order H_2 Design Frequency Response

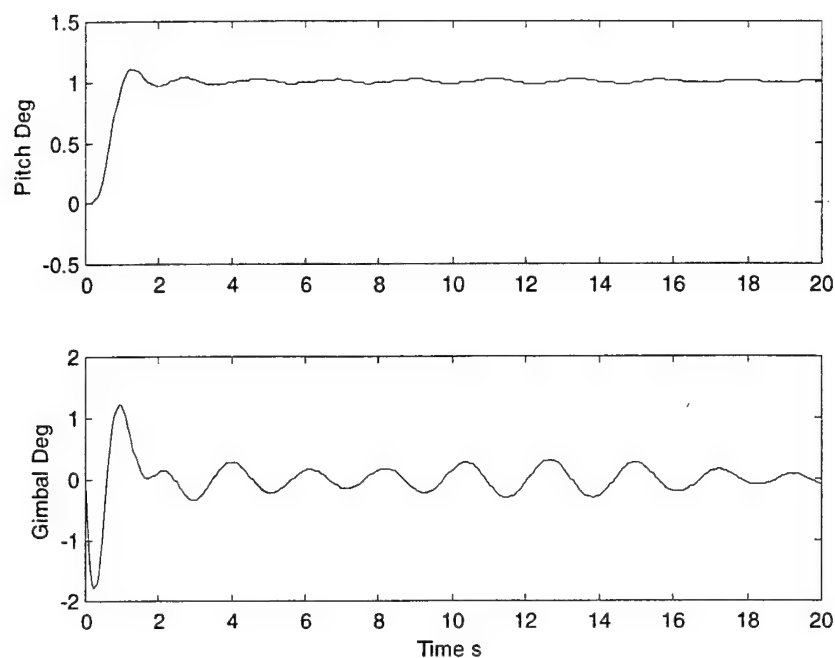


Figure 5.16 – Optimal Full-Order H_∞ Design Step Response

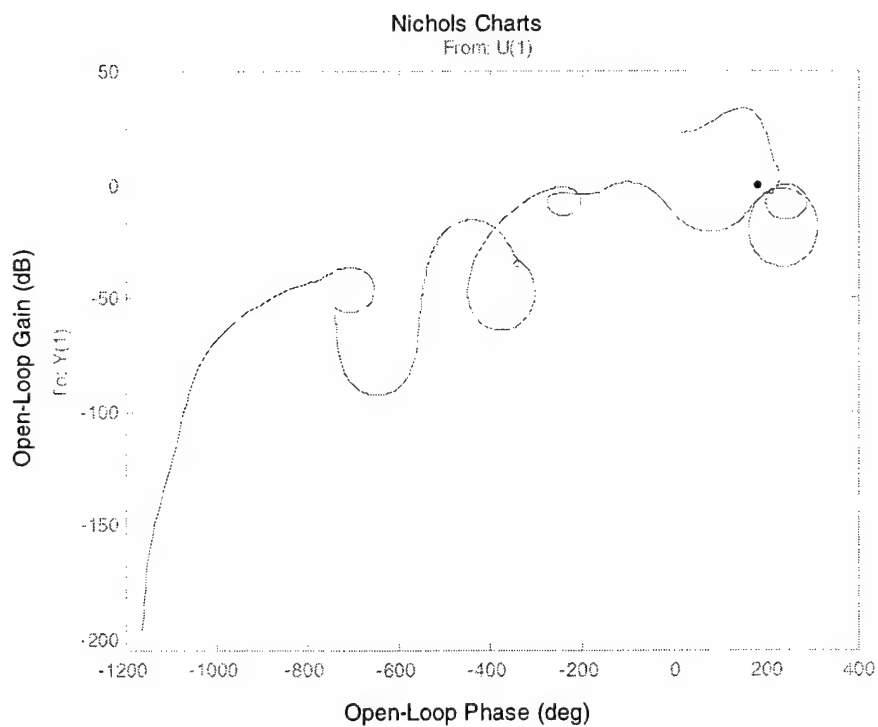


Figure 5.17 – Optimal Full-Order H_∞ Design Frequency Response

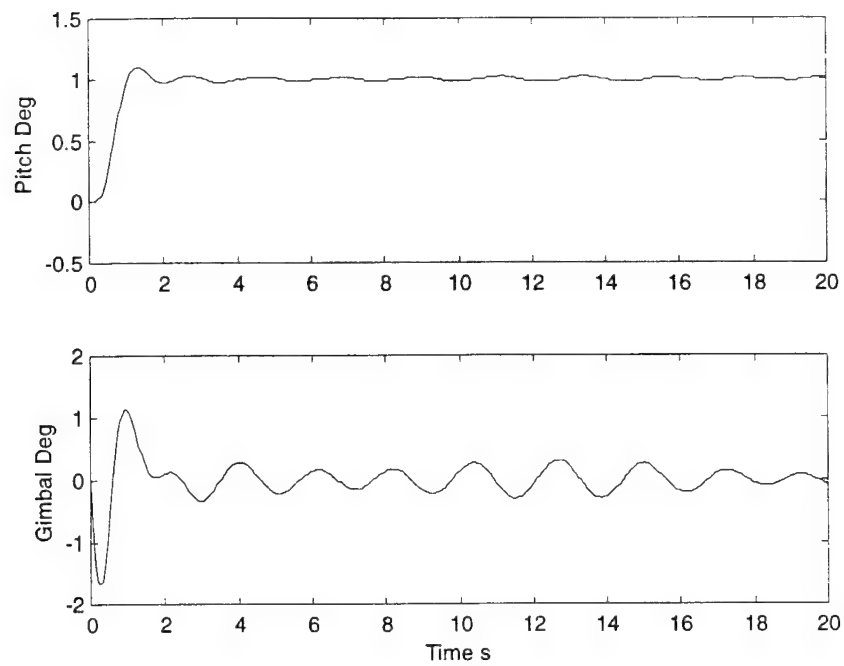


Figure 5.18 – Sub-Optimal Full-Order Design Step Response

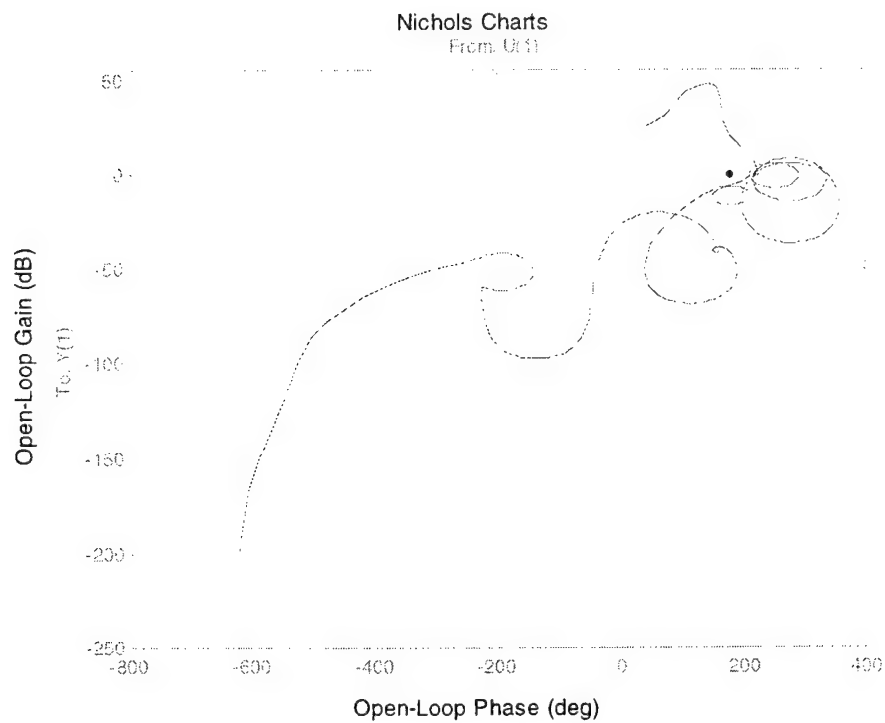


Figure 5.19 – Sub-Optimal Full-Order Design Frequency Response

5.3.2 Robust Design

Using the same control effort and pitch error weights from the full-order design problem, the sensitivity of the full-order design solutions was addressed by implementing two types of uncertainty structures into the design model. GA and MU were used to mitigate design model parameter sensitivity. Additionally, compensation order was addressed by the elimination of insignificant system dynamics. The resulting controllers of the robust design phase not only had acceptable nominal performance, but they also maintained robust stability.

5.3.2.1 GA Robust Design

In order to develop a reduced-order design using GA techniques, it was first necessary to find a minimum order, plant model realization to use in the synthesis design model. This reduced model contained only the bare minimum of dynamics necessary to characterize critical regions of the K1 plant model frequency response. This is best seen in Figure 5.20, which shows the reduced-order model's Nichols plot as a dark line superimposed on the full-order model's plot light line. An inspection of the 10 flex modes in the full-order system in Chapter 2 revealed that the fifth mode dominates all others. By removing all but the fifth flex mode in the reduced-order model, the high frequency dynamics of the plant model were essentially unchanged. The critical regions in Figure 5.20, where GM, PM, and gain attenuation are determined, were preserved by the reduced order model. Furthermore, the dynamics of the three low frequency slosh modes were not important to those critical regions and were also omitted.

A physically intuitive reasoning was used to further justify the removal of the three slosh modes. During the full-order design procedures, it was observed that the engines were being used to actively control slosh modes. However, in the physical implementation, the dynamic compensation would only be capable of controlling these modes if the exact slosh parameters and state are known, which is not provided for in the feedback architecture. Indeed, results in Appendix F reveal that the full-order optimal H_2 design failed for several

perturbation cases, in which expected levels of uncertainty were tested for the three slosh modes. Furthermore, analysis from SISO designs indicated that the slosh modes were not threats to stability if they remained phase-stabilized, because these modes have a tendency to add phase before increasing in gain. Thus, when these dynamics were removed from the reduced-order model, the compensation designs no longer attempted to actively control the modes, and the self-stabilizing properties of the modes were exploited.

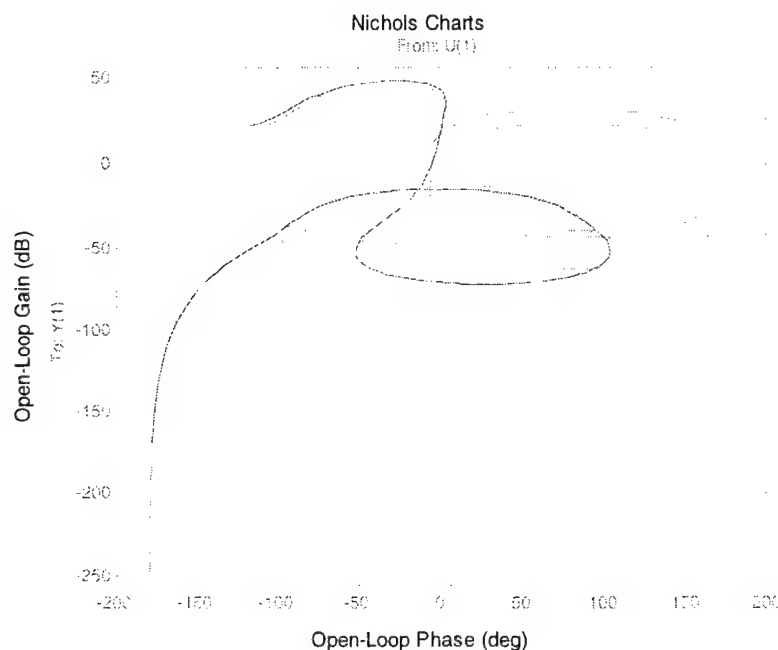


Figure 5.20 – K1 Plant Comparison

Once the reduced-order plant model had been established, the remaining task in the GA technique was to find the forward path gain that would achieve adequate performance. Two different models were used to calculate performance requirements. First, a design-response model provided information on performance levels attained using the reduced-order plant dynamics. Second, the actual-response model incorporated the full K1 dynamics and established the actual stability margins and performance of the compensation in the K1 system. A comparison of the two models provided insight to the performance metric reduction that occurred using a reduced-order plant.

An initial guess of the forward path gain was made to begin the H_2/H_∞ solution process. Using a gain value of 1.0, the optimal H_2 solution produced acceptable performance levels for the reduced-order design system. Table 5.2 summarizes the design and actual performance levels. The resulting design-response model open-loop had 6 dB of GM, 38° of PM, and Figure 5.22 shows adequate gain attenuation. However, the implementation of the optimal H_2 control law into the full-order, actual-response model created a significant reduction in PM and an increase in ITAE. The increase in ITAE was attributed to the added oscillations in the pitch response, as seen in Figure 5.21, which resulted from the addition of slosh dynamics. This addition also resulted the loss in PM. In Figure 5.22, the actual system dynamic passed much closer to the stability point than the designed response as a result of the additional gain near the open-loop crossover frequency.

Table 5.2 – $G=1.0$, GA H_2 Design Performance Metrics

Metric	Design	Actual
GM	6.14	5.91
PM	38.20	23.70
ITAE	8.43	13.26
WRM	0.0014	0.0017

By increasing the forward path gain, G , to 2.0, the phase of the design model seen by the optimization process at the 0 dB crossover was reduced from its original value, and the resulting optimal H_2 solution provided additional phase compensation at that point. Table 5.3 summarizes the design and actual performance metrics, and Figure 5.23 and Figure 5.24 present the step and frequency responses of the design, respectively. Implementing this new controller in the design-response model generated a GM of 12 dB and a PM of 43° . With this increased margin level in the design-response model, the actual stability margins were able to meet performance requirements in spite of the margin reductions associated with the inclusion of slosh dynamics. Acceptable

ITAE and WRM were also achieved. Therefore, this control design was tested using the $3\text{-}\sigma$ and $1\text{-}\sigma$ dispersion analysis. Results in Appendix F show that this controller design maintained robust stability. Thus, this control law was an acceptable robust H_2 design.

Table 5.3 – $G=2$, GA H_2 Design Performance Metrics

Metric	Design	Actual
GM	12.21	9.52
PM	43.21	35.32
ITAE	9.98	14.93
WRM	0.0028	0.0034

Although previous analysis indicated that extremely significant advantages could not be gained from using the optimal H_∞ control law, the upper-bound provided by the H_2 solution, $\gamma=11.2$, was used in the optimal H_∞ solution process to generate the lower-bound for the sub-optimal H_∞ solution process. These results are summarized by Table 5.4, and Figure 5.25 and Figure 5.26 provide the step response and Nichols plot of the resulting system. The optimal H_∞ control law did achieve stable time domain performance. However, inspection of the open-loop system's Nichols plot reveals several encirclements of the stability point and is an undesirable open-loop configuration. Additionally, Table 5.4 shows that the encirclement of the stability point is much closer in the actual-response model. Again, the optimal H_∞ solution process failed to yield an acceptable control law design.

Table 5.4 – GA H_∞ Design Performance Metrics

Metric	Design	Actual
GM	8.92	0.77
PM	35.69	3.26
ITAE	20.95	40.54
WRM	0.0408	0.0450

Using the upper- and lower-bounds from the H_2 and H_∞ designs, the mid-range γ values were tested for designs that met performance specifications. The lowest mid-range value that achieved adequate stability margins and gain attenuation was $\gamma=9.8$, and its results are summarized in Table 5.5. At this γ value, the step response in Figure 5.27 showed improvement. The implementation of the sub-optimal controller in the actual-response model also generated adequate stability margins in Figure 5.28. Because this design met nominal performance specifications, it was tested against the 3- σ and combined 1- σ perturbation cases, and it is shown to have maintained robust stability in Appendix F. As a result, sub-optimal solution was also an acceptable robust control law for the K1 pitch problem.

Table 5.5 -- GA Sub-Optimal Design Performance Metrics

Metric	Design	Actual
GM	11.95	9.94
PM	48.63	33.96
ITAE	5.06	13.96
WRM	0.0104	0.0128

A comparison of the two successful robust control laws developed using GA techniques revealed that both have almost identical performance characteristics. The sub-optimal solution provides a small increase in GM and a small reduction in ITAE. However, it has a smaller PM than the optimal H_2

controller. Furthermore, the optimal H_2 controller has a WRM one order-of-magnitude smaller than the sub-optimal solution. Thus, the optimal H_2 control law was selected for subsequent model order reduction analysis. Table 5.6 summarizes the actual performance metrics of the four designs developed using GA techniques.

Table 5.6 – GA Robust Design Summary

Metric \ Design	G=1.0 H_2	G=2.0 H_2	Optimal H_∞	Sub-Optimal
GM (dB)	5.91	9.52	0.77	9.94
PM (deg)	23.7	35.32	3.26	33.96
ITAE	13.26	14.93	40.54	13.96
WRM	0.0014	0.0034	0.045	0.0128
High Freq Attenuation	Yes	Yes	No	Yes
Robust Stability	No	Yes	No	Yes

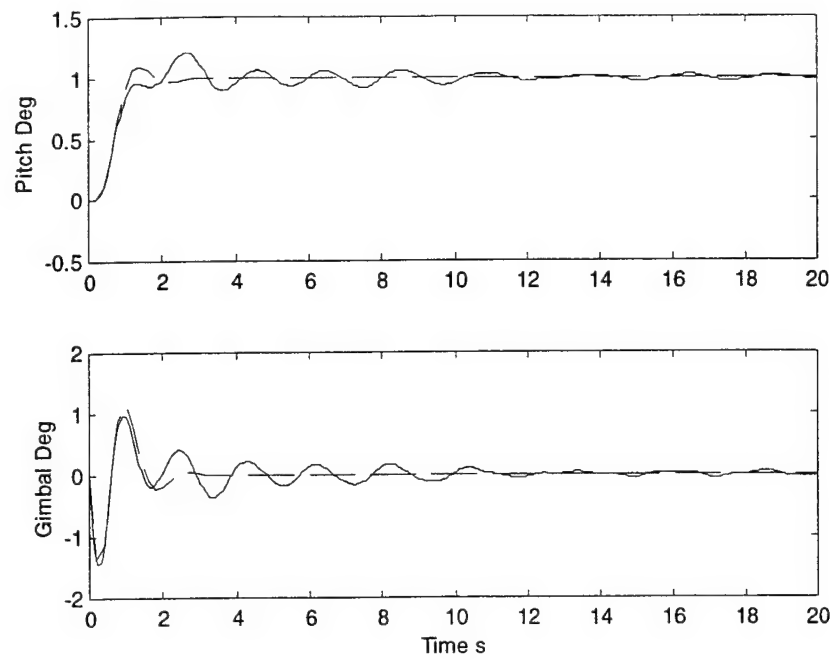


Figure 5.21 – $G=1.0$, GA H_2 Design Step Response

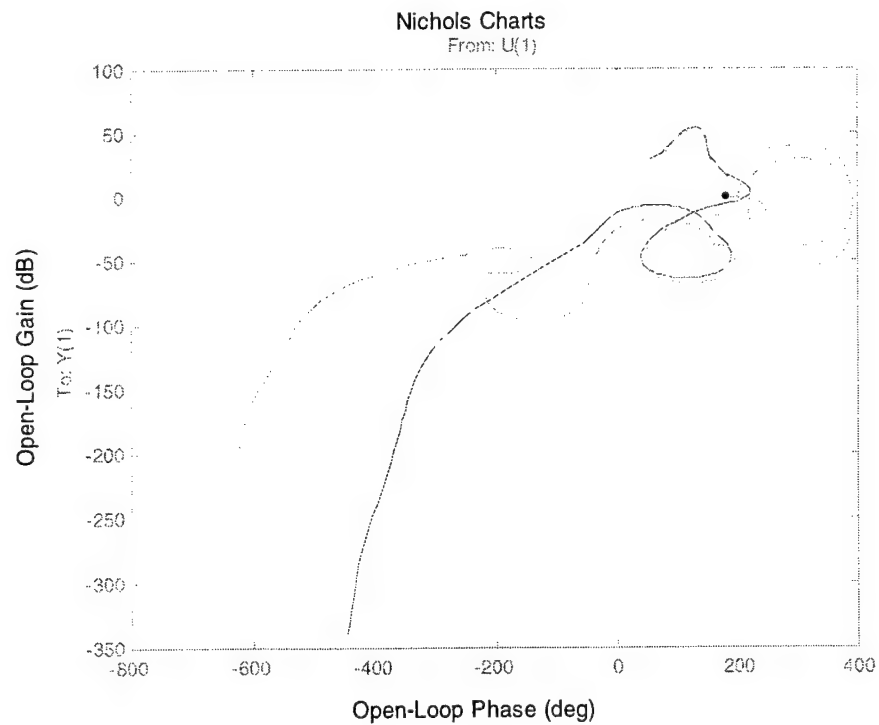


Figure 5.22 – $G=1.0$, GA H_2 Design Frequency Response

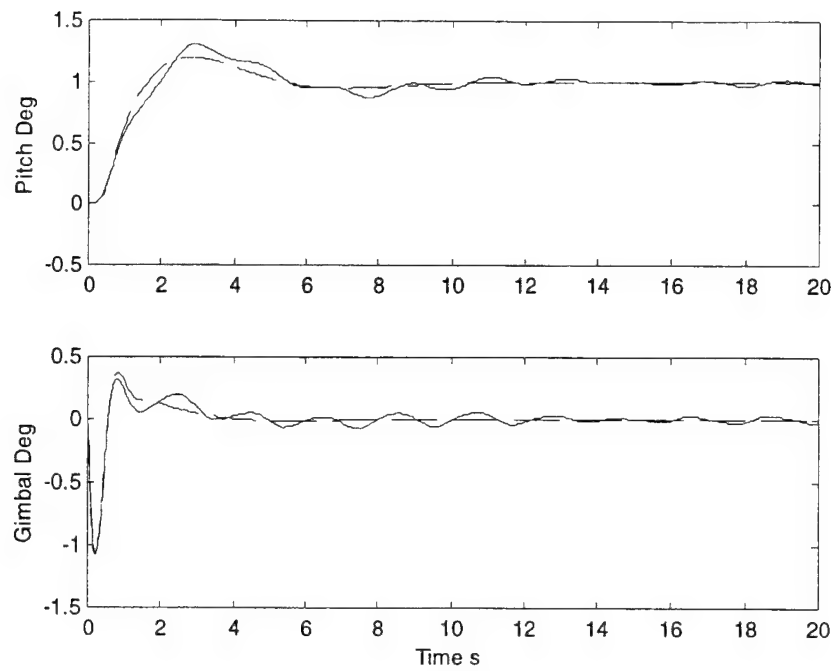


Figure 5.23 – $G=2.0$, GA H_2 Design Step Response

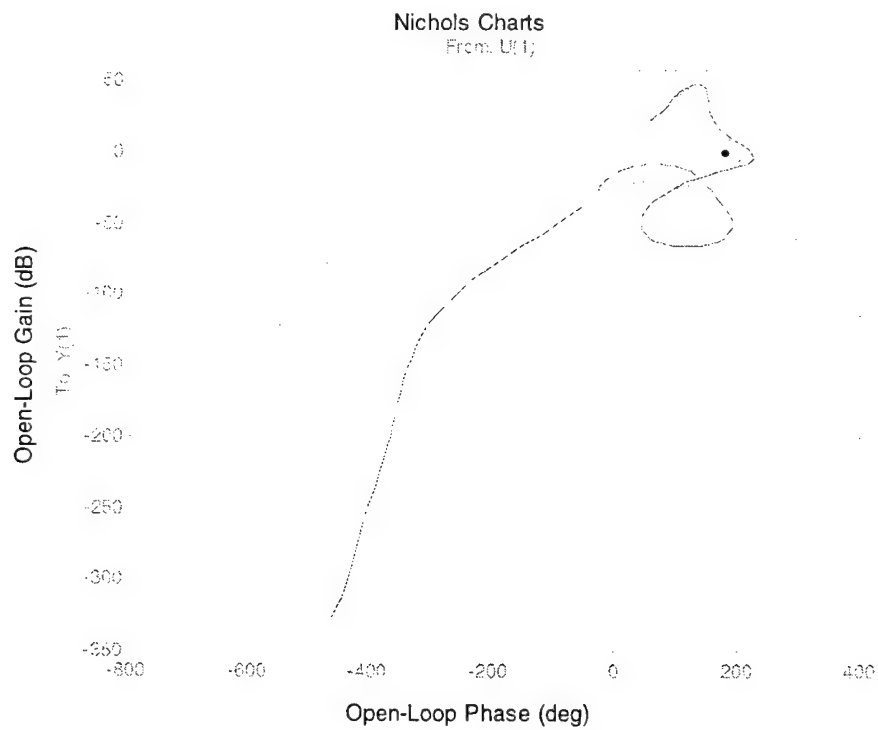


Figure 5.24 – $G=2.0$, GA H_2 Design Frequency Response

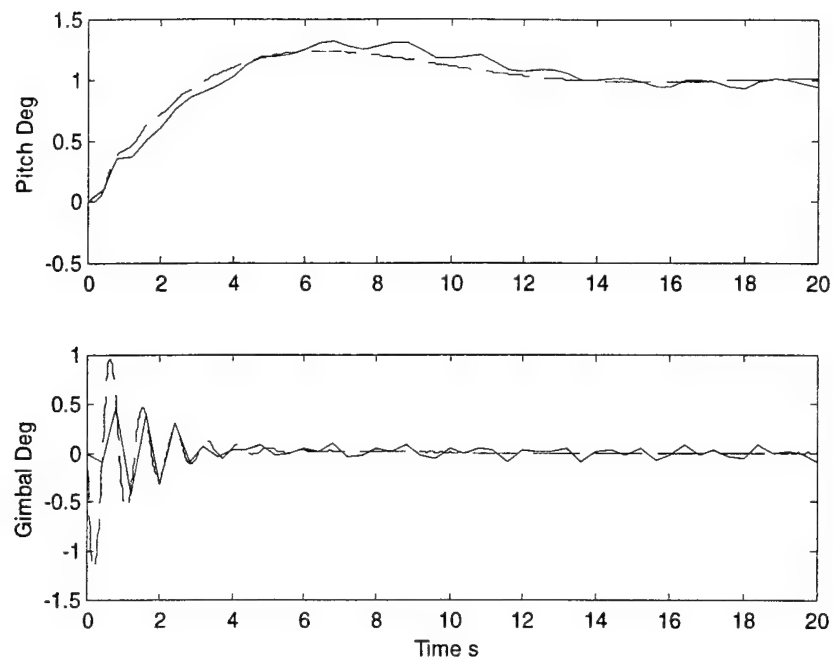


Figure 5.25 – GA H_∞ Design Step Response

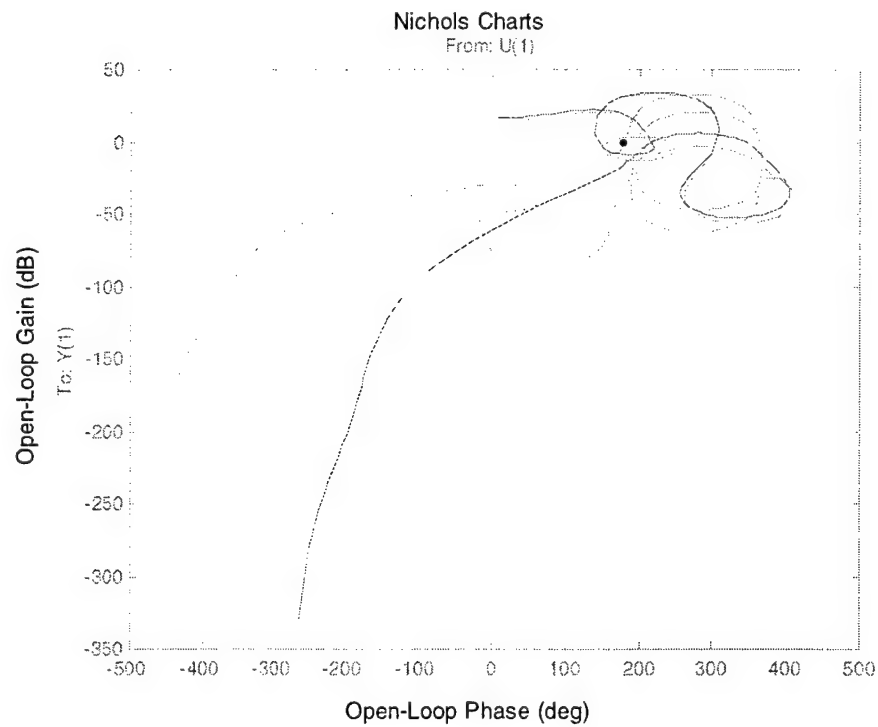


Figure 5.26 – GA H_∞ Design Frequency Response

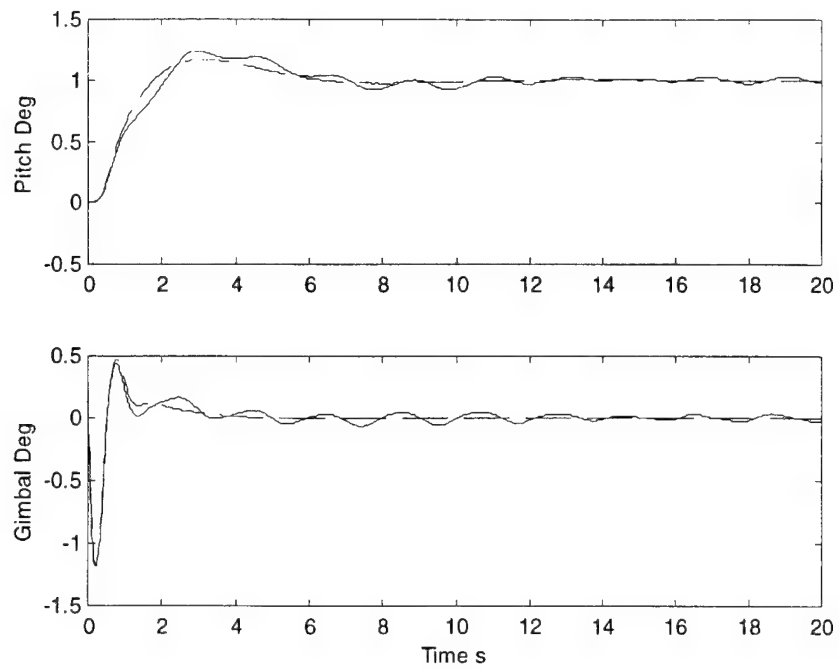


Figure 5.27 – GA Sub-Optimal Design Step Response

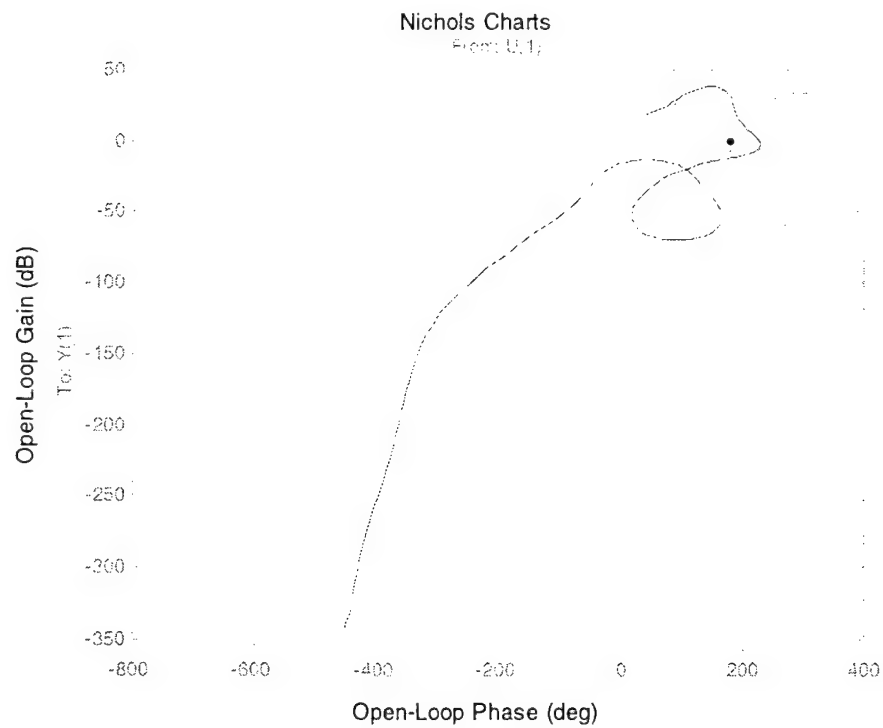


Figure 5.28 – GA Sub-Optimal Design Frequency Response

5.3.2.2 MU Robust Design

Much of the same architecture used in the GA technique was retained for use in the MU process. The same control effort and pitch error cost weights developed in the full-order design problem were applied, along with the same reduced-order K1 plant model. Following the guidelines in Chapter 4 for including the MU structures into the design model, robust control synthesis using MU techniques was essentially reduced to two tasks. The first was to develop the uncertainty input shaping filter. The second to find the uncertainty cost output gain value which produced acceptable controller designs.

The uncertainty input weight and its development were provided in Chapter 4 during the development of the MU approach. Summarizing those results, the shaping filter implemented in the system was a 6th order system which roughly defined the exact difference between the full-order and reduced-order K1 plant models. The uncertainty input and the rest of the MU architecture can be seen in Figure 5.4.

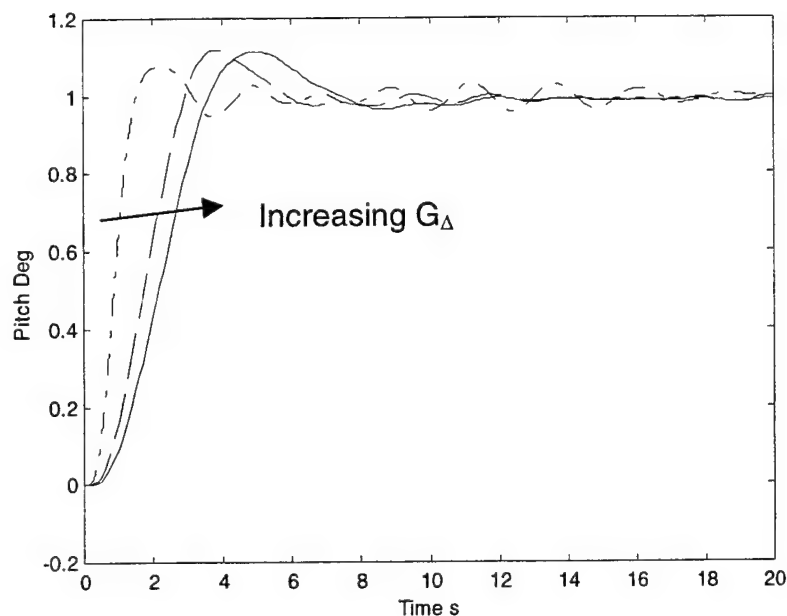


Figure 5.29 – Step Response Comparison

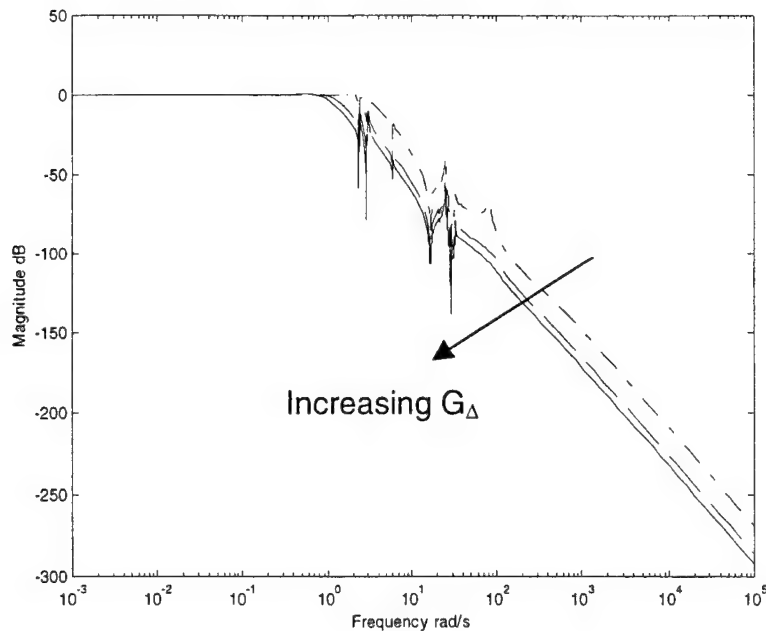


Figure 5.30 – Frequency Response Comparison

The remaining task was to establish the uncertainty cost output gain value, G_{Δ} . This gain value is most easily viewed as a tool with which the level of system robustness can be increased or decreased. By beginning with an initial value of 1.0 and slowly increasing its value, the robustness of the system was increased. However, increases in system robustness also led to decreases in system performance. Figure 5.29 shows the time domain performance losses that occurred from increasing the cost output gain. The performance losses illustrated in Figure 5.29 were also realized as closed-loop bandwidth reductions shown in Figure 5.30. Therefore, the objective was to find the lowest gain level that would provide robust stability. In this way, the time domain performance of the closed-loop system was preserved to the fullest extent possible.

Beginning with a cost gain value of 1.0, the optimal H_2 control law was generated. The design-response and actual-response metrics are summarized in Table 5.7. There are two important features in the time and frequency domain responses of the actual-response model, Figure 5.31 and Figure 5.32, respectively. First, the large amount of control effort in the step response plot is

similar to that of the full-order H_2 design. Second, the Nichols plot of the frequency response shows that the actual-response model lacks sufficient high frequency attenuation. Both of these features are indicative of a sensitive control law, and accordingly, this controller did not maintain stability during the dispersion analysis summarized in Appendix F.

Table 5.7 – $G_\Delta=1.0$, MU H_2 Design Performance Metrics

Metric	Design	Actual
GM	12.50	14.70
PM	53.00	53.00
ITAE	6.90	10.60
WRM	0.0002	0.0002

To add robust stability, the uncertainty cost gain was raised to 10, and the optimal H_2 design was generated. Again, the nominal performance characteristics of the design were satisfactory, although some of the expected deterioration was noticed. They are summarized in Table 5.8. An inspection of the time domain response, Figure 5.33, and the frequency domain response, Figure 5.34, of the actual-response model showed improvements in control effort and high frequency attenuation. However, subsequent robust stability analysis contained in Appendix F, revealed that this controller did not meet robust performance requirements.

Table 5.8 – $G_\Delta=10$, MU H_2 Design Performance Metrics

Metric	Design	Actual
GM	21.70	21.30
PM	43.50	42.10
ITAE	14.15	15.70
WRM	0.0012	0.0015

The uncertainty cost gain was increased to add robustness to the resulting control law. In this case, the gain was raised to 20. Table 5.9 presents the nominal performance metrics of this design. A deterioration in the nominal performance was noticeable. Yet, this controller did maintain stability during dispersion analysis. The added level of high frequency attenuation in the Nichols plot, Figure 5.36, and the reduced control effort in the time response, Figure 5.35, provided the system with enough robustness to maintain stability during all of the dispersion cases. The time response histories and frequency response histories of these cases are contained in Appendix F.

Table 5.9 – $G_A=20$, MU H_2 Design Performance Metrics

Metric	Design	Actual
GM	20.50	18.80
PM	38.61	37.82
ITAE	18.05	20.37
WRM	0.0021	0.0025

The gain value of 20 was the lowest level in which the resulting control law exhibited robust stability. Therefore, this design was used as the accepted optimal H_2 solution in the H_2/H_∞ Solution Process.

Continuing the H_2/H_∞ Solution Process, the optimal H_∞ design was obtained. The nominal performance metrics for this design are shown in Table 5.10. In the design-response model, the optimal H_∞ control did achieve adequate nominal performance. However, implementation into the actual-response model showed that the closed-loop system was unstable. The cause for actual system instability can be seen in its Nichols plot, Figure 5.38, in which the high frequency dynamics are not sufficiently gain stabilized. The optimal H_∞ design obviously was not acceptable.

Table 5.10 – MU H_∞ Design Performance Metrics

Metric	Design	Actual
GM	7.00	0
PM	70.61	0
ITAE	15.86	Inf
WRM	0.0014	–

The γ bounds from the H_2 and H_∞ problems were 714 and 415, respectively. Using these bounds, the mid-range values were searched for a stabilizing controller. To this end, the value of γ had to be raised nearly all the way to the upper bound before a controller that would guarantee nominal stability was produced. The performance metrics of this controller are shown in Table 5.11, and the time and frequency responses are shown in Figure 5.39 and Figure 5.40. However, results in Appendix F show this controller failed the dispersion analysis. This failure was due in large part to a reduced level of attenuation for high frequency modes. Like the optimal H_∞ controller, the sub-optimal controller was not an acceptable robust control law.

Table 5.11 – MU Sub-Optimal Design Performance Metrics

Metric	Design	Actual
GM	21.74	20.04
PM	46.82	45.10
ITAE	17.07	19.03
WRM	0.0019	0.0023

Therefore, the only acceptable control design developed using MU techniques was the optimal H_2 design, and it was selected for model order reduction analysis. Table 5.12 summarizes the actual performance metrics of the MU robust designs.

Table 5.12 – MU Robust Design Summary

Metric \ Design	$G_{\Delta}=1.0 H_2$	$G_{\Delta}=10 H_2$	$G_{\Delta}=20 H_2$	Optimal H_{∞}	Sub-Optimal
GM (dB)	14.7	21.3	18.8	0	20.04
PM (deg)	53	42.1	37.82	0	45.1
ITAE	10.6	15.7	20.37	Inf	19.03
WRM	0.0002	0.0015	0.0025	-	0.0023
High Freq Attenuation	Yes	Yes	Yes	No	Yes
Robust Stability	No	No	Yes	-	No

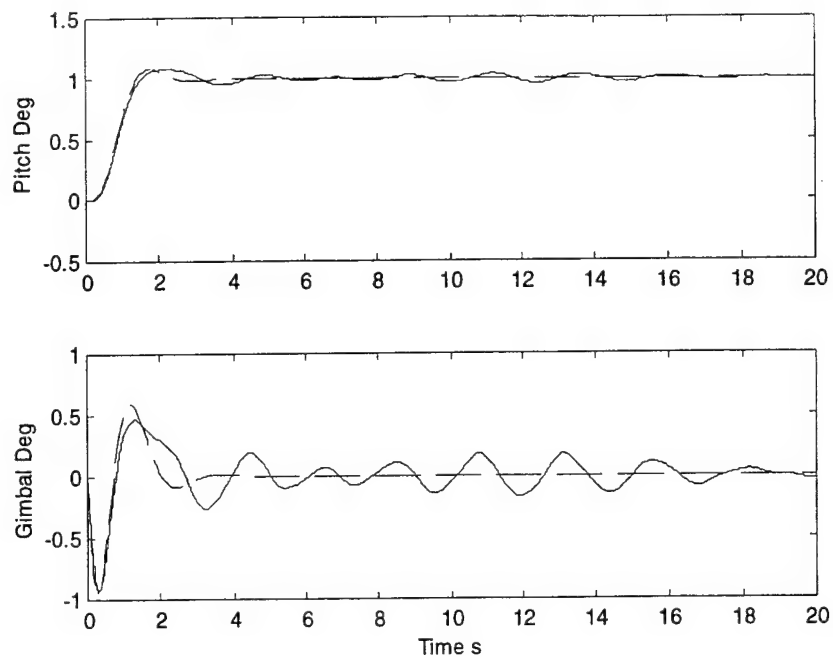


Figure 5.31 – $G_{\Delta}=1.0$, MU H_2 Design Step Response

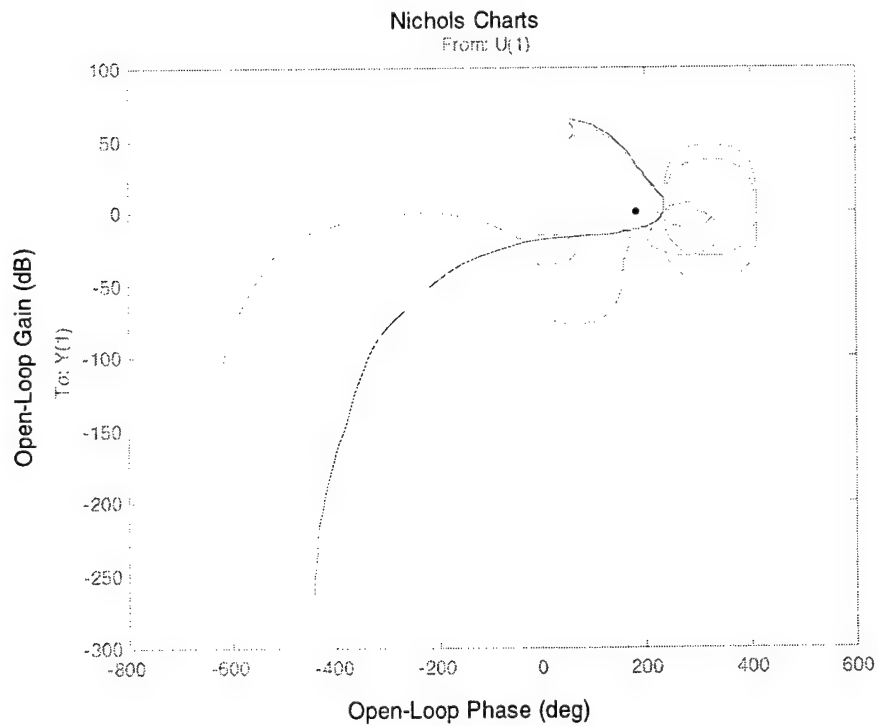


Figure 5.32 – $G_{\Delta}=1.0$, MU H_2 Design Frequency Response

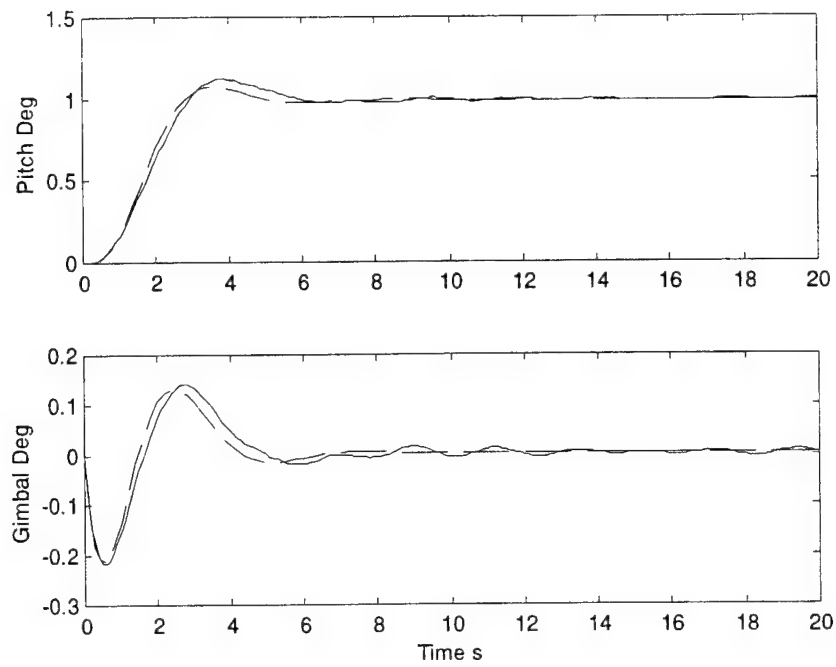


Figure 5.33 – $G_{\Delta}=10$, MU H_2 Design Step Response

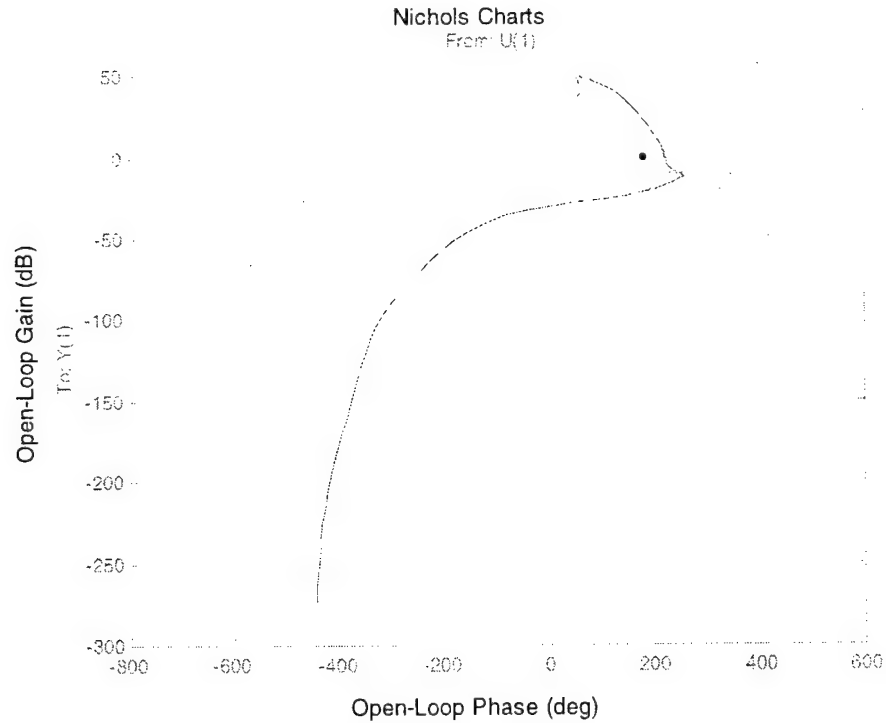


Figure 5.34 – $G_{\Delta}=10$, MU H_2 Design Frequency Response

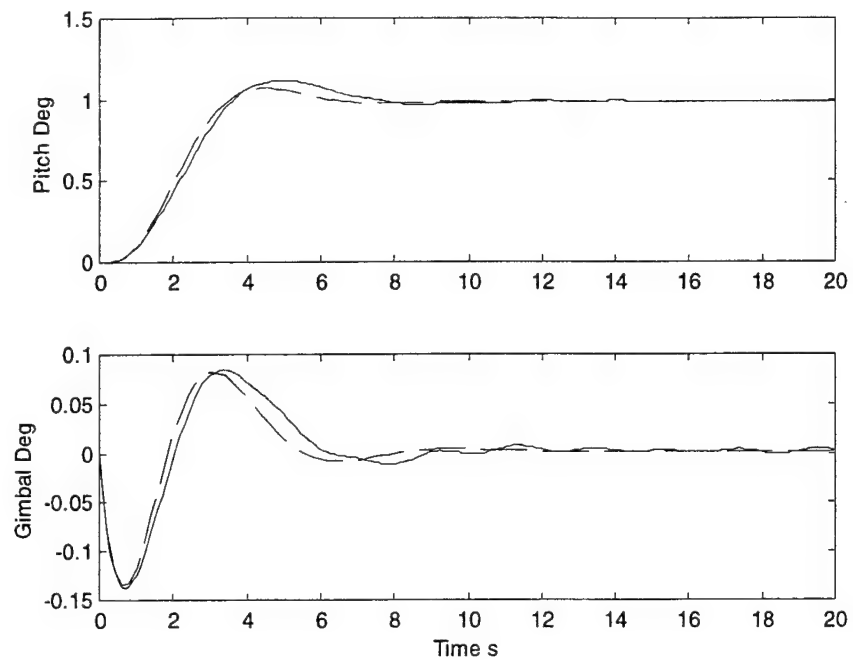


Figure 5.35 – $G_{\Delta}=20$, MU H_2 Design Step Response

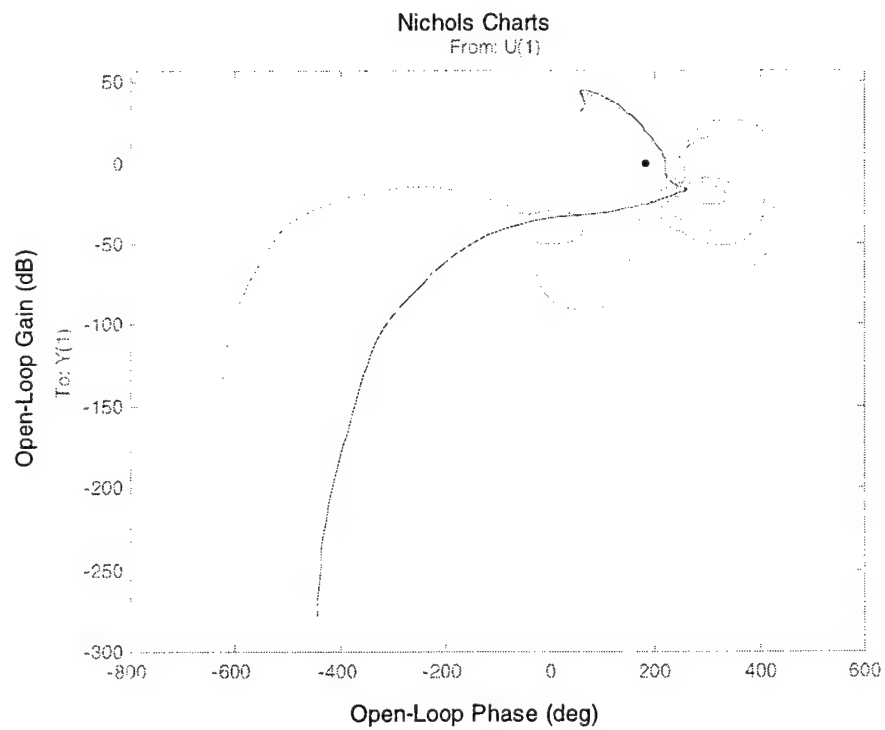


Figure 5.36 – $G_{\Delta}=20$, MU H_2 Design Frequency Response

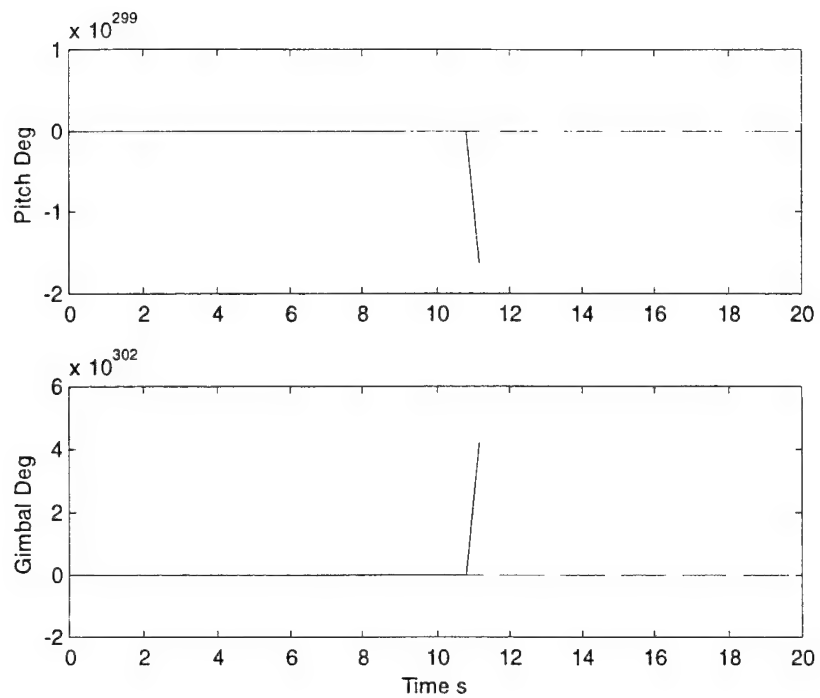


Figure 5.37 – MU H_∞ Design Step Response

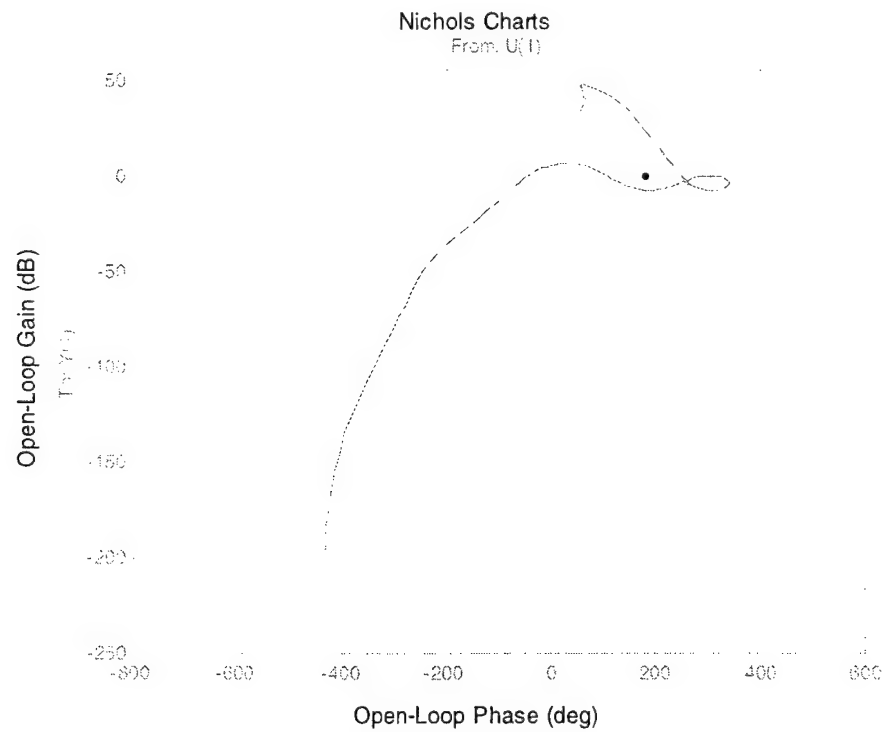


Figure 5.38 – MU H_∞ Design Frequency Response

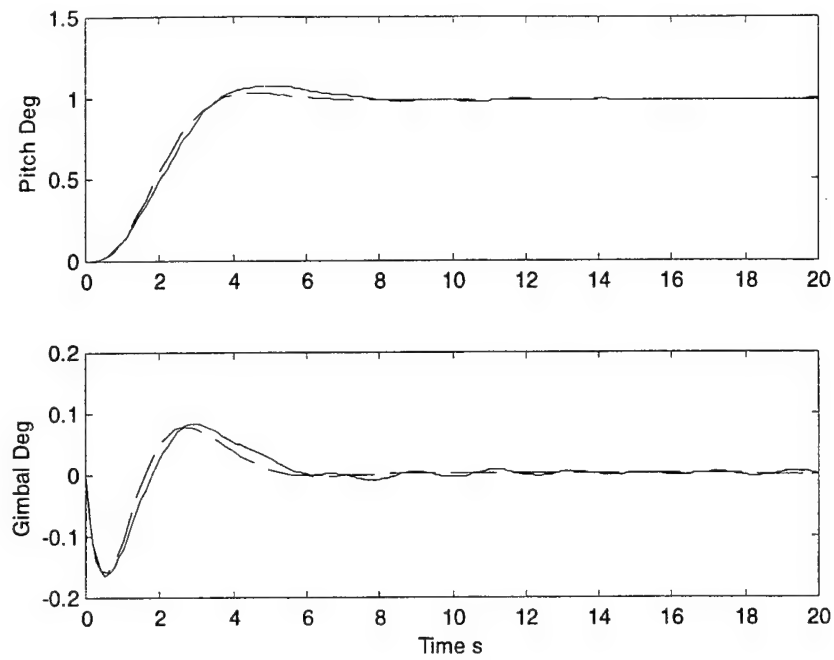


Figure 5.39 – MU Sub-Optimal Design Step Response

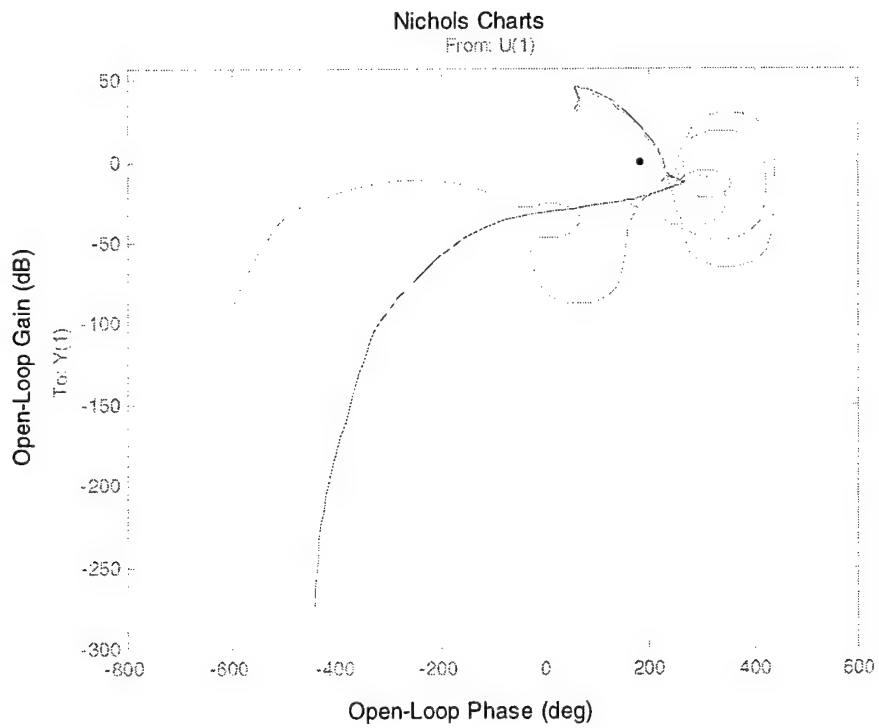


Figure 5.40 – MU Sub-Optimal Design Frequency Response

5.3.3 Reduced Order Design

The final phase in the Control Synthesis Hierarchy was to analyze and reduce, if possible, the order of the robust designs. Using the technique described in Chapter 4, which incorporates methods of HSV analysis and model truncation, BMOR was applied to selected robust control laws. The resulting controllers were attained by eliminating the maximum number of states possible before significant losses in performance occurred.

The first controller analyzed was the optimal H_2 design using GA techniques. This system was originally a 15th order system, and its HSVs are presented in Table 5.13. Inspecting the relative magnitudes of the HSVs revealed that several of the states were significantly less observable and less controllable. Initially 3 states were eliminated, and this continued until a total of 11 states were removed. The performance metrics at each level of reduction are shown in Table 5.14. Degradation in performance increased as the number of truncated states increased, and a significant increase in ITAE occurs with the elimination of 8 states. Therefore, 7 states were removed in an attempt to preserve the performance qualities of the original system, while minimizing the controller's size. Dispersion analysis of the resulting 8 state controller showed that it did maintain the robust stability performance of the original system as well. Appendix F contains the time and frequency response histories of this analysis.

Table 5.13 – GA Robust H_2 Design HSVs

1.4796	1.2576	0.5564	0.3036	0.3015
0.2667	0.0740	0.0671	0.0036	0.0015
0.0003	0.0001	0.0000	0.0000	0.0000

Table 5.14 – GA Robust H_2 Design Order Reduction Summary

States Removed	GM	PM	ITAE	WRM
3	9.52	35.32	14.93	0.0034
4	9.52	35.32	14.95	0.0034
5	9.52	35.40	15.03	0.0034
6	9.52	35.40	14.84	0.0034
7	9.52	35.29	17.42	0.0034
8	9.38	33.29	55.96	0.0032
9	9.31	33.51	45.03	0.0032
10	9.25	20.99	40.77	0.0033
11	3.81	0.94	2049	0.0029

To reveal the cause of the break point in the reduction summary in Table 5.14, the reduced-order controller was compared to its associated full-order form. It was discovered that the reduction in the less controllable and observable controller states was permissible only as long as the controller's frequency response was unchanged over the frequency range of expected K1 dynamics. Otherwise, the truncation began to change significantly the controller's frequency response. Figure 5.41 shows a comparison of frequency response, logarithmic magnitude for the reduced-order controller with 8 states (solid), and the full-order controller (dashed) for each I/O channel.

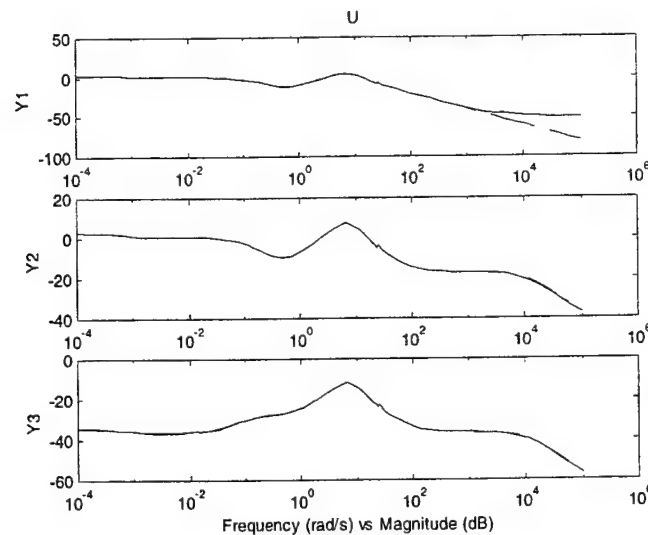


Figure 5.41 – Controller Order Comparison

In a process identical to the first controller's reduction, the optimal H_2 design using MU techniques was also reduced in order. The HSVs of this controller are shown Table 5.15. The original system had 21 states. Again, inspection of the HSVs indicates that several of the states can be truncated from the system with little performance loss. Table 5.16 presents a summary of the performance metrics that resulted from multiple levels of reduction. A significant performance loss occurred after 10 states were removed. Therefore, 9 states were removed from the system, and robust stability was checked. Results contained in Appendix F confirmed that the 12th order controller maintained stability for all of the perturbation cases. Therefore, the 12th order control law was viewed as an acceptable product of the control synthesis process.

Table 5.15 – MU Robust H_2 Design HSVs

18.9840	16.3586	7.0317	6.9857	2.1886
1.9539	1.4988	0.9868	0.2865	0.2054
0.1850	0.0665	0.0266	0.0127	0.0042
0.0007	0.0000	0.0000	0.0000	0.0000
0.0000				

Table 5.16 – MU Robust H_2 Design Order Reduction Summary

States Removed	GM	PM	ITAE	WRM
5	18.79	37.81	20.39	0.0025
6	18.80	37.81	20.44	0.0025
7	18.77	37.88	20.92	0.0026
8	19.17	36.67	23.98	0.0025
9	19.31	34.23	18.51	0.0025
10	19.67	31.07	45.46	0.0026
11	10.47	5.98	159.2	0.0036

BMOR techniques produced two different compensator designs, one 8th order and one 12th order, which met nominal and robust performance requirements. Table 5.17 summarizes these two reduced-order compensators

and their associated full-order, robust designs. The state-space representation of the reduced-order, robust GA design is presented in equations 5.2 through 5.5, and the representation of the reduced-order, robust MU design is given in equations 5.6 through 5.9. The step and frequency responses for the 8th order and 12th order designs are shown in Figure 5.42 and Figure 5.43, and Figure 5.44 and Figure 5.45, respectively.

Table 5.17 – Reduced-Order Design Summary

Metric \ Design	Full GA	Reduced GA	Full MU	Reduced MU
Order	15	8	21	12
GM (dB)	9.52	9.52	18.8	19.67
PM (deg)	35.32	35.29	37.82	34.23
ITAE	14.93	17.42	20.37	18.51
WRM	0.0034	0.0034	0.0025	0.0025
High Freq Attenuation	Yes	Yes	Yes	Yes
Robust Stability	Yes	Yes	Yes	Yes

Reduced-Order, GA Robust H_2 Design:

$$A_{e_{11}} = \begin{bmatrix} -9312.3 & 0 & 0 & 0 & 0 & 0 & 0 & 0 & 0 \\ 0 & -0.1856 & 25.061 & 0 & 0 & 0 & 0 & 0 & 0 \\ 0 & -25.061 & -0.1856 & 0 & 0 & 0 & 0 & 0 & 0 \\ 0 & 0 & 0 & -3.7834 & 6.3991 & 0 & 0 & 0 & 0 \\ 0 & 0 & 0 & -6.3991 & -3.7834 & 0 & 0 & 0 & 0 \\ 0 & 0 & 0 & 0 & 0 & -6.4348 & 0 & 0 & 0 \\ 0 & 0 & 0 & 0 & 0 & 0 & -0.0998 & 0 & 0 \\ 0 & 0 & 0 & 0 & 0 & 0 & 0 & 0 & -0.00057 \end{bmatrix} \quad (5.2)$$

$$B_{e_1} = \begin{bmatrix} -1.4377 & 35.193 & 3.8909 \\ 0.3816 & -0.5023 & -0.5576 \\ -0.0652 & 0.2203 & 0.0242 \\ 2.7387 & -3.2734 & -0.3698 \\ -3.9479 & 5.5622 & 0.6067 \\ -2.2294 & 2.9597 & 0.3164 \\ -0.2491 & 0.2376 & -0.0066 \\ -0.0139 & 0.0111 & 0.0001 \end{bmatrix} \quad (5.3)$$

$$C_{e_1} = [35.384 \quad -0.3024 \quad 0.1457 \quad -1.6719 \quad 2.5715 \quad -2.427 \quad 0.3319 \quad 0.0178] \quad (5.4)$$

$$D_{e_1} = [0.0027 \quad 0.0025 \quad 0.0003] \quad (5.5)$$

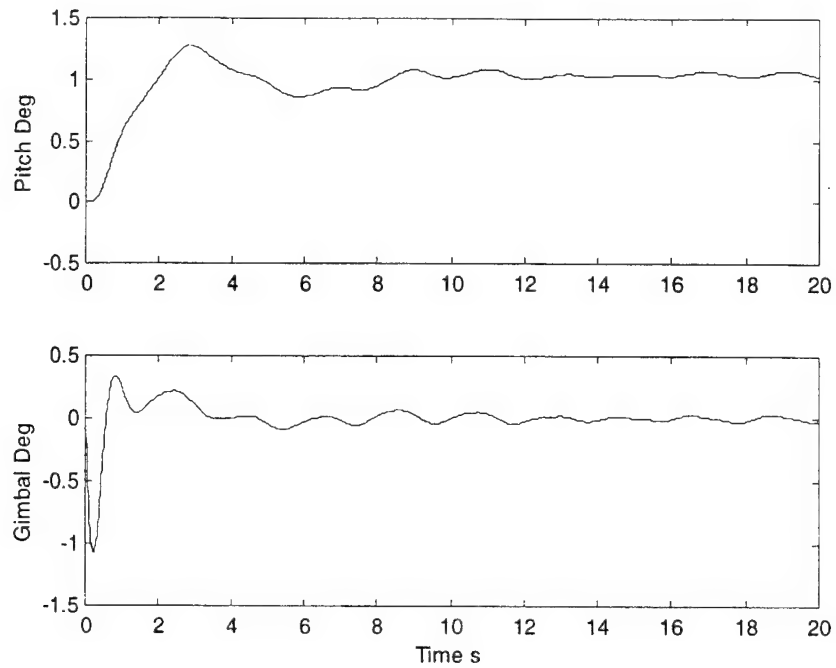


Figure 5.42 – Reduced-Order, GA Robust H_2 Design Step Response

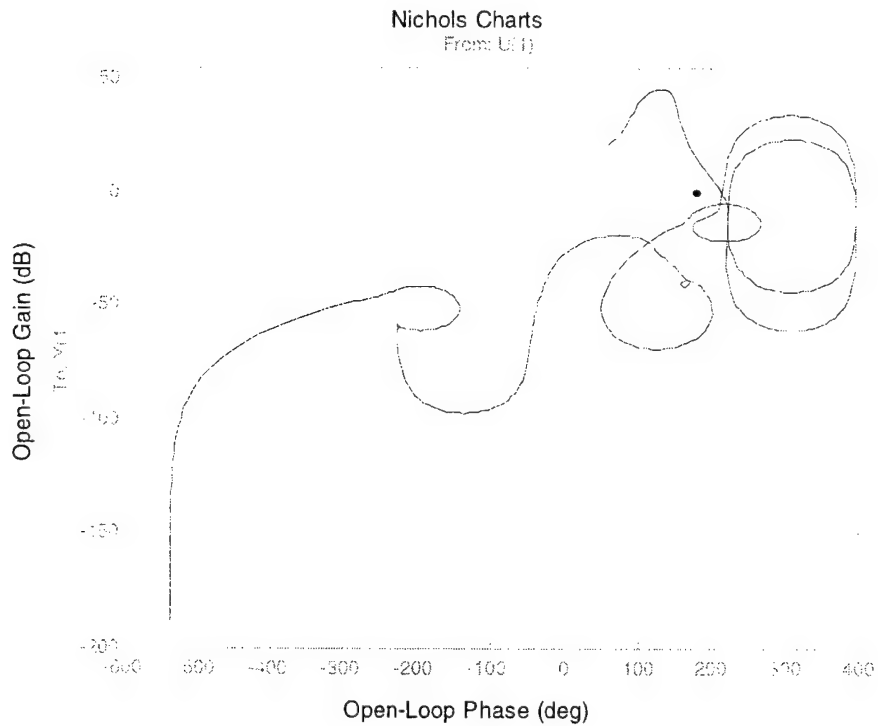


Figure 5.43 – Reduced-Order, GA Robust H_2 Design Frequency Response

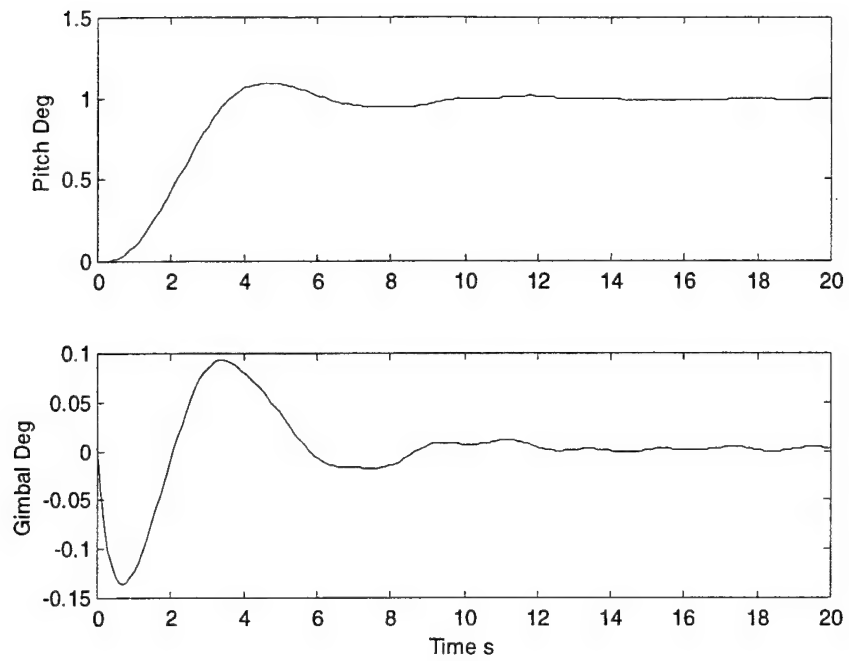


Figure 5.44 – Reduced-Order, MU Robust H_2 Design Step Response

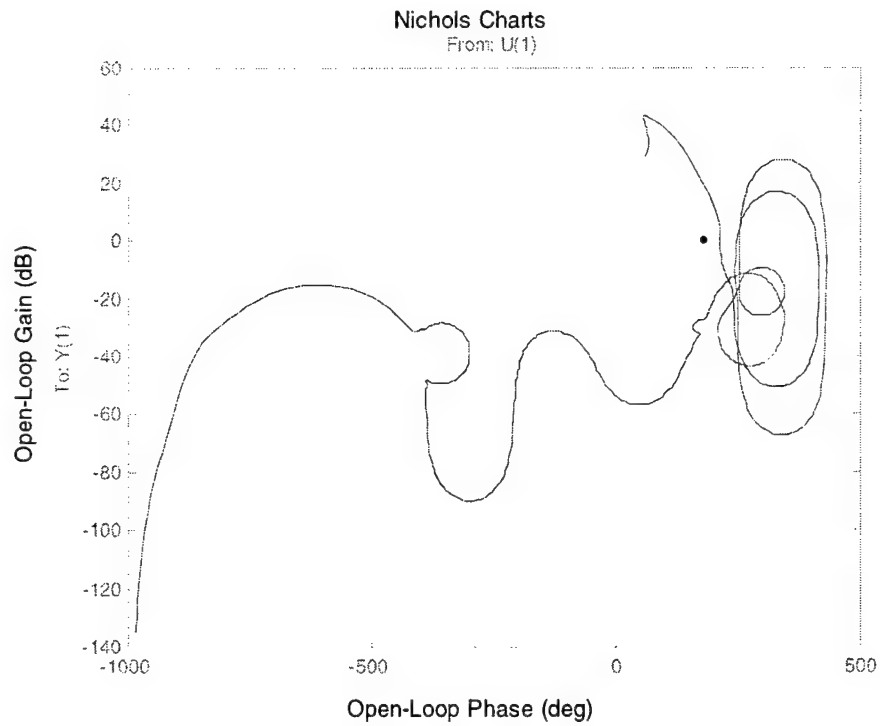


Figure 5.45 – Reduced-Order, MU Robust H_2 Design Frequency Response

Design Analysis and Modified Iteration

With the development of the 8th and 12th order control laws presented in state-space form by equations 5.2 through 5.9, one iteration of the Control Synthesis Hierarchy was completed. Both of these designs appeared to exhibit acceptable nominal and robust performance. However, a close look at the structure of the control laws revealed that both had undesirable characteristics and an iteration in the design process was necessary.

The Jordan block form used to define the system matrices of the 8th and 12th order controllers in equations 5.2 and 5.6 shows that each design has a pole located at approximately $-10,000$. The extreme magnitude of the poles led to two conclusions. First, their frequency was well beyond that of the closed-loop system, and the pole was not needed to achieve desirable performance. Second, the speed of these poles would become an issue in trying to implement the control law digitally. Together, these reasons motivated research into the removal of the extremely high frequency poles.

Before taking any steps to remove the high frequency poles from the designs, it was important to understand why they were present. H_2/H_∞ control synthesis has already been shown to generate compensation that contains state estimates of the design model dynamics. Looking at the pole locations in matrix 5.2, it was possible to associate most of the modes in the 8th order design to dynamics in the design model. The complex pair and 3 real poles at low frequencies were attributed to the actuator and AOA dynamics included in the design model. The lightly damped complex pair near the 25 rad/s frequency resulted from the 5th flex mode, which was also in the design model. However, the pole at approximately 10,000 rad/s was not due to any specific mode.

The same analysis was performed for the 12th order control law. Again, the presence of low frequency poles was attributed to actuator and AOA dynamics, and the presence of a complex mode near 20 rad/s resulted from the 5th flex mode. There were also two additional complex pole pairs, one at approximately 100 rad/s and another at approximately 700 rad/s, and one

additional pole at 500 rad/s. The poles were associated with the 6th order, uncertainty shaping filter because they very closely matched its poles. Yet again, there were no dynamics in the design model which could account for the pole near 10,000 rad/s.

It was not the dynamics of the design model, but the actual loop architecture that was forcing the H_2/H_∞ solutions to contain these high-frequency poles. During the selection of exogenous inputs in Chapter 4, the noise in the feedback channel was physically interpreted as errors in the pitch angle sensed by the IMU. Because this placed the noise inputs as inputs into the IMU, measurement noise was not directly present in the control inputs, and “false” inputs were necessary to satisfy the singularity conditions. Each of these channels was then scaled with a small number (0.0001) to ensure that they would have little effect during the minimization of the objective function. However, it was these extremely small gains that were producing the rapid poles in the control designs. Essentially, the exponential decay created by a pole at -10,000 approximated the 0.0001 gain used to scale the “false” input channels.

Understanding the source of problem, there were two options for removing the undesirable and unnecessary poles from the control designs. The first option was to continue with the 8th and 12th order designs and apply more complicated model order reduction techniques. Unfortunately, attempts at frequency-weighted, model order reduction proved through experience to yield unacceptable results. By artificially reducing the controllability and observability of the high frequency mode, it was possible to remove it from each of the control designs. However, the resulting controllers were not able to stabilize the closed-loop system.

In light of this, a second approach was taken to remove the poles. Using an alternative control-loop architecture, a second iteration of the Control Synthesis Hierarchy was performed, in which the only variation was the loop structure. Figure 5.46 presents the alternative architecture that shows the “false” noise inputs removed from the problem formulation. In order to maintain

singularity conditions, the noise inputs were moved from the input of the IMU to its output. This noise placement physically corresponded to errors that result from IMU computation and was an acceptable alternative interpretation of how noise enters the feedback path. In hindsight, this was probably a more correct representation, because the IMU actually senses pitch acceleration and uses integration to provide pitch rate and pitch angle.

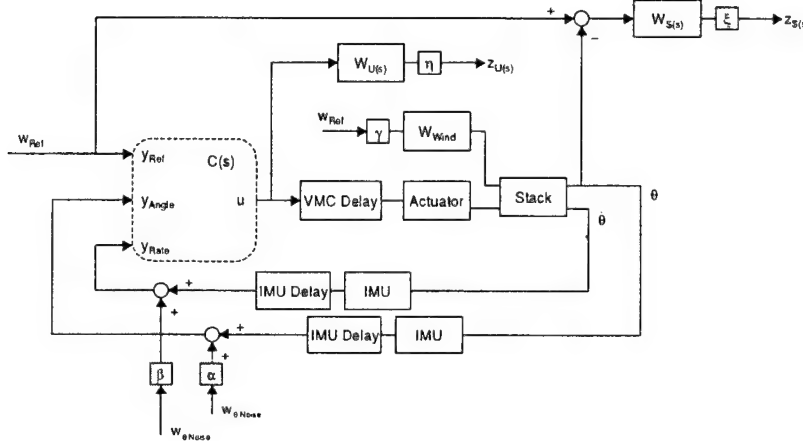


Figure 5.46 – Modified Control Loop Architecture

The controllers that resulted from the new architecture were nearly identical to those produced using the “false” inputs throughout the entire design process. This was expected because only the loop structure had been changed. No other parameters were varied. To alleviate redundancy that would result from including the results of the second iteration of the design process, only the final reduced-order designs have been provided. The new reduced-order design based on GA techniques using $G=2$ is referred to as design Gamma. The new reduced-order design based on MU techniques using $G_{\Delta}=20$ is referred to as design Delta. The state-space representations of designs Gamma and Delta are presented by equations 5.10 through 5.13 and equations 5.14 through 5.17, respectively.

Design Gamma:

$$A_{c_{it}} = \begin{bmatrix} -0.1551 & 25.04 & 0 & 0 & 0 & 0 & 0 \\ -25.04 & -0.1551 & 0 & 0 & 0 & 0 & 0 \\ 0 & 0 & -3.6909 & 6.527 & 0 & 0 & 0 \\ 0 & 0 & -6.527 & -3.6909 & 0 & 0 & 0 \\ 0 & 0 & 0 & 0 & -6.0318 & 0 & 0 \\ 0 & 0 & 0 & 0 & 0 & -0.0987 & 0 \\ 0 & 0 & 0 & 0 & 0 & 0 & -0.0006 \end{bmatrix} \quad (5.10)$$

$$B_{c_i} = \begin{bmatrix} -0.3753 & 0.5208 & 0.0588 \\ 0.0872 & -0.1233 & -0.0137 \\ 4.531 & -6.3236 & -0.7113 \\ -0.6700 & 1.0121 & 0.1030 \\ 2.0234 & -2.854 & -0.3101 \\ 0.2488 & -0.2398 & 0.0065 \\ 0.0134 & -0.112 & -0.0010 \end{bmatrix} \quad (5.11)$$

$$C_{c_i} = [0.2441 \quad -0.2220 \quad -3.0249 \quad 0.5954 \quad 2.3643 \quad -0.3311 \quad -0.0179] \quad (5.12)$$

$$D_{c_i} = [-0.0031 \quad 0.0043 \quad 0.0005] \quad (5.13)$$

Design Delta:

$$A_{c_{11}} = \begin{bmatrix} -187.2 & 176.23 & 0 & 0 & 0 & 0 & 0 & 0 & 0 & 0 \\ -176.23 & -187.2 & 0 & 0 & 0 & 0 & 0 & 0 & 0 & 0 \\ 0 & 0 & -49.67 & 83.395 & 0 & 0 & 0 & 0 & 0 & 0 \\ 0 & 0 & -83.395 & -49.67 & 0 & 0 & 0 & 0 & 0 & 0 \\ 0 & 0 & 0 & 0 & -0.1316 & 17.35 & 0 & 0 & 0 & 0 \\ 0 & 0 & 0 & 0 & -17.35 & -0.1316 & 0 & 0 & 0 & 0 \\ 0 & 0 & 0 & 0 & 0 & 0 & -1.3791 & 0.8473 & 0 & 0 \\ 0 & 0 & 0 & 0 & 0 & 0 & -0.8473 & -1.3791 & 0 & 0 \\ 0 & 0 & 0 & 0 & 0 & 0 & 0 & 0 & -0.0065 & 0 \\ 0 & 0 & 0 & 0 & 0 & 0 & 0 & 0 & 0 & -0.0006 \end{bmatrix} \quad (5.14)$$

$$B_{c_1} = \begin{bmatrix} 0.0997 & -0.7613 & -106.67 \\ -0.0142 & 0.0873 & -57.065 \\ -0.0590 & 0.0863 & -32.022 \\ -0.0303 & 0.5925 & 3.5572 \\ -0.0010 & 0.1546 & 0.7480 \\ -0.0004 & -0.0391 & 2.6042 \\ 0.5797 & -1.5767 & 0.0149 \\ -0.3671 & 1.8449 & 0.7088 \\ 0.1143 & -0.1142 & 0.0017 \\ -0.0012 & -0.0087 & 0.0034 \end{bmatrix} \quad (5.15)$$

$$C_{c_1} = [-12.532 \quad -36.109 \quad 13.268 \quad 2.5879 \quad 0.8026 \quad 1.0928 \quad -0.8359 \quad -0.0067 \quad -0.1597 \quad 0.0098] \quad (5.16)$$

$$D_{c_1} = [0.0016 \quad -0.0061 \quad -0.0252] \quad (5.17)$$

Inspection of each design's modes in equations 5.10 and 5.14 revealed that the extremely high frequency poles had been successfully removed from the designs. A comparison to the previous 8th and 12th order designs revealed that the minimum order of the designs was also lowered.

In the case of GA techniques, the new loop architecture produced a system in which the poles were nearly identical to the original poles of the 8th order controller. The only significant change was the elimination of the pole near $-10,000$. The step and frequency responses of the new 7th order control design, Gamma, are compared to the 8th order control design in Figure 5.47 and Figure 5.48. The 8th order design is dashed, and Gamma is solid. From these plots, it is easy to see that there is only a small change in nominal performance between the two designs. In fact, design Gamma achieves better steady-state performance than the original 8th order design, and it shows only slight differences at high frequencies in the open-loop response. The details of design Gamma's dispersion analysis in Appendix E show that Gamma's robust performance is also nearly the same.

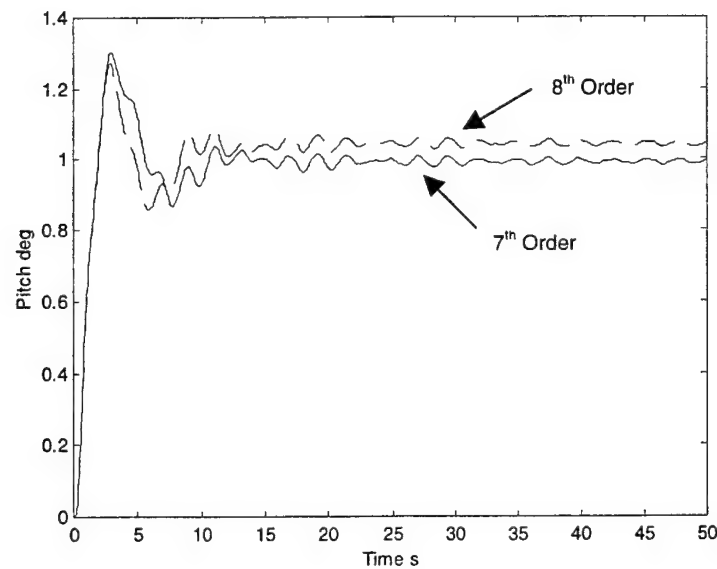


Figure 5.47 – Step Response of 7th and 8th Order Controllers

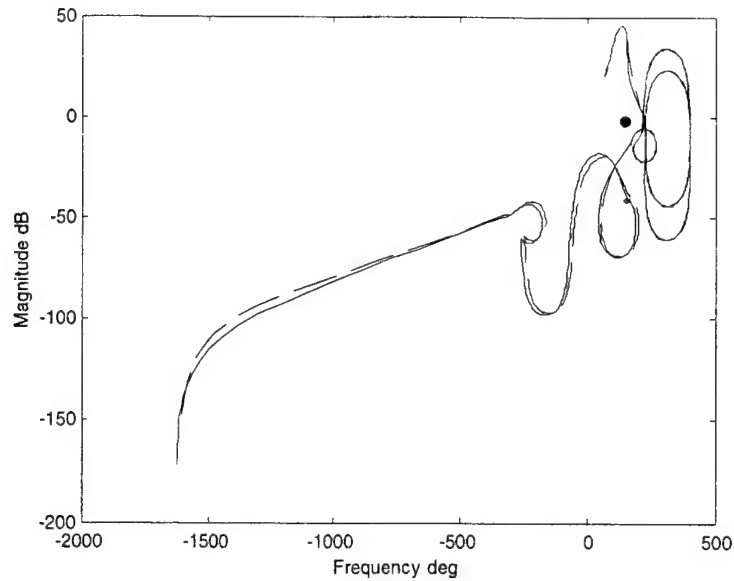


Figure 5.48 – Frequency Response of 7th and 8th Order Controllers

Considering the new design based on MU techniques, the similarity to the original 12th order design is even more striking. The modes of the new 10th order controller, Delta, were nearly the same as those in the original 12th order controller. The notable differences were the elimination of the mode at $-10,000$ and the mode at -500 . Additionally, the high frequency complex pair near 700 rad/s in the 12th order model had been reduced in frequency to approximately 250 rad/s. The result of these changes was a more desirable system with poles at lower frequencies. Figure 5.49 shows the step response comparison of the 10th order design (solid) and the 12th order design (dashed). Obviously, the difference between the designs is minimal. The Nichols plot in Figure 5.50 also shows that there is little difference between the two closed-loop systems, especially at frequencies near the system bandwidth. Furthermore, details of the dispersion analysis for design Delta are contained in Appendix E and show that it exhibits robust stability.

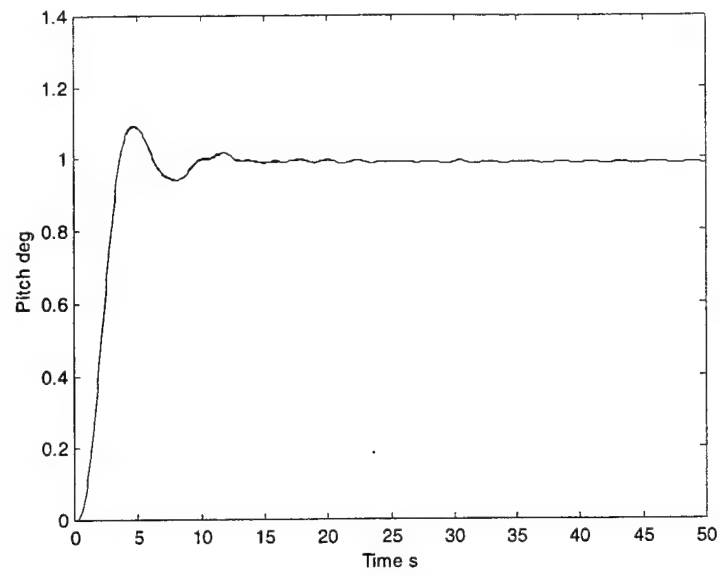


Figure 5.49 – Step Response of 10th and 12th Order Controllers

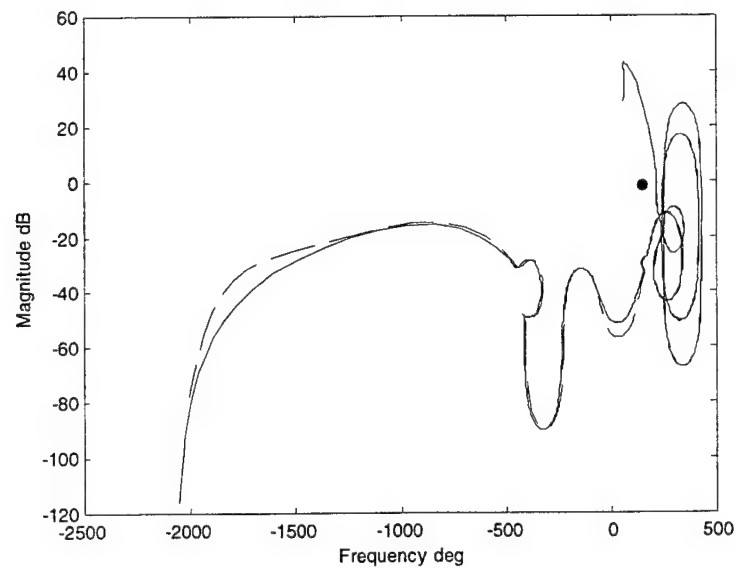


Figure 5.50 – Frequency Response of 10th and 12th Order Controllers

To summarize the changes in the reduced-order models, Table 5.18 presents the performance metrics for the original reduced-order controllers, as well as designs Gamma and Delta. With the elimination of the high frequency

poles, designs Gamma and Delta were successful products of the MCS process which meet nominal and robust performance requirements.

Table 5.18 – Final Control Design Summary

Metric \ Design	Original GA	New GA	Original MU	New MU
Order	8	7	12	10
GM (dB)	9.52	9.46	19.67	19.27
PM (deg)	35.29	34.57	34.23	33.96
ITAE	17.42	16.74	18.51	18.32
WRM	0.0034	0.0034	0.0025	0.0025
High Freq Attenuation	Yes	Yes	Yes	Yes
Robust Stability	Yes	Yes	Yes	Yes

5.4 MCS Conclusions

In reviewing the MCS process, the transformation of full-order, sensitive controllers into reduced-order, robust controllers produced a general trend of time domain performance degradation. Table 5.19 summarizes the designs created during each phase of the MCS process that had adequate stability margins. The controllers developed during the full-order design phase showed superior time domain performance. Then, by adding robustness to the designs and reducing their order, the time domain performance of the design was reduced along with the closed-loop system bandwidth. It was, however, possible to achieve adequate stability margins and high frequency attenuation throughout the entire process, although this was possible only with optimal H_2 designs. The optimal H_∞ solutions did not provide sufficient stability margins and never achieved robust stability. The sub-optimal designs did not prove to be valuable alternatives either. In large part, this was specifically due to the K1 pitch control problem. The similarity in the closed-loop design model SVs indicated that there

was not large separation between the two optimal designs. This small separation in γ bounds, coupled with the ineffectiveness of the optimal H_∞ designs, forced the mid-range γ values to be raised nearly all the way to the upper-bound provided by the optimal H_2 solution. Nevertheless, insight into the significant issues involved in the development of robust weighted H_2/H_∞ control laws was provided by these additional control designs.

The two designs that resulted from the 2nd iteration of the Control Synthesis Hierarchy using the modified control-loop architecture provided performance equivalent to the reduced-order designs that contained the undesirable poles. These results verified both the source of the high frequency poles and the manner in which to remove them. Together, designs Gamma and Delta represent typical compensation that can be generated using MCS methods with minimum iteration and effort.

Table 5.19 – MCS Summary

Design \ Metric	Order	GM	PM	ITAE	WRM	Roll-Off	Robust
Full-Order							
Optimal H_2	39	6	38	10.5	0.0014	Yes	No
Sub-Optimal	39	6	39	8.5	0.0028	Yes	No
GA Robust							
Optimal H_2	15	9.52	35.32	14.93	0.0034	Yes	Yes
Sub-Optimal	15	9.94	33.96	13.96	0.0128	Yes	Yes
MU Robust							
Optimal H_2	21	18.8	37.82	20.37	0.0025	Yes	Yes
Sub-Optimal	21	20.04	45.1	19.03	0.0023	Yes	No
Reduced-Order							
GA H_2	8	9.52	35.29	17.42	0.0034	Yes	Yes
MU H_2	12	19.67	34.23	18.51	0.0025	Yes	Yes
2nd Iteration							
Gamma	7	9.46	34.57	16.74	0.0034	Yes	Yes
Delta	10	19.27	33.96	18.32	0.0025	Yes	Yes

CHAPTER 6

Comparative Analysis of Classical and MCS Design Methods

To explore the viability of applying MCS methods to launch vehicle ascent and, specifically, the K1 pitch control problem, two different control synthesis methods have been presented. The synthesis approach in Chapter 3 was used to create acceptable SISO control laws and demonstrate a typical application of the classical PD and lead-lag methods. The MCS framework developed in Chapter 5 was used to apply modern control techniques.

Using the classical methods as the benchmark of existing performance, the value of the MCS approach in the K1 pitch control problem was assessed. This chapter presents the evaluation in two ways. First, classical and modern control laws developed within this thesis are comparatively analyzed to determine if the MCS approach is capable of generating control laws with performance at least equivalent to those produced by classical means. Second, the two design architectures are compared to reveal the advantages and disadvantages of using the MCS approach. In this manner, both the product and the process are evaluated to discover the true viability of the MCS framework considered here in launch vehicle applications.

6.1 Control Law Comparison

In Chapter 3, two SISO control laws were developed, which met frequency and time domain performance specifications. Those designs, Alpha and Beta, provide an expectation for the performance that the modern controllers should be capable of achieving. The two designs, Gamma and Delta, developed in Chapter 5 provide an example of typical control laws that can be developed using MCS methods. To realize the capabilities of these two different synthesis approaches, it is beneficial to compare the nominal and robust characteristics of the four controller designs.

6.1.1 Nominal Performance Comparison

To understand how the four different controllers contrast in nominal performance, the time domain and frequency domain responses of the controllers are presented as comparison plots in Figure 6.1, Figure 6.2, and Figure 6.3. Additionally, Table 6.1 provides a summary of the performance metrics for the classical and modern designs. The last two columns in Table 6.1 refer to the level of attenuation achieved for the retention tank slosh mode and the minimum level of attenuation at frequencies greater than 10 rad/s.

Table 6.1 – Performance Metric Summary

Design	Type	GM	PM	ITAE	Ret. LOX	High Freq
Alpha	Classical	9.90	35.3	9.36	-6	-10
Beta	Classical	8.16	30.33	6.18	-4	-16
Gamma	Modern	9.46	34.57	16.74	-6	-20
Delta	Modern	19.27	33.96	18.32	-10	-18

Using Table 6.2 to interpret the figures, Figure 6.1 presents the K1 pitch angle response and engine gimbal response to a step reference input. Figure 6.2 shows the open-loop Nichols plot of the four designs. Finally, Figure 6.3

presents the Bode plot of the closed-loop frequency response for the different controllers.

Table 6.2 – Figure Legend

Design	Line Style
Alpha	Dotted
Beta	Dash-Dot
Gamma	Dashed
Delta	Light Solid

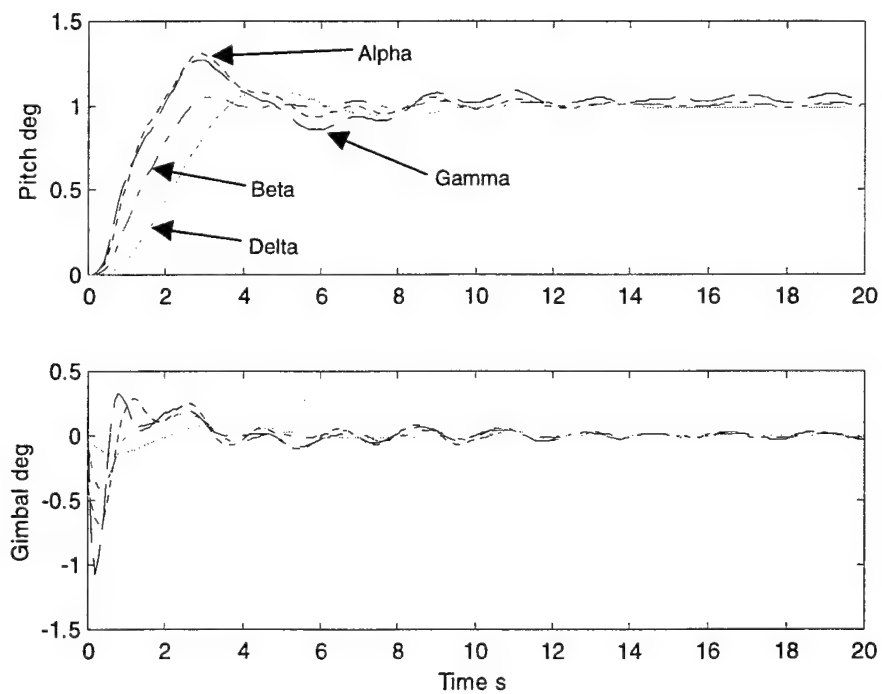


Figure 6.1 – Step Response Comparison

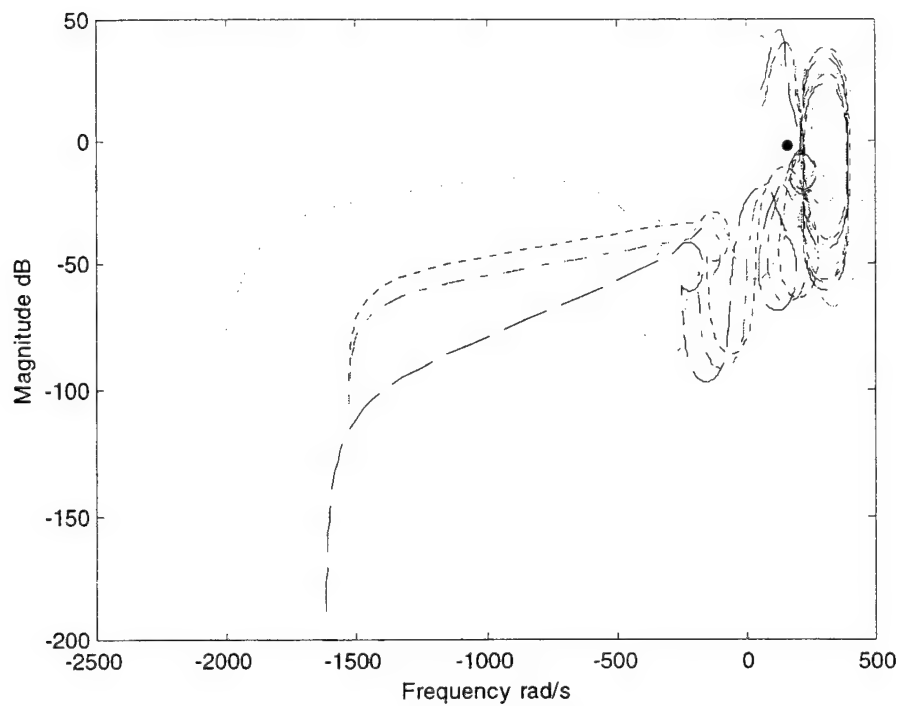


Figure 6.2 – Nichols Frequency Response Comparison

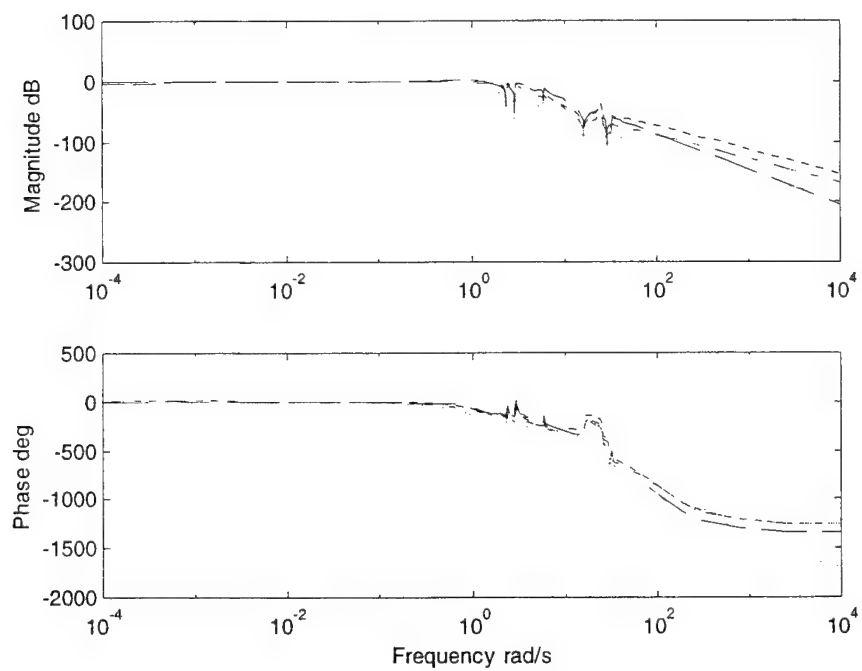


Figure 6.3 – Bode Frequency Response Comparison

The nominal performance evaluation provides several observations, which collectively indicate that the MCS designs do exhibit performance consistent with the expectations established by the SISO designs.

The first significant difference among the designs occurs in their system bandwidth. Figure 6.3 shows that design Delta provides the smallest closed-loop bandwidth, while, the remaining designs appear to produce nearly the same system bandwidth. This explains the transient difference among the pitch responses in Figure 6.1, and much of the disparity in the ITAE metrics of Table 6.1. Designs Alpha and Gamma have the largest bandwidth, and thus, they also have the most rapid response to pitch angle error. The speed of these responses also helps to create the dramatic level of overshoot, ~30%, which both designs exhibit. The smaller bandwidth designs, Beta and Delta, have slower responses that result in less overshoot and slosh mode excitation. However, with only slight bandwidth differences, the pitch responses remain similar in performance.

The second notable feature for each design is its level of control effort. In Figure 6.1, the gimbal response shows that each control design has a different level of control effort. Considering the maximum engine deflection, design Gamma requires the largest motion at approximately 1.0° of engine deflection for each degree of pitch error, while, design Delta requires the least at 0.4° . Design Delta also has the minimum integrated gimbal response. However, the other three designs require similar control effort because their large initial deflections excite the slosh modes and produce extended oscillations in both pitch response and engine gimbal response. Additionally, the lightly damped modes also take a long time to decay, and they drive up the ITAE values of designs Beta and Gamma as these designs create the most excitation.

The third way in which the four controllers can be compared is through their GMs and PMs. From Table 6.2, all four designs successfully meet the primary GM and PM requirements. Design Delta does exceed the minimum 6 dB GM by 13 dB. However, this was necessary during the design process to

achieve the 34° of PM. Three of the four designs satisfy the requirement for -6 dB of attenuation for the retention tank LOX slosh mode. The Nichols plots in Figure 6.2 show that designs Alpha, Gamma, and Delta provide -6 dB of gain attenuation. However, design considerations in Chapter 3 led to design Beta providing only -4 dB. Concerning high-frequency attenuation, each design provides the required -10 dB of attenuation. In fact, the modern designs provide the most high-frequency attenuation at nearly -20 dB in each design.

The three observations on system bandwidth, control effort, and frequency requirements evaluate only how the four control designs compare in response to reference inputs. However, several of the features in the MCS framework are focused on minimizing the pitch response to disturbance inputs. In order to compare the MCS designs to the classical designs, which did not specifically account for disturbance inputs, it is beneficial to examine the different I/O channels.

Figure 6.4, Figure 6.5, and Figure 6.6 present the maximum singular values of the three disturbance input to pitch angle output channels. To incorporate these I/O channels into the classical design, disturbance inputs were added to the classical architecture in the same fashion as they were added to the MIMO design architecture. Figure 6.4 shows the maximum singular value for the pitch angle to wind disturbance. Figure 6.5 shows the maximum singular value of the pitch response to noise in the angular position feedback channel. And, Figure 6.6 presents the maximum singular value of the pitch response to noise in the angular rate feedback. Together, these plots illustrate the relative amplification/attenuation in each design over the frequency spectrum. Table 6.2 once again serves as the legend for these plots.

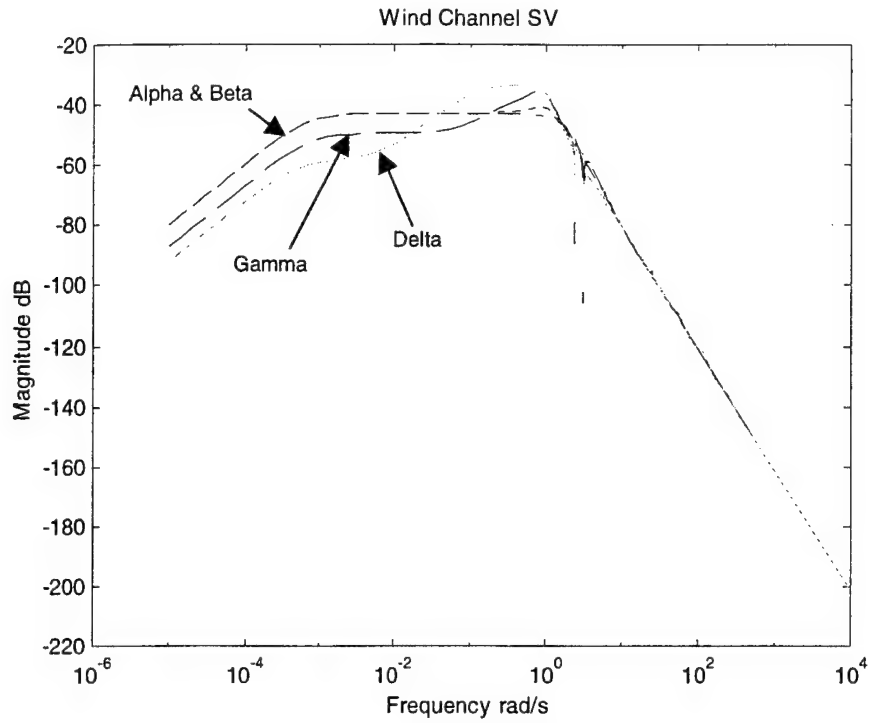


Figure 6.4 – Wind Response Maximum Singular Value

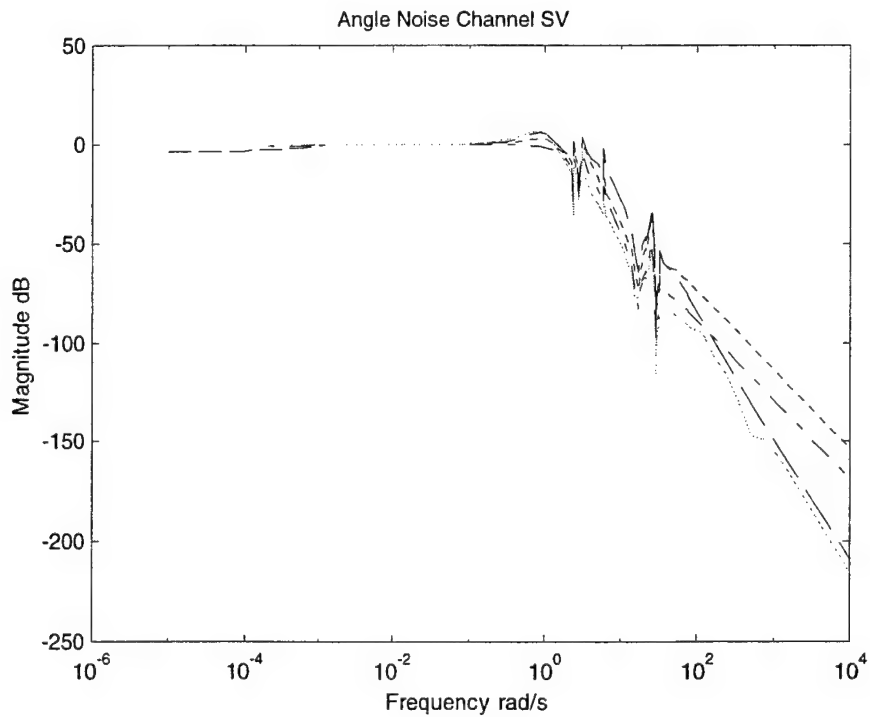


Figure 6.5 – Angular Position Noise Response Maximum Singular Value

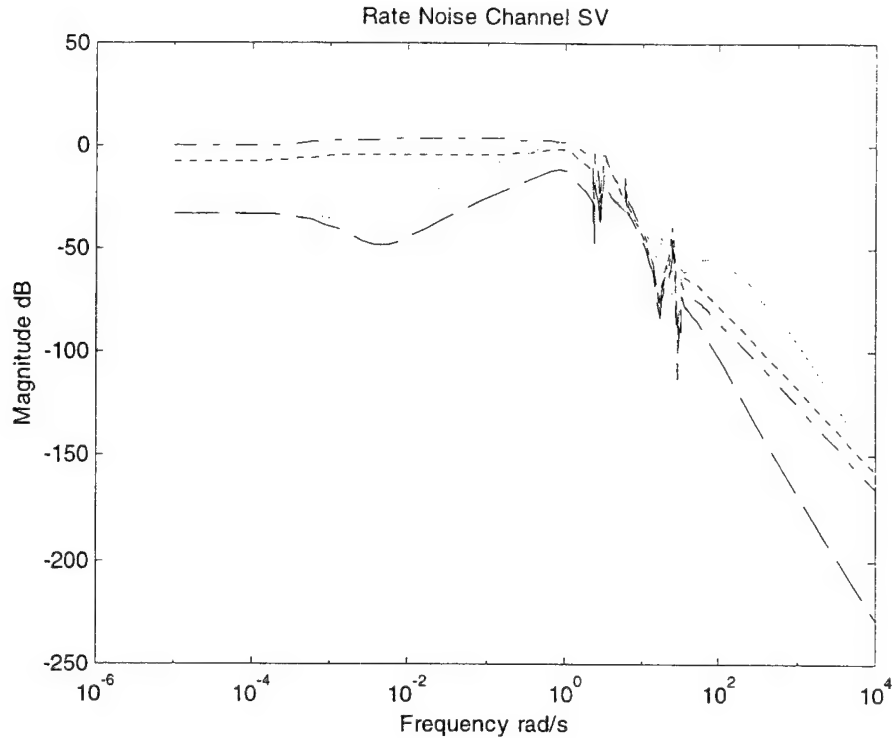


Figure 6.6 – Angular Rate Noise Response Maximum Singular Value

In Figure 6.4, there is a high level of attenuation for all of the control designs. Although there is noticeable difference in the designs at lower frequencies, they appear nearly identical at high frequencies. The MCS designs, especially design Gamma, have higher gain over only a small range of frequencies, which indicates that the minimization used in their development did provide the wind rejection for which it was designed.

In the pitch angle noise channel, all four designs appear to have very similar maximum singular values. Figure 6.5 shows that all four designs pass low frequency noise through to the control system. This makes sense because pitch angle feedback should closely match the bandwidth of the closed-loop reference to pitch angle response. At higher frequencies, the MCS designs do provide increased attenuation over their classical counterparts.

The maximum singular values in Figure 6.6 present the most significant difference among the designs. The classical designs' singular values in Figure 6.6 are very similar to those in Figure 6.5. However, the MCS designs have

considerable low-frequency attenuation, which suggests that these designs are more resilient to rate feedback noise.

One final way in which the nominal performance of the four designs can be analyzed is by generating each design's pitch response to expected reference and disturbance inputs. In order to perform this simulation, the control loop architecture was constructed in SIMULINK. This simulation included a reference input, a wind gust input, and noise inputs consistent with those used in the MCS design framework. Each of the input profiles was created to remain consistent with expected reference command and system disturbance profiles. Figure 6.7 shows the reference command input used in the simulation, which is a gradual ramped increase in pitch angle. This profile was modeled after the nominal pitch profile in Appendix B for consistency in its rate of change. The wind gust input was created using the NASA model presented in Chapter 4, and the repeated sequence is shown in Figure 6.8. The AOA disturbance due to wind includes both positive and negative gusts, and the varying inputs shapes represent the expected duration of 60 m and 300 m gust bases at Mach 1.0. The two independent noise inputs into the simulation were created as a random number sequence with a 0.001 variance. The pitch and gimbal command response results of the simulation are presented in Figure 6.9 for each of the four designs. A solid reference line has also been included in the pitch response plot.

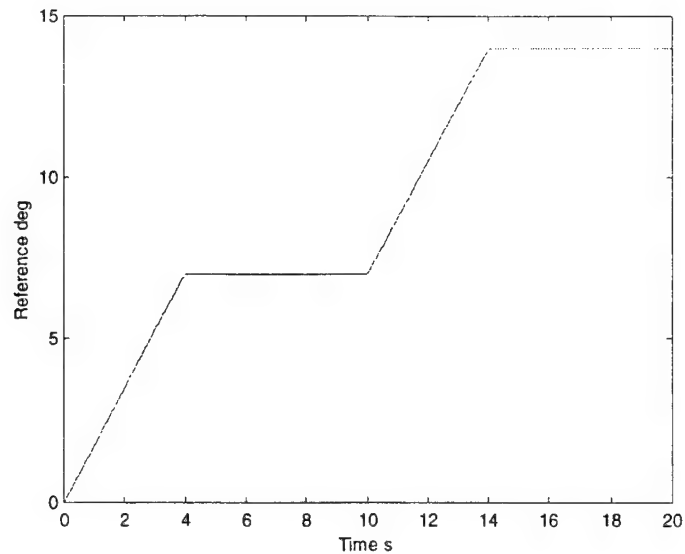


Figure 6.7 – Simulated Reference Input

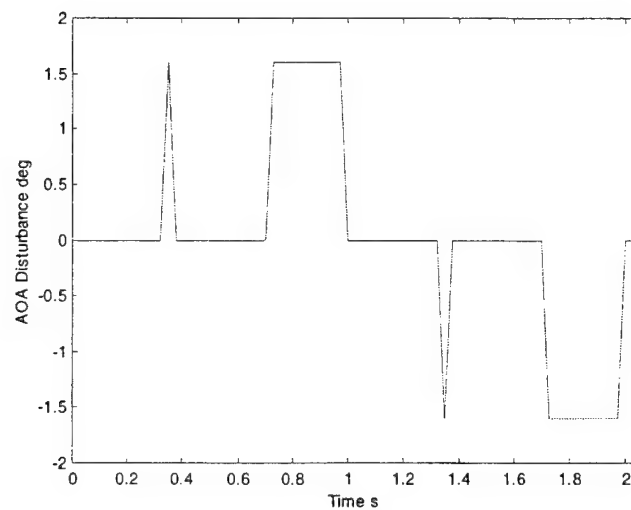


Figure 6.8 – Simulated Wind Gust Input

First, a comparison of the pitch response shows that all four of the designs adequately reject the disturbance inputs. Furthermore, designs Alpha and Gamma have approximately the same pitch response and are the quickest to begin tracking the change in pitch reference. This is expected from their step response characteristics, which also explains the relative lag in designs, Beta

and Delta. However, all the designs adequately track the pitch reference with similar degrees of performance.

An inspection of the engine gimbal responses does indicate that noise has been passed through the controller into the gimbal command signal. This noise obviously gets filtered by the engine actuators and the vehicle dynamics, because there is no noise present in the pitch angle responses. The relative levels of control effort are also consistent with earlier analysis. However, the maximum amount required has been reduced by changing from a step in the reference input to a ramp. These simulated results confirm that the MCS process is capable of creating controllers with nominal performance equivalent to the classical design in the K1 pitch-control problem.

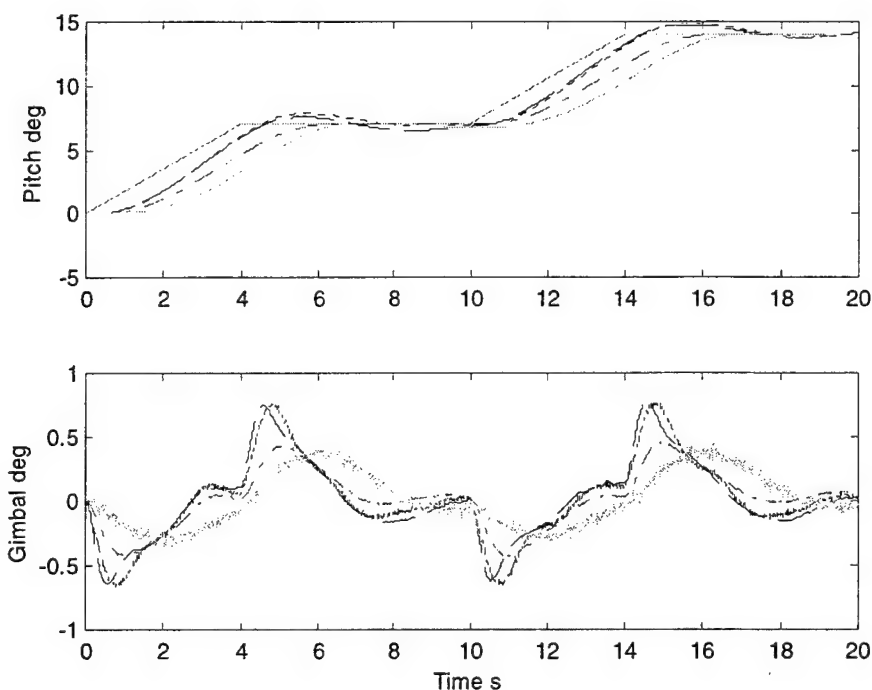


Figure 6.9 – Comparison of Simulated Pitch and Gimbal Responses

6.1.2 Robust Performance Comparison

Another benefit of the MCS design process is that information about system uncertainties can be used to make the resulting control law less sensitive

to vehicle parameter variations. This is not specifically addressed during the classical design process. So, it is of interest to explore the relative robust performance of the four controllers.

Each of the four control laws has been previously tested using 3- σ and combined 1- σ perturbation cases. Details of these results are summarized in Appendix E, and they show that these designs are able to remain stable for all the cases. Therefore, each of these designs has acceptable robust stability. However, a closer inspection of the results contained in Appendix E reveals that the MCS designs are less sensitive to important model perturbations than the classical designs. Table 6.3 presents the perturbation results for the 3- σ case in which the actuators have been perturbed high. Experience has shown that this case has one of the most significant impacts on the performance metrics.

Table 6.3 – Actuator Perturbation Results

Design	ΔGM (%)	ΔPM (%)	$\Delta ITAE$ (%)
Alpha	37.6	12.5	8.4
Beta	32.6	8.8	3.3
Gamma	17.4	7.1	8.3
Delta	8.6	1.1	8.1

Initially, it must be mentioned that design Delta has about twice the nominal GM as do the other designs. Thus, it has essentially the same change in GM as does design Gamma. Regardless, there is a significant reduction in the loss of GM between the classical and modern designs. Although this is only one case, a cursory inspection of the remaining data in Appendix E does support the contention that the MCS designs are more robust to parameter changes. This added robustness is the primary advantage of using a design processes that can account for uncertainty in the plant. It did, however, come at the cost of bandwidth in the MU approach, and design Delta exhibits the slowest response of the four designs.

In spite of this negative aspect in the MU approach, a comparison of the nominal and robust performance has shown that the MCS controllers achieve roughly equivalent performance compared to the classical pitch control laws. This equivalence only confirms the ability of the MCS process to develop acceptable controllers for the K1 pitch control problem, as well as for other launch vehicle applications.

6.2 Synthesis Approach Comparison

However, it is not enough to compare only the products of the two design processes. To fully assess MCS as an alternative synthesis process, the capabilities and limitations of the two architectures, classical and modern, should be addressed. By accounting for the number of design parameters, computational demands, physical intuition, and experience base required in each method, the feasibility of applying the MCS approach to future, more sophisticated problems can be realized.

Each of the two approaches has been shown to possess a large number of design parameters. In the classical framework, the bending filter and PD gains created approximately 22 free parameters that were free to choose. To reduce this number, the bending filter had to be reduced in size and fixed in form. Yet, even after these simplifications, the execution of the vector search algorithm was computationally intensive, and the problem required further reduction to complete the search in a reasonable amount of time on a high performance personal computer. The MCS approach also contained a similar number of design parameters, but instead of constraining the controller to a specified form and size that may not maximize performance, the hierarchical process, developed in Chapter 5, uses physical characteristics of the vehicle dynamics and design experience to create a problem manageable in size without restricting possible solutions.

Another advantage of the MCS process is the way in which it incorporates information about the vehicle, disturbances, and uncertainties into the design

framework. This information is then used to help minimize variations such as pitch error and engine deflection. All of the inputs and outputs of the system are physical and give the problem a very intuitive feel. Classical methods, on the other hand, do not provide clear-cut ways in which to address physical quantities directly, and an iterative approach is needed to develop and test designs to produce quality results. The design process executed in this thesis is a good example. Nearly 2000 different designs were created during the search algorithm used to generate designs Alpha and Beta. By comparison, only 11 designs were needed to develop the original pair of reduced-order controllers in the MCS approach.

Another aspect that is central to the classical versus modern comparison is the controller which results from each process. In the classical approach, the final form and size of compensation are included as design parameters, and the control engineer has exacting control over the form of the compensation. However, in the MCS framework the compensation is model-based, and the form and order of the controller result from the optimization of the objective function. In this respect, designs developed using MCS techniques are generally high-order and sensitive to model variations. With the inclusion of uncertainty structures, procedures for controller order reduction, and flexibility in formulating the design model, the sensitivity and order of the controllers are, to a large degree, free to choose in the design process. This was proven by the reduction from 15th order to 7th order in design Gamma and from 21st order to 10th order in design Delta. Additionally, the modifications made to the design model during the 2nd iteration of the MCS process revealed how problem formulation can be used to influence the structure of the control law when the high-frequency modes were successfully eliminated. These reduced-order MCS designs are comparable in order to the classical designs and allow easier digital implementation than their associated high-order forms.

The manageable size, physically intuitive nature, and type of control law which characterize the MSC architecture show that the process does have advantages over classical methods for the pitch control problem posed in this

thesis. However, the true advantage of the MCS process is its flexibility in addressing other problems, and using two examples will demonstrate how easily the process can be adapted to accommodate different design issues and objectives.

First, consider a more aggressive attenuation requirement in the LOX retention tank slosh mode. Instead of requiring -6 dB, assume that -15 dB is required. At this requirement level, the MCS designs, Gamma and Delta, cannot provide adequate attenuation. The MCS design process, however, does provide a tool to help achieve the needed attenuation level. Simply by adding gain to a small range of frequencies near the 5 rad/s point, the optimization process will be guided to provide added attenuation at the retention mode frequency. This approach is analogous in reasoning used in the GA uncertainty technique, but now, the effect is localized over a specific range of frequencies. This concept can actually be implemented into the design model in two ways. First, instead of using a scalar gain in the GA technique, a small band-pass filter could be used to raise gain over a small frequency band. Second, the MU technique could be used to raise the level of uncertainty over the retention-mode frequency by raising the gain over that same frequency in the uncertainty input shaping filter. Both of these methods would provide avenues by which to address greater attenuation requirements.

For the second example, consider a change in design objective. Instead of wind gust rejection, the secondary goal of the design is load relief, in which the vehicle steers into the prevailing wind in order to minimize aerodynamic loads on the vehicle. This objective can be address by analyzing how load relief relates to the states of the vehicle dynamics. By turning into the wind, the AOA of the vehicle is minimized. Therefore, the load relief objective can be recast as AOA regulation. In the MCS framework, the change in design objective corresponds to a change in the exogenous I/O selection. By specifying the AOA state as a cost output in addition to pitch error and control effort, the AOA response to wind gust can be penalized with the relative weighting of the design channels. The resulting optimization would produce control designs capable of load relief.

Together, the flexibility, manageable size, physically intuitive nature, and resulting control laws of the MSC architecture show that the process does have advantages over classical methods. Although there is no substitute for a wealth of experience in designing controllers efficiently and effectively, the MCS framework takes advantage of a practical experience base, in which valuable insight into the vehicle dynamics and other physical information specific to the problem can be exploited using a small, but powerful set of design tools.

6.3 MCS Assessment

Both the product and the process substantiate the viability of the MCS approach in designing launch vehicle pitch control laws. A comparison of the two classical designs, Alpha and Beta, and the MCS designs, Gamma and Delta, reveals that each design architecture is capable of creating controllers with equivalent nominal performance. In fact, simulated responses of designs Alpha and Gamma show almost identical nominal performance. With respect to robust performance, the results of dispersion analysis show that the MCS designs are more robust to parameter variations. However, the benefit in the MCS approach largely arises from the design process itself. During application to the K1 pitch control problem, modern methods appear to be more manageable in terms of their design parameters and to require less iteration than classical methods. Furthermore, successful approaches were presented which overcame the traditional obstacles of sensitivity and high-order associated with MCS methods. Finally, two examples of problem modification showed how the MCS process can be adapted to accommodate a multitude of objectives. It is for these reasons that the MCS approach should be viewed as a viable alternative in the development of launch vehicle ascent controls.

CHAPTER 7

Conclusions & Recommendations

7.1 Conclusions

An application of robust H_2/H_∞ control synthesis to launch vehicle ascent has been presented in this thesis to assess its viability as an alternative approach to classical control synthesis methods. Specifically, a Modern Control Synthesis (MCS) architecture was developed to address the K1 pitch control problem. Through this investigation, the successful extension of like techniques to a large class of launch vehicles is seen to be plausible.

The MCS architecture begins fundamentally from the development and verification of a high fidelity set of launch vehicle equations of motion. With a minimum of simplification, a set of linearized pitch plane equations of motion were developed to provide the dynamic models for both the design and analysis of robust weighted H_2/H_∞ controllers. The full dynamic model included rigid-body, aerodynamic, fuel-sloshing, tail-wags-dog, and body-bending effects. The development of the math model proved to be very beneficial during the MCS process. The intimate knowledge of the different dynamic effects and their relative importance made the process of order reduction in the design model a trivial task. An understanding of the dynamics was also beneficial in developing the uncertainty structures used to implement unstructured multiplicative uncertainty.

With the introduction of the high fidelity vehicle model into the existing classical control loop architecture, it was concluded that performance specifications, 6 dB GM and 30° PM, could not be satisfied with a simple PD architecture. Additional performance specifications were also established to ensure levels of attenuation for the retention tank LOX mode, -6 dB, and the body-bending modes, -10 dB. These new requirements were needed because the more advanced dynamics of slosh, tail-wags-dog, and flex had not been previously addressed in the K1 pitch control problem, and no requirements existed. With these requirements in place, it was not obvious which filter design would achieve the desired performance levels. To make the bending filter design more tractable, the general form of the 10th order filter was simplified to a 4th order lead-lag network, and the actual design process was implemented as MATLAB code, which searched for the optimum selection of filter parameters.

Faced with the same problem of numerous design variables in the MCS architecture, a control synthesis hierarchy was developed to introduce order to the design problem and make it manageable in size. The iterative nature of the problem was not fully exploited. Though, it was used to show how modifications in the problem formulation influence the form of the design solutions. Instead, a minimum of iterations was used to demonstrate the capability and efficiency of the MCS process. In just one iteration of the control synthesis hierarchy, two model-based designs were developed that met performance specifications. After a second iteration, in which the control loop architecture was modified to eliminate high frequency poles, two more designs were established with adequate performance.

The comparison of control designs produced by each design method, classical and modern, revealed the robust H_2/H_∞ control synthesis approach provides an adequate means for developing compensation that meets nominal and robust performance criteria. Additionally, a comparison of the two design architectures showed that the physically intuitive nature of the H_2/H_∞ problem formulation was an easier task than trying to manually create the classical

bending filter. Two examples also demonstrated how the MCS process can be adapted to accommodate other design objectives, a procedure which is not as clear in classical design methods. These conclusions confirm that the MCS framework is an alternative which offers benefits over classical methods.

7.2 Recommendations for Future Work

Although a basic design framework and preliminary control designs have indicated that there are additional capabilities and benefits provided by the MCS approach, the research presented in this thesis has several areas which were not pursued in order to narrow its focus. Several steps still remain in the development of a total K1 pitch control law. The results presented here were based on a "point" design for the Mach 1.0 point in the trajectory, and additional control designs must be developed for several other points along the trajectory. Then, the designs can be carefully blended together to form a continuous pitch control design for the entire boost phase. Issues surrounding the complexity involved in integrating the various control laws will also be of interest in the final boost phase implementation.

Furthermore, the issue of load relief was also not addressed in the design framework to narrow the focus of this thesis. For the MCS designs presented here, the response to the wind gust input was minimized. Thus, the controllers essentially rejected wind disturbances. However, this is not always advantageous, because large angles-of-attack induced by wind gusts can create large structural loads on the launch vehicle. A not uncommon approach is to design a control system which steers into the wind to provide a measure of load relief. Although a scheme for developing a load relief control law was briefly presented, the full development of a load relief control law is a logical extension of the fundamental development presented in this thesis.

Exploration into the extension of the MCS approach to the entire boost phase and the load relief concept above are not inclusive of all the possible areas in which the MCS architecture can be further refined for use in launch

vehicle ascent. They are, however, reasonable continuations of the work presented here and are necessary to truly understand the viability of the MCS approach in practical launch vehicle applications.

APPENDIX A

Pitch Plane Equations of Motion

In developing the longitudinal equations of motion (EOMs) for the Kistler launch vehicle, the effects of gravity, thrust, aerodynamic lift and drag, engine inertia, fuel-sloshing, and body-bending were modeled for their force and moment contributions. The following is a complete description of the pitch plane EOMs as they were derived from first principles.

A.1 Variable Declaration

Variables used in the development of the pitch plane EOMs are listed by section in the order they appear.

General

Δ, o	denotes perturbation and steady state terms
F_x, F_y, F_z	total force components
M_x, M_y, M_z	total moment components
m, dm	total and incremental body mass
$U_0, \Delta u$	body x-axis velocity
$V_0, \Delta v$	body y-axis velocity
$W_0, \Delta w$	body z-axis velocity
ω	angular velocity of body relative velocity vector
$P_0, \Delta p$	roll rate
$Q_0, \Delta q$	pitch rate
$R_0, \Delta r$	yaw rate
r	inertial position vector of body center of gravity
H, dH	vehicle total and incremental angular momentum
M, dM	vehicle total and incremental moment

I_{xx}, I_{yy}, I_{zz}	body moments of inertia
I_{xy}, I_{yz}, I_{xz}	body inertial cross-products
$\phi_o, \Delta\phi$	roll angle
$\theta_o, \Delta\theta$	pitch angle
$\psi_o, \Delta\psi$	yaw angle
$\mathbf{1}_v$	unit vector in the direction of velocity
$\mathbf{1}_H$	unit vector in the direction of angular momentum

Gravity

F_G, M_G	gravity force and moment
g_o	gravitational acceleration

Thrust

F_T, M_T	thrust force and moment
T	vehicle thrust
δ_p	pitch plane engine gimbal angle
l_p	engine gimbal location with respect to body reference frame

Engine Inertia

F_E, M_E	tail-wags-dog force and moment
F_p	force at pivot due to engine rotation
m_e	engine mass
a_e	acceleration of engine mass
T_p	torque at pivot due to engine rotation
l_e	absolute distance from engine center of gravity to engine gimbal point
α_e	engine angular acceleration
ω_e	engine angular velocity
e_r, e_o	radial and tangential polar coordinate components
$I_e, I_{xxe}, I_{yye}, I_{zze}$	engine inertia matrix and moments of inertia

Aerodynamics

F_A, M_A	aerodynamic force and moment
S	cross sectional area
q	dynamic pressure
L_{cp}	length of center of pressure from center of gravity
α	angle of attack
γ	flight path angle
C_{xu}, C_{xo}	axial velocity derivative and trim coefficients for longitudinal perturbations
C_{zu}, C_{zo}	vertical velocity derivative and trim coefficients for longitudinal perturbations
C_{mu}, C_{mo}	pitch moment derivative and trim coefficients for

	longitudinal perturbations
$C_{x\alpha}$	axial velocity derivative coefficient for angle of attack perturbations
$C_{z\alpha}$	vertical velocity derivative coefficient for angle of attack perturbations
$C_{m\alpha}$	pitch moment derivative coefficient for angle of attack perturbations
C_{xq}	axial velocity derivative coefficient due to pitch damping
C_{zq}	vertical velocity derivative coefficient due to pitch damping
C_{mq}	pitch moment derivative coefficient due to pitch damping
V	airspeed
M	velocity to body frame rotation matrix
a_V, a_B	vehicle center of gravity acceleration in velocity and body reference frames

Slosh

F_S, M_S	slosh force and moment
A_s	acceleration of slosh mass with respect to inertial space
l_s	position of slosh mass with respect to body center of gravity
$V_{S/B}$	velocity of slosh mass with respect to vehicle center of gravity
$a_{S/B}$	acceleration of slosh mass with respect to vehicle center of gravity
ω_B	body angular velocity
m_s	slosh mass
ω_s	slosh frequency
ζ_s	slosh damping coefficient
X_s, Y_s, Z_s	slosh mass x-axis, y-axis, and z-axis perturbation displacements
U_s, V_s, W_s	slosh mass velocities

IMU

a_{cgaa}	acceleration sensed by body center of gravity
A_{cg}	acceleration of body center of gravity in inertial frame
l_{aa}	distance from center of gravity to accelerometer
a_{aa}	acceleration sensed by accelerometer

Flex

q_j	j^{th} flex mode state
m_j	j^{th} flex mode modal mass
ζ_j	j^{th} flex mode damping coefficient
ω_j	j^{th} flex mode frequency

Φ_j^T	j^{th} flex mode parameter vector
$\phi_{xe}, \phi_{ye}, \phi_{ze}$	gimbal node translation parameters
$\sigma_{xe}, \sigma_{ye}, \sigma_{ze}$	gimbal node rotation parameters
ϕ_{zaa}	accelerometer node z-translation parameter
$\sigma_y \text{ gyros}$	gyro node rotation parameter

A.2 General Equations

Beginning with Newton's 2nd law, the forces acting on the launch vehicle are equal to its rate of change of momentum,

$$\Sigma F = \frac{d}{dt}(mV_1) \quad (\text{A.1})$$

Because these equations are eventually linearized for points along the nominal trajectory, the mass flow rate of the launch vehicle can be neglected. Making this assumption, equation A.1 reduces to,

$$\Sigma F = m \frac{dV}{dt} \quad (\text{A.2})$$

This can be transformed into the local (body) reference frame using equation A.3, which accounts for changes in both the magnitude and direction of the vehicle velocity vector in a rotating reference frame,

$$\frac{dV}{dt} = 1_v \frac{dV}{dt} + \omega \times V \quad (\text{A.3})$$

The velocity of the vehicle center of gravity (CG) and its angular velocity are defined by equations A.4 and A.5, respectively.

$$V = U\hat{i} + V\hat{j} + W\hat{k} \quad (\text{A.4})$$

$$\omega = P\hat{i} + Q\hat{j} + R\hat{k} \quad (\text{A.5})$$

The $\langle i, j, k \rangle$ unit vectors define the inertial frame of reference. The inertial axis set is right handed and orthonormal centered at the body CG. These vectors are initially aligned with the vehicle body roll, pitch, and yaw axes. The body reference frame is presented in Chapter 2. Substitution of equations A.4 and A.5 into A.3 results in equations A.6 through A.8, which are the generic forms of the force equations.

$$\Sigma F_x = m(\dot{U} + WQ - VR) \quad (A.6)$$

$$\Sigma F_y = m(\dot{V} + UR - WP) \quad (A.7)$$

$$\Sigma F_z = m(\dot{W} + VP - UQ) \quad (A.8)$$

The rotational equivalent to equation A.2 is,

$$\Sigma M = \frac{dH}{dt} \quad (A.9)$$

Again, this can be translated to the body frame using the chain rule.

$$\Sigma M = I_H \frac{dH}{dt} + \omega \times H \quad (A.10)$$

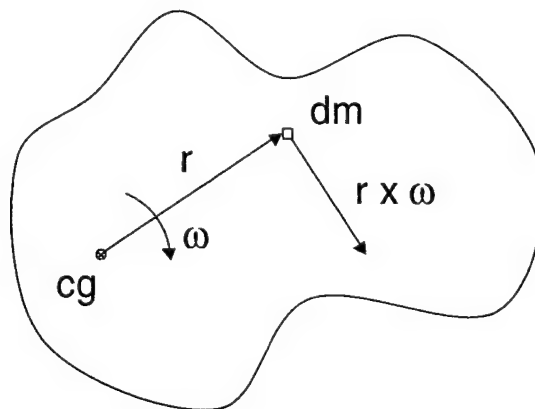


Figure A.1 – General body with rotation about CG

Figure A.1 shows the approach for deriving an expression of the vehicle's angular momentum. Using position vector of an incremental mass (equation A.11) and its angular velocity, incremental momentum can be found with equation A.12. The incremental moment of momentum is just the cross product of the incremental

$$\mathbf{r} = x\hat{i} + y\hat{j} + z\hat{k} \quad (\text{A.11})$$

$$d\mathbf{M} = (\omega \times \mathbf{r}) dm \quad (\text{A.12})$$

$$d\mathbf{H} = \mathbf{r} \times (\omega \times \mathbf{r}) dm \quad (\text{A.13})$$

momentum and its distance from the body CG, shown by equation A.13. The total angular momentum expressed in integral form is

$$\mathbf{H} = \int \mathbf{r} \times (\omega \times \mathbf{r}) dm \quad (\text{A.14})$$

After expanding the integral form of angular momentum, it is convenient to make the following six substitutions:

$$\int xy dm = I_{xy} \quad (\text{A.15})$$

$$\int y^2 + z^2 dm = I_{xx} \quad (\text{A.16})$$

$$\int xz dm = I_{xz} \quad (\text{A.17})$$

$$\int x^2 + z^2 dm = I_{yy} \quad (\text{A.18})$$

$$\int yz dm = I_{yz} \quad (\text{A.19})$$

$$\int x^2 + y^2 dm = I_{zz} \quad (\text{A.20})$$

Equations A.15 through A.20 define the body products and cross products of inertia. However, the K1 vehicle is symmetric about the local x-z plane. Thus,

$$I_{xy} = I_{yz} = 0 \quad (\text{A.21})$$

Simplification reveals the generic form of the moment equations.

$$\Sigma M_x = \dot{P}I_{xx} + QR(I_{zz} - I_{yy}) - (PQ + \dot{R})I_{xz} \quad (\text{A.22})$$

$$\Sigma M_y = \dot{Q}I_{yy} + PR(I_{xx} - I_{zz}) - (R^2 - P^2)I_{xz} \quad (\text{A.23})$$

$$\Sigma M_z = \dot{R}I_{zz} + PQ(I_{yy} - I_{xx}) + (RQ + \dot{P})I_{xz} \quad (\text{A.24})$$

Some attention should be given to axes conversions. The Euler angle to body frame conversion is defined as,

$$P = \dot{\phi} - \dot{\psi} \sin \theta \quad (\text{A.25})$$

$$Q = \dot{\theta} \cos \phi + \dot{\psi} \cos \theta \sin \phi \quad (\text{A.26})$$

$$R = \dot{\psi} \cos \theta \cos \phi - \dot{\theta} \sin \phi \quad (\text{A.27})$$

However, zero roll angle, roll rate, and yaw rate trim conditions (equations A.28 and A.29) permit reduction in equations A.25, A.26, and A.27.

$$\phi_o = 0^\circ \quad (\text{A.28})$$

$$P_o = R_o = 0 \quad (\text{A.29})$$

By applying small angle approximations and separating the perturbation and steady-state terms from equations A.25, A.26, and A.27, and employing the trim conditions, the following bias equations result:

$$P_o = \dot{\phi}_o - \dot{\psi}_o \sin \theta_o = 0 \quad (\text{A.30})$$

$$Q_o = \dot{\theta}_o \quad (\text{A.31})$$

$$R_o = \dot{\psi}_o \cos \theta_o = 0 \quad (\text{A.32})$$

Further inspection reveals that because the steady-state pitch angle is free to vary in equations A.30 and A.32, the steady-state yaw rate must be zero.

$$\dot{\psi}_o \equiv 0 \quad (\text{A.33})$$

Thus, the final form of the Euler angle to body axes conversion is,

$$\Delta p = \Delta \dot{\phi} - \sin \theta_o \Delta \dot{\psi} \quad (\text{A.34})$$

$$\Delta q = \Delta \dot{\theta} \quad (\text{A.35})$$

$$\Delta r = \cos \theta_o \Delta \dot{\psi} - \dot{\theta}_o \Delta \phi \quad (\text{A.36})$$

A.3 Longitudinal EOMs

The longitudinal and lateral plane motions can be decoupled by assuming that forces in the body x-axis and z-axis directions as well as rotation about the y-axis has zero effect outside the longitudinal (pitch) plane. This implies that the pitch axis is in the plane of the local horizon during trim, $\phi_o = 0^\circ$, and that the vehicle is in a state of pitch moment trim. Another decoupling assumption is,

$$P = R = V = 0 \quad (\text{A.37})$$

Applying these simplifications to the generic force and moment equations produces the following 3 degree of freedom (DOF) equation set for the pitch plane EOMs,

$$\Sigma F_x = m(\dot{U} + WQ) \quad (\text{A.38})$$

$$\Sigma F_z = m(\dot{W} - UQ) \quad (\text{A.39})$$

$$\Sigma M_y = \dot{Q}I_{yy} \quad (\text{A.40})$$

A standard process, utilized earlier in the Euler conversion development (equations A.34 – A.36), will be used throughout this derivation to produce the necessary linear time invariant (LTI) perturbation EOMs. The process will be outlined for equations A.38 through A.40, and only alluded to for the sake of brevity in subsequent applications. First, all applicable terms are expanded into steady-state and perturbation elements.

$$Q = Q_o + \Delta q \quad (A.41)$$

$$U = U_o + \Delta u \quad (A.42)$$

$$W = W_o + \Delta w \quad (A.43)$$

After expanding equations A.38 through A.40 with equations A.41 through A.43, products of perturbation terms are neglected in order to linearize the equations. Finally, the bias, or steady-state, terms are collected and removed.

$$\Sigma F_{x_o} = m [\dot{U}_o + W_o Q_o] \quad (A.44)$$

$$\Sigma F_{z_o} = m [\dot{W}_o - U_o Q_o] \quad (A.45)$$

$$\Sigma M_{y_o} = \dot{Q}_o I_{yy} \quad (A.46)$$

The remaining terms, equations A.47, A.48, and A.49, are identified as perturbation EOMs called perturbation equations, and characterize the vehicle dynamics in response to small deviations from the nominal trajectory conditions.

$$\Sigma \Delta F_x = m [\Delta \dot{u} + W_o \Delta q + \Delta w Q_o] \quad (A.47)$$

$$\Sigma \Delta F_z = m [\Delta \dot{w} - U_o \Delta q - \Delta u Q_o] \quad (A.48)$$

$$\Sigma \Delta M_y = \Delta \dot{q} I_{yy} \quad (A.49)$$

A.4 Pitch Plane External Stimuli

The perturbation forces and moments acting on the vehicle are due to gravity, aerodynamics, thrust, engine motion, fuel sloshing, and body bending. For now, the effects of body bending, also referred to as flex, will be neglected and will be introduced later in the EOM development.

Expanding the perturbation forces as a Taylor series about the steady-state operating point and linearizing by neglecting higher order terms in the series results in the following pitch plane EOM's.

$$\begin{aligned} \Sigma \Delta F_x = & \frac{\partial F_x}{\partial \Delta u} \Delta u + \frac{\partial F_x}{\partial \Delta \dot{u}} \Delta \dot{u} + \frac{\partial F_x}{\partial \Delta w} \Delta w + \frac{\partial F_x}{\partial \Delta \dot{w}} \Delta \dot{w} + \frac{\partial F_x}{\partial \Delta q} \Delta q + \\ & \frac{\partial F_x}{\partial \Delta \dot{q}} \Delta \dot{q} + \frac{\partial F_x}{\partial \Delta \delta} \Delta \delta \end{aligned} \quad (A.50)$$

$$\begin{aligned} \Sigma \Delta F_z = & \frac{\partial F_z}{\partial \Delta u} \Delta u + \frac{\partial F_z}{\partial \Delta \dot{u}} \Delta \dot{u} + \frac{\partial F_z}{\partial \Delta w} \Delta w + \frac{\partial F_z}{\partial \Delta \dot{w}} \Delta \dot{w} + \frac{\partial F_z}{\partial \Delta q} \Delta q + \\ & \frac{\partial F_z}{\partial \Delta \dot{q}} \Delta \dot{q} + \frac{\partial F_z}{\partial \Delta \delta} \Delta \delta \end{aligned} \quad (A.51)$$

$$\begin{aligned} \Sigma \Delta M_y = & \frac{\partial M_y}{\partial \Delta u} \Delta u + \frac{\partial M_y}{\partial \Delta \dot{u}} \Delta \dot{u} + \frac{\partial M_y}{\partial \Delta w} \Delta w + \frac{\partial M_y}{\partial \Delta \dot{w}} \Delta \dot{w} + \frac{\partial M_y}{\partial \Delta q} \Delta q + \\ & \frac{\partial M_y}{\partial \Delta \dot{q}} \Delta \dot{q} + \frac{\partial M_y}{\partial \Delta \delta} \Delta \delta \end{aligned} \quad (A.52)$$

The partial derivatives with respect to pitch angle and gimbal angle represent gravitational and engine effects, respectively. All other derivatives relate to effects caused by aerodynamic forces.

A.4.1 Gravity

The force of gravity in the x-axis and z-axis directions is found as,

$$F_{Gx} = -mg_o \sin \theta \quad (A.53)$$

$$F_{GZ} = mg_o \cos \theta \cos \phi \quad (A.54)$$

from Figure A.2.

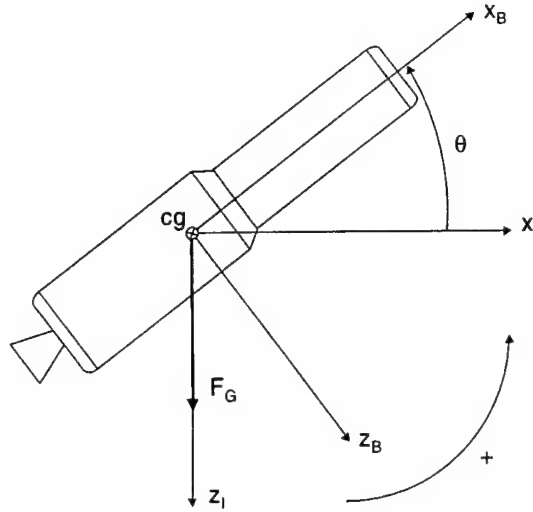


Figure A.2 – Gravity Free-Body Diagram

Using the same technique delineated in the development of the generic pitch plane EOMs, equations A.53 and A.54 are expanded into steady-state and perturbation elements.

$$F_{GX_o} + \Delta F_{GX} = -mg_o \sin(\theta_o + \Delta\theta) \quad (A.55)$$

$$F_{GZ_o} + \Delta F_{GZ} = mg_o \cos(\theta_o + \Delta\theta) \cos(\phi_o + \Delta\phi) \quad (A.56)$$

Using basic trigonometric identities (equations A.57 and A.58), the sine and cosine expressions are further expanded. Small perturbation magnitudes allow the use of small angle approximations (equations A.59 and A.60) to simplify the expanded equations.

$$\sin(\alpha + \beta) = \sin \alpha \cos \beta + \cos \alpha \sin \beta \quad (A.57)$$

$$\cos(\alpha + \beta) = \cos \alpha \cos \beta - \sin \alpha \sin \beta \quad (A.58)$$

$$\sin \alpha \approx \alpha \quad (A.59)$$

$$\cos \alpha \approx 1 \quad (A.60)$$

Applying steady-state conditions, equations A.28 and A.29, the following bias equations and perturbation EOM's result and define the effects of gravity on the K1.

$$F_{GX_o} = -mg_o \sin \theta_o \quad (A.61)$$

$$F_{GZ_o} = mg_o \cos \theta_o \quad (A.62)$$

$$\Delta F_{GX} = -mg_o \cos \theta_o \Delta \theta \quad (A.63)$$

$$\Delta F_{GZ} = -mg_o \sin \theta_o \Delta \theta \quad (A.64)$$

$$\Delta M_{GY} = 0 \quad (A.65)$$

One final note is that gravity gradient torque on the body was neglected because of its insignificance in the very short and dynamic flight.

A.4.2 Thrust

To support the decoupling of lateral and longitudinal dynamics, engine motion has been restricted to the pitch plane. Figure A.3 shows the configuration of pitch plane thrust.

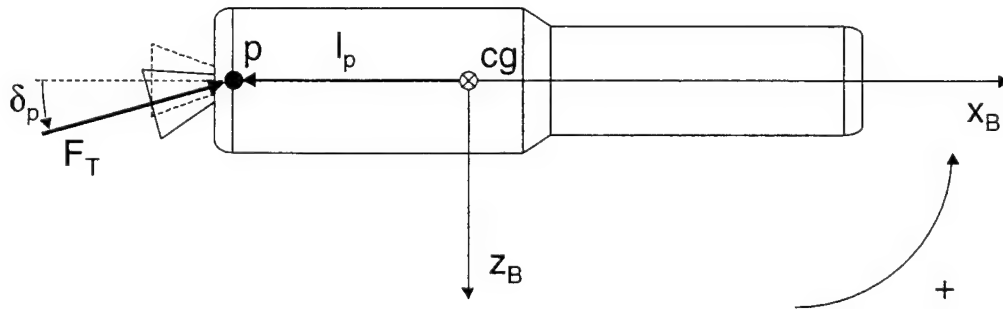


Figure A.3 – Thrust Free-Body Diagram

The x and z-direction forces are then,

$$F_{TX} = T \cos \delta_p \quad (A.66)$$

$$F_{TZ} = -T \sin \delta_p \quad (A.67)$$

Using the same procedure as before. These equations are expanded into bias and perturbation terms. Then, appropriate trigonometric identities are applied along with small angle approximations. The resulting bias equations are,

$$F_{TXo} = T \cos \delta_{po} \quad (A.68)$$

$$F_{TZo} = -T \sin \delta_{po} \quad (A.69)$$

The thrust perturbation force is defined by,

$$\Delta F_{TX} = -T \sin \delta_{po} \Delta \delta_p \quad (A.70)$$

$$\Delta F_{TZ} = -T \cos \delta_{po} \Delta \delta_p \quad (A.71)$$

In order to find the moment due to perturbation thrust, the perturbation force must be crossed with its moment arm from the vehicle CG, I_p . As indicated in Figure A.3, I_p is the vector representing the location of the engine gimbal with respect to the body CG. Thus, its x-direction component will always be negative. Continuing, the roll and yaw moments are neglected for longitudinal analysis in equation A.72, and the pitch moment perturbation equation A.73 results.

$$\Delta M_T = I_p \times \Delta F \quad (A.72)$$

$$\Delta M_{TY} = I_{pz} \Delta F_{TX} - I_{px} \Delta F_{TZ} \quad (A.73)$$

Substituting the force equations A.70 and A.71, into the pitch moment perturbation equation A.73 produces the final form of the pitch plane perturbation moment due to thrust.

$$\Delta M_{TY} = T (I_{px} \cos \delta_{po} - I_{pz} \sin \delta_{po}) \Delta \delta_p \quad (A.74)$$

A.4.3 Engine Motion (“Tail-Wags-Dog”)

This derivation of the Tail-Wags-Dog effect is simplified in that it does not account for the additional kinematics involved with the motion of the vehicle through inertial space.

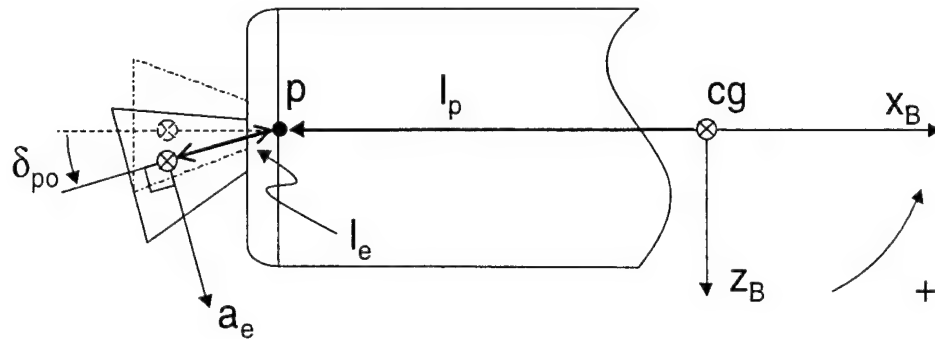


Figure A.4 – TWD Free-Body Diagram

For a derivation of TWD effects including CG motion refer to [3]. Figure A.4 presents the problem formulation implemented here, in which only the engine's motion with respect to the vehicle CG is considered. The relationship between steady-state and perturbation elements of the gimbal angle, rate and acceleration are,

$$\delta = \delta_0 + \Delta\delta \quad (\text{A.75})$$

$$\dot{\delta} = \Delta \dot{\delta} \quad (\text{A.76})$$

$$\ddot{\delta} = \Delta \ddot{\delta} \quad (\text{A.77})$$

From first principles, the reaction force and moment at the engine pivot, p , are equal and opposite to those of the engine, and are defined by,

$$\mathbf{F}_p = -m_e \mathbf{a}_e \quad (\text{A.78})$$

$$\mathbf{T}_p = -I_e \alpha_e \quad (\text{A.79})$$

From the general form of circular acceleration, equation A.80, the acceleration of the engine nozzle is written as equation A.81 in the absence of acceleration.

$$\mathbf{a}_e = -r\omega_e^2 \hat{\mathbf{e}}_r + r\dot{\omega}_e \hat{\mathbf{e}}_\theta \quad (\text{A.80})$$

$$\mathbf{a}_e = I_e \Delta \ddot{\delta} \quad (\text{A.81})$$

Translating equation A.81 into the body coordinate frame results in,

$$\mathbf{a}_e = \begin{bmatrix} I_e \Delta \ddot{\delta}_p \sin \delta_{p0} \\ 0 \\ I_e \Delta \ddot{\delta}_p \cos \delta_{p0} \end{bmatrix} \quad (\text{A.82})$$

Directly from equation A.82 the pitch plane TWD perturbation force equations are,

$$\Delta F_{ex} = -m_e I_e \Delta \ddot{\delta}_p \sin \delta_{p0} \quad (\text{A.83})$$

$$\Delta F_{ez} = -m_e I_e \Delta \ddot{\delta}_p \cos \delta_{p0} \quad (\text{A.84})$$

Returning to the reaction moment at the engine gimbal, the engine inertia matrix and angular acceleration are define as,

$$I_e = \begin{bmatrix} I_{xxe} & 0 & 0 \\ 0 & I_{yye} & 0 \\ 0 & 0 & I_{zze} \end{bmatrix} \quad (\text{A.85})$$

$$\alpha_e = \begin{bmatrix} 0 \\ \Delta \ddot{\delta}_p \\ 0 \end{bmatrix} \quad (\text{A.86})$$

The reaction forces at the pivot will also create moments about the vehicle CG.

$$\Delta \mathbf{M} = \mathbf{I}_p \times \Delta \mathbf{F}_e = (I_{pz} \Delta F_{ex} - I_{px} \Delta F_{ez}) \hat{\mathbf{j}} \quad (\text{A.87})$$

Therefore, the total pitch moment due to TWD is the sum of the reaction moment at the pivot and the moment generated by the reaction forces. The result is a moment equation for perturbations caused by engine rotation, equation A.88.

$$\Delta M_{ey} = \{m_e I_e (I_{px} \cos \delta_{po} - I_{pz} \sin \delta_{po}) - I_{yye}\} \Delta \ddot{\delta}_p \quad (\text{A.88})$$

Because the Tail-Wags-Dog effect is dependent on the motion of the engines, there are obviously no steady-state contributions from TWD forces and moments.

A.4.4 Aerodynamics

From the previous Taylor series expansion, the aerodynamic forces and moments are represented by,

$$\Delta F_{ax} = \frac{\partial F_x}{\partial u} \Delta u + \frac{\partial F_x}{\partial \dot{u}} \Delta \dot{u} + \frac{\partial F_x}{\partial w} \Delta w + \frac{\partial F_x}{\partial \dot{w}} \Delta \dot{w} + \frac{\partial F_x}{\partial \dot{\theta}} \Delta \dot{\theta} \quad (\text{A.89})$$

$$\Delta F_{az} = \frac{\partial F_z}{\partial u} \Delta u + \frac{\partial F_z}{\partial \dot{u}} \Delta \dot{u} + \frac{\partial F_z}{\partial w} \Delta w + \frac{\partial F_z}{\partial \dot{w}} \Delta \dot{w} + \frac{\partial F_z}{\partial \dot{\theta}} \Delta \dot{\theta} \quad (\text{A.90})$$

$$\Delta M_{ay} = \frac{\partial M_y}{\partial u} \Delta u + \frac{\partial M_y}{\partial \dot{u}} \Delta \dot{u} + \frac{\partial M_y}{\partial w} \Delta w + \frac{\partial M_y}{\partial \dot{w}} \Delta \dot{w} + \frac{\partial M_y}{\partial \dot{\theta}} \Delta \dot{\theta} \quad (\text{A.91})$$

The stability coefficients are based on “quasi steady flow,” which assumes the airflow around the vehicle changes instantaneously when the vehicle is disturbed from equilibrium. To simplify expressions A.89 through A.91, several further assumptions can be made. First, the partial derivatives with respect to perturbations in axial acceleration can be ignored due to their relative insignificance when compared to the large steady-state acceleration. Second, empirical data has shown that the change in pitch rate effect on axial force is negligible. Finally, the remaining derivatives with respect to axial acceleration perturbations are important only in a small regime of the flight profile, and can be neglected for this level of detail. The resulting series is then

$$\Delta F_{ax} = \frac{\partial F_x}{\partial u} \Delta u + \frac{\partial F_x}{\partial w} \Delta w \quad (A.92)$$

$$\Delta F_{az} = \frac{\partial F_z}{\partial u} \Delta u + \frac{\partial F_z}{\partial w} \Delta w + \frac{\partial F_z}{\partial \dot{\theta}} \Delta \dot{\theta} \quad (A.93)$$

$$\Delta M_{ay} = \frac{\partial M_y}{\partial u} \Delta u + \frac{\partial M_y}{\partial w} \Delta w + \frac{\partial M_y}{\partial \dot{\theta}} \Delta \dot{\theta} \quad (A.94)$$

Several aerodynamic references were used to find the form of the dynamic derivatives that would be compatible with aerodynamic derivative coefficient data provided by Kistler Aerospace [5, 6]. The form of the u-derivatives are,

$$\frac{\partial F_x}{\partial u} = 2 \frac{(C_{xu} + C_{xo})Sq}{U_o} \quad (A.95)$$

$$\frac{\partial F_z}{\partial u} = 2 \frac{(C_{zu} + C_{zo})Sq}{U_o} \quad (A.96)$$

$$\frac{\partial M_y}{\partial u} = 2SqL_{cp} C_{mu} \quad (A.97)$$

The w-derivatives were replaced with α -derivatives to allow for high angle of attack flight, which is not permitted when using the small angle assumptions involved in deriving the w-derivatives. This was important because the K1 Launch Assist Platform (LAP) does experience high angles of attack during its return flight phase. The α -derivatives are,

$$\Delta F_x = SqC_{x\alpha} \Delta \alpha \quad (A.98)$$

$$\Delta F_z = SqC_{z\alpha} \Delta \alpha \quad (A.99)$$

$$\Delta M_y = SqL_{cp} C_{m\alpha} \Delta \alpha \quad (A.100)$$

The q-derivatives, or pitch rate derivatives, are,

$$\partial F_z = \frac{SqL_{cp}C_{zq}}{2U_o} \Delta q \quad (A.101)$$

$$\partial M_y = \frac{SqL_{cp}^2 C_{mq}}{2U_o} \Delta q \quad (A.102)$$

By summing together the corresponding effects of equations A.95 through A.102, the EOMs for perturbations due to aerodynamic forces are,

$$\Delta F_{ax} = 2 \frac{Sq(C_{xu} + C_{xo})}{U_o} \Delta u + SqC_{x\alpha} \Delta \alpha \quad (A.103)$$

$$\Delta F_{az} = 2 \frac{Sq(C_{zu} + C_{zo})}{U_o} \Delta u + SqC_{z\alpha} \Delta \alpha + \frac{SqL_{cp}C_{zq}}{2U_o} \Delta q \quad (A.104)$$

$$\Delta M_{ay} = 2SqL_{cp}C_{mu} \Delta u + SqL_{cp}C_{m\alpha} \Delta \alpha + \frac{SqL_{cp}^2 C_{mq}}{2U_o} \Delta q \quad (A.105)$$

The bias equations for aerodynamics are given as,

$$F_{ax_o} = SqC_{x_o} \quad (A.106)$$

$$F_{az_o} = SqC_{z_o} \quad (A.107)$$

$$M_{ay_o} = SqL_{cp}C_{m_o} \quad (A.108)$$

In theory, L_{cp} is the distance from the body CG to the center of pressure (CP). However, it is common practice to use a standard reference length which is associated to experimental coefficient data. This practice is preferred, as the CP location is derived from experimentation and can be highly inaccurate at small angles of attack.

Yet, this is not complete. An angle of attack state equation is necessary to fully characterize the vehicle's motion. Figure A.5 shows the general setup for developing an α state equation, in which three different axes systems are used.

The inertial, velocity, and body frames are all aligned in the y-direction, and the pitch angle is the sum of the angle of attack and the flight path angle,

$$\gamma = \theta - \alpha \quad (\text{A.109})$$

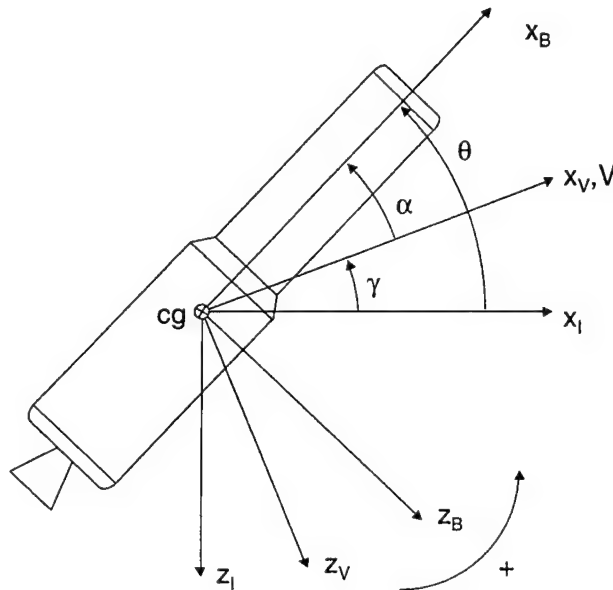


Figure A.5 – Angle of Attack Definition

The acceleration of the vehicle CG is easily expressed in the velocity frame in its tangential and radial velocity components.

$$\mathbf{a}_v = \begin{bmatrix} \dot{V} \\ 0 \\ -V\dot{\gamma} \end{bmatrix} \quad (\text{A.110})$$

Using equation A.111, the vehicle acceleration can be translated into body frame coordinates with the rotation matrix, M , defined in equation A.112.

$$\mathbf{a}_B = M \cdot \mathbf{a}_v \quad (\text{A.111})$$

$$M = \begin{bmatrix} \cos \alpha & 0 & -\sin \alpha \\ 0 & 1 & 0 \\ \sin \alpha & 0 & \cos \alpha \end{bmatrix} \quad (A.112)$$

The resulting acceleration expression is

$$a_B = \begin{bmatrix} \dot{V} \cos \alpha + V \dot{\gamma} \sin \alpha \\ 0 \\ \dot{V} \sin \alpha - V \dot{\gamma} \cos \alpha \end{bmatrix} \quad (A.113)$$

Two assumptions lead to the angle of attack state equation. First, the velocity of the vehicle is constant in short period mode analysis. Thus,

$$\dot{V} = 0 \quad (A.114)$$

Second, the steady-state flight path angle rate is another slow dynamic in comparison others, and it is neglected. By performing the standard process of separating the bias terms, applying trigonometric identities, and removing higher order perturbations, the resulting acceleration in the body z-direction is

$$\Delta a_{B_z} = -V \Delta q \cos \alpha_o + V \Delta \dot{\alpha} \cos \alpha_o \quad (A.115)$$

By equating equation A.115 to the general z-force EOM, the final form of the angle of attack state equation is completed.

$$V \cos \alpha_o \Delta \dot{\alpha} = \Delta \dot{w} - Q_o \Delta u - (U_o - V \cos \alpha_o) \Delta q \quad (A.116)$$

The value of the velocity, V , in equation A.116 can be calculated by rotating the original velocity vector from the body frame to the velocity frame using equation A.118.

$$V_v = \begin{bmatrix} V \\ 0 \\ 0 \end{bmatrix}_v \quad (A.117)$$

$$V_v = M^{-1} \cdot V \quad (A.118)$$

The resulting expression for vehicle velocity in body frame coordinates is,

$$V = U_o \cos \alpha_o + W_o \sin \alpha_o \quad (\text{A.119})$$

A.4.5 Fuel Sloshing

The sloshing of fuel within propellant tanks will be modeled as a spring-mass-damper system located a distance, l_s , from the vehicle CG. Similar to l_p , the vector l_s defines the slosh mass location with respect to the vehicle CG. The motion of the slosh mass is restricted to the y-z plane in the body coordinate system. Figure A.6 depicts the fuel sloshing problem formulation. To aid in lateral and longitudinal decoupling, the slosh mass is further restricted to motion in only the body z-direction. The steady-state position is assumed to be along the center line of the vehicle (body x-axis).

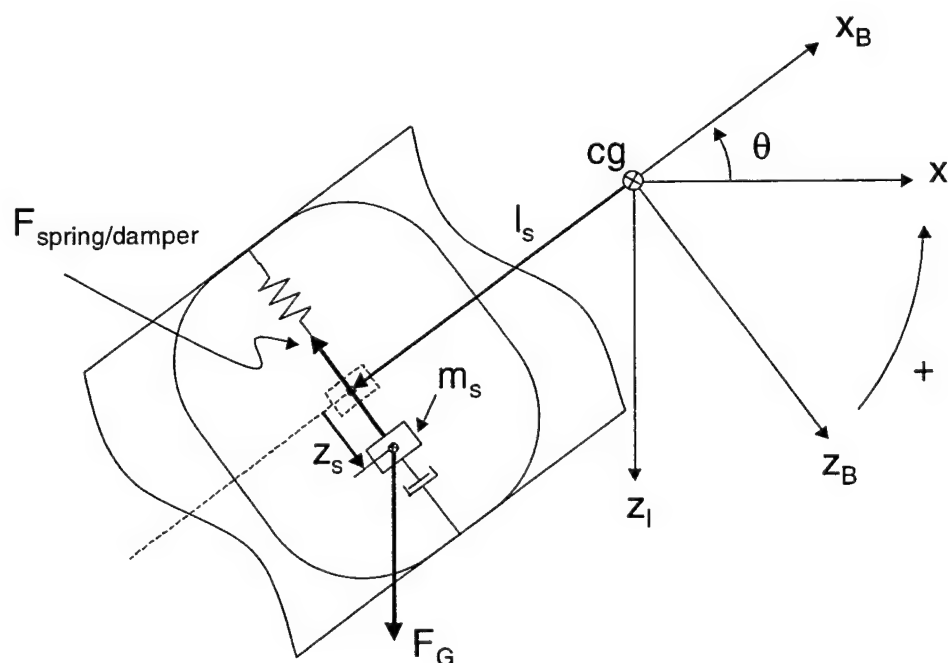


Figure A.6 – Slosh Free-Body Diagram

Using the chain rule, A.120 describes the acceleration of the slosh mass with respect to the vehicle body in body coordinates.

$$\mathbf{A}_s = \mathbf{a}_B + \mathbf{a}_{s/B} + 2(\boldsymbol{\omega} \times \mathbf{v}_{s/B}) + \boldsymbol{\omega} \times (\boldsymbol{\omega} \times \mathbf{l}_s) + \dot{\boldsymbol{\omega}} \times \mathbf{l}_s \quad (\text{A.120})$$

Expanding equation A.120 into vectors and reducing the expression results in

$$\mathbf{A}_s = \begin{bmatrix} \dot{U} + QW - VR + 2QW_s - 2RV_s + Q(\dot{P}l_{sy} - \dot{Q}l_{sx}) \\ -R(Rl_{sx} - Pl_{sz}) + \dot{Q}l_{sz} - \dot{R}l_{sy} \\ \dot{V} + UR - WP + a_{sy} - 2PW_s + R(\dot{P}l_{sz} - \dot{R}l_{sy}) \\ -P(\dot{P}l_{sy} - \dot{Q}l_{sx}) + \dot{R}l_{sx} - \dot{P}l_{sz} \\ \dot{W} - QV + VP + a_{sz} + 2PV_s + P(Rl_{sx} - Pl_{sz}) \\ -Q(\dot{Q}l_{sz} - \dot{R}l_{sy}) + \dot{P}l_{sy} - \dot{Q}l_{sx} \end{bmatrix} \quad (\text{A.121})$$

In the body x-direction, the force of the body on the slosh mass is equal to the x-direction force of the slosh mass minus the force of gravity on the slosh mass in the x-direction.

$$\mathbf{F}_{x \text{ Body on Slosh}} = m_s \mathbf{A}_{s_x} - \mathbf{F}_{x \text{ gravity}} \quad (\text{A.122})$$

Because the x-direction force on the slosh by the vehicle is equal and opposite to the force on the vehicle by the slosh mass, the x-direction slosh force is

$$\mathbf{F}_{sx} = \mathbf{F}_{x \text{ gravity}} - m_s \mathbf{A}_{s_x} \quad (\text{A.123})$$

The steady-state and slosh model conditions are

$$V_o = P_o = R_o = \dot{P}_o = \dot{Q}_o = \dot{R}_o = 0 \quad (\text{A.124})$$

$$\phi_o = 0 \quad (\text{A.125})$$

$$W_{so} = V_{so} = 0 \quad (\text{A.126})$$

$$X_s = 0 \quad (\text{A.127})$$

$$l_{sy} = 0 \quad (\text{A.128})$$

$$Y_s = 0 \quad (A.129)$$

Expanding into bias and perturbation terms, applying trigonometric identities, and eliminating the products of perturbation terms produce the bias and perturbation equations for x-direction slosh force.

$$F_{sx_o} = -m_s [\dot{U}_o + Q_o W_o - Q_o^2 I_{sx} + g_o \sin \theta_o] \quad (A.130)$$

$$\Delta F_{sx} = -m_s \left[\begin{array}{l} \Delta \dot{u} + Q_o \Delta w + I_{sz} \Delta \dot{q} + (W_o - 2Q_o I_{sx}) \Delta q \\ + g_o \cos \theta_o \Delta \theta + 2Q_o \dot{Z}_s \end{array} \right] \quad (A.131)$$

Returning to Figure A.6 to develop the slosh state equation, analysis of the forces acting on the slosh mass yields

$$m_s A_{sz} = F_{z \text{ gravity}} - F_{z \text{ spring}} - F_{z \text{ damp}} \quad (A.132)$$

Substituting equation A.121 into equation A.132 and applying the same process that produced the x-direction force EOMs, result in the bias equation A.133 and the perturbation equation A.134 for the slosh state equation.

$$0 = m_s [\dot{W}_o - Q_o U_o - Q_o^2 I_{sz} - g_o \cos \theta_o] + F_{z_o \text{ spring}} + F_{z_o \text{ damp}} \quad (A.133)$$

$$0 = m_s \left[\begin{array}{l} -Q_o \Delta u + \Delta \dot{w} - \Delta \dot{q} I_{sx} - (U_o + 2Q_o I_{sz}) \Delta q \\ + g_o \sin \theta_o \Delta \theta + \ddot{Z}_s - Q_o^2 Z_s \end{array} \right] + \Delta F_{z \text{ spring}} + \Delta F_{z \text{ damp}} \quad (A.134)$$

The standard form for the forces due to a spring and a damper apply.

$$\Delta F_{z \text{ spring}} = m_s \omega_s^2 Z_s \quad (A.135)$$

$$\Delta F_{z \text{ damp}} = 2m_s \omega_s \zeta_s \dot{Z}_s \quad (A.136)$$

The slosh force in the body z-direction, from Figure A.6, is

$$F_{z \text{ Slosh on Body}} = F_{z \text{ spring}} + F_{z \text{ damp}} \quad (A.137)$$

To eliminate the redundancy in explaining the same process used to derive the x-direction force equations, the resulting bias and perturbation equations for the slosh force in the body z-direction are

$$F_{sz_o} = m_s (\omega_s^2 I_{sz} + 2\zeta_s \omega_s W_{s_o}) \quad (A.138)$$

$$\Delta F_{sz} = m_s \omega_s^2 Z_s + 2m_s \zeta_s \omega_s \dot{Z}_s \quad (A.139)$$

The moment the slosh imparts on the vehicle is determined by the moment arm, I_s , from the CG and the slosh forces on the launch vehicle.

$$M_s = I_s x F_s \quad (A.140)$$

The pitch moment due to slosh can be found by applying the x and z-direction force equations to equation A.140 and gives,

$$M_{sy} = (I_{sz} + Z_s)(F_{sx_o} + \Delta F_{sx}) - (I_{sx} + X_s)(F_{sz_o} + \Delta F_{sz}) \quad (A.141)$$

Separating the steady-state terms and neglecting higher order perturbations yields,

$$M_{sy_o} = I_{sz} F_{sx_o} - I_{sx} F_{sz_o} \quad (A.142)$$

$$\Delta M_{sy} = I_{zs} \Delta F_{sx} + Z_s F_{sx_o} - I_{sx} \Delta F_{sz} \quad (A.143)$$

Substituting equations A.130, A.131, and A.139 results in the slosh bias and perturbation moment equations:

$$M_{sy_o} = -I_{sz} m_s (\dot{U}_o + Q_o W_o - Q_o^2 I_{sx} + g_o \sin \theta_o) - I_{sx} m_s (\omega_s^2 I_{sz} + 2\zeta_s \omega_s W_{s_o}) \quad (A.144)$$

$$\Delta M_{sy} = -I_{sz} m_s \left[\Delta \dot{u} + Q_o \Delta w + I_{sz} \Delta \dot{q} + (w_o - 2Q_o I_{sx}) \Delta q \right] + g_o \cos \theta_o \Delta \theta + 2Q_o \dot{Z}_s - Z_s m_s (\dot{U}_o + Q_o W_o - Q_o^2 I_{sx} + g_o \sin \theta_o) - I_{sx} m_s (\omega_s^2 Z_s + 2\zeta_s \omega_s \dot{Z}_s) \quad (A.145)$$

Equations A.146, A.147, A.148, and A.149 summarize the force, moment, and state expressions for perturbations due to fuel sloshing.

$$\Delta F_{sx} = -m_s \left[\begin{array}{l} \Delta \dot{u} + Q_o \Delta w + I_{sz} \Delta \dot{q} + (W_o - 2Q_o I_{sx}) \Delta q \\ + g_o \cos \theta_o \Delta \theta + 2Q_o \dot{Z}_s \end{array} \right] \quad (A.146)$$

$$\Delta F_{sz} = m_s (\omega_s^2 Z_s + 2\zeta_s \omega_s \dot{Z}_s) \quad (A.147)$$

$$\Delta M_{sy} = -m_s \left[\begin{array}{l} I_{sz} \Delta \dot{u} + Q_o I_{sz} \Delta w + I_{sz}^2 \Delta \dot{q} + (W_o - 2Q_o I_{sx}) I_{sz} \Delta q \\ + g_o I_{sz} \cos \theta_o \Delta \theta + 2(I_{zx} \omega_s \zeta_s + Q_o I_{sz}) \dot{Z}_s \\ + (\dot{U}_o + Q_o W_o + g_o \sin \theta_o + (\omega_s^2 - Q_o^2)_{sx}) Z_s \end{array} \right] \quad (A.148)$$

$$\begin{aligned} \ddot{Z}_s = & Q_o \Delta u - \Delta \dot{w} + I_{sx} \Delta \dot{q} + (U_o + 2Q_o I_{sz}) \Delta q - g_o \sin \theta_o \Delta \theta \\ & - 2\omega_s \zeta_s \dot{Z}_s - (\omega_s^2 - Q_o^2) Z_s \end{aligned} \quad (A.149)$$

A.4.6 Accelerometer/Gyroscope

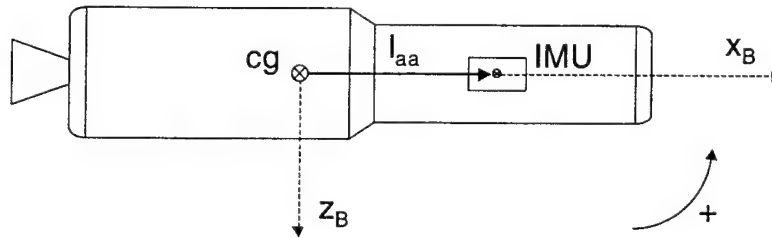


Figure A.7 – IMU Reference Diagram

The acceleration sensed by an accelerometer at the body CG is

$$a_{cg_{aa}} = A_{cg} - g_o \quad (A.150)$$

Neglecting all but the normal acceleration component of equation A.150 yields,

$$a_{cg_{aaz}} = \dot{W} - QV - g_o \cos \theta \cos \phi \quad (A.151)$$

The acceleration sensed by an accelerometer located a distance, l_{aa} , from the vehicle CG is

$$a_{aa} = a_{cg_{aa}} + \omega \times (\omega \times l_{aa}) + \dot{\omega} \times l_{aa} \quad (A.152)$$

Again, the x and y components of acceleration are neglected after equation A.152 has been reduced, which results in the following z-direction acceleration sensed at the Inertial Measurement Unit (IMU) location.

$$a_{aaz} = \dot{W} - QU - g_o \cos \theta \cos \phi + P(Rl_{aax} - Pl_{aaz}) - Q(Ql_{aaz} - Rl_{aay}) + \dot{P}l_{aay} - \dot{Q}l_{aax} \quad (A.153)$$

By applying the steady-state conditions and pitch plane decoupling assumptions summarized in equations A.154 and A.155, and performing the typical reduction process of separating the bias and perturbation terms and neglecting higher order

$$V_o = P_o = R_o = \dot{P}_o = \dot{Q}_o = \dot{R}_o = \phi_o = 0 \quad (A.154)$$

$$\Delta p = \Delta \dot{p} = \Delta r = \Delta \dot{r} = \Delta \phi = 0 \quad (A.155)$$

perturbation terms, the steady-state and perturbation body z-direction accelerometer expressions are

$$a_{aaz_o} = \dot{W}_o - Q_o U_o - Q_o^2 l_{aaz} - g_o \cos \theta_o \quad (A.156)$$

$$\Delta a_{aaz} = -Q_o \Delta u + \Delta \dot{W} - l_{aax} \Delta \dot{q} - (U_o + 2Q_o l_{aaz}) \Delta q + g_o \sin \theta_o \Delta \theta \quad (A.157)$$

There are no additional gyroscope dynamics due to the effects analyzed here. Therefore, the gyroscope equation simply remains

$$\Delta q = \Delta q_{sensed} \quad (A.158)$$

A.4.7 Pitch Plane EOM Summary for Inelastic Launch Vehicle

Equations A.159 through A.164 summarize the total perturbation dynamics of an inelastic launch vehicle. Formed by combining the individual

effects of gravity, thrust, TWD, aerodynamics, and slosh and equating the corresponding elements with the general form of the perturbation equations A.159, A.160, and A.161 are the x-direction and z-direction force and pitch moment expressions, respectively.

$$\Sigma \Delta F_x$$

$$\begin{aligned} m[\Delta \dot{u} + W_o \Delta q + \Delta w Q_o] = & -mg_o \cos \theta_o \Delta \theta - \sum_{i=1}^{\#eng} T_i \sin \delta_{po_i} \Delta \delta_{p_i} \\ & - \sum_{i=1}^{\#eng} m_{e_i} I_{e_i} \sin \delta_{po_i} \Delta \ddot{\delta}_{p_i} \\ & + \frac{2Sq}{U_o} (C_{xu} + C_{xo}) \Delta u + Sq C_{x\alpha} \Delta \alpha + \frac{Sq L_{cp} C_{xq}}{2U_o} \Delta q \\ & - \sum_{j=1}^{\#slosh} m_{s_j} \left[\Delta \dot{u} + Q_o \Delta w + I_{sz} \Delta \dot{q} + (W_o - 2Q_o I_{sx}) \Delta q \right. \\ & \left. + g_o \cos \theta_o \Delta \theta + 2Q_o \dot{Z}_{s_j} \right] \end{aligned} \quad (A.159)$$

$$\Sigma \Delta F_z$$

$$\begin{aligned} m[\Delta \dot{w} - U_o \Delta q - \Delta u Q_o] = & -mg_o \sin \theta_o \Delta \theta - \sum_{i=1}^{\#eng} T_i \cos \delta_{po_i} \Delta \delta_{p_i} \\ & - \sum_{i=1}^{\#eng} m_{e_i} I_{e_i} \cos \delta_{po_i} \Delta \ddot{\delta}_{p_i} \\ & + \frac{2Sq}{U_o} (C_{zu} + C_{zo}) \Delta u + Sq C_{z\alpha} \Delta \alpha + \frac{Sq L_{cp} C_{zq}}{2U_o} \Delta q \\ & + \sum_{j=1}^{\#slosh} m_{s_j} \left[\omega_{s_j}^2 Z_{s_j} + 2\zeta_{s_j} \omega_{s_j} \dot{Z}_{s_j} \right] \end{aligned} \quad (A.160)$$

$$\begin{aligned}
& \Sigma \Delta M_y \\
& \Delta \dot{q} I_{yy} = \sum_{i=1}^{\#eng} T_i [I_{px_i} \cos \delta_{po_i} - I_{pz_i} \sin \delta_{po_i}] \Delta \delta_{p_i} \\
& + \sum_{i=1}^{\#eng} [m_{e_i} I_{e_i} (I_{px_i} \cos \delta_{po_i} - I_{pz_i} \sin \delta_{po_i}) - I_{yy e_i}] \Delta \ddot{\delta}_{p_i} \\
& + \frac{2 S q L_{cp} C_{mu}}{U_o} \Delta u + S q L_{cp} C_{m\alpha} \Delta \alpha + \frac{S q L_{cp}^2 C_{mq}}{2 U_o} \Delta q \\
& - \sum_{j=1}^{\#slosh} m_{s_j} \left[\begin{aligned} & I_{sz_j} \Delta \dot{u} + Q_o I_{sz_j} \Delta w + I_{sz_j}^2 \Delta \dot{q} + (W_o - 2 Q_o I_{sx_j})_{sz_j} \Delta q \\ & + g_o I_{sz_j} \cos \theta_o \Delta \theta + 2 (I_{sx_j} \omega_{s_j} \zeta_{s_j} + Q_o I_{sz_j}) \dot{z}_{s_j} \\ & + (\dot{U}_o + Q_o W_o + g_o \sin \theta_o + (\omega_{s_j}^2 - Q_o^2) I_{sx_j}) z_{s_j} \end{aligned} \right]
\end{aligned} \tag{A.161}$$

Equations A.162 and A.163 are the two state equations, slosh and angle of attack, necessary to this set of pitch plane EOMs.

$$\begin{aligned}
\ddot{z}_s = & Q_o \Delta u - \Delta \dot{w} + I_{sx} \Delta \dot{q} + (U_o + 2 Q_o I_{sz}) \Delta q - g_o \sin \theta_o \Delta \theta \\
& - 2 \omega_s \zeta_s \dot{z}_s + (\omega_s^2 - Q_o^2) z_s
\end{aligned} \tag{A.162}$$

$$\Delta \dot{w} - V \Delta \dot{\alpha} \cos \alpha_o = Q_o \Delta u + (U_o - V \cos \alpha_o) \Delta q \tag{A.163}$$

The output equation, equation A.164, defines additional dynamics that arise from the rotation of the IMU about the CG.

$$\Delta a_{aaz} = -Q_o \Delta u + \Delta \dot{w} - I_{aax} \Delta \dot{q} - (U_o + 2 Q_o I_{aaz}) \Delta q + g_o \sin \theta_o \Delta \theta \tag{A.164}$$

A.4.8 Body Bending (Flex)

Body flexure affects the vehicle state equations in various ways. Engine bell translation and rotation due to flex affects the x-direction force, z-direction force, and the pitch moment. Body bending influences the slosh mass displacement. Also, translation of the body-fixed accelerometer affects the normal acceleration equation. Finally, the rotation of the body-fixed gyroscopes changes the measured pitch and pitch rate feedback signals.

To model body flexure , each location of interest along the body is represented by a second order spring-mass-damper system for each mode considered. Therefore, the standard equation for the j^{th} mode is,

$$m_j [\ddot{q}_j + 2\zeta_j \omega_j \dot{q}_j + \omega_j^2 q_j] = \Phi_j^T F \quad (\text{A.165})$$

The matrix of rotational and translational flex parameters for each node in the body is defined by equation A.166. The force vector associated with equation A.165 is defined by equation A.167.

$$\Phi_j^T = \begin{bmatrix} \phi_x & & \phi_x \\ \phi_y & & \phi_y \\ \phi_z & \dots & \phi_z \\ \sigma_x & & \sigma_x \\ \sigma_y & & \sigma_y \\ \underbrace{\sigma_z}_{\text{Node 1}} & & \underbrace{\sigma_z}_{\text{Node N}} \end{bmatrix}_j \quad (\text{A.166})$$

$$F^T = \begin{bmatrix} F_x & & F_x \\ F_y & & F_y \\ F_z & \dots & F_z \\ M_x & & M_x \\ M_y & & M_y \\ \underbrace{M_z}_{\text{Node 1}} & & \underbrace{M_z}_{\text{Node N}} \end{bmatrix} \quad (\text{A.167})$$

When expanded, equation A.165 will generate a state equation for each desired flex mode. However, the forces that comprise equation A.167 must be updated from those summarized in equations A.159 through A.164 to include the effects of body bending.

Thrust Flex Effects

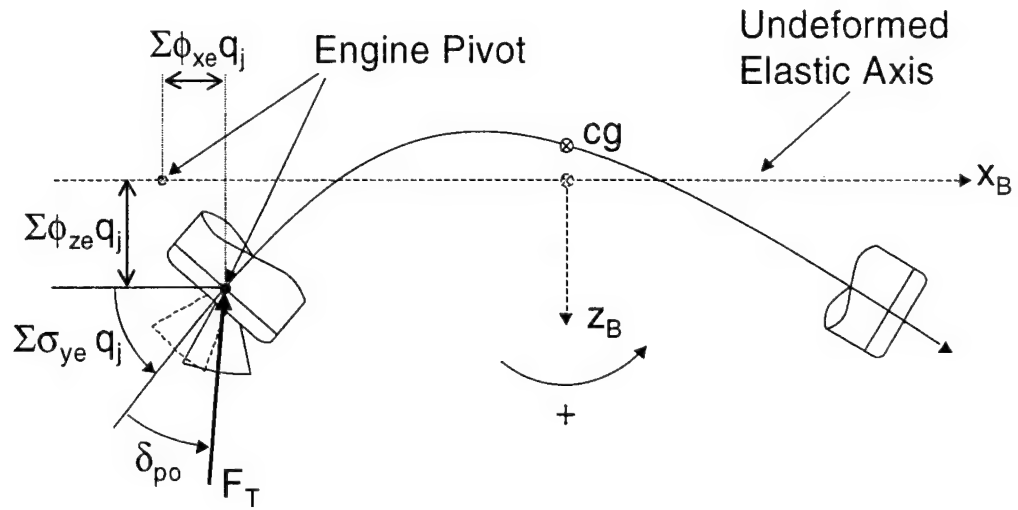


Figure A.8 – Body Bending Effects on Engine Gimbal

As stated before, the effect of flex is realized as additional translation and rotation of points, or nodes, along the body axis. Figure A.8 shows the effect of body bending on the engine gimbal node. The translation and rotation of the gimbal causes additions to the engine rotation angle, equation A.168, body x-direction translation, equation A.169, and body z-direction translation, equation A.170.

$$\delta_{\rho_{TOT}} = \delta_{\rho} + \sum_{j=1}^{\# \text{ flex modes}} \sigma_{ye} q_j \quad (\text{A.168})$$

$$l_{px_{TOT}} = l_{px} + \sum_{j=1}^{\# \text{ flex modes}} \phi_{xe} q_j \quad (\text{A.169})$$

$$l_{pz_{TOT}} = l_{pz} + \sum_{j=1}^{\# \text{ flex modes}} \phi_{ze} q_j \quad (\text{A.170})$$

The only impact of flex on the forces in the x-axis and z-axis directions is additional rotation. This gives the new x and z force perturbation EOM's due to thrust,

$$\Delta F_{TX} = -T \sin \delta_{po} \left(\Delta \delta_p + \sum_{j=1}^{\# \text{ flex modes}} \sigma_{ye} q_j \right) \quad (\text{A.171})$$

$$\Delta F_{TZ} = -T \cos \delta_{po} \left(\Delta \delta_p + \sum_{j=1}^{\# \text{ flex modes}} \sigma_{ye} q_j \right) \quad (\text{A.172})$$

However, both rotation and translation affect the pitch moment equation due to thrust.

$$M_T + \Delta M_T = (r + \Delta r)x(F + \Delta F) \quad (\text{A.173})$$

Focusing on only the pitch moment equation, equation A.174, substitution and linearization yields the final form of the pitch moment due to thrust perturbations, equation A.175.

$$M_y + \Delta M_y = (z + \Delta z)(F_x + \Delta F_x) - (x + \Delta x)(F_z + \Delta F_z) \quad (\text{A.174})$$

$$\Delta M_{Ty} = T \left[\begin{array}{l} -I_{pz} \sin \delta_{po} (\Delta \delta_p + \sigma_{ye} q_j) + \cos \delta_{po} \sum_{j=1}^{\# \text{ flex modes}} \phi_{ze} q_j \\ + \sin \delta_{po} \sum_{j=1}^{\# \text{ flex modes}} \phi_{xe} q_j + I_{px} \cos \delta_{po} \left(\Delta \delta_p + \sum_{j=1}^{\# \text{ flex modes}} \sigma_{ye} q_j \right) \end{array} \right] \quad (\text{A.175})$$

Engine Motion Flex Effects

Analogous to the effects of flex on thrust perturbation dynamics, the impact on the TWD x and z force equations is an additional angular acceleration term.

$$\Delta F_{ex} = -m_e l_e \sin \delta_{po} \left(\Delta \ddot{\delta}_p + \sum_{j=1}^{\# \text{ flex modes}} \sigma_{ye} \ddot{q}_j \right) \quad (\text{A.176})$$

$$\Delta F_{ez} = -m_e l_e \cos \delta_{po} \left(\Delta \ddot{\delta}_p + \sum_{j=1}^{\# \text{ flex modes}} \sigma_{ye} \ddot{q}_j \right) \quad (\text{A.177})$$

Again, the moment depends on both rotation and translation due to flexure as shown by equation A.178. After substitution and elimination of higher order disturbances, equation A.179 expresses the pitch moment generated by the reaction forces at the engine gimbal.

$$M_{ey} = (r + \Delta r) \times \Delta F \quad (\text{A.178})$$

$$\begin{aligned} \Delta M_{ey} = & l_{px} m_e l_e \cos \delta_{po} \left(\Delta \ddot{\delta}_p + \sum_{j=1}^{\# \text{ flex modes}} \sigma_{ye} \ddot{q}_j \right) \\ & - l_{pz} m_e l_e \sin \delta_{po} \left(\Delta \ddot{\delta}_p + \sum_{j=1}^{\# \text{ flex modes}} \sigma_{ye} \ddot{q}_j \right) \end{aligned} \quad (\text{A.179})$$

The reaction moment also contributes to the total moment due to engine motion.

$$-I_{yye} \alpha_e = -I_{yye} \left(\Delta \ddot{\delta}_p + \sum_{j=1}^{\# \text{ flex modes}} \sigma_{ye} \ddot{q}_j \right) \quad (\text{A.180})$$

Adding equations A.179 and A.180 produces the total moment due to engine motion.

$$\Delta M_{ey} = (l_{px} m_e l_e \cos \delta_{po} - l_{pz} m_e l_e \sin \delta_{po} - I_{yye}) \left(\Delta \ddot{\delta}_p + \sum_{j=1}^{\# \text{ flex modes}} \sigma_{ye} \ddot{q}_j \right) \quad (\text{A.181})$$

Slosh Flex Effects

Slosh flex effects are caused by the translation of the propellant tank walls. As modeled, the translation of the walls acts to decrease the

compression of the spring and the tension on the damper when Z_s moves positively. To account for flex, only the slosh state equation needs modification. All other slosh force and moment equations are based on this equation, and changes to the slosh state equation will adjust the others as well. The new expressions for the forces due to the spring and damper are,

$$\Delta F_{z \text{ spring}} = -m_s \omega_s^2 \left(Z_s - \sum_{j=1}^{\# \text{ flex modes}} \phi_{zs} q_j \right) \quad (\text{A.182})$$

$$\Delta F_{z \text{ damp}} = -2m_s \omega_s \zeta_s \left(\dot{Z}_s - \sum_{j=1}^{\# \text{ flex modes}} \phi_{zs} \dot{q}_j \right) \quad (\text{A.183})$$

Substituting equations A.182 and A.183 into the original slosh state equation produces,

$$\begin{aligned} \ddot{Z}_s = & Q_o \Delta u - \Delta \dot{w} + I_{sx} \Delta \dot{q} + (U_o + 2Q_o I_{sz}) \Delta q - g_o \sin \theta_o \Delta \theta \\ & - 2\omega_s \zeta_s \left(\dot{Z}_s - \sum_{j=1}^{\# \text{ flex modes}} \phi_{zs} \dot{q}_j \right) + Q_o^2 Z_s - \omega_s^2 \left(Z_s - \sum_{j=1}^{\# \text{ flex modes}} \phi_{zs} q_j \right) \end{aligned} \quad (\text{A.184})$$

Sensor Flex Effects

The effect of flex on the normal acceleration equation is an additional translational acceleration term generated by the motion of the IMU due to body bending. Adding this term to the accelerometer equation yields the new form

$$\begin{aligned} \Delta a_{aaz} = & Q_o \Delta u - \Delta \dot{w} + I_{aax} \Delta \dot{q} + (U_o + 2Q_o I_{aaz}) \Delta q \\ & - g_o \sin \theta_o \Delta \theta - \sum_{j=1}^{\# \text{ flex modes}} \phi_{zaa} \ddot{q}_j \end{aligned} \quad (\text{A.185})$$

Also, the additional rotation of the IMU due to flexure necessitates an updated gyroscope output equation. The new form is

$$\Delta \dot{q}_{\text{actual}} = \Delta \dot{q}_{\text{sensed}} - \sum_{j=1}^{\# \text{ flex modes}} \sigma_{y \text{ gyros}} \ddot{q}_j \quad (\text{A.186})$$

Flex State Equation

Having updated all of the perturbation force and moment equations, the flex state equation can be developed. Slightly rewriting its earlier form, equation A.187 is expressed fully in the pitch plane EOM summary as equation A.195.

$$\ddot{q}_j = \Phi^T \frac{F}{m_j} - 2\zeta_j \omega_j \dot{q}_j - \omega_j^2 q_j \quad (\text{A.187})$$

A.5 Elastic Body Pitch Plane EOM Summary

Equations A.191 through A.195 are the state and output equations necessary to characterize launch vehicle pitch plane dynamics due to perturbations from nominal flight conditions. This set of continuous LTI equations incorporates the dynamic effects associated with rigid body motion, gravity, thrust, aerodynamic forces, engine motion, fuel sloshing, and body bending. These equations have also been updated to allow for the possibility of multiple engines, slosh masses, and flex modes, which are present in the K1 as well as a larger class of launch vehicles.

$$\begin{aligned}
m[\Delta\dot{u} + W_o\Delta q + \Delta w Q_o] = & -mg_o \cos \theta_o \Delta\theta \\
& - \sum_{i=1}^{\#eng} T_i \sin \delta_{po_i} \left(\Delta\delta_{p_i} + \sum_{j=1}^{\#flex \text{ modes}} \sigma_{ye} q_j \right) \\
& - \sum_{i=1}^{\#eng} m_{e_i} l_{e_i} \sin \delta_{po_i} \left(\Delta\ddot{\delta}_{p_i} + \sum_{j=1}^{\#flex \text{ modes}} \sigma_{ye} \ddot{q}_j \right) \\
& + 2 \frac{Sq}{U_o} (C_{xu} + C_{xo}) \Delta u + Sq C_{x\alpha} \Delta\alpha + \frac{Sq L_{cp} C_{xq}}{2U_o} \Delta q \\
& - \sum_{k=1}^{\#slosh \text{ mass}} m_{s_k} \left[\Delta\dot{u} + Q_o \Delta w + l_{sz_k} \Delta\dot{q} + (W_o - 2Q_o l_{sx_k}) \Delta q \right. \\
& \quad \left. + g_o \cos \theta_o \Delta\theta + 2Q_o \dot{Z}_{s_k} \right]
\end{aligned} \tag{A.188}$$

$$\begin{aligned}
m[\Delta\dot{U} + W_o\Delta q + \Delta w Q_o] = & -mg_o \sin \theta_o \Delta\theta - \sum_{i=1}^{\#eng} T_i \cos \delta_{p_i} (\Delta\delta_{p_i} + \sum_{j=1}^{\#flex \text{ modes}} \sigma_{ye} q_j) \\
& - \sum_{i=1}^{\#eng} m_{e_i} l_{e_i} \cos \delta_{p_i} (\Delta\ddot{\delta}_{p_i} + \sum_{j=1}^{\#flex \text{ modes}} \sigma_{ye} \ddot{q}_j) \\
& - 2 \frac{Sq}{U_o} (C_{zu} + C_{zo}) \Delta u + Sq C_{z\alpha} \Delta\alpha + \frac{Sq L_{cp} C_{zq}}{2U_o} \Delta q \\
& + \sum_{k=1}^{\#slosh \text{ mass}} m_{s_k} (\omega_{s_k}^2 Z_{s_k} + 2c_{s_k} \omega_{s_k} \dot{Z}_{s_k})
\end{aligned} \tag{A.189}$$

$$\begin{aligned}
\Delta\dot{q} l_{yy} = & \sum_{j=1}^{\#flex \text{ modes}} \sum_{i=1}^{\#eng} T_i \left[(l_{px_i} \cos \delta_{po_i} - l_{pz_i} \sin \delta_{po_i}) (\Delta\delta_{p_i} + \sigma_{ye} q_j) \right. \\
& \quad \left. + \phi_{xe} q_j \sin \delta_{po_i} + \phi_{ze} q_j \cos \delta_{po_i} \right] \\
& + \sum_{i=1}^{\#eng} (m_{e_i} l_{e_i} (l_{px_i} \cos \delta_{po_i} - l_{pz_i} \sin \delta_{po_i}) - l_{yye_i}) (\Delta\ddot{\delta}_{p_i} + \sum_{j=1}^{\#flex \text{ modes}} \sigma_{ye} \ddot{q}_j) \\
& + \frac{2Sq L_{cp} C_{mo}}{U_o} \Delta u + Sq L_{cp} C_{m\alpha} \Delta\alpha + \frac{Sq L_{cp}^2 C_{mq}}{2U_o} \Delta q \\
& - \sum_{k=1}^{\#slosh \text{ mass}} m_{s_k} \left[l_{sz_k} \Delta\dot{u} + Q_o l_{sz_k} \Delta w + l_{sz_k}^2 \Delta\dot{q} + (W_o - 2Q_o l_{sx_k}) l_{sz_k} \Delta q \right. \\
& \quad + g_o l_{sz_k} \cos \theta_o \Delta\theta + 2(l_{sx_k} \omega_{s_k} c_{s_k} + Q_o l_{sz_k}) \dot{Z}_{s_k} \\
& \quad \left. + (\dot{U}_o + Q_o W_o + g_o \sin \theta_o + (\omega_{s_k}^2 - Q_o^2) l_{sx_k}) Z_{s_k} \right]
\end{aligned} \tag{A.190}$$

$$\begin{aligned}\ddot{Z}_{s_k} = & Q_o \Delta u - \Delta \dot{w} + I_{s_k} \Delta \dot{q} + (U_o + 2Q_o I_{sz_k}) \Delta q - g_o \sin \theta_o \Delta \theta \\ & - 2\omega_{s_k} \zeta_{s_k} \left(\dot{Z}_{s_k} - \sum_{j=1}^{\# \text{ flex modes}} \phi_{zs_k} \dot{q}_j \right) + Q_o^2 Z_{s_k} - \omega_{s_k}^2 \left(Z_{s_k} - \sum_{j=1}^{\# \text{ flex modes}} \phi_{zs_k} q_j \right)\end{aligned}\quad (\text{A.191})$$

$$\begin{aligned}\Delta a_{aaz} = & Q_o \Delta u - \Delta \dot{w} + I_{aax} \Delta \dot{q} + (U_o + 2Q_o I_{aaz}) \Delta q \\ & - g_o \sin \theta_o \Delta \theta - \sum_{j=1}^{\# \text{ flex modes}} \phi_{zaa} \ddot{q}_j\end{aligned}\quad (\text{A.192})$$

$$\Delta \dot{q}_{\text{actual}} = \Delta \dot{q}_{\text{sensed}} - \sum_{j=1}^{\# \text{ flex modes}} \sigma_{\text{gyros}} \ddot{q}_j \quad (\text{A.193})$$

$$\Delta \dot{w} - V \Delta \dot{\alpha} \cos \alpha_o = Q_o \Delta u + (U_o - V \cos \alpha_o) \Delta q \quad (\text{A.194})$$

$$\begin{aligned}
\ddot{q}_m = & -2\zeta_m \omega_m \dot{q}_m - \omega_m^2 q_m \\
& - \sum_{k=1}^{\# \text{slosh mass}} \phi_{xs_{k,m}} \frac{m_{s_k}}{m_m} \left[\Delta \dot{u} + Q_o \Delta w + l_{sx_k} \Delta \dot{q} + (W_o - 2Q_o l_{sx_k}) \Delta q \right] \\
& + \sum_{k=1}^{\# \text{slosh mass}} \phi_{zs_{k,m}} \frac{m_{s_k}}{m_m} (2\zeta_{s_k} \omega_{s_k} \dot{Z}_{s_k} + \omega_{s_k}^2 Z_{s_k}) \\
& - \sum_{k=1}^{\# \text{slosh mass}} \sigma_{ys_{k,m}} \frac{m_{s_k}}{m_m} \left[l_{sz_k} \Delta \dot{u} + Q_o l_{sx_k} \Delta w + l_{sz_k}^2 \Delta \dot{q} + (W_o - 2Q_o l_{sx_k}) l_{sz_k} \Delta q \right. \\
& \quad \left. + g_o l_{sz_k} \cos \theta_o \Delta \theta + 2(l_{sx_k} \omega_{s_k} \zeta_{s_k} + Q_o l_{sz_k}) \dot{Z}_{s_k} \right. \\
& \quad \left. + (\dot{U}_o + Q_o W_o + g_o \sin \theta_o + (\omega_{s_k}^2 - Q_o^2) l_{sx_k}) Z_{s_k} \right] \\
& - \sum_{j=1}^{\# \text{flex modes}} \sum_{i=1}^{\# \text{eng}} \phi_{xe_{i,m}} \frac{T_i}{m_m} \sin \delta_{po_i} (\Delta \delta_{p_i} + \sigma_{ye_{i,j}} q_j) \\
& - \sum_{j=1}^{\# \text{flex modes}} \sum_{i=1}^{\# \text{eng}} \phi_{ze_{i,m}} \frac{T_i}{m_m} \cos \delta_{po_i} (\Delta \delta_{p_i} + \sigma_{ye_{i,j}} q_j) \\
& + \sum_{j=1}^{\# \text{flex modes}} \sum_{i=1}^{\# \text{eng}} \sigma_{ye_{i,m}} \frac{T_i}{m_m} \left[(l_{px_i} \cos \delta_{po_i} - l_{pz_i} \sin \delta_{po_i}) (\Delta \delta_{p_i} + \sigma_{ye_{i,j}} q_j) \right. \\
& \quad \left. + \phi_{xe_i} q_j \sin \delta_{po_i} + \phi_{ze_i} q_j \cos \delta_{po_i} \right] \\
& - \sum_{j=1}^{\# \text{flex modes}} \sum_{i=1}^{\# \text{eng}} \phi_{xe_{i,m}} \frac{m_{e_i}}{m_m} l_{e_i} \sin \delta_{po_i} (\Delta \ddot{\delta}_{p_i} + \sigma_{ye_{i,j}} \ddot{q}_j) \\
& - \sum_{j=1}^{\# \text{flex modes}} \sum_{i=1}^{\# \text{eng}} \phi_{ze_{i,m}} \frac{m_{e_i}}{m_m} l_{e_i} \cos \delta_{po_i} (\Delta \ddot{\delta}_{p_i} + \sigma_{ye_{i,j}} \ddot{q}_j) \\
& - \sum_{j=1}^{\# \text{flex modes}} \sum_{i=1}^{\# \text{eng}} \sigma_{ye_{i,m}} \frac{m_{e_i}}{m_m} (l_{yye_i} - m_{e_i} l_{e_i} (l_{px_i} \cos \delta_{po_i} - l_{pz_i} \sin \delta_{po_i})) (\Delta \ddot{\delta}_{p_i} + \sigma_{ye_{i,j}} \ddot{q}_j)
\end{aligned} \tag{A.195}$$

APPENDIX B

Nominal Trajectory Profiles

Based on simulation results from the UNIX simulation framework at Draper Laboratory and values presented on the nominal K1 trajectory [6], the following figures are provided as nominal profiles of individual K1 system parameters. This data was used for trim conditions in the pitch plane math model.

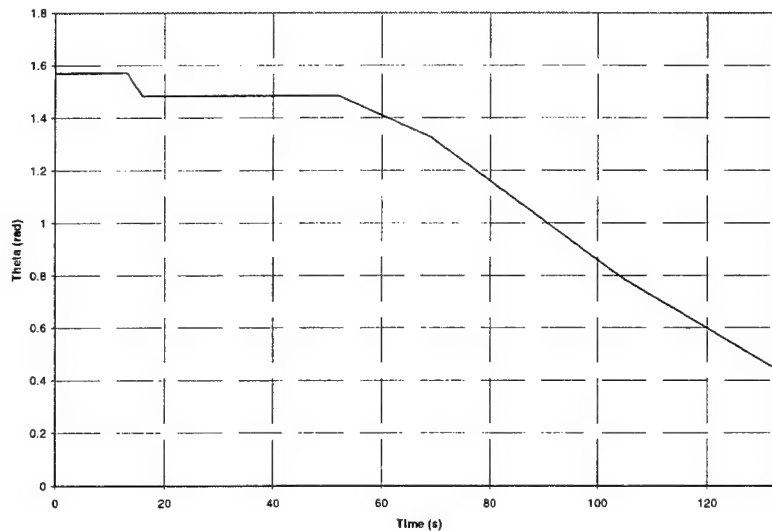


Figure B.1 -- Steady-State Pitch Angle Profile

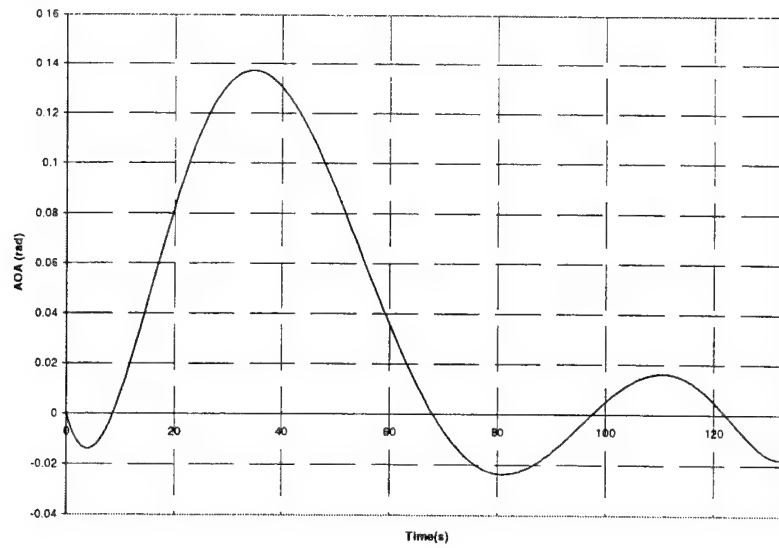


Figure B.2 – Steady-State Angle of Attack Profile

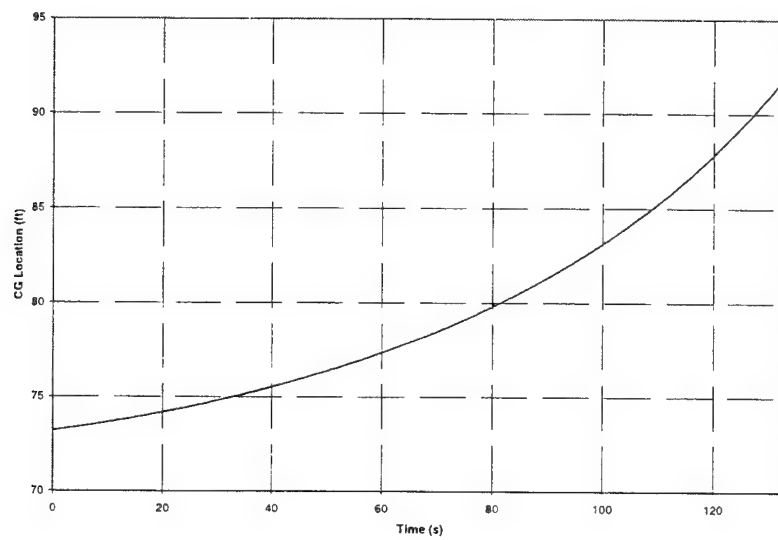


Figure B.3 – Steady-State Center of Gravity Location Profile

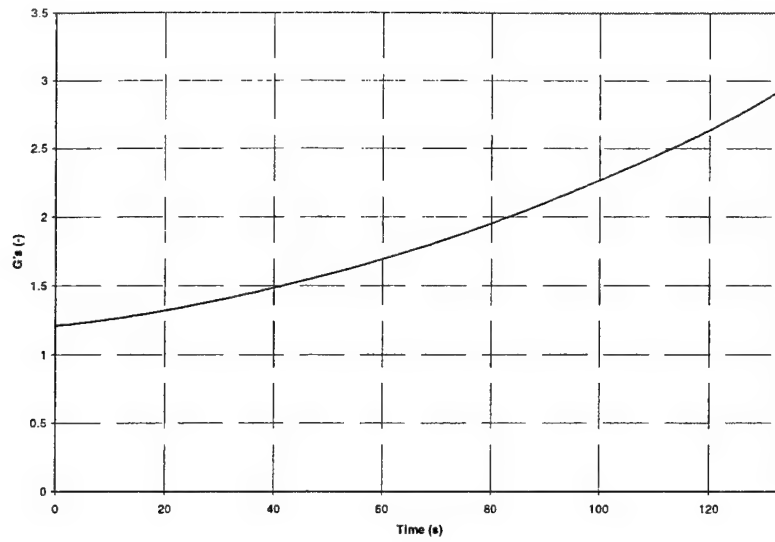


Figure B.4 – Steady-State Acceleration Profile

APPENDIX C

Model Verification

A systematic approach was taken to verify the MATLAB based launch vehicle model, which will be referred to as the system model. By analyzing each dynamic individually and comparing the model to similar reference models, each dynamic effect was verified. The results of this process are summarized here.

Several methods were employed in verifying the system model. Frequency responses based on the Mach 1.0 point ($t = 72$ seconds) utilize model values corresponding to this time. These Mach 1.0 parameters are summarized in Chapter 2. However, many times it is beneficial to look at the entire history of system poles and zeros when making model comparisons and evaluating dynamic effects. When a time history is shown, poles are represented by dark dots, and zeros by light dots, unless otherwise indicated. Arrows have also been added to show the direction of the pole/zero progression in time.

C.1 Rigid Body Response

The verification of the rigid body response in the presence of no other dynamics effects is trivial, considering the resulting double integrator system. Using a simple model presented by Corvin and defined by equations C.1 and C.2,

$$\frac{\theta}{\delta} = \frac{K_v}{s^2} \quad (C.1)$$

$$K_v = \frac{T \cdot I_{px}}{I_{yy}} \quad (C.2)$$

a comparison can be made [10]. Figure C.1 shows the response of both the simple model and the rigid body system model.

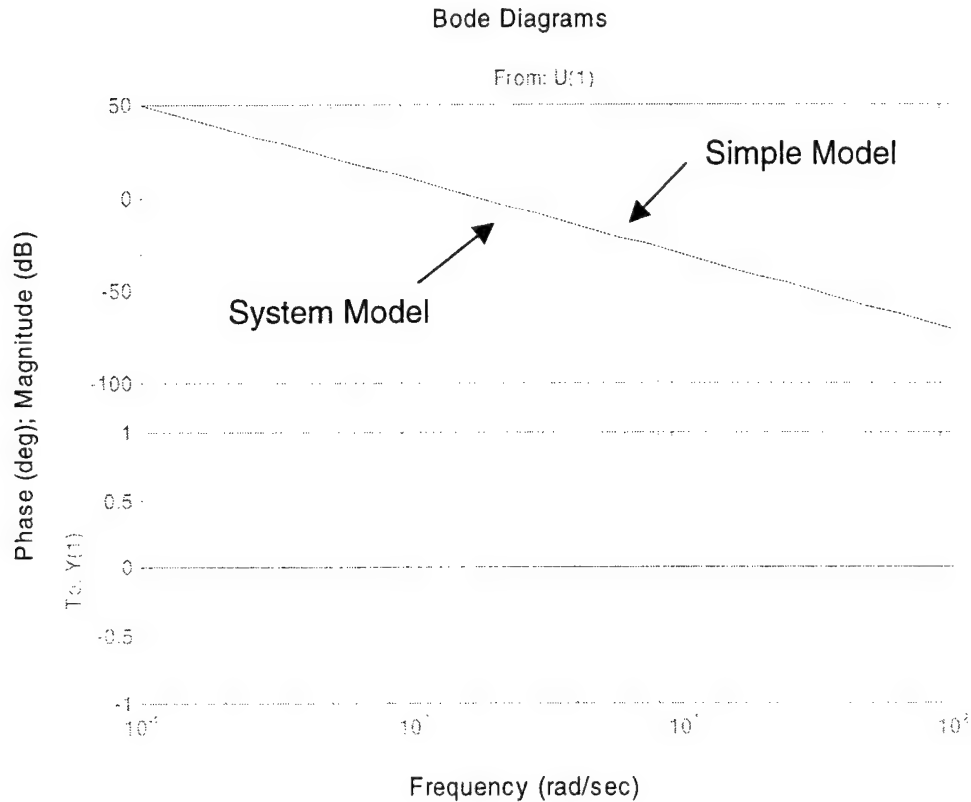


Figure C.1 – Rigid Body Response Comparison

The system responses are identical, which verifies the system model rigid body response.

C.2 Aerodynamic Response

There were several interesting aspects in confirming the modeled aerodynamic effects. First, a comparison of the system model response including only rigid body and aerodynamic effects was made using a simple aerodynamic reference model defined by equations C.2, C.3, and C.4, which was developed by Corvin as well [10].

$$\frac{\theta}{\delta} = \frac{K_v}{s^2 - \omega_v^2} \quad (C.3)$$

$$\omega_v = \sqrt{\frac{S \cdot \bar{q} \cdot L \cdot C_{m\alpha}}{I_{yy}}} \quad (C.4)$$

Figure C.2 shows a comparison of the two frequency responses. There is a noticeable difference in the gain and phase at extremely low frequencies. However, both models exhibit similar response characteristics in the mid to high frequency ranges. This is directly attributable to the introduction of angle-of-attack dynamics in the system model.

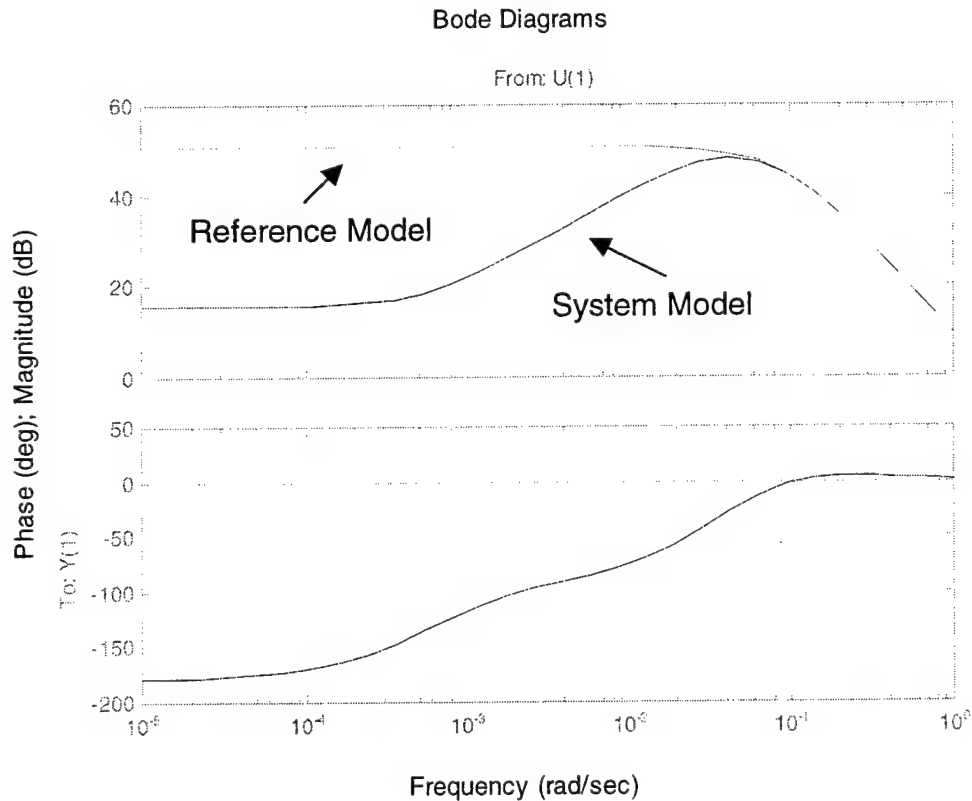


Figure C.2 – Simple Aerodynamic Response Comparison

Figure C.3 shows a comparative history of the system poles for both models, which further illustrates the effect of including angle-of-attack dynamics.

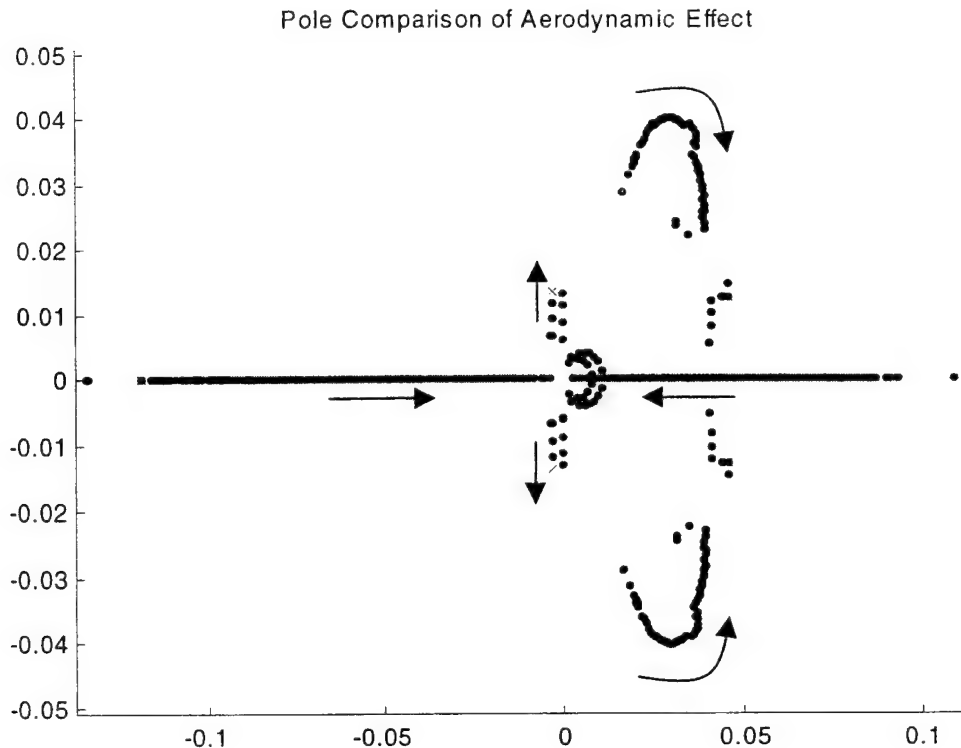


Figure C.3 – Simple Aerodynamic Model Comparison

Again, there are obvious differences between the two models. The reference model poles are shown as light dots, and the system model poles are shown as dark dots. The reference model begins as two real poles (one positive and one negative). As the flight progresses, the poles migrate towards the origin, and once they reach the origin, they track outward along the imaginary axis. This is physically intuitive, as the vehicle CG progresses forward during the flight profile and eventually passes the CP, making the vehicle marginally stable. In comparison, the system model has one negative real pole and a complex pole pair with a positive real part. However, it still exhibits the same pole progression during the flight profile. The complex poles migrate to the real axis, and all the poles come together at the origin. Finally, a zero cancels one pole, and the remaining two travel outward along the imaginary axis.

To address apparent differences in the pole histories, first notice that the reference model does not account for pitch damping, which has been included in

the system model. Pitch damping physically occurs as a resistance to a change in the pitch attitude of the vehicle. This is realized as the left shift in the entire system pole history in Figure C.3. The second difference is the appearance of extra complex poles in the right half plane. The complex pole pair in the right half plane (RHP) precipitates from the inclusion of angle-of-attack dynamics. The reference model applies the small angle assumption, which neglects the dynamics associated with angle-of-attack and simplifies the system to two real poles.

To support the effect of angle attack dynamics, a second reference model presented by Greensite is defined by equations C.5, C.6, and C.7, which includes angle-of-attack dynamics [13].

$$\frac{\theta}{\delta} = \frac{\mu_c \cdot \left(s + \frac{C_{m\alpha}}{M \cdot U_0} \left(1 + \frac{L}{I_{px}} \right) \right)}{s^3 + \frac{C_{m\alpha}}{M \cdot U_0} s^2 - \mu_\alpha s + \frac{\mu_\alpha \cdot g_0 \cdot \cos(\theta_0)}{U_0}} \quad (C.5)$$

$$\mu_c = \frac{T \cdot I_{px}}{I_{yy}} \quad (C.6)$$

$$\mu_\alpha = \frac{C_{m\alpha} \cdot L}{I_{yy}} \quad (C.7)$$

Figure C.4 shows the frequency responses of the system and second reference models. The two are almost identical, and much of the large low-frequency error that was present in Figure C.2 is now replaced by small deviations. A comparative history of poles between the second reference model and the system model is presented by Figure C.5. The reference model is again shown as light dots, and the system model poles are shown as dark dots.

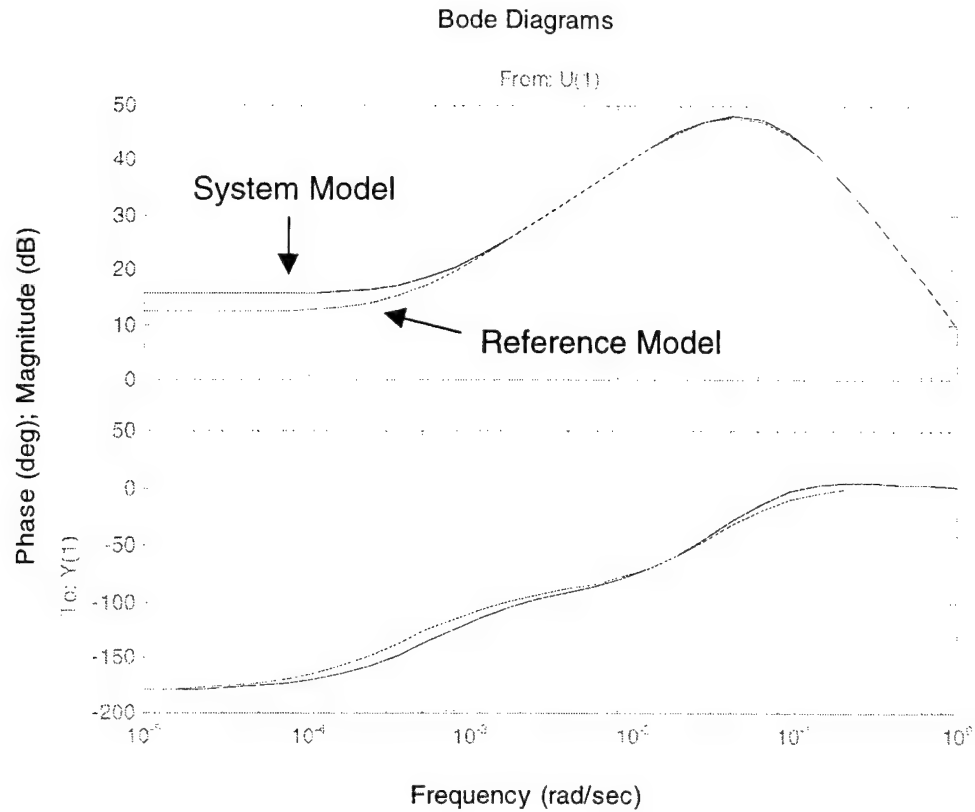


Figure C.4 – Complex Aerodynamic Response Comparison

Notice the presence of complex pole pairs in both models, which characterize angle-of-attack dynamics. This verifies the system model's aerodynamic response. However, some error does exist in Figure C.4 and Figure C.5 between the models. The second reference model, like the first, does not account for pitch damping, which is the cause for the characteristic shift in the pole history and the small differences in the bode response comparison.

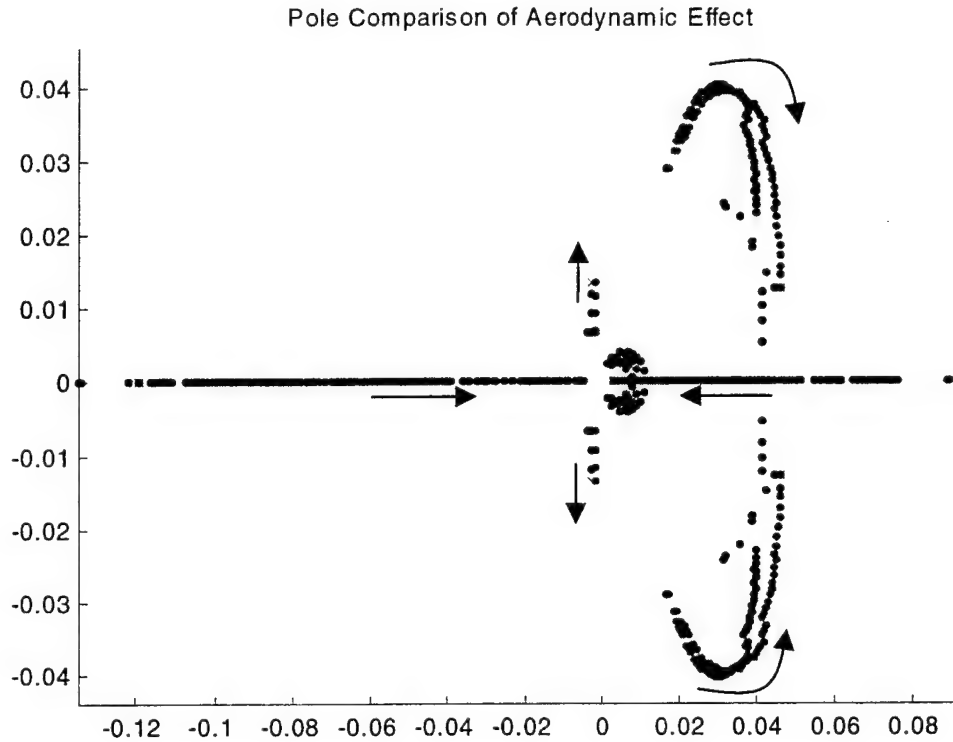


Figure C.5 – Complex Aerodynamic Model Comparison

In further analysis, the usefulness of the small angle assumption was explored. Greensite also presents a model of the response from pitch angle to angle-of-attack given by equations C.8, C.9, and C.10 [13].

$$\frac{\theta}{\alpha} = \frac{\tau_1 s + 1}{\tau_1 s (\tau_2 s + 1)} \quad (\text{C.8})$$

$$\tau_1 = \frac{M \cdot U_0}{C_{m\alpha} \left(1 + \frac{L}{I_{px}} \right)} \quad (\text{C.9})$$

$$\tau_2 = \frac{1}{M \cdot U_0 \cdot I_{px}} \quad (\text{C.10})$$

Figure C.6 compares this angle-of-attack to pitch angle model to its associated transfer function within the system model. The reference model magnitude is characterized by a smooth response with large low and high frequency gain and unity gain for mid-range frequencies. Clearly the approximation of small angles holds only for a finite band of mid-range frequencies. However, more remarkable is how this frequency band is decreased in the presence of higher frequency dynamics, which emphasizes that caution should be used in applying the small angle assumption. The system model with full dynamics is shown in Figure C.6, and exhibits more dramatic mid-to-high frequency dynamics. The allowable range of the small angle assumption is shown below by the area between the dashed vertical lines.

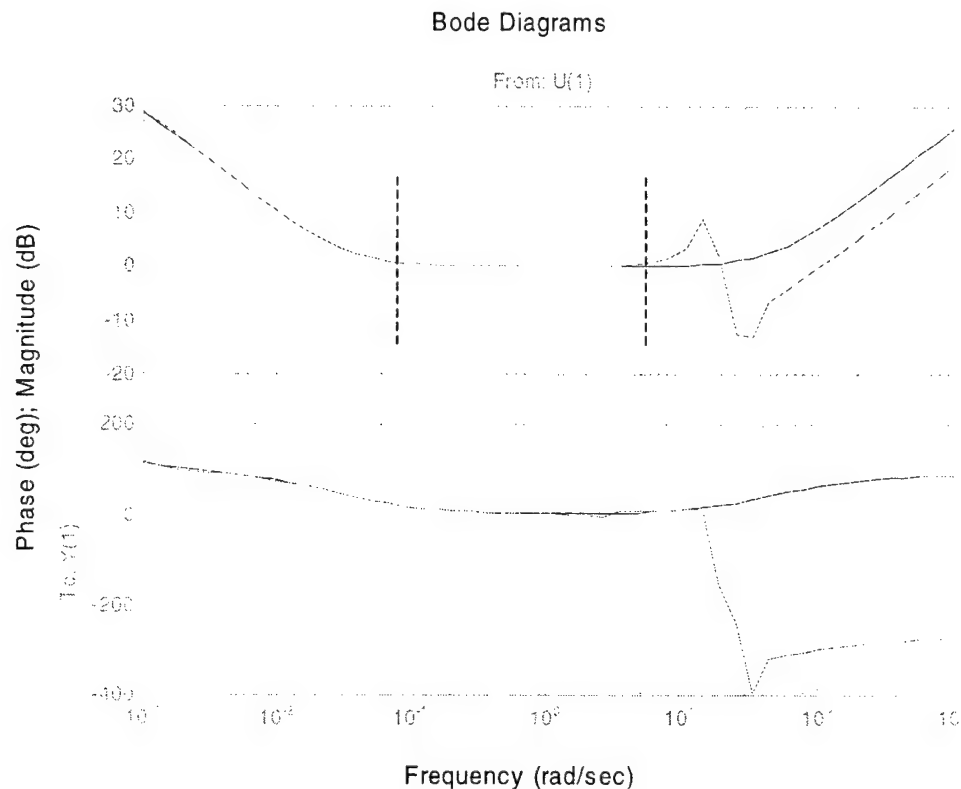


Figure C.6 – Small Angle Approximation Region of Validity

C.3 Engine Dynamics

The effect of engine dynamics (or Tail-Wags-Dog) is characterized by the presence of a complex zero pair [19]. Physically, this represents the frequency at which the actuator can drive the system and achieve no pitch response. Analytically, these poles have been shown to be located at the following frequency [6]:

$$\omega = \sqrt{\frac{T}{\frac{I_{yye}}{l_{px}} + m_e l_e}} \quad (C.11)$$

Using this formula for comparison, Figure C.7 shows the TWD zeros of the system model over time being superimposed with the analytic solution from equation C.11 at each step. This supports the system model implementation of TWD effects.

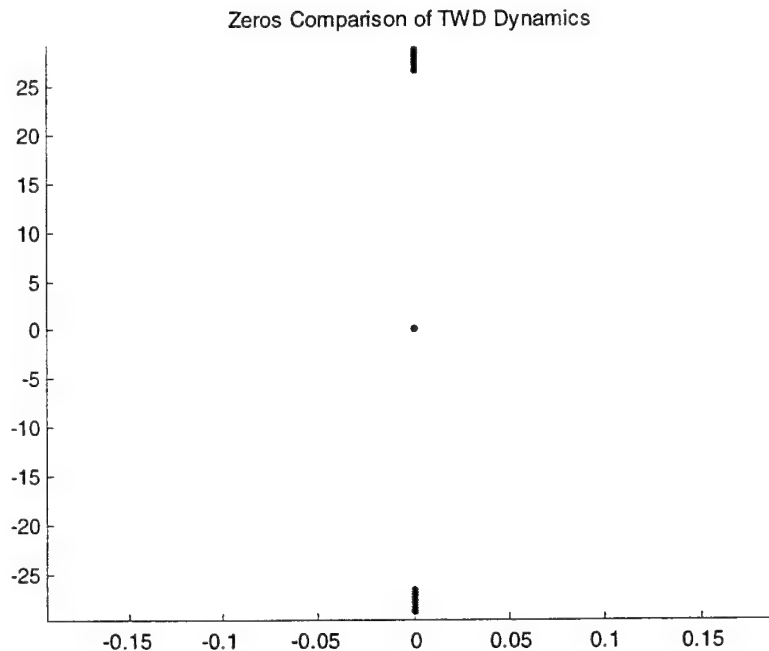


Figure C.7 – Comparison of Tail-Wags-Dog Zero Histories

However, it is important to understand that the zeros of a system are not independent of each other. In fact they are highly dependent. Therefore, when all dynamics effects are included in the system model, TWD zeros are slightly perturbed from their analytic locations as shown in Figure C.8 in a highly magnified view.

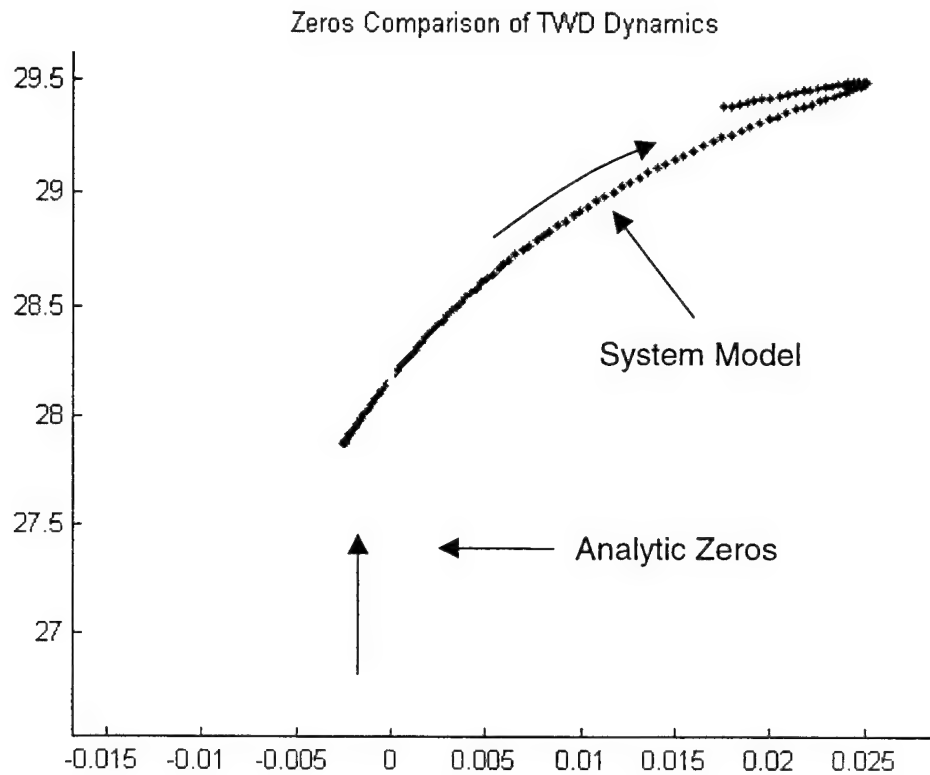


Figure C.8 – Magnified View of Tail-Wags-Dog Histories

C.4 Slosh Modes

Fuel sloshing modes appear as lightly damped complex pole pairs [19]. This is consistent with the system model as each slosh mode was modeled as a 2nd order spring-mass-damper system. The best way to verify the three different slosh modes is through a visual inspection of how the damping ratio and frequency of the poles change over the flight profile and a comparison to the parameter values, which are referenced by the MATLAB based model. Figure

C.9 and Figure C.10 show the reference data used by the system model for RP mode damping ratio and the frequency over the flight profile.

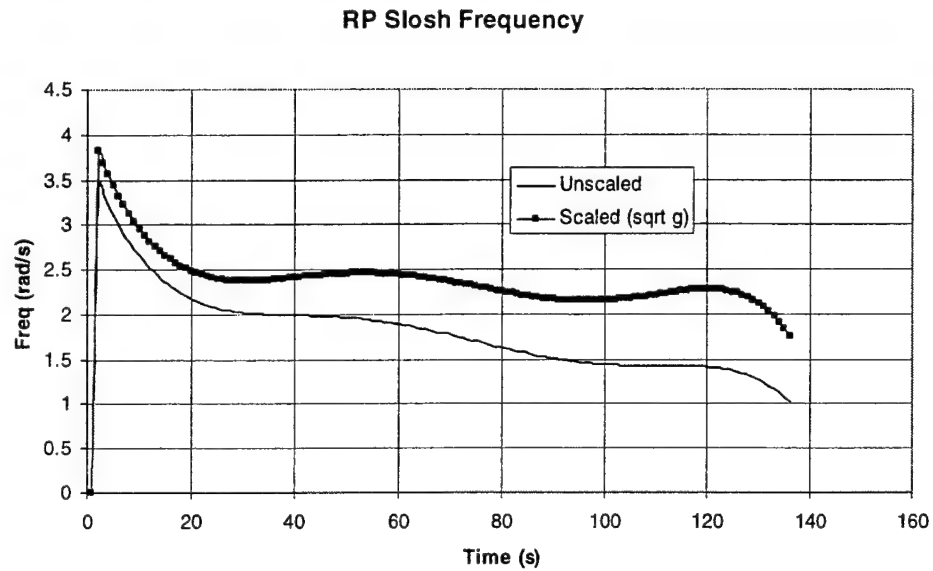


Figure C.9 – RP Slosh Frequency

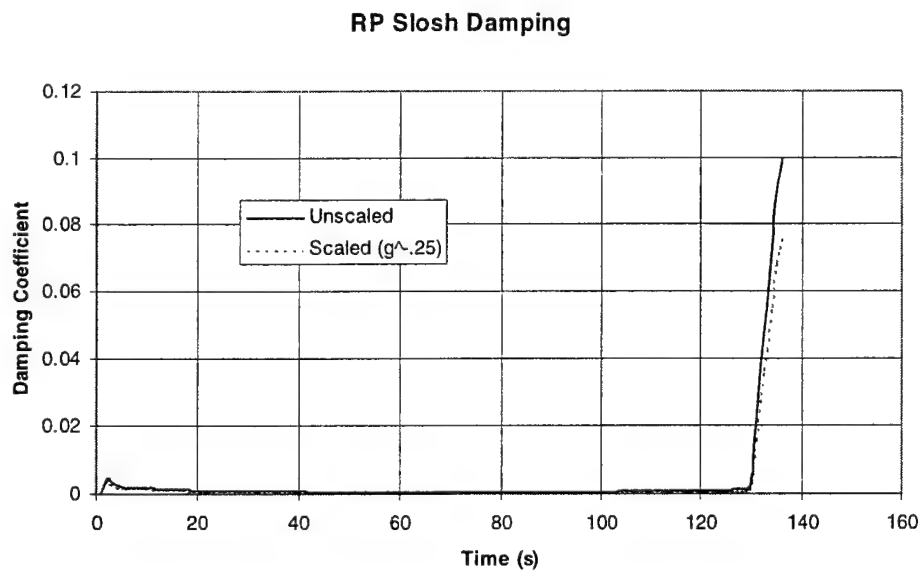


Figure C.10 – RP Damping Coefficient

A careful inspection of the RP mode pole-zero history in Figure C.11 will support the system model. The system model poles are displayed as dark dots,

and the zeros are shown as light dots. It is not obvious from this representation, but the RP mode is always phase stabilized, or in a zero-before-pole orientation.

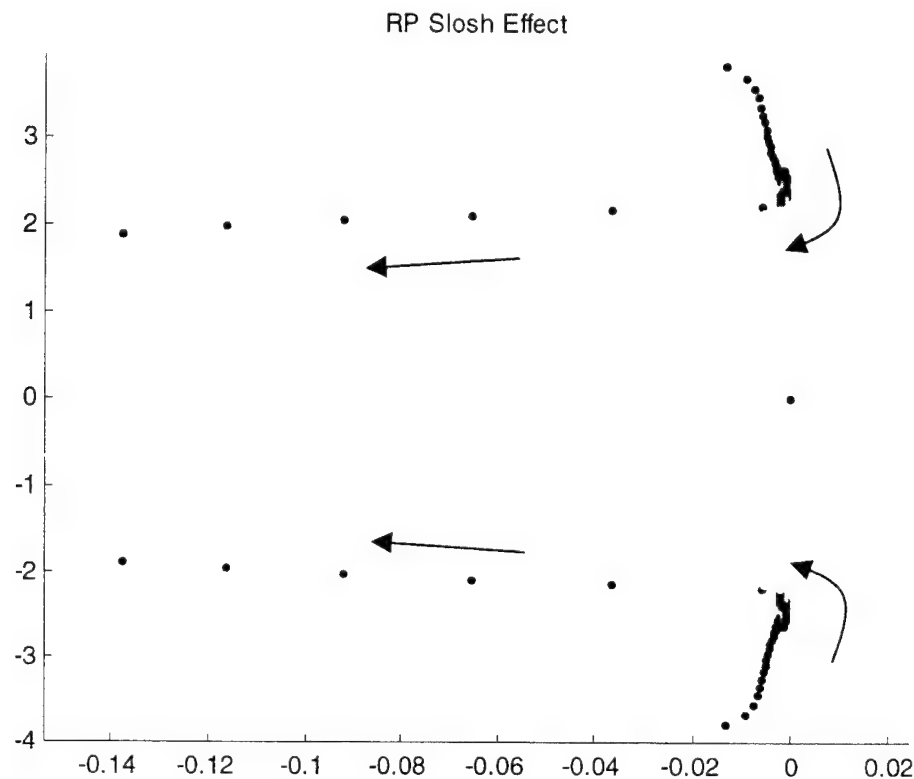


Figure C.11 – RP Slosh Mode Pole/Zero History

By realizing the Figure C.9 oscillations in frequency as oscillations in the absolute distance of the pole-zero pair from the origin, and the Figure C.10 changes in damping ratio as changes in the angle of the pole-zero pair from the positive imaginary axis, the reference data and the system model history appear consistent.

The same analysis can be performed for both of the LOX slosh modes. Figure C.12 and Figure C.13 display the frequency and damping reference data for both the main and retention LOX modes, and Figure C.14 and Figure C.15 present the pole-zero histories of the main LOX mode and the retention LOX mode, respectively. Again, it is presented without proof that the LOX slosh modes are zero-before-pole oriented. Much like the RP modes, the main LOX

mode has oscillations that appear in both the frequency and damping ratio graphs below.

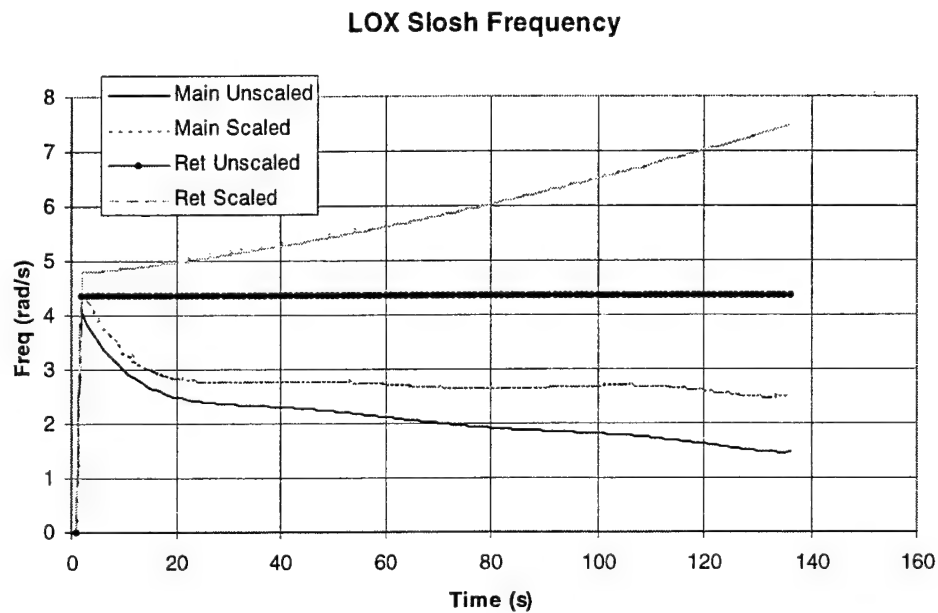


Figure C.12 – LOX Slosh Frequencies

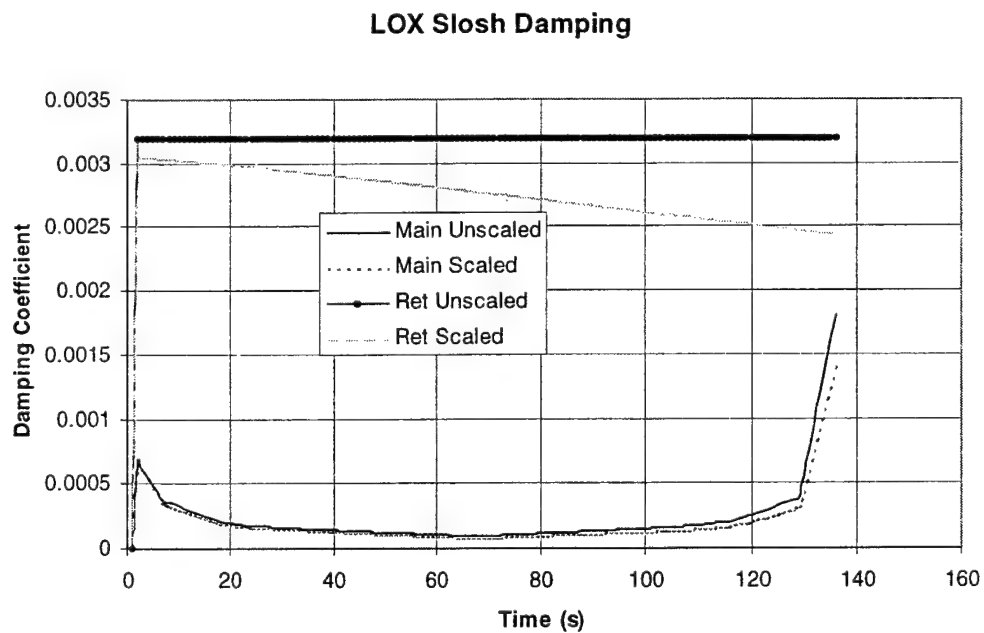


Figure C.13 – LOX Damping Coefficients

These changes result in the unique shape of the pole-zero history of the main LOX slosh mode in Figure C.14. Analyzing the retention tank mode, Figure C.12 and Figure C.13 show that there should be no change in the slosh parameters other than that which is produced by the g's dependent scaling coefficient used to properly model the sloshing parameters. The pole-zero history for the retention tank slosh mode in Figure C.15 supports that conclusion. It is easy to see an almost straight line indicating the effects of the scaling coefficient, increased frequency and slightly decreased damping.

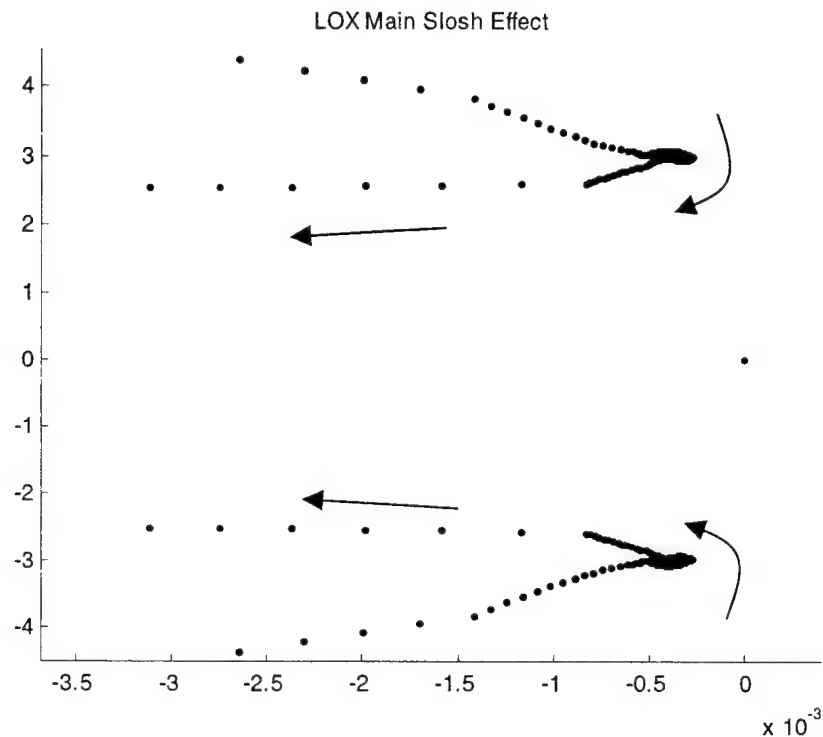


Figure C.14 – LOX Main Slosh Mode Pole/Zero History

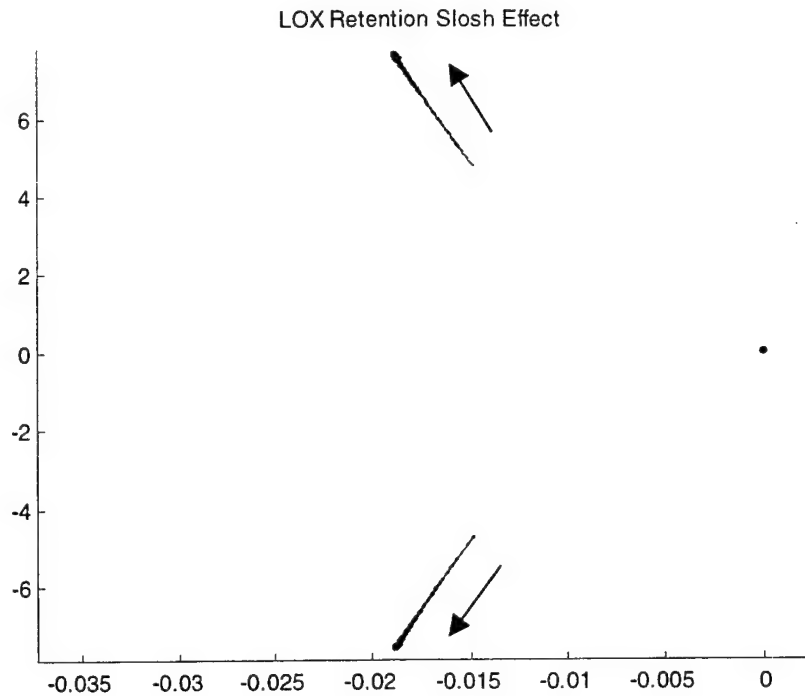


Figure C.15 – LOX Retention Mode Pole/Zero History

C.5 Flex Modes

Similarly, using flex coefficient data presented in Chapter 2, it is possible to visually inspect the pole placement of the flex modes using frequency and damping ratio data. Again, each mode should appear as a lightly damped complex pole pair. Figure C.16 shows that pole-zero map of the flex modes at the Mach 1.0 design point.

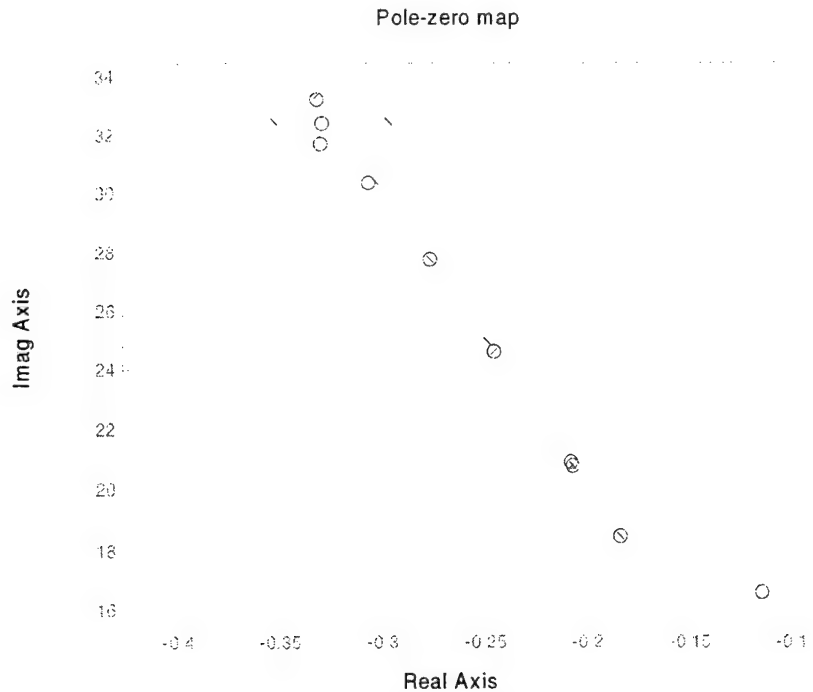


Figure C.16 – Flex Mode Pole/Zero Pairs at Mach 1.0

The alignment of the poles indicates the 0.01 damping coefficient that they share as well as the successive increase in frequency for each mode. The amount of separation of each pole and zero identifies which flex modes will dominate at that particular instant in the mission profile. Even though the parameters of the different flex modes are constant, the migration of the stack center of gravity forward in the body creates changes in the sensitivity of the thrust beam and IMU to each of the bending modes. Thus, different modes will dominate at different times during the mission profile.

C.6 Baseline Model for T=72 sec (Mach 1.0)

The results of this verification process support the MATLAB-based, boost phase model. By assessing each dynamic effect individually against reference models, the system model appears to be consistent with the available sources. Therefore, it is with a heightened level of confidence that this model is implemented in the development of an MCS synthesis process.

APPENDIX D

Gain Vector Search Algorithm

The MATLAB code used to perform the parameter search during the SISO design process is presented in Section D.1. This algorithm was modeled from a similar application used to develop the K1 LAP return phase control system [6]. Using a graphically based technique, SIMULINK models were created to aid in system transfer function generation and analysis. The SIMULINK models accessed by the vector search algorithm are presented in Section D.2.

D.1 MATLAB Code

```
% ClassicalGainSearch.m
%
% Author Nick Hague
% Date 5 NOV 99
%
% This routine will search vectors of gains used in the classical
% control law. This includes proportional and derivative gains as well
% as a lead and lag filter (both are second order). The results of
% this search are saved in a text file for only those cases which meet
% the margin criteria.
%-----
clear all
tic;
attempts = 0;
count = 0;

% Plant and Actuator Dynamics
aero = 1;
flex = 10;
twd = 1;
lox = 2;
rp = 1;
```

```

time = 72;          % Mach 1
out = 0;
act = actuator(twd,time);
[Aact,Bact,Cact,Dact] = ssdata(act);
sys_plant = plant(aero,flex,twd,lox,rp,time,0);
[Ap,Bp,Cp,Dp] = ssdata(sys_plant);
s = tf([1 0],1);

veh = series(act,sys_plant);
StackT = tf(veh(2,1));

% High Order Pade Approximations for lags
[num60,den60] = pade(.06,1);
D60 = tf(num60,den60);
[num20,den20] = pade(.0205,1);
D20 = tf(num20,den20);

% PD Gain Vectors
pgain = [.5 1 1.5];
dgain = [.3 .5 .7];

% Lead Filter (Low Freq) Gain Vectors
ldz_w = [2 3 4 5];
ldz_z = [.6 .707 .8];
ldp_w = [3 4 5 6];
ldp_z = [.6 .707 .8];

% Lag Filter (High Freq) Gain Vectors
lgz_w = [10 20 30 40];
lgz_z = [.6 .707 .8];
lgp_w = [6 8 10 20];
lgp_z = [.6 .707 .8];

% Figure Number of Combinations and Estimated Calculation Time
pd_combos = size(pgain,2)*size(pgain,2);
lead_combos = size(ldz_z,2)*size(ldz_w,2)*size(ldp_z,2)*size(ldp_w,2);
lag_combos = size(lgz_z,2)*size(lgz_w,2)*size(lgp_z,2)*size(lgp_w,2);
combos = pd_combos*lead_combos*lag_combos;
est_time = .019 * combos;

% Display Gain Vector Information
disp('Number of Possible Combinations to be Searched');
disp(combos);
disp('This search will take approximately');
disp(est_time);
disp('minutes to complete.')
disp(' ');

% Time and Input Vectors for Simulation
dt = .05;
tfinal = 50;
in_time = 0:dt:tfinal;
step_input = ones(1,size(in_time,2));

% Frequency Vectors for Response
w = logspace(-1,2,1000);
index1 = find((w>5)&(w<10));

```



```

w_lox = w(index1(1):index1(length(index1)));
index2 = find((w>15)&(w<100));
w_flex = w(index2(1):index2(length(index2)));

% Controlled System Responses for Each Case
for i = 1:length(pgain)
    for j = 1:length(dgain)
        for k = 1:length(ldz_w)
            for l = 1:length(ldz_z)
                for m = 1:length(ldp_w)
                    for n = 1:length(ldp_z)
                        for o = 1:length(lgz_w)
                            for p = 1:length(lgz_z)
                                for q = 1:length(lgp_w)
                                    for r = 1:length(lgp_z)
                                        if (ldz_w(k)<ldp_w(m) & lgp_w(q)<lgz_w(o) & ldp_w(m)<lgp_w(q))
                                            attempts = attempts + 1;

% Control Gains
Kp = pgain(i);
Kd = dgain(j);

% Bending Filter
ldnum = (s^2+2*ldz_z(l)*ldz_w(k)*s+ldz_w(k)^2);
ldden = (s^2+2*ldp_z(n)*ldp_w(m)*s+ldp_w(m)^2);
ldgain = (ldp_w(m)/ldz_w(k))^2;
lead = ldgain*ldnum/ldden;
lgnum = (s^2+2*lgz_z(p)*lgz_w(o)*s+lgz_w(o)^2);
lgden = (s^2+2*lgp_z(r)*lgp_w(q)*s+lgp_w(q)^2);
lggain = (lgp_w(q)/lgz_w(o))^2;
lag = lggain*lgnum/lgden;
bf = lead*lag;
[ba,bb,bc,bd] = ssdata(bf);

% Using Simulink to Get Frequency Response on Inner Loop
[A_il,B_il,C_il,D_il] = linmod('cldesign_search_freq');
inner_loop = ss(A_il,B_il,C_il,D_il);

% Gain Margin and Phase Margin
[iloop_mag,iloop_phase] = bode(inner_loop,w);
mag = reshape(iloop_mag,[length(w) 1]);
phase = reshape(iloop_phase,[length(w) 1]);
[GM,PM,Wg,Wp]=imargin(mag,phase,w);
GM_dB = 20*log10(GM);

if (GM_dB>=6 & PM>=30)
% Gain Margin for LOX Retention Mode
[lox_mag,lox_phase] = bode(inner_loop,w_lox);
lox_mag = reshape(lox_mag,[length(w_lox) 1]);
lox_GM = max(lox_mag);
lox_GM_dB = 20*log10(lox_GM);

% Gain Margin for Flex modes
[flex_mag,flex_phase] = bode(inner_loop,w_flex);
flex_mag = reshape(flex_mag,[length(w_flex) 1]);
flex_GM = max(flex_mag);
flex_GM_dB = 20*log10(flex_GM);

```


generated automatically, eliminating the need for manual block diagram reduction. This method is also beneficial when changes are made to the control loop structure. Changes can be made by drawing lines and by deleting old elements or dragging in new ones. Figure D.1 and Figure D.2 present the two SISO control loop models used to execute the gain vector search algorithm.

Figure D.1 shows the SISO loop model used to generate the system loop transfer function, which is used to calculate GM and PM.

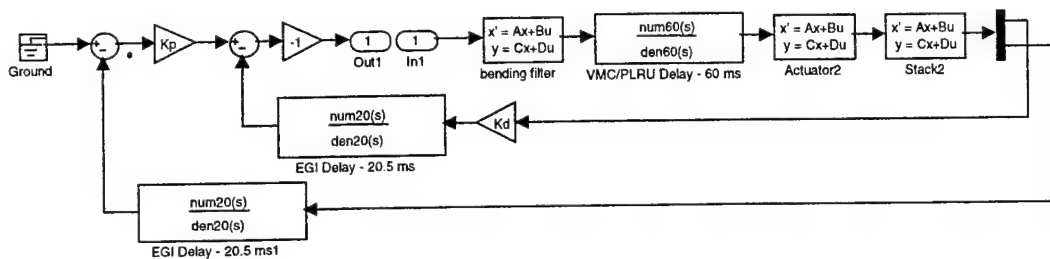


Figure D.1 – SISO Loop Transfer Function SIMULINK Model

The negative unity gain in the forward loop has been introduced to offset negative feedback assumptions applied by the *nichols.m* MATLAB command, which is used to generate the Nichols plots of the loop transfer function.

Figure D.2 presents the SISO loop model used to generate the closed loop system response. This transfer function was used to help generate the step response of the system and, subsequently, the ITAE of the closed loop system.

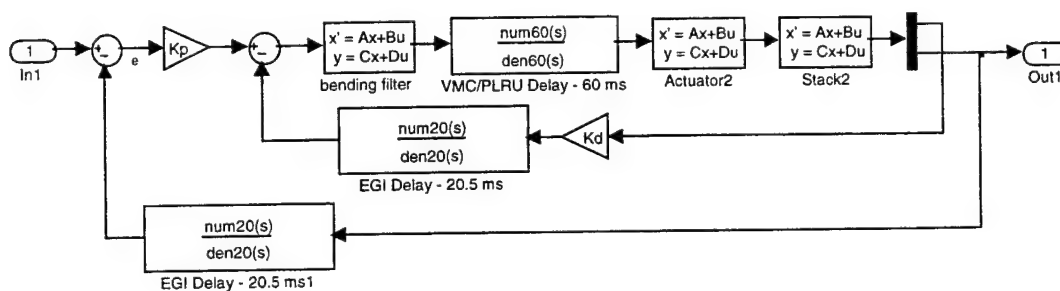


Figure D.2 – SISO Closed Loop Transfer Function SIMULINK Model

APPENDIX E

Dispersion Analysis Summary

E.1 Individual 3- σ Perturbation Cases

For each run of the 3- σ analysis, only one parameter value was disturbed. All others were set to their nominal values. Table E.1 summarizes the 84 cases used in this analysis. High signifies a positive 3- σ perturbation. Low indicates a negative 3- σ perturbation.

Table E.1 – Individual 3- σ Test Cases

Run #	Parameter		
1	Nominal	17	ξ_{srp} High
2	T High	18	I_{srxp} High
3	Actuator High	19	q High
4	I_{px} High	20	$C_{z\alpha}$ High
5	CG Location High	21	$C_{m\alpha}$ High
6	I_{yy} High	22	C_{mq} High
7	m_{slx} High	23	ω_1 High
8	ω_{slx} High	24	ζ_1 High
9	ξ_{slx} High	25	ω_2 High
10	I_{sxlx} High	26	ζ_2 High
11	m_{slx_ret} High	27	ω_3 High
12	ω_{slx_ret} High	28	ζ_3 High
13	ξ_{slx_ret} High	29	ω_4 High
14	I_{sxlx_ret} High	30	ζ_4 High
15	m_{srp} High	31	ω_5 High
16	ω_{srp} High	32	ζ_5 High

33	ω_6 High	60	I_{sxp} Low
34	ζ_6 High	61	q Low
35	ω_7 High	62	$C_{z\alpha}$ Low
36	ζ_7 High	63	$C_{m\alpha}$ Low
37	ω_8 High	64	C_{mq} Low
38	ζ_8 High	65	ω_1 Low
39	ω_9 High	66	ζ_1 Low
40	ζ_9 High	67	ω_2 Low
41	ω_{10} High	68	ζ_2 Low
42	ζ_{10} High	69	ω_3 Low
43	Design Point Time High	70	ζ_3 Low
44	T Low	71	ω_4 Low
45	Actuator Low	72	ζ_4 Low
46	I_{px} Low	73	ω_5 Low
47	CG Location Low	74	ζ_5 Low
48	I_{yy} Low	75	ω_6 Low
49	m_{slx} Low	76	ζ_6 Low
50	ω_{slx} Low	77	ω_7 Low
51	ξ_{slx} Low	78	ζ_7 Low
52	I_{slx} Low	79	ω_8 Low
53	m_{slx_ret} Low	80	ζ_8 Low
54	ω_{slx_ret} Low	81	ω_9 Low
55	ξ_{slx_ret} Low	82	ζ_9 Low
56	I_{slx_ret} Low	83	ω_{10} Low
57	m_{srp} Low	84	ζ_{10} Low
58	ω_{srp} Low	85	Design Point Time Low
59	ξ_{srp} Low		

In order to represent off-nominal configurations of the engine actuators, limits on actuator specifications were used to generate transfer functions that represented High and Low perturbations. Figure E.1 shows the three possible actuator representations (nominal, high, low).

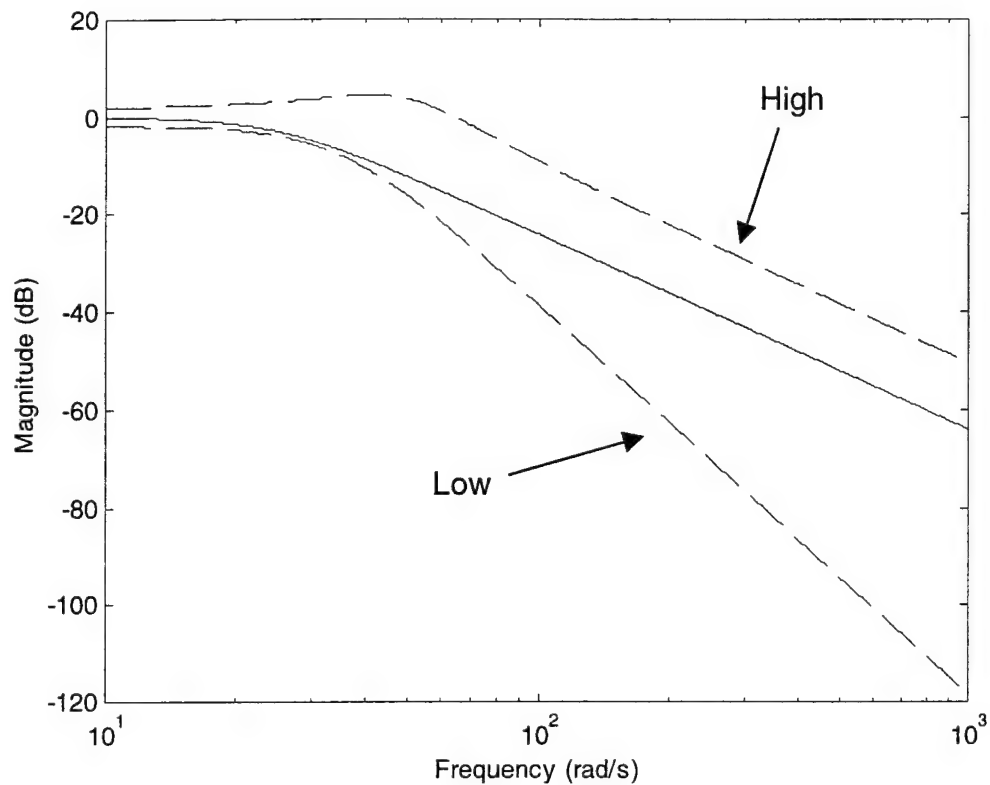


Figure E.1 – Actuator Uncertainty Representations

E.2 Combined 1- σ Perturbation Cases

Table E.2 presents runs used to perform combined perturbation analysis for each controller design. A zero indicates a nominal parameter value. Negative one is a negative 1- σ perturbation, and positive one is a positive 1- σ perturbation. Due to a lack of information and non-linearity concerning the uncertainty of the engine actuators, the same high and low perturbation transfer functions that were used in the 3- σ analysis were also used for the actuator perturbations here.

Table E.2 – Combined 1- σ Test Cases

Run #	Actuator	ω_x	m_{slx_ret}	ω_{slx_ret}	c_{slx_ret}	l_{slx_ret}	ω_5
1	0	0	0	0	0	0	0
2	0	0	0	-1	-1	-1	0
3	0	0	0	1	-1	-1	0
4	0	0	0	-1	1	-1	0
5	0	0	0	1	1	-1	0
6	0	0	0	-1	-1	1	0
7	0	0	0	1	-1	1	0
8	0	0	0	-1	1	1	0
9	0	0	0	1	1	1	0
10	-1	0	0	0	0	-1	-1
11	1	0	0	0	0	-1	-1
12	-1	0	0	0	0	1	-1
13	1	0	0	0	0	1	-1
14	-1	0	0	0	0	-1	1
15	1	0	0	0	0	-1	1
16	-1	0	0	0	0	1	1
17	1	0	0	0	0	1	1
18	0	-1	0	0	-1	0	-1
19	0	1	0	0	-1	0	-1
20	0	-1	0	0	1	0	-1
21	0	1	0	0	1	0	-1
22	0	-1	0	0	-1	0	1
23	0	1	0	0	-1	0	1
24	0	-1	0	0	1	0	1
25	0	1	0	0	1	0	1
26	-1	-1	0	-1	0	0	0
27	1	-1	0	-1	0	0	0
28	-1	1	0	-1	0	0	0
29	1	1	0	-1	0	0	0
30	-1	-1	0	1	0	0	0
31	1	-1	0	1	0	0	0
32	-1	1	0	1	0	0	0
33	1	1	0	1	0	0	0
34	0	0	-1	-1	0	0	-1
35	0	0	1	-1	0	0	-1
36	0	0	-1	1	0	0	-1
37	0	0	1	1	0	0	-1
38	0	0	-1	-1	0	0	1
39	0	0	1	-1	0	0	1
40	0	0	-1	1	0	0	1
41	0	0	1	1	0	0	1
42	-1	0	-1	0	-1	0	0
43	1	0	-1	0	-1	0	0

44	-1	0	1	0	-1	0	0
45	1	0	1	0	-1	0	0
46	-1	0	-1	0	1	0	0
47	1	0	-1	0	1	0	0
48	-1	0	1	0	1	0	0
49	1	0	1	0	1	0	0
50	0	-1	-1	0	0	-1	0
51	0	1	-1	0	0	-1	0
52	0	-1	1	0	0	-1	0
53	0	1	1	0	0	-1	0
54	0	-1	-1	0	0	1	0
55	0	1	-1	0	0	1	0
56	0	-1	1	0	0	1	0
57	0	1	1	0	0	1	0

E.3 Design Alpha – 3- σ Results

Table E.3 summarizes the results of 3- σ perturbation analysis on design Alpha.

Table E.3 – Design Alpha 3- σ Results

Run #	GM	PM	Δ GM (%)	Δ PM (%)	Δ ITAE (%)
1	9.7575	35.3583	0	0	0
2	9.6692	35.2559	-0.9055	-0.2896	-0.5743
3	6.0935	30.921	-37.5504	-12.5495	-8.4411
4	9.695	35.294	-0.6403	-0.1818	-0.4606
5	9.8414	35.4635	0.8599	0.2975	0.3868
6	9.6229	35.0514	-1.3797	-0.868	-0.3164
7	9.7221	34.6737	-0.3629	-1.9363	0.1242
8	9.5887	30.0978	-1.7298	-14.8777	-1.7306
9	9.7576	35.3615	0.0009	0.0091	-0.0053
10	9.6795	34.2787	-0.8	-3.0533	-0.0194
11	9.5601	35.3956	-2.0235	0.1054	0.105
12	10.5067	35.3354	7.6778	-0.0649	-0.1787
13	9.9584	35.3586	2.0587	0.0007	-0.0204
14	9.4143	35.4072	-3.5174	0.1382	0.1801
15	9.7349	35.0967	-0.2314	-0.7399	0.0447
16	9.6651	33.6574	-0.9468	-4.8104	-16.8754
17	9.7578	35.3626	0.0024	0.0121	-0.1297
18	9.7068	34.8829	-0.5203	-1.3446	-0.2551
19	9.7577	35.3586	0.0023	0.0007	1.3607
20	9.787	35.521	0.3024	0.4601	-0.4973

21	9.7575	35.3582	-0.0001	-0.0003	0.187
22	9.7814	35.4887	0.245	0.3686	1.764
23	9.7575	35.3583	0	0	0
24	9.7575	35.3583	0	0	0
25	9.7574	35.3583	-0.0011	-0.0002	-0.0003
26	9.7575	35.3583	0	0	0
27	9.755	35.357	-0.0257	-0.0036	-0.006
28	9.7575	35.3583	0	0	0
29	9.7526	35.3561	-0.0508	-0.0064	-0.0091
30	9.7575	35.3583	0	0	0
31	9.641	35.3013	-1.1946	-0.1612	-0.2386
32	9.7576	35.3584	0.0006	0.0001	0
33	9.7575	35.3583	0	0	0
34	9.7575	35.3583	0	0	0
35	9.7574	35.3583	-0.0013	-0.0002	-0.0001
36	9.7575	35.3583	0	0	0
37	9.7585	35.3582	0.0104	-0.0005	-0.0087
38	9.7575	35.3583	0	0	0
39	9.7457	35.3528	-0.1207	-0.0157	-0.0243
40	9.7575	35.3583	0	0	0
41	9.7565	35.3578	-0.0108	-0.0014	-0.0023
42	9.7575	35.3583	0	0	0
43	9.5025	35.3514	-2.6134	-0.0196	-0.3058
44	9.8468	35.4594	0.9152	0.286	0.5845
45	8.7665	28.9964	-10.156	-17.9928	23.8679
46	9.8205	35.4218	0.645	0.1797	0.4676
47	9.6729	35.2504	-0.8676	-0.3051	-0.3895
48	9.6229	35.0514	-1.3797	-0.868	-0.3164
49	9.7925	36.0674	0.3588	2.0054	-0.2164
50	9.8919	40.1223	1.3776	13.4734	-14.8676
51	9.7574	35.3551	-0.0009	-0.0091	0.0053
52	9.8294	36.4418	0.7367	3.0644	-1.3121
53	9.9501	35.3211	1.9737	-0.1052	-0.1046
54	10.3154	35.3958	5.7172	0.1059	0.3503
55	9.5175	35.3581	-2.4601	-0.0007	0.023
56	10.0888	35.3119	3.3949	-0.1314	-0.1606
57	9.78	35.6198	0.2304	0.7394	-0.2913
58	9.8346	36.4514	0.7903	3.0914	5.694
59	9.7573	35.354	-0.0024	-0.0121	0.1302
60	9.8038	35.7957	0.4748	1.2369	-2.8195
61	9.7573	35.3581	-0.0023	-0.0007	-1.1906
62	9.7279	35.1957	-0.3038	-0.4599	0.5026
63	9.7575	35.3584	0.0001	0.0003	-0.1835
64	9.7335	35.228	-0.2459	-0.3685	-1.3491
65	9.7575	35.3583	0	0	0
66	9.7575	35.3583	0	0	0

67	9.7577	35.3584	0.0016	0.0002	0.0004
68	9.7575	35.3583	0	0	0
69	9.761	35.3601	0.0361	0.005	0.0081
70	9.7575	35.3583	0	0	0
71	9.7644	35.3614	0.0706	0.0087	0.0123
72	9.7575	35.3583	0	0	0
73	5.9237	35.4347	-39.2904	0.216	0.3318
74	9.7575	35.3583	-0.0006	-0.0001	0
75	9.7575	35.3583	0	0	0
76	9.7575	35.3583	0	0	0
77	9.7577	35.3584	0.0018	0.0002	0.0002
78	9.7575	35.3583	0	0	0
79	9.7561	35.3585	-0.0143	0.0006	0.0117
80	9.7575	35.3583	0	0	0
81	9.7737	35.3658	0.166	0.0213	0.0329
82	9.7575	35.3583	0	0	0
83	9.759	35.359	0.0148	0.002	0.0031
84	9.7575	35.3583	0	0	0
85	10.0721	35.2338	3.2237	-0.3521	-3.2077

E.4 Design Alpha – 1- σ Results

Table E.4 summarizes the results of 1- σ perturbation analysis on design Alpha.

Table E.4 – Design Alpha 1- σ Results

Run #	GM	PM	Δ GM (%)	Δ PM (%)	Δ ITAE (%)
1	9.7575	35.3583	0	0	0
2	9.6791	35.7886	-0.8037	1.217	-0.3148
3	9.8646	35.7705	1.0971	1.1657	-0.3795
4	9.7938	35.7888	0.3722	1.2175	-0.3255
5	10.0115	35.7706	2.6034	1.1661	-0.3897
6	9.6187	34.8802	-1.4225	-1.3522	-3.2081
7	9.8084	34.8603	0.5218	-1.4084	-3.5368
8	9.7333	34.8804	-0.2477	-1.3517	-3.225
9	9.9602	34.8605	2.0772	-1.408	-3.5445
10	8.8388	29.4299	-9.4157	-16.7667	24.2786
11	4.3409	31.4288	-55.5124	-11.1133	-8.4513
12	8.7615	28.5125	-10.2073	-19.3612	19.194
13	4.3409	30.4365	-55.5123	-13.9199	-10.0469
14	8.7725	29.4029	-10.0949	-16.843	23.9941
15	7.1411	31.3513	-26.8142	-11.3325	-8.5652

16	8.6958	28.4831	-10.8812	-19.4443	18.9565
17	7.0825	30.3578	-27.4153	-14.1424	-10.1626
18	9.5126	37.0616	-2.5105	4.8171	0.047
19	9.5126	33.6489	-2.5106	-4.8344	-0.9555
20	9.5126	37.0617	-2.5105	4.8175	0.0292
21	9.5126	33.6491	-2.5106	-4.8339	-0.9689
22	9.6872	37.016	-0.7203	4.6883	-0.1067
23	9.5878	33.608	-1.7399	-4.9502	-1.1512
24	9.8332	37.0162	0.7757	4.6887	-0.1248
25	9.7333	33.6082	-0.2483	-4.9496	-1.1649
26	8.4594	31.0035	-13.3035	-12.3161	22.1475
27	6.0935	32.4575	-37.5506	-8.2042	-7.016
28	8.3323	26.9459	-14.6063	-23.7919	25.3818
29	6.0935	29.3608	-37.5502	-16.9622	-10.2055
30	9.2364	30.9895	-5.3408	-12.3559	22.1155
31	6.0935	32.4301	-37.5505	-8.2816	-7.1002
32	9.0934	26.929	-6.8065	-23.8397	24.8963
33	6.0936	29.3301	-37.5501	-17.0488	-10.6094
34	9.5126	35.379	-2.5105	0.0586	0.2396
35	9.5126	35.4043	-2.5105	0.1301	0.2891
36	9.5126	35.3605	-2.5105	0.0062	-0.0342
37	9.5126	35.3848	-2.5106	0.0749	0.0076
38	9.7249	35.335	-0.3348	-0.0659	0.0537
39	9.6075	35.3605	-1.5376	0.0062	0.104
40	9.9589	35.3165	2.0641	-0.1181	-0.2221
41	9.7953	35.3407	0.3868	-0.0497	-0.1803
42	8.8173	28.9856	-9.6359	-18.0231	23.8292
43	6.0935	30.9041	-37.5504	-12.5973	-8.4738
44	8.4646	29.0069	-13.2501	-17.963	23.9148
45	6.0935	30.9378	-37.5503	-12.5022	-8.3789
46	9.0482	28.9858	-7.2695	-18.0226	23.8227
47	6.0935	30.9043	-37.5504	-12.5968	-8.5001
48	8.6976	29.0071	-10.8629	-17.9624	23.9065
49	6.0935	30.9379	-37.5503	-12.5017	-8.4097
50	9.8934	37.5323	1.3922	6.1484	0.1077
51	9.795	33.967	0.3839	-3.9349	-0.7384
52	9.7702	37.5567	0.1297	6.2175	0.1547
53	9.669	33.9908	-0.9069	-3.8676	-0.6547
54	9.8382	36.4362	0.8264	3.0483	-6.7514
55	9.739	33.2084	-0.1902	-6.0804	-2.6805
56	9.7137	36.4612	-0.4488	3.1192	-6.7009
57	9.6117	33.2333	-1.4944	-6.0098	-2.6247

E.5 Design Beta – 3- σ Results

Table E.5 summarizes the results of 3- σ perturbation analysis on design Beta.

Table E.5 – Design Beta 3- σ Results

Run #	GM	PM	Δ GM (%)	Δ PM (%)	Δ ITAE (%)
1	8.0406	30.3286	0	0	0
2	7.9523	30.2928	-1.0989	-0.1181	-0.2988
3	5.4234	27.6495	-32.5505	-8.8336	-3.3056
4	7.9782	30.307	-0.7761	-0.0715	-0.2375
5	8.1257	30.3622	1.0577	0.1107	0.1027
6	7.9025	30.2169	-1.7175	-0.3685	-0.2588
7	8.0039	30.0519	-0.4564	-0.9126	-0.266
8	7.8674	27.9895	-2.1546	-7.7126	-2.7097
9	8.0407	30.333	0.001	0.0145	-0.0064
10	7.9612	29.9178	-0.9881	-1.3547	-0.7472
11	7.828	30.3416	-2.6443	0.0427	0.0624
12	7.5712	30.3205	-5.8387	-0.0269	-0.1197
13	8.2158	30.3289	2.1784	0.0009	-0.0167
14	7.6974	30.345	-4.2693	0.0539	0.0986
15	8.0174	30.2326	-0.2884	-0.3166	-0.1734
16	7.9462	29.6713	-1.1739	-2.1674	-20.0722
17	8.0409	30.334	0.0028	0.0175	-0.1082
18	7.989	30.1617	-0.6419	-0.5506	-0.8521
19	8.0409	30.3276	0.003	-0.0036	2.943
20	8.0683	30.5046	0.3438	0.5802	-0.329
21	8.0406	30.3292	-0.0003	0.0019	0.4032
22	8.063	30.4687	0.2788	0.4619	4.3509
23	8.0406	30.3286	0	0	0
24	8.0406	30.3286	0	0	0
25	8.0405	30.3286	-0.0013	-0.0001	-0.0001
26	8.0406	30.3286	0	0	0
27	8.0381	30.3282	-0.0311	-0.0015	-0.003
28	8.0406	30.3286	0	0	0
29	8.0357	30.3278	-0.0615	-0.0026	-0.0046
30	8.0406	30.3287	0	0	0
31	7.9243	30.3084	-1.4465	-0.0667	-0.121
32	8.0407	30.3287	0.0007	0.0001	-0.0001
33	8.0406	30.3286	0	0	0
34	8.0406	30.3286	0	0	0
35	8.0405	30.3286	-0.0015	-0.0001	-0.0001
36	8.0406	30.3286	0	0	0

37	8.0417	30.3286	0.0126	-0.0001	-0.0045
38	8.0406	30.3286	0	0	0
39	8.0289	30.3267	-0.1462	-0.0064	-0.0122
40	8.0406	30.3287	0	0	0
41	8.0396	30.3285	-0.013	-0.0006	-0.0012
42	8.0406	30.3286	0	0	0
43	7.6138	30.328	-5.3083	-0.0021	2.2287
44	8.1299	30.3643	1.1108	0.1176	0.3099
45	6.9511	22.9542	-13.5503	-24.315	21.8181
46	8.1035	30.3504	0.7818	0.0717	0.2459
47	7.9548	30.2943	-1.0672	-0.1134	-0.1041
48	7.9025	30.2169	-1.7175	-0.3685	-0.2588
49	8.0769	30.6109	0.4513	0.9305	-0.1341
50	8.1787	32.2321	1.717	6.276	-12.047
51	8.0405	30.3243	-0.001	-0.0145	0.0064
52	8.1138	30.7295	0.9103	1.3216	-1.2698
53	8.2455	30.3157	2.5485	-0.0426	-0.0629
54	10.0952	30.3421	25.5528	0.0443	-0.0095
55	7.8325	30.3284	-2.5887	-0.0009	0.0193
56	8.3681	30.3132	4.0724	-0.0509	-0.0909
57	8.0637	30.4238	0.2873	0.3137	-0.0371
58	8.1194	30.7222	0.98	1.2975	6.8471
59	8.0404	30.3233	-0.0028	-0.0175	0.1086
60	8.0878	30.4804	0.586	0.5002	-1.6955
61	8.0404	30.3297	-0.003	0.0036	-2.6208
62	8.0129	30.1527	-0.3452	-0.5802	0.3361
63	8.0407	30.3281	0.0003	-0.0019	-0.3963
64	8.0181	30.1886	-0.2797	-0.4619	-3.5389
65	8.0406	30.3286	0	0	0
66	8.0406	30.3286	0	0	0
67	8.0408	30.3287	0.0019	0.0001	0.0002
68	8.0406	30.3286	0	0	0
69	8.0441	30.3293	0.0437	0.0021	0.0041
70	8.0406	30.3286	0	0	0
71	8.0475	30.3297	0.0855	0.0036	0.0062
72	8.0406	30.3286	0	0	0
73	8.2046	30.3563	2.0389	0.0912	0.1651
74	8.0406	30.3286	-0.0007	-0.0001	0.0001
75	8.0406	30.3286	0.0001	0	0
76	8.0406	30.3286	0	0	0
77	8.0408	30.3287	0.0021	0.0001	0.0001
78	8.0406	30.3286	0	0	0
79	8.0392	30.3287	-0.0173	0.0001	0.0061
80	8.0406	30.3286	0	0	0
81	8.0568	30.3313	0.201	0.0087	0.0165
82	8.0406	30.3286	0	0	0

83	8.0421	30.3289	0.0179	0.0008	0.0016
84	8.0406	30.3286	0	0	0
85	8.577	30.2773	6.6713	-0.1691	-8.4522

E.6 Design Beta – 1- σ Results

Table E.6 summarizes the results of 1- σ perturbation analysis on design Beta.

Table E.6 – Design Beta 1- σ Results

Run #	GM	PM	Δ GM (%)	Δ PM (%)	Δ ITAE (%)
1	8.0406	30.3286	0	0	0
2	8.5619	30.4863	6.4829	0.5198	0.4104
3	7.6847	30.4799	-4.4263	0.4986	0.3669
4	8.6483	30.4865	7.5571	0.5205	0.4042
5	7.8356	30.48	-2.55	0.4991	0.3664
6	8.5021	30.1495	5.7396	-0.5907	-4.9592
7	7.6284	30.1423	-5.127	-0.6144	-5.2838
8	8.5896	30.1497	6.8277	-0.59	-4.9741
9	7.779	30.1425	-3.2544	-0.6139	-5.2901
10	7.0241	23.138	-12.6423	-23.709	24.1368
11	5.4979	27.8558	-31.623	-8.1534	-3.8081
12	6.9456	22.7478	-13.6192	-24.9958	14.1565
13	5.4376	27.4406	-32.3737	-9.5226	-5.2003
14	6.9576	23.1255	-13.4697	-23.7502	23.9432
15	5.4119	27.8293	-32.6926	-8.2408	-3.9098
16	6.8796	22.7343	-14.4401	-25.0403	13.9868
17	5.3521	27.4129	-33.4373	-9.614	-5.2098
18	8.0732	31.0259	0.4045	2.2991	-0.0745
19	7.97	29.6008	-0.8785	-2.3999	-1.2786
20	8.2002	31.0261	1.9848	2.2996	-0.0812
21	8.0969	29.601	0.6993	-2.3992	-1.2876
22	7.9816	31.0101	-0.7336	2.2469	-0.1319
23	7.8794	29.5853	-2.0058	-2.4511	-1.4114
24	8.1085	31.0103	0.844	2.2474	-0.1381
25	8.006	29.5855	-0.4307	-2.4504	-1.4207
26	7.0321	23.8881	-12.5425	-21.2359	18.2935
27	5.7981	28.3607	-27.8896	-6.4888	-0.1154
28	6.8992	21.9785	-14.1959	-27.5322	23.39
29	5.6817	26.8958	-29.3372	-11.3189	-6.1026
30	7.1628	23.8822	-10.9178	-21.2554	18.2057
31	5.289	28.3514	-34.2217	-6.5193	-0.3767

32	7.02	21.9704	-12.6932	-27.559	23.4494
33	5.1921	26.884	-35.4271	-11.3579	-6.3321
34	8.6822	30.3361	7.9794	0.0247	0.0144
35	8.5715	30.345	6.6028	0.054	0.0551
36	7.8738	30.3295	-2.0745	0.0029	-0.027
37	7.6874	30.338	-4.3928	0.0307	0.013
38	8.5904	30.3205	6.8375	-0.0269	-0.0758
39	8.4795	30.3294	5.4585	0.0023	-0.0351
40	7.7826	30.3139	-3.2096	-0.0486	-0.1189
41	7.5982	30.3223	-5.503	-0.0209	-0.0789
42	7.0147	22.9496	-12.7589	-24.3302	21.8106
43	5.4231	27.6431	-32.5538	-8.8547	-3.3309
44	6.6564	22.9586	-17.2151	-24.3005	21.8262
45	5.2579	27.6558	-34.6086	-8.813	-3.2544
46	7.2364	22.9498	-10.0015	-24.3296	21.8088
47	5.583	27.6433	-30.5657	-8.8542	-3.3543
48	6.9413	22.9589	-13.672	-24.2998	21.825
49	5.4139	27.6559	-32.668	-8.8125	-3.2811
50	8.1865	31.194	1.8145	2.8532	2.2042
51	8.0854	29.7221	0.5571	-2	0.0956
52	8.0474	31.2021	0.0846	2.88	2.2303
53	7.9437	29.7308	-1.2059	-1.9713	0.1528
54	8.1301	30.798	1.1124	1.5477	-8.1156
55	8.0281	29.43	-0.1553	-2.9631	-4.2686
56	7.9898	30.8067	-0.6323	1.5763	-8.0636
57	7.8851	29.4395	-1.9339	-2.9318	-4.2223

E.7 Design Gamma – 3- σ Results

Table E.7 summarizes the results of 3- σ perturbation analysis on design Gamma.

Table E.7 – Design Gamma 3- σ Results

Run #	GM	PM	Δ GM (%)	Δ PM (%)	Δ ITAE (%)
1	9.9394	33.8980	0.0000	0.0000	0.0000
2	9.8509	33.8705	-0.8905	-0.0810	-0.5750
3	8.2052	31.4913	-17.4481	-7.0999	-8.3124
4	9.8861	33.8827	-0.5360	-0.0450	-0.4659
5	10.0289	33.9252	0.9003	0.0802	0.3472
6	9.7821	33.7916	-1.5830	-0.3137	-0.2837

7	9.8975	33.4053	-0.4221	-1.4535	0.2028
8	9.7439	29.4300	-1.9668	-13.1808	3.8902
9	9.9394	33.9099	0.0001	0.0350	-0.0091
10	9.8520	33.3193	-0.8800	-1.7071	0.2406
11	9.5841	33.9115	-3.5750	0.0398	0.0796
12	11.9212	33.8898	19.9388	-0.0241	-0.3654
13	10.0295	33.8984	0.9066	0.0012	-0.0295
14	9.2663	33.9129	-6.7718	0.0439	0.1595
15	9.9133	33.7969	-0.2626	-0.2983	0.3935
16	9.8347	32.8667	-1.0535	-3.0424	-2.4958
17	9.9394	33.9090	0.0002	0.0325	-0.0260
18	9.8830	33.7085	-0.5681	-0.5589	1.5302
19	9.9398	33.8957	0.0040	-0.0068	1.9377
20	9.9401	34.1428	0.0069	0.7222	-0.6258
21	9.9393	33.8999	-0.0009	0.0057	0.3019
22	9.9404	34.0933	0.0097	0.5763	2.5226
23	9.9394	33.8980	0.0000	0.0000	0.0000
24	9.9394	33.8980	0.0000	0.0000	0.0000
25	9.9394	33.8980	0.0000	0.0000	0.0000
26	9.9394	33.8980	0.0000	0.0000	0.0000
27	9.9377	33.8977	-0.0173	-0.0009	-0.0057
28	9.9394	33.8980	0.0000	0.0000	0.0000
29	9.9361	33.8975	-0.0330	-0.0016	-0.0083
30	9.9394	33.8980	0.0000	0.0000	0.0000
31	9.8607	33.8843	-0.7922	-0.0403	-0.2227
32	9.9394	33.8980	-0.0001	0.0001	0.0000
33	9.9394	33.8980	0.0000	0.0000	0.0000
34	9.9394	33.8980	0.0000	0.0000	0.0000
35	9.9393	33.8980	-0.0008	0.0000	-0.0001
36	9.9394	33.8980	0.0000	0.0000	0.0000
37	9.9400	33.8980	0.0062	0.0001	-0.0094
38	9.9394	33.8980	0.0000	0.0000	0.0000
39	9.9317	33.8967	-0.0781	-0.0037	-0.0225
40	9.9394	33.8980	0.0000	0.0000	0.0000
41	9.9387	33.8979	-0.0070	-0.0003	-0.0022
42	9.9394	33.8980	0.0000	0.0000	0.0000
43	9.5584	33.9875	-3.8339	0.2641	-3.2986
44	10.0289	33.9260	0.9000	0.0827	0.5920
45	12.0715	26.7038	21.4505	-21.2232	22.8955
46	9.9930	33.9134	0.5395	0.0454	0.4774
47	9.8489	33.8715	-0.9112	-0.0780	-0.3447
48	9.7821	33.7916	-1.5830	-0.3137	-0.2837
49	9.9805	34.3991	0.4135	1.4783	-0.2176
50	10.0916	37.7378	1.5306	11.3276	-5.2990
51	9.9394	33.8861	-0.0001	-0.0350	0.0091
52	10.0198	34.4538	0.8085	1.6398	-0.1193

53	10.1642	33.8847	2.2617	-0.0391	-0.0954
54	8.6417	33.9115	-13.0563	0.0398	-0.7393
55	9.8510	33.8976	-0.8894	-0.0012	0.0328
56	10.4402	33.8840	5.0384	-0.0412	-0.1668
57	9.9653	34.0252	0.2607	0.3754	-0.5466
58	10.0261	34.4482	0.8717	1.6232	1.4947
59	9.9394	33.8870	-0.0002	-0.0325	0.0261
60	9.9909	34.0795	0.5183	0.5354	-2.2049
61	9.9390	33.9003	-0.0040	0.0068	-1.8601
62	9.9387	33.6532	-0.0069	-0.7221	0.6349
63	9.9395	33.8961	0.0009	-0.0057	-0.2992
64	9.9385	33.7027	-0.0096	-0.5762	-2.3442
65	9.9394	33.8980	0.0000	0.0000	0.0000
66	9.9394	33.8980	0.0000	0.0000	0.0000
67	9.9394	33.8980	0.0000	0.0000	0.0000
68	9.9394	33.8980	0.0000	0.0000	0.0000
69	9.9418	33.8984	0.0242	0.0013	0.0076
70	9.9394	33.8980	0.0000	0.0000	0.0000
71	9.9440	33.8987	0.0458	0.0022	0.0113
72	9.9394	33.8980	0.0000	0.0000	0.0000
73	10.0498	33.9168	1.1109	0.0555	0.3038
74	9.9394	33.8980	0.0001	-0.0001	0.0000
75	9.9394	33.8980	0.0000	0.0000	0.0000
76	9.9394	33.8980	0.0000	0.0000	0.0000
77	9.9395	33.8980	0.0011	0.0001	0.0002
78	9.9394	33.8980	0.0000	0.0000	0.0000
79	9.9386	33.8980	-0.0085	-0.0001	0.0127
80	9.9394	33.8980	0.0000	0.0000	0.0000
81	9.9501	33.8997	0.1073	0.0051	0.0305
82	9.9394	33.8980	0.0000	0.0000	0.0000
83	9.9404	33.8982	0.0096	0.0005	0.0029
84	9.9394	33.8980	0.0000	0.0000	0.0000
85	8.4812	33.6867	-14.6708	-0.6232	-2.3081

E.8 Design Gamma – 1- σ Results

Table E.8 summarizes the results of 1- σ perturbation analysis on design Gamma.

Table E.8 – Design Gamma 1- σ Results

Run #	GM	PM	Δ GM (%)	Δ PM (%)	Δ ITAE (%)
1	9.9394	33.8980	0.0000	0.0000	0.0000
2	9.4633	34.1281	-4.7904	0.6787	-0.3899
3	9.0410	34.1195	-9.0389	0.6534	-0.4421
4	9.5042	34.1284	-4.3790	0.6796	-0.3986
5	9.2285	34.1197	-7.1530	0.6541	-0.4458
6	9.3817	33.6287	-5.6116	-0.7945	-1.6567
7	9.0095	33.6191	-9.3555	-0.8226	-1.4614
8	9.4224	33.6290	-5.2017	-0.7936	-1.6757
9	9.1942	33.6194	-7.4980	-0.8220	-1.4821
10	12.1233	26.8852	21.9718	-20.6880	22.5274
11	8.2663	31.7757	-16.8335	-6.2609	-7.8544
12	12.0714	26.3493	21.4494	-22.2690	20.9743
13	8.2049	31.1871	-17.4507	-7.9974	-10.6310
14	12.0726	26.8757	21.4614	-20.7161	22.2603
15	8.2066	31.7585	-17.4335	-6.3116	-7.9578
16	12.0210	26.3387	20.9428	-22.3002	20.6993
17	8.1457	31.1690	-18.0467	-8.0505	-10.7466
18	9.9969	35.2909	0.5785	4.1091	-0.6678
19	9.8827	32.4689	-0.5711	-4.2158	1.7611
20	10.0573	35.2911	1.1861	4.1098	-0.6935
21	9.9417	32.4692	0.0230	-4.2149	1.7461
22	9.9351	35.2772	-0.0435	4.0688	-0.8253
23	9.8216	32.4564	-1.1851	-4.2527	1.5706
24	9.9952	35.2775	0.5607	4.0695	-0.8517
25	9.8804	32.4567	-0.5942	-4.2518	1.5553
26	11.9449	28.2533	20.1773	-16.6521	19.9786
27	7.8482	32.9251	-21.0399	-2.8700	-9.8956
28	11.8119	24.9778	18.8385	-26.3147	25.4685
29	7.6981	30.0254	-22.5496	-11.4241	-6.7939
30	10.2324	28.2454	2.9474	-16.6753	20.4047
31	7.1894	32.9153	-27.6677	-2.8990	-9.9806
32	10.2141	24.9698	2.7639	-26.3385	25.1315
33	7.1471	30.0132	-28.0937	-11.4603	-6.6855
34	9.6346	33.9027	-3.0666	0.0139	-0.2586
35	9.3046	33.9119	-6.3872	0.0411	-0.1855
36	9.0806	33.8961	-8.6407	-0.0056	0.1760

37	9.2215	33.9048	-7.2229	0.0201	0.2237
38	9.5743	33.8921	-3.6739	-0.0174	-0.4310
39	9.2466	33.9013	-6.9709	0.0096	-0.3575
40	9.0137	33.8855	-9.3139	-0.0368	0.0135
41	9.1568	33.8942	-7.8743	-0.0113	0.0624
42	12.0359	26.6957	21.0923	-21.2469	22.8850
43	8.2451	31.4854	-17.0468	-7.1174	-8.3552
44	11.9972	26.7115	20.7028	-21.2003	22.9166
45	8.0838	31.4970	-18.6688	-7.0830	-8.2347
46	12.1323	26.6960	22.0629	-21.2460	22.8718
47	8.3152	31.4856	-16.3415	-7.1167	-8.3873
48	12.0827	26.7118	21.5630	-21.1993	22.9039
49	8.1459	31.4972	-18.0443	-7.0824	-8.2715
50	10.1103	35.5145	1.7187	4.7688	-1.9609
51	10.0028	32.6984	0.6381	-3.5390	1.3160
52	9.9245	35.5241	-0.1498	4.7970	-1.9609
53	9.8044	32.7052	-1.3582	-3.5188	1.3681
54	10.0505	34.9272	1.1174	3.0362	-2.5669
55	9.9414	32.2387	0.0200	-4.8949	-0.1417
56	9.8591	34.9359	-0.8084	3.0620	-2.4149
57	9.7371	32.2479	-2.0354	-4.8677	-0.0932

E.9 Design Delta – 3- σ Results

Table E.9 summarizes the results of 3- σ perturbation analysis on design Delta.

Table E.9 – Design Delta 3- σ Results

Run #	GM	PM	Δ GM (%)	Δ PM (%)	Δ ITAE (%)
1	19.3125	34.2330	0.0000	0.0000	0.0000
2	19.3968	34.2425	0.4361	0.0279	-0.5316
3	20.9699	33.8328	8.5819	-1.1691	-8.0775
4	19.3800	34.2408	0.3492	0.0227	-0.4298
5	19.2522	34.2156	-0.3124	-0.0509	0.2332
6	19.3447	34.2313	0.1666	-0.0050	-0.1880
7	19.2587	34.2238	-0.2787	-0.0268	0.4063
8	19.1593	34.2075	-0.7934	-0.0744	1.2166
9	19.3125	34.2330	0.0000	-0.0001	0.0001
10	19.1141	34.1917	-1.0273	-0.1205	1.2988
11	19.3050	34.2316	-0.0391	-0.0041	0.0436
12	19.3113	34.2328	-0.0062	-0.0005	0.0041
13	19.3125	34.2330	0.0000	0.0000	-0.0001

14	19.2984	34.2298	-0.0730	-0.0093	0.0731
15	19.2459	34.2183	-0.3448	-0.0429	0.5379
16	19.2049	34.2140	-0.5573	-0.0553	0.6715
17	19.3125	34.2329	0.0000	-0.0003	0.0000
18	19.1224	34.1842	-0.9846	-0.1426	1.3843
19	19.0418	34.2261	-1.4019	-0.0202	3.4245
20	19.7467	34.5991	2.2482	1.0695	-0.9492
21	19.2733	34.2319	-0.2031	-0.0032	0.4914
22	19.2227	34.5150	-0.4649	0.8237	4.4796
23	19.3125	34.2330	0.0000	0.0000	0.0000
24	19.3125	34.2330	0.0000	0.0000	0.0000
25	19.3125	34.2330	0.0000	0.0000	0.0000
26	19.3125	34.2330	0.0000	0.0000	0.0000
27	19.3133	34.2331	0.0042	0.0002	-0.0054
28	19.3125	34.2330	0.0000	0.0000	0.0000
29	19.3137	34.2331	0.0061	0.0004	-0.0080
30	19.3125	34.2330	0.0000	0.0000	0.0000
31	19.3440	34.2363	0.1632	0.0096	-0.2110
32	19.3125	34.2330	0.0000	0.0000	0.0000
33	19.3125	34.2330	0.0000	0.0000	0.0000
34	19.3125	34.2330	0.0000	0.0000	0.0000
35	19.3125	34.2330	0.0001	0.0000	-0.0001
36	19.3125	34.2330	0.0000	0.0000	0.0000
37	19.3139	34.2331	0.0070	0.0005	-0.0085
38	19.3125	34.2330	0.0000	0.0000	0.0000
39	19.3157	34.2333	0.0164	0.0010	-0.0213
40	19.3125	34.2330	0.0000	0.0000	0.0000
41	19.3128	34.2330	0.0016	0.0001	-0.0020
42	19.3125	34.2330	0.0000	0.0000	0.0000
43	18.8844	34.2001	-2.2168	-0.0961	2.9190
44	19.2274	34.2231	-0.4406	-0.0289	0.5426
45	16.3371	31.8279	-15.4067	-7.0257	16.7516
46	19.2445	34.2250	-0.3520	-0.0233	0.4368
47	19.3732	34.2504	0.3143	0.0509	-0.2326
48	19.3447	34.2313	0.1666	-0.0050	-0.1880
49	19.3679	34.2424	0.2869	0.0276	-0.3160
50	19.5207	34.2679	1.0778	0.1021	-1.3044
51	19.3125	34.2330	0.0000	0.0001	-0.0001
52	19.4976	34.2684	0.9584	0.1035	-1.1708
53	19.3201	34.2344	0.0391	0.0041	-0.0434
54	19.3141	34.2332	0.0084	0.0006	-0.0130
55	19.3125	34.2330	0.0000	0.0000	0.0001
56	19.3256	34.2358	0.0675	0.0083	-0.0686
57	19.3801	34.2478	0.3497	0.0433	-0.5323
58	19.4592	34.2599	0.7593	0.0785	-0.5862
59	19.3125	34.2331	0.0000	0.0003	0.0000

60	19.4878	34.2754	0.9077	0.1238	-1.2038
61	19.5971	34.2399	1.4735	0.0201	-3.3996
62	18.8863	33.8668	-2.2069	-1.0698	0.9618
63	19.3520	34.2341	0.2044	0.0032	-0.4904
64	19.3781	33.9504	0.3397	-0.8254	-4.4027
65	19.3125	34.2330	0.0000	0.0000	0.0000
66	19.3125	34.2330	0.0000	0.0000	0.0000
67	19.3125	34.2330	0.0000	0.0000	0.0000
68	19.3125	34.2330	0.0000	0.0000	0.0000
69	19.3114	34.2329	-0.0056	-0.0003	0.0073
70	19.3125	34.2330	0.0000	0.0000	0.0000
71	19.3109	34.2328	-0.0082	-0.0005	0.0107
72	19.3125	34.2330	0.0000	0.0000	0.0000
73	19.2439	34.2286	-0.3554	-0.0129	0.2872
74	19.3125	34.2330	0.0000	0.0000	0.0000
75	19.3125	34.2330	0.0000	0.0000	0.0000
76	19.3125	34.2330	0.0000	0.0000	0.0000
77	19.3125	34.2330	-0.0001	0.0000	0.0002
78	19.3125	34.2330	0.0000	0.0000	0.0000
79	19.3107	34.2328	-0.0095	-0.0006	0.0115
80	19.3125	34.2330	0.0000	0.0000	0.0000
81	19.3083	34.2325	-0.0221	-0.0013	0.0289
82	19.3125	34.2330	0.0000	0.0000	0.0000
83	19.3121	34.2329	-0.0021	-0.0001	0.0028
84	19.3125	34.2330	0.0000	0.0000	0.0000
85	20.1349	34.2632	4.2584	0.0883	-7.8403

E.10 Design Delta – 1- σ Results

Table E.10 summarizes the results of 1- σ perturbation analysis on design Delta.

Table E.10 – Design Delta 1- σ Results

Run #	GM	PM	Δ GM (%)	Δ PM (%)	Δ ITAE (%)
1	19.3125	34.2330	0.0000	0.0000	0.0000
2	19.3567	34.2410	0.2288	0.0234	-0.2652
3	19.3558	34.2409	0.2241	0.0230	-0.2569
4	19.3567	34.2410	0.2288	0.0234	-0.2651
5	19.3558	34.2409	0.2241	0.0230	-0.2568
6	19.2736	34.2260	-0.2018	-0.0204	0.3228
7	19.2726	34.2259	-0.2065	-0.0207	0.3331
8	19.2736	34.2260	-0.2018	-0.0204	0.3228

9	19.2726	34.2259	-0.2065	-0.0207	0.3331
10	12.2238	31.8354	-36.7054	-7.0038	16.7039
11	20.2468	33.8380	4.8374	-1.1538	-7.9023
12	12.2313	31.8185	-36.6666	-7.0531	17.3207
13	20.2485	33.8266	4.8466	-1.1871	-7.8128
14	17.3552	31.8381	-10.1348	-6.9960	16.4607
15	21.0252	33.8396	8.8680	-1.1492	-7.9910
16	17.2720	31.8212	-10.5657	-7.0452	17.0810
17	20.9420	33.8282	8.4373	-1.1824	-7.9335
18	19.3619	34.2422	0.2557	0.0268	-0.2234
19	19.2436	34.2223	-0.3567	-0.0313	0.4442
20	19.3619	34.2422	0.2557	0.0268	-0.2234
21	19.2436	34.2223	-0.3567	-0.0313	0.4441
22	19.3862	34.2446	0.3813	0.0339	-0.3677
23	19.2680	34.2248	-0.2307	-0.0238	0.2852
24	19.3862	34.2446	0.3813	0.0339	-0.3678
25	19.2680	34.2248	-0.2307	-0.0238	0.2851
26	16.3233	31.8394	-15.4782	-6.9921	16.2598
27	21.0325	33.8410	8.9061	-1.1450	-8.3093
28	16.3445	31.8177	-15.3684	-7.0554	17.2289
29	20.9143	33.8255	8.2938	-1.1902	-7.6353
30	16.3303	31.8392	-15.4420	-6.9926	16.2694
31	21.0316	33.8409	8.9013	-1.1453	-8.3111
32	16.3515	31.8175	-15.3321	-7.0559	17.2333
33	20.9134	33.8255	8.2890	-1.1905	-7.6364
34	19.3028	34.2322	-0.0506	-0.0023	0.0620
35	19.2977	34.2313	-0.0765	-0.0050	0.0900
36	19.3019	34.2321	-0.0552	-0.0027	0.0717
37	19.2968	34.2311	-0.0814	-0.0054	0.1004
38	19.3270	34.2347	0.0752	0.0050	-0.1007
39	19.3220	34.2338	0.0493	0.0023	-0.0728
40	19.3262	34.2346	0.0706	0.0047	-0.0909
41	19.3211	34.2337	0.0444	0.0020	-0.0623
42	16.3357	31.8284	-15.4141	-7.0242	16.7296
43	20.9724	33.8331	8.5949	-1.1680	-8.0872
44	16.3386	31.8274	-15.3992	-7.0272	16.7736
45	20.9674	33.8324	8.5689	-1.1701	-8.0677
46	16.3356	31.8284	-15.4142	-7.0242	16.7296
47	20.9724	33.8331	8.5949	-1.1680	-8.0873
48	16.3385	31.8274	-15.3994	-7.0272	16.7736
49	20.9674	33.8324	8.5689	-1.1701	-8.0678
50	19.4210	34.2516	0.5615	0.0544	-0.2716
51	19.3026	34.2321	-0.0515	-0.0027	0.0363
52	19.4159	34.2507	0.5352	0.0518	-0.2461
53	19.2976	34.2311	-0.0775	-0.0054	0.0685
54	19.3377	34.2369	0.1301	0.0116	0.0816

55	19.2195	34.2170	-0.4816	-0.0467	0.4592
56	19.3326	34.2360	0.1040	0.0088	0.1109
57	19.2145	34.2161	-0.5074	-0.0494	0.4893

APPENDIX F

Dispersion Analysis Time & Frequency Response Histories

The purpose of the $3\text{-}\sigma$ and combined $1\text{-}\sigma$ dispersion cases is to test the robust stability of the control design in question. Appendix E contains detailed information on the GM, PM and percent change of these quantities for the four final designs. However, the tabular data does not lend itself well for interpretation. It is a much more concise presentation, and it is easier to determine the stability of a control design by looking a plot of all the dispersion cases' time and frequency responses. In this manner, the stability of the control law to the parameter changes can be quickly deduced. The following appendix presents response histories of control dispersion analysis.

Note: The condition for stability in the Nichols plot is understood as no right-to-left crossings over any of the multiple stability points, which occur at $[180^\circ \pm n \cdot 360^\circ, 0 \text{ dB}]$. For a majority of the designs, the only stability point of importance is the one at $[180^\circ, 0 \text{ dB}]$, because there are no 0 dB crossovers below 180° .

F.1 Full-Order Optimal H_2 Design

From Figure F.1 and Figure F.2 the full-order optimal H_2 design is unstable. The time response shows exponential growth, and the Nichols plot presents several cases with right-to-left crossings over the $[180^\circ, 0 \text{ dB}]$ stability point.

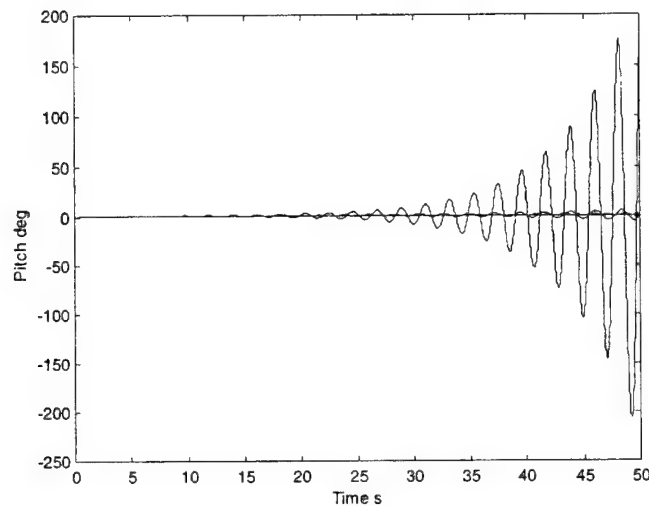


Figure F.1 – Full-Order Optimal H_2 Design $3\text{-}\sigma$ Step Response History

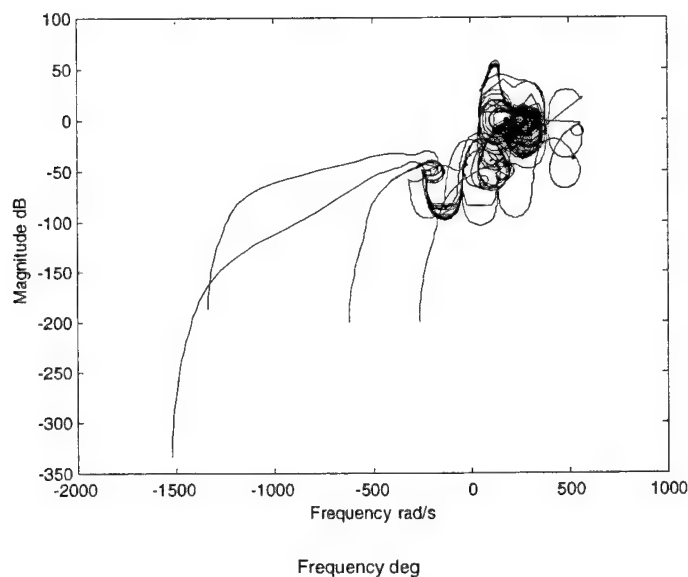


Figure F.2 – Full-Order Optimal H_2 Design $3\text{-}\sigma$ Nichols Plot History

F.2 GA Optimal H_2 Design

Figure F.3 and Figure F.4 show that this controller design is stable for all the $3\text{-}\sigma$ dispersion cases. Figure F.5 and Figure F.6 presents the same conclusion for the $1\text{-}\sigma$ dispersion cases.

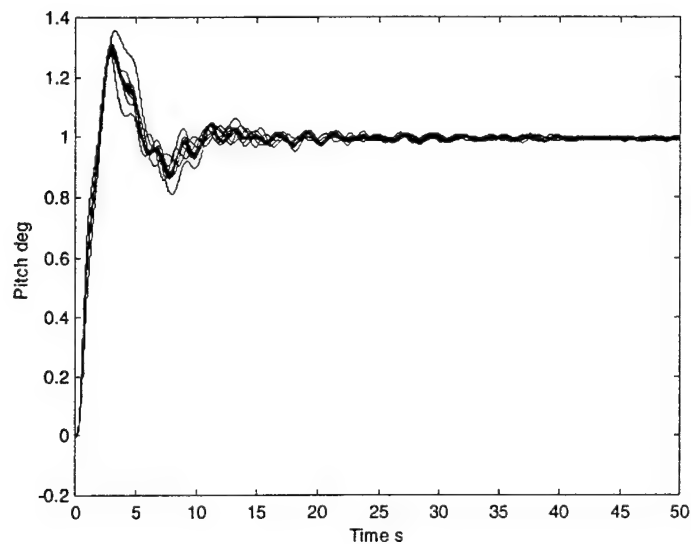


Figure F.3 – GA Optimal H_2 Design $3\text{-}\sigma$ Step Response History

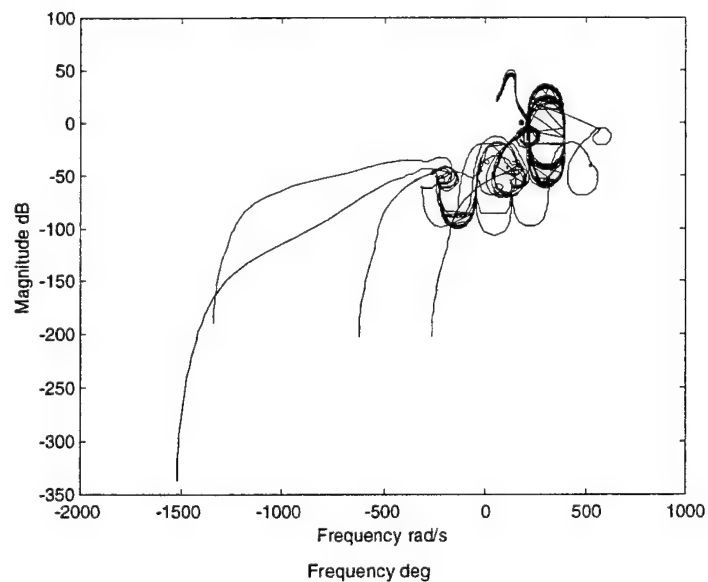


Figure F.4 – GA Optimal H_2 Design $3\text{-}\sigma$ Nichols Plot History

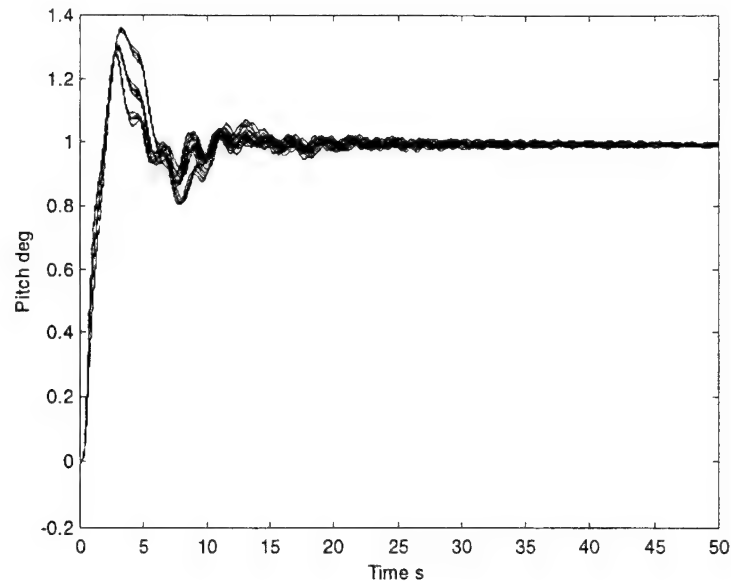


Figure F.5 – GA Optimal H_2 Design 1- σ Step Response History

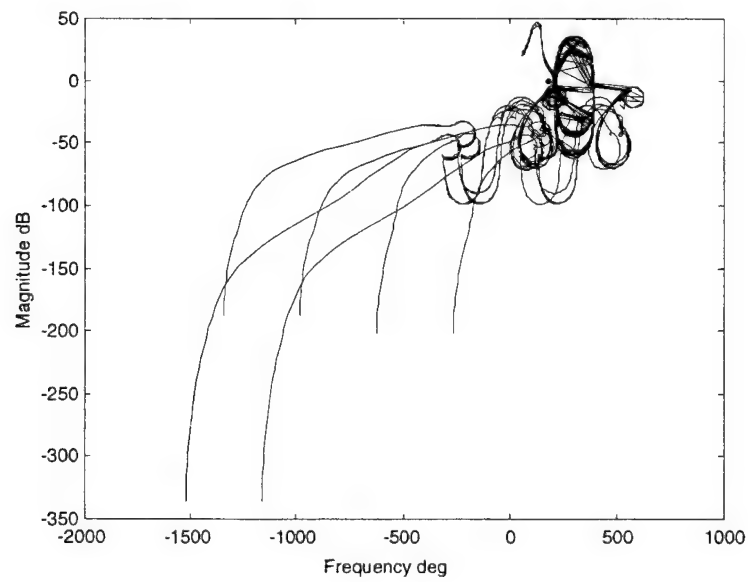


Figure F.6 – GA Optimal H_2 Design 1- σ Nichols Plot History

F.3 GA Sub-Optimal Design

The GA sub-optimal design is shown to be also shown to be stable for all 3- σ and 1- σ cases by Figure F.7, Figure F.8, Figure F.9, and Figure F.10

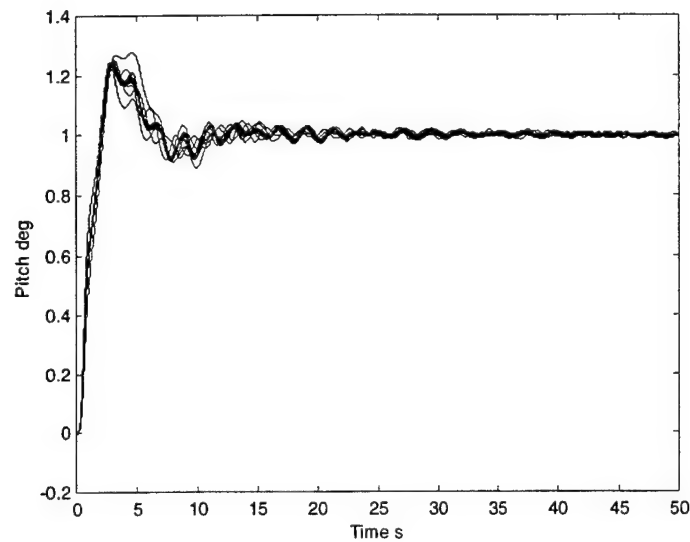


Figure F.7 – GA Sub-Optimal Design 3- σ Step Response History

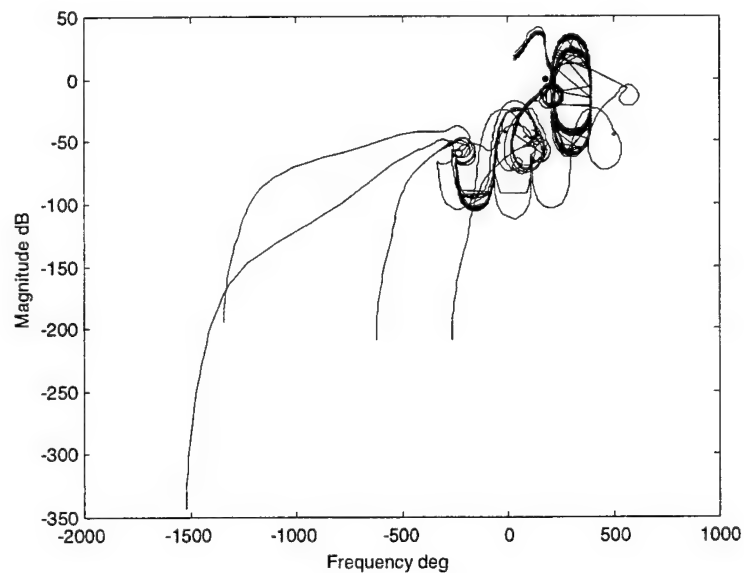


Figure F.8 – GA Sub-Optimal Design 3- σ Nichols Plot History

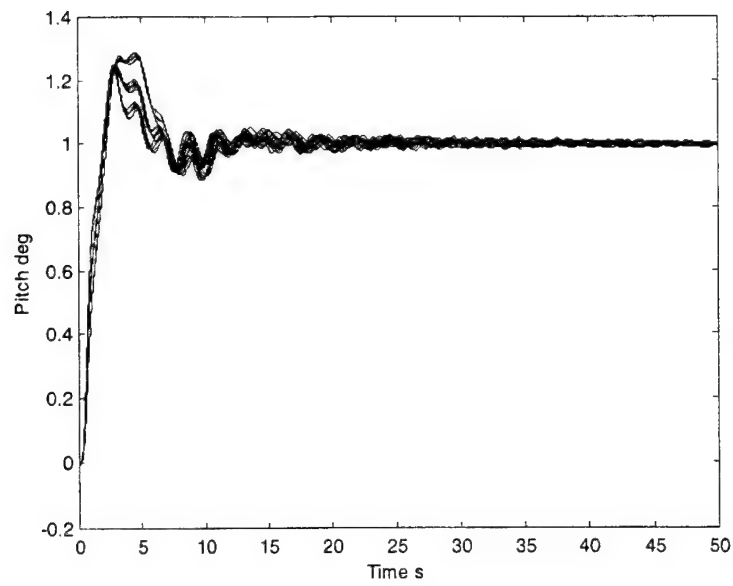


Figure F.9 – GA Sub-Optimal Design 1- σ Step Response History

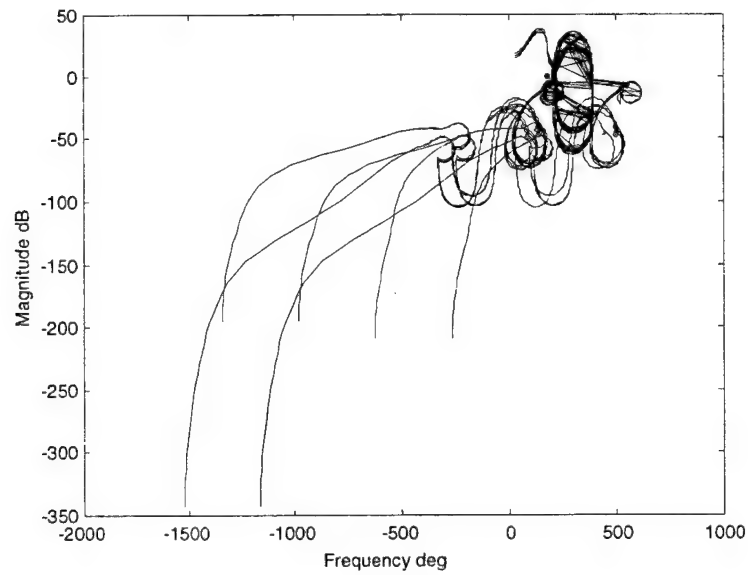


Figure F.10 – GA Sub-Optimal Design 1- σ Nichols Plot History

F.4 $G_{\Delta}=1$, MU Optimal H_2 Design

The instability of this design for both 3- σ cases is obvious in Figure F.11. This can also be determined from the Nichols plot in Figure F.12 as the right-to-left crossing over the $[-540, 0]$ dB stability point.

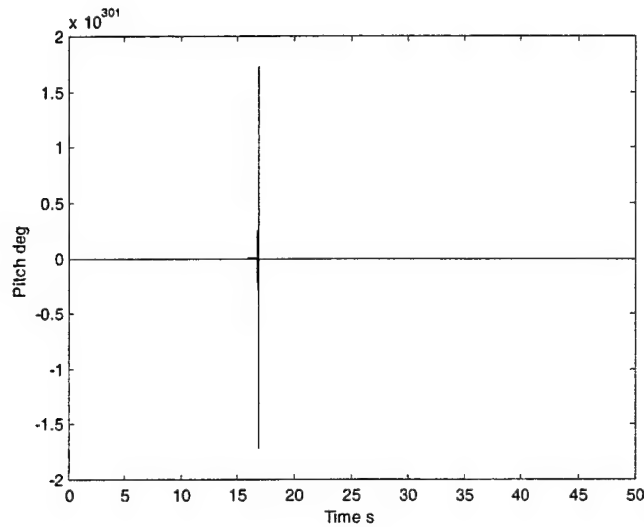


Figure F.11 – $G_{\Delta}=1$, MU Optimal H_2 Design 3- σ Step Response History

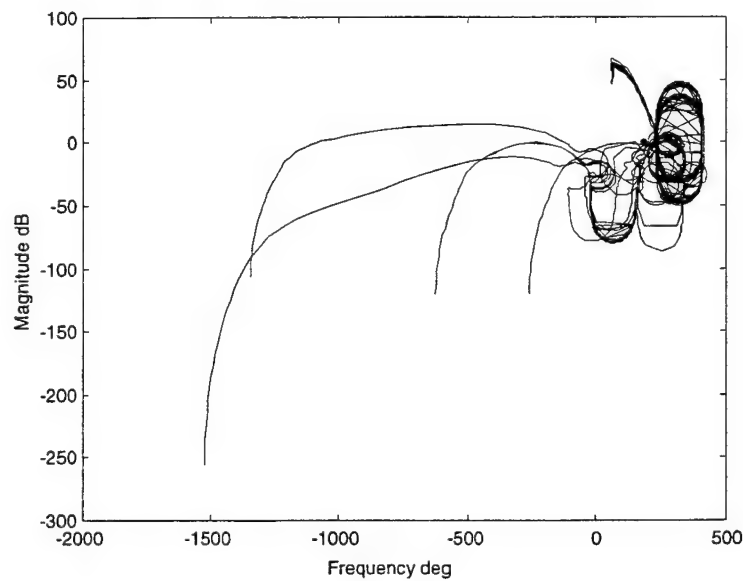


Figure F.12 – $G_{\Delta}=1$, MU Optimal H_2 Design 3- σ Nichols Plot History

F.5 $G_{\Delta}=10$, MU Optimal H_2 Design

Even with the increased cost gain, this design remains unstable as shown by Figure F.13. The results of Figure F.14 do show that the design is closer to preventing the $[-540^\circ, 0^\circ]$ crossing with high frequency attenuation.

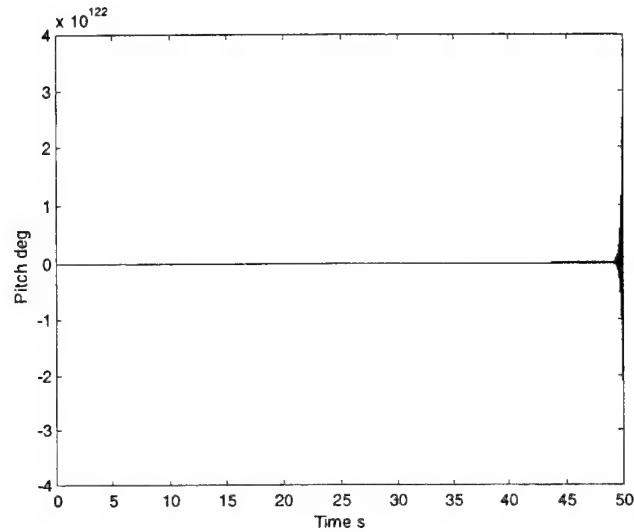


Figure F.13 – $G_{\Delta}=10$, MU Optimal H_2 Design 3- σ Step Response History

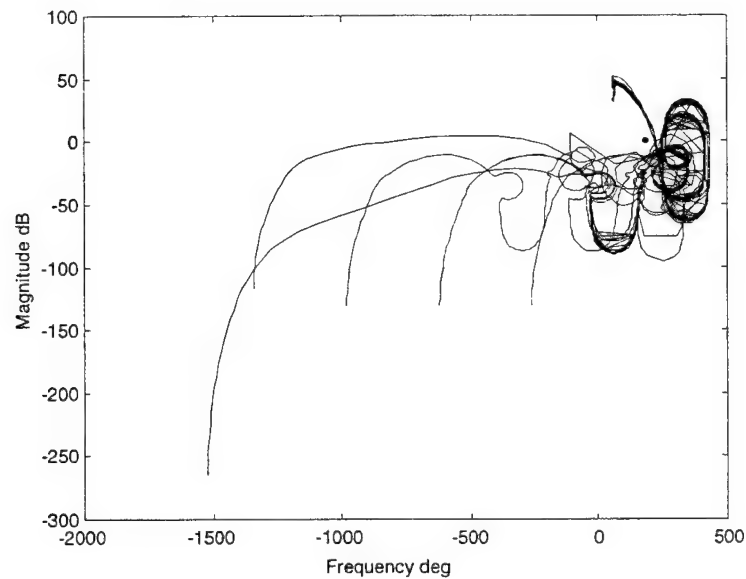


Figure F.14 – $G_{\Delta}=10$, MU Optimal H_2 Design 3- σ Nichols Plot History

F.6 $G_{\Delta}=20$, MU Optimal H_2 Design

After raising the cost gain again, Figure F.15 and Figure F.17 show that the design is stable for all of the perturbation cases. The unstable crossing has also been eliminated in Figure F.16. Also, stability points are added in Figure F.18 to relate the position of areas of open-loop, high frequency amplification.

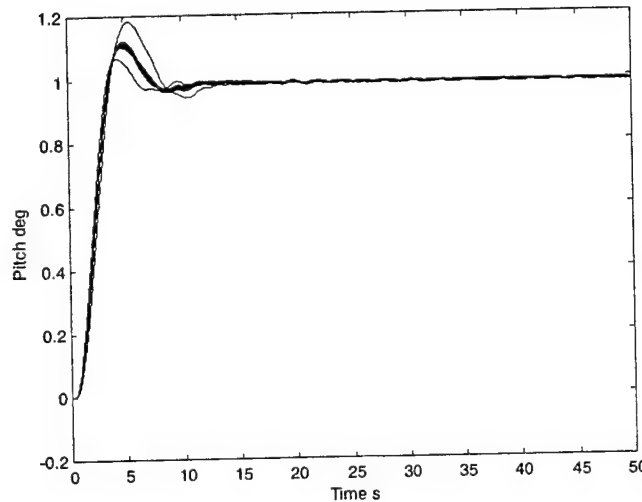


Figure F.15 – $G_{\Delta}=20$, MU Optimal H_2 Design 3- σ Step Response History

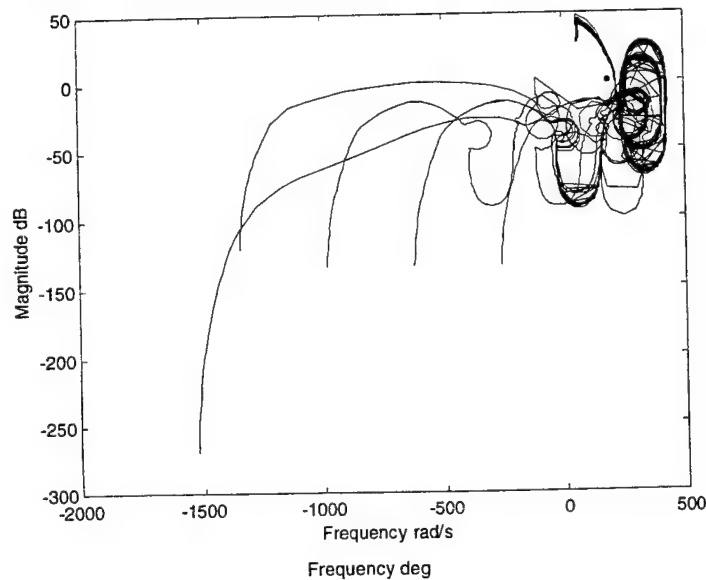


Figure F.16 – $G_{\Delta}=20$, MU Optimal H_2 Design 3- σ Nichols Plot History

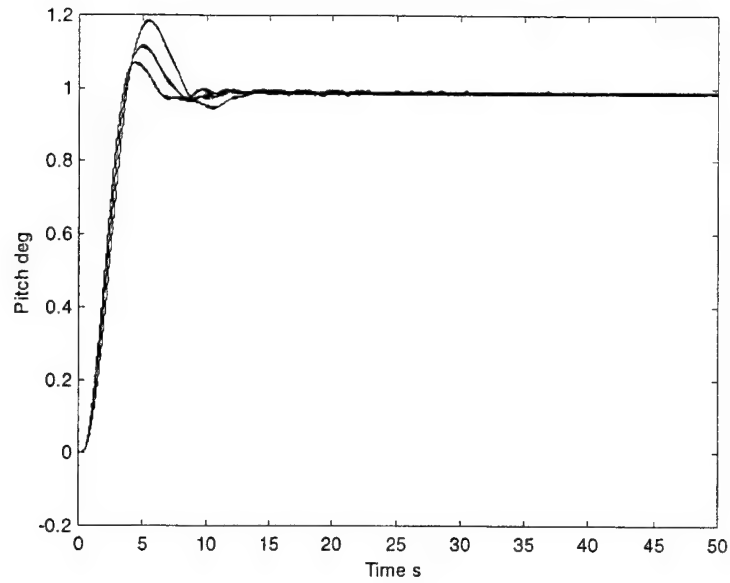


Figure F.17 – $G_{\Delta}=20$, MU Optimal H_2 Design 1- σ Step Response History

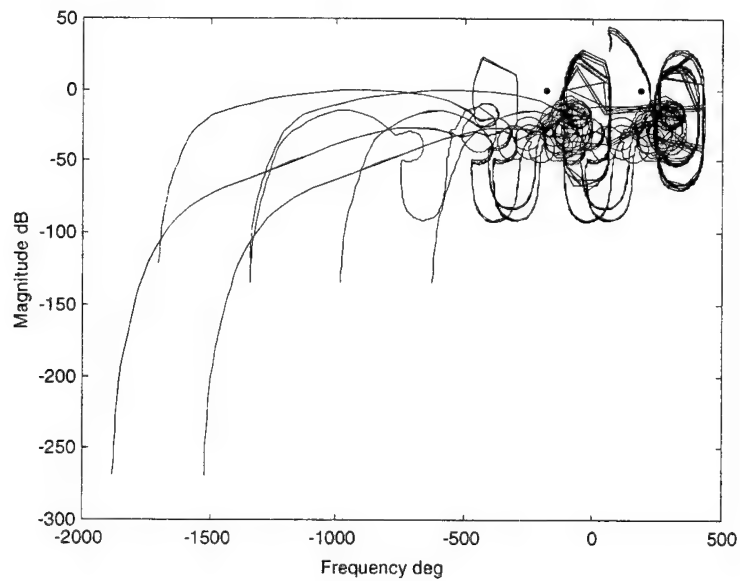


Figure F.18 – $G_{\Delta}=20$, MU Optimal H_2 Design 1- σ Nichols Plot History

F.7 MU Sub-Optimal Design

This sub-optimal design is unstable, Figure F.19 due to a crossing over the $[-540, 0 \text{ dB}]$ stability point in Figure F.20.

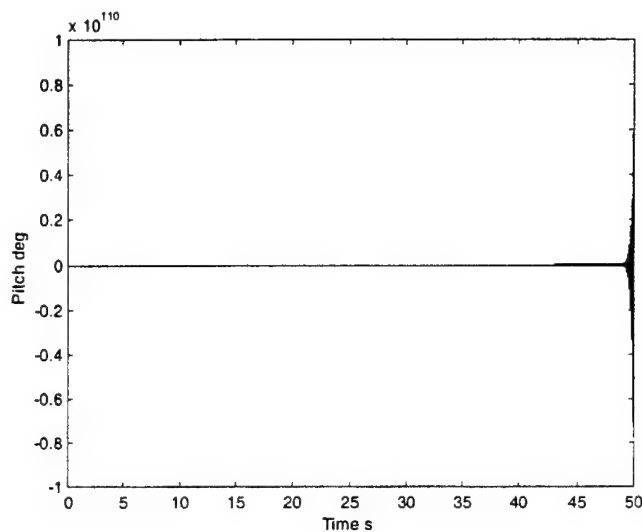


Figure F.19 – MU Sub-Optimal Design 3- σ Step Response History

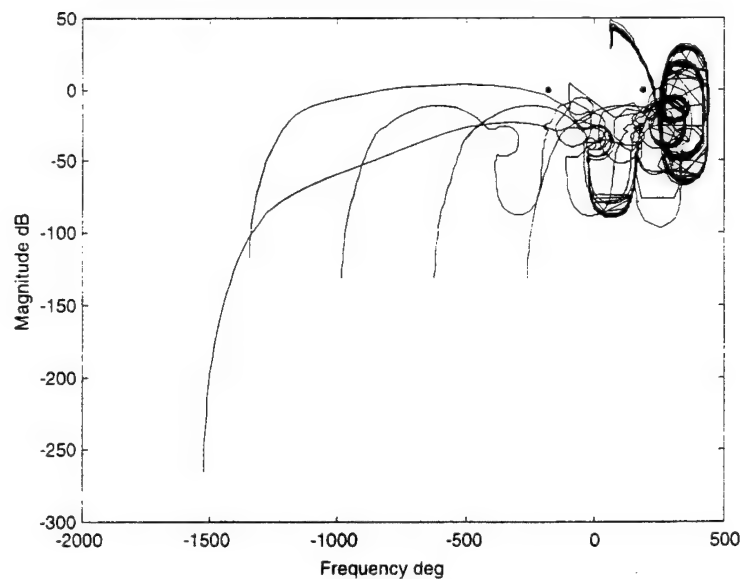


Figure F.20 – MU Sub-Optimal Design 3- σ Nichols Plot History

F.8 Reduced-Order GA Optimal H_2 Design

This reduced-order design shows that it is stable for all of the perturbation cases in Figure F.21, Figure F.22, Figure F.23, and Figure F.24.

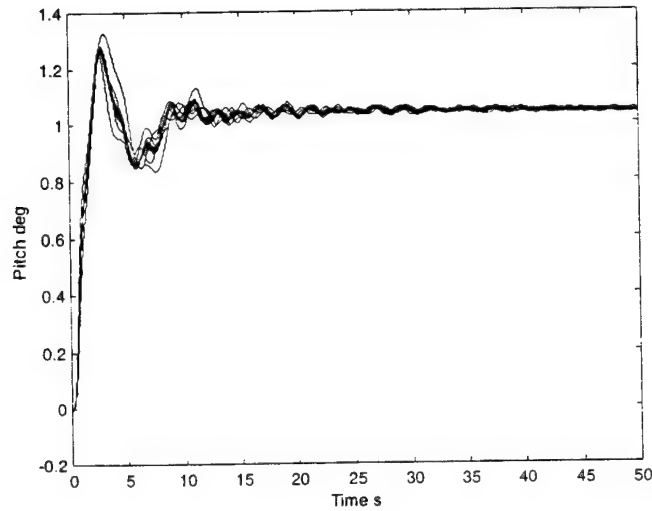


Figure F.21 – Reduced-Order GA Optimal H_2 Design 3- σ Step Response History

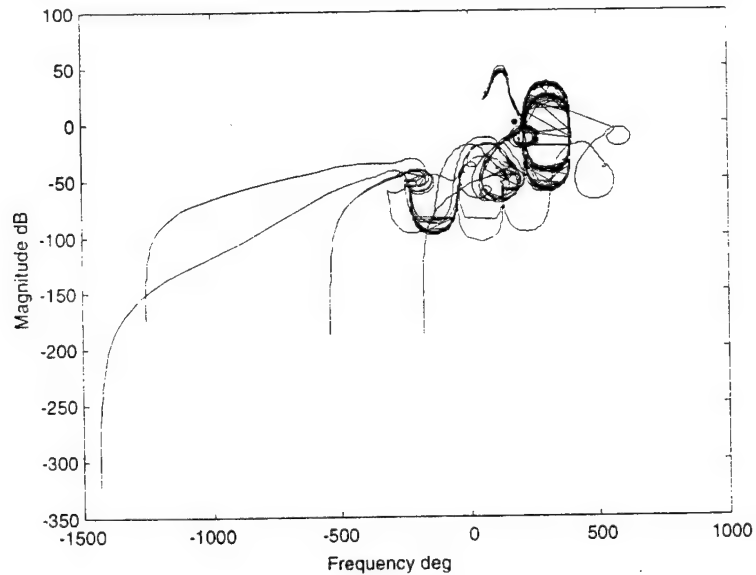


Figure F.22 – Reduced-Order GA Optimal H_2 Design 3- σ Nichols Plot History

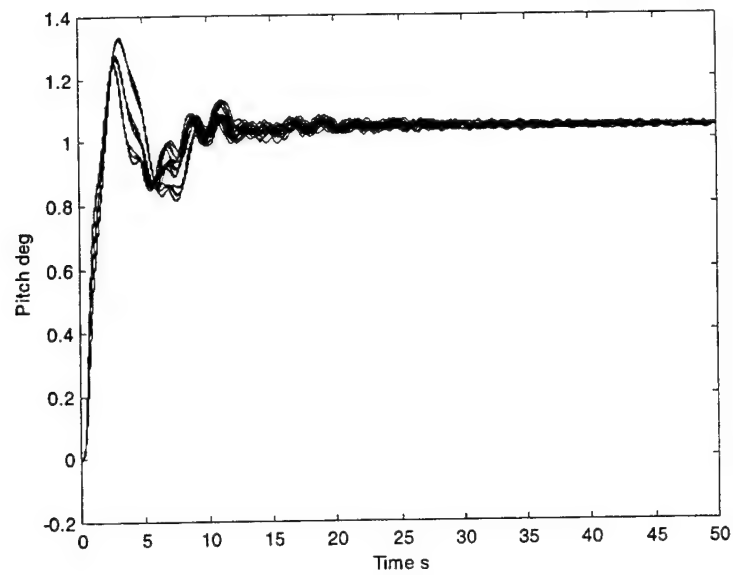


Figure F.23 – Reduced-Order GA Optimal H_2 Design $1-\sigma$ Step Response History

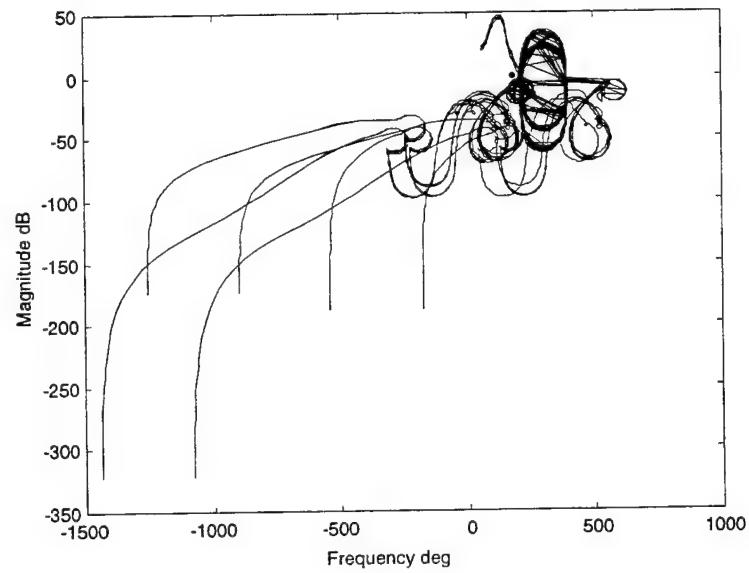


Figure F.24 – Reduced-Order GA Optimal H_2 Design $1-\sigma$ Nichols Plot History

F.9 Reduced-Order MU Optimal H_2 Design

The reduced-order, optimal H_2 Design using MU also shows that it maintains stability for all of the perturbation cases in Figure F.25 and Figure F.27. The responses in Figure F.26 and Figure F.28 show that this stability is maintain in the presence of open-loop, high frequency amplification. However, the multiple stability points all maintain good margins.

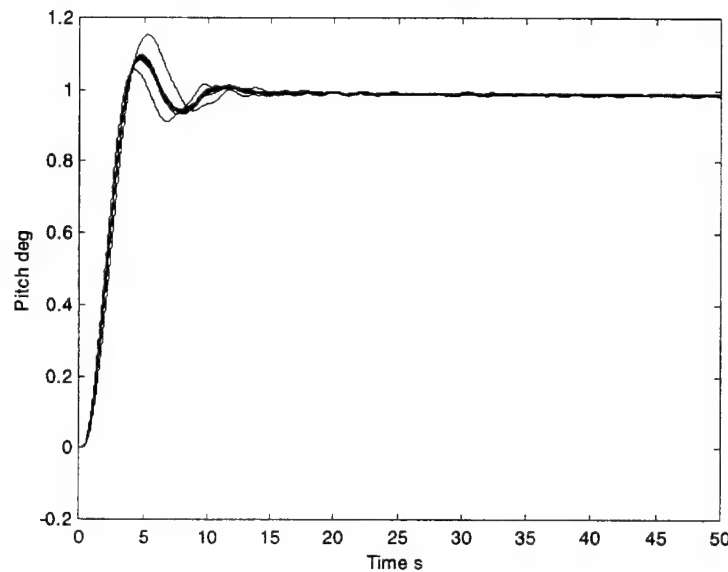


Figure F.25 – Reduced-Order MU Optimal H_2 Design 3- σ Step Response History

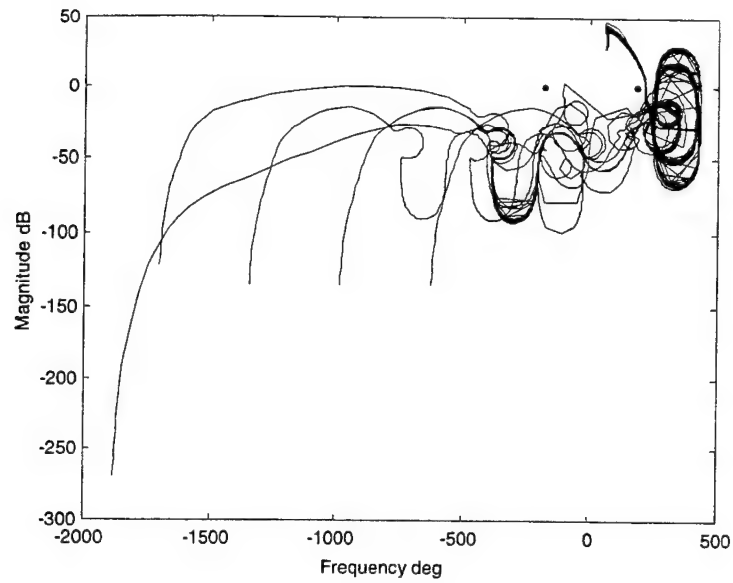


Figure F.26 – Reduced-Order MU Optimal H_2 Design 3- σ Nichols Plot History

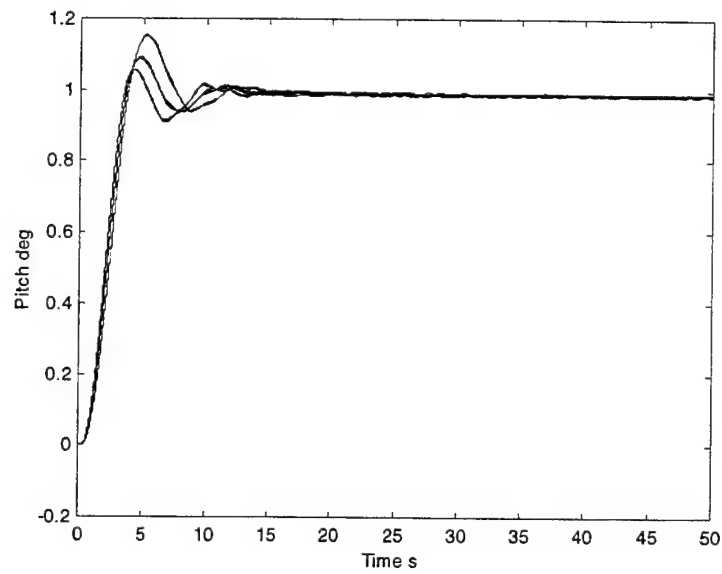


Figure F.27 – Reduced-Order MU Optimal H_2 Design 1- σ Step Response History

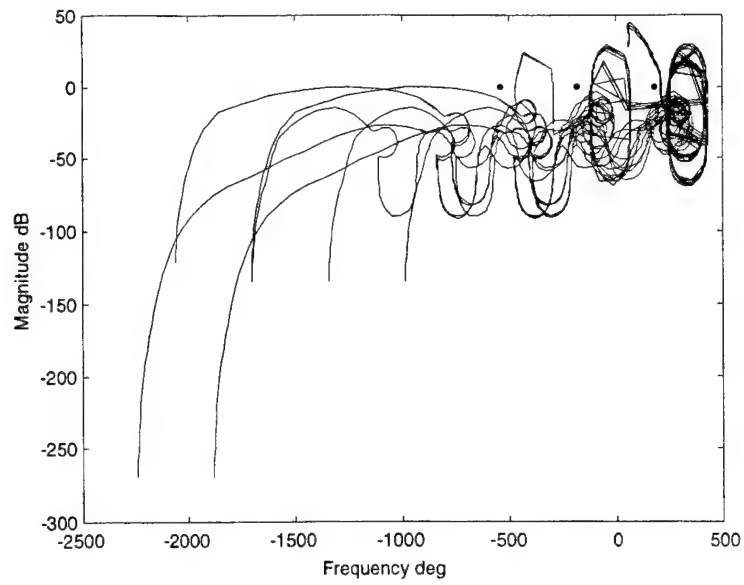


Figure F.28 – Reduced-Order MU Optimal H_2 Design 1- σ Nichols Plot History

Bibliography

- [1] Jean-Pierre Babka, *H₂ and H-Infinity Control-Structure Integrated Design*. Masters Thesis, MIT, CSDL-T-1138, June 1992.
- [2] Nazareth Sarkis Bedrossian, *Nonlinear Control Using Linearizing Transformations*. Masters Thesis, MIT, CSDL-T-1104, September 1991.
- [3] Michael E. Begley, *Derivation of the Shuttle Ascent Equations of Motion for Linear Stability Analysis*. Lockheed Engineering & Sciences Company, GN&C D&AS-95-101, Preliminary Release, January 1995.
- [4] John J. Best, *Model-Reference Adaptive Techniques Applied to a Ballistic Missile Autopilot*. Masters Thesis, MIT, January 1961.
- [5] John H. Blakelock, *Automatic Control of Aircraft and Missiles*, Second Edition. John Wiley & Sons, Inc. New York, 1991.
- [6] Frederick W. Boelitz, "Kistler Launch Assist Platform Return Burn Control," *Proceedings of the AIAA Guidance, Navigation, and Control Conference*, Boston, MA, August 1998.
- [7] William Fenton Bonnice, *Steering of a Boost Vehicle to a Desired Flight Path Angle Trajectory Using Angle of Attack Control*. Masters Thesis, MIT, CSDL-T-802, February 1983.
- [8] Patrick D. Brown, *Micro Air Vehicle Control Design: A Comparison of Classical and Dynamic Inversion Techniques*. Masters Thesis, MIT, June 1999.
- [9] Bernd Clauberg, *Adaptive Control of a Small Autonomous Underwater Vehicle*. Masters Thesis, MIT, CSDL-T-1102, July 1991.

- [10] Michael A. Corvin, *Ascent Guidance for a Winged Boost Vehicle*. Masters Thesis, MIT, CSDL-T-1002, August 1988.
- [11] Gene F. Franklin, J. David Powell, and Abbas Emami-Naeini, *Feedback Control of Dynamic Systems*, Addison-Wesley Publishing Company, Reading, Massachusetts, 1986.
- [12] J. Doyle, K Glover, P. Khargonekar, and B. Francis, "State-Space Solutions to Standard H_2 and H_∞ Control Problems," *IEEE Transactions on Automatic Control*, vol. AC-34, 1989.
- [13] Arthur L Greensite, *Analysis and Design of Space Vehicle Flight Control Systems*, Spartan Books, New York, 1970.
- [14] Irene M. Gregory, "Dynamic Inversion to Control Large Flexible Transport Aircraft," *Proceedings of the AIAA Guidance, Navigation, and Control Conference*, Boston, MA, August 1998.
- [15] Simon C. O. Grocott, Jonathan P. How, and David W. Miller, *Comparison of Control Techniques for Robust Performance on Uncertain Structural Systems*. MIT Space Engineering Research Center, SERC #2-94, January 1994.
- [16] Kelly Douglas Hammett, *Application of Multivariable Control System Design Methodologies to Robust Beam Control of a Space-Based Laser*. Masters Thesis, MIT, CSDL-T-1078, June 1991.
- [17] Michael Brain Jamoom, *Constrained Optimization for Hierarchical Control System Design*. Masters Thesis, MIT, CSDL-T-1344, June 1999.
- [18] D. L. Johnson, editor, *Terrestrial Environment (Climatic) Criteria Guidelines for Use in Aerospace Vehicle Development*, Revision, NASA Technical Memorandum 4511, August 1993.
- [19] Cornelius T. Leondes, editor, *Guidance and Control of Aerospace Vehicles*, McGraw Hill, New York, 1963.

- [20] Beau V. Lintereur, *Constrained H_2 Design via Convex Optimization with Applications*. Masters Thesis, MIT, CSDL-T-1306, June 1998.
- [21] Timothy McQuade, Lt Col, USAF, *Astro 444: Modern Control*, Course Lecture Notes, United States Air Force Academy, Spring 1998.
- [22] Alexandre Megretski, 6.241: *Dynamic Systems and Control*, Course Lecture Notes, MIT, Fall 1998.
- [23] Alexandre Megretski, 6.245: *Modern Control Systems*, Course Lecture Notes, MIT, Spring 1999.
- [24] Douglas C. Montgomery, *Design and Analysis of Experiments*, Fourth Edition, John Wiley & Sons, New York, 1997.
- [25] Katsuhiko Ogata, *Modern Control Engineering*, Third Edition, Prentice Hall, Upper Saddle River, NJ, 1997.
- [26] Charles L. Phillips, and Royce D. Harbor, *Feedback Control Systems*, Second Edition, Prentice Hall, Englewood Cliffs, NJ, 1991.
- [27] William C. Reigelsperger, Siva S. Banda, and David P. Lemaster, "Application of Multivariable Control Theory to Aircraft Control Laws," *Final Report*, Flight Dynamics Directorate, Wright Laboratory, Wright-Patterson AFB, OH, WL-TR-96-3099, May 1996.
- [28] Amitabh Saraf, Girish Deodhare, and Debasish Ghose, "A Feedback Linearization Based Nonlinear Controller Synthesis to Recover an Unstable Aircraft from Post-Stall Regime," *Proceedings of the AIAA Guidance, Navigation, and Control Conference*, Boston, MA, August 1998.
- [29] G. Stubbs, A Penchuk, and R. Schlundt, "Apollo Guidance, Navigation, and Control," *Proceedings of the AIAA Guidance, Control, and Flight Mechanics Conference*, Princeton, NJ, August 1969.
- [30] H. Phillip Whitaker, *Design Capabilities of Model Reference Adaptive Systems*. MIT Instrumentation Laboratory, R-374, July 1962.

- [31] Gary Thomas Wilson, *Applications of H-Infinity and MU Synthesis*.
Masters Thesis, California State University, Long Beach, December 1992.
- [32] Kemin Zhou, *Essentials of Robust Control*, Prentice Hall, Upper Saddle
River, NJ, 1998.